Silesian University of Technology

Ph.D. Thesis

Optimization of polygeneration systems using hydrogen as an energy carrier

Hamed Ghiasirad

Supervisor: Prof. Anna Skorek-Osikowska

Discipline: Environmental Engineering, Mining and Energy

Gliwice, Poland, 2025

Author:
Hamed Ghiasirad, MEng.
Silesian University of Technology
Joint Doctoral School
hamed.ghiasirad@polsl.pl

Supervisor:
Anna Skorek-Osikowska, Prof.
Silesian University of Technology
Faculty of Energy and Environmental Engineering
Department of Power Engineering and Turbomachinery
anna.skorek-osikowska@polsl.pl

Polish title:

Optymalizacja systemów poligeneracyjnych wykorzystujących wodór jako nośnik energii

Acknowledgements

I owe my deepest gratitude to my supportive supervisor, Prof. Anna Skorek-Osikowska, for her steadfast guidance, and generous encouragement throughout this work. I am especially grateful for her trust and for the inspiring research environment she fostered, one that I hope to continue contributing to after the PhD.

I also thank Towhid Gholizadeh for collaboration on our publications and projects, and Prof. Łukasz Bartela, Dr. Michał Jurczyk, and Jakub Ochmann for providing invaluable datasets and technical insights from the CAES energy storage experiments.

I am deeply grateful to my MSc supervisors, Prof. Rahim Khoshbakhti Saray and Dr. Siamak Mirmasoumi, for their guidance and for providing access to the experimental dataset from the anaerobic digestion system.

I gratefully acknowledge the formative LCA training received during my internships: at Karlstad University in Sweden with Dr. Ali Mohammadi and Dr. Farinaz Ebrahimian, and at Forschungszentrum Jülich in Germany with Dr. Christina Wulf.

I am profoundly grateful to my supportive family, whose encouragement helped me overcome life's challenges. I also thank all my colleagues at HMC and my Iranian friends in Gliwice. Without their companionship and support, living here would have been difficult.

I also wish to thank the Silesian University of Technology and the TrANsMIT COST Action CA21127 entitled Techno-economic analysis of carbon mitigation technologies for the awards and grants for accommodation, publications, my participation in internships, conferences, workshops, and training courses.

Finally, I gratefully acknowledge the support of the National Science Centre, Poland. Financial assistance was provided by grant no. 2021/41/B/ST8/02846 within the framework of the research project entitled Production of fuels and energy in the systems with negative CO2 emissions using high-temperature electrolysis and with oxygen management.

Abstract

Achieving deep decarbonization of fuels while preserving energy security demands pathways that convert renewable electricity and biogenic carbon into drop-in energy carriers with credible efficiency, cost, and environmental performance. Hydrogen is central to this challenge: as a clean intermediate and design variable, it can couple electrolysis, heat recovery, oxygen and carbon management, and fuel synthesis into polygeneration systems that co-produce gaseous and liquid fuels. This dissertation tests the hypothesis that electrolyzer-centric integration of hydrogen with targeted separations and thermal–power coupling can systematically raise conversion efficiency, reduce levelized costs, and lower cradle-to-gate impacts. Using Aspen Plus, EES, and SimaPro software, a unified framework links detailed thermodynamic modeling with techno-economic assessment and both attributional and consequential life-cycle analysis (LCA) across eight configurations: biogas-to-methanol (baseline and with LNG cold-energy recovery and oxy-fuel gas turbine), biomass-to-methanol via gasification (with and without compressed-air/thermal energy storage), three green-ammonia plants using electrolysis or gasification and water gas-shift (WGS) reactions, and a Fischer–Tropsch sustainable aviation fuel (SAF) route. Key performance indicators include overall energy efficiency, levelized cost of fuel, global warming potential (GWP), and fossil resource depletion (FDP).

Across routes, integration around the solid-oxide electrolysis cell (SOEC) is the dominant lever. The biomass-to-methanol system augmented with compressed-air and thermal energy storage converts transient waste heat into steady biomethanol and delivers approximately 95% efficiency, a levelized cost near 602 $/tonne, and a GWP around 0.135 kgCO2eq/kgFuel. In a gasification-based polygeneration case that co-produces natural gas and biomethanol with utilized oxygen and CO2 management, the plant attains about 82% efficiency, a levelized cost near 961 $/tonne, a GWP around 0.167 kgCO2eq/kgFuel, and an FDP around 0.0345 kgoileq/kgFuel. capital expenditure is concentrated in the electrolyzer and synthesis loop. A wind-powered biogas-to-methanol configuration with LNG cold-energy recovery and an oxy-fuel turbine achieves a GWP near 0.206 kgCO2eq/kgFuel and an FDP near 0.042 kgoileq/kgFuel.

For ammonia, outcomes hinge on the WGS design and the electrolyzer operating window. The biomass-to-ammonia plant with a counter-current membrane WGS reactor is preferred, reaching roughly 54.6% efficiency, a levelized cost near 513 $/tonne, and a GWP around 0.175 kgCO2eq/kgFuel due to superior hydrogen recovery and integrated management of hydrogen, oxygen, and nitrogen.

The sustainable aviation fuel pathway clarifies trade-offs for highly electrified fuels: electrical efficiency is about 56.2%, and a representative cost around 1893 $/tonne with a GWP near 0.464 kgCO2eq/kgFuel.

The electrolyzer and fuel-synthesis sections dominate investment. Electricity sourcing is decisive: wind power markedly improves environmental indicators, reducing GWP and FDP significantly relative to Poland's grid, while current grid prices remain more economical.

Collectively, for optimizing the design rules: prefer high-temperature SOEC where thermal integration is feasible. adopt counter-current membrane water-gas-shift for ammonia. recover LNG cold energy and use oxy-fuel gas turbines where grid relief and flue-gas recycling are priorities. co-produce gaseous and liquid fuels to hedge electricity-price volatility. and prioritize renewable electricity when environmental performance dominates.

Keywords:

Optimization, Hydrogen energy, LCA, Techno-economic analysis, Biofuels, CCUS

Streszczenie

Osiągnięcie głębokiej dekarbonizacji paliw przy równoczesnym zachowaniu bezpieczeństwa energetycznego wymaga ścieżek, które przekształcają odnawialną energię elektryczną oraz biogeniczny węgiel w nośniki energii typu drop-in, o wiarygodnych parametrach sprawnościowych, kosztowych i środowiskowych. Wodór odgrywa w tym kluczową rolę: jako czysty produkt pośredni i zmienna projektowa może sprzęgać elektrolizę, odzysk ciepła, zarządzanie tlenem i węglem oraz syntezę paliw w układy poligeneracyjne współwytwarzające paliwa gazowe i ciekłe. Niniejsza rozprawa weryfikuje hipotezę, że integracja zorientowana na elektrolizer, łącząca wodór z ukierunkowanymi separacjami oraz sprzężeniem cieplno-elektrycznym, może systematycznie podnosić sprawność konwersji, obniżać poziomowy koszt paliwa i redukować oddziaływania typu cradle-to-gate. Z wykorzystaniem Aspen Plus 12.1 i SimaPro 10.2 opracowano zunifikowane ramy analityczne łączące szczegółowe modelowanie termodynamiczne z oceną techno-ekonomiczną oraz atrybucyjną i konsekwencyjną analizą cyklu życia dla ośmiu konfiguracji: biogaz → metanol (układ bazowy oraz wariant z odzyskiem chłodu LNG i turbiną tlenową), biomasa → metanol przez gazyfikację (z magazynowaniem energii w sprężonym powietrzu i cieple oraz bez niego), trzy zielone ścieżki produkcji amoniaku oparte na elektrolizie lub gazyfikacji oraz reakcji water–gas shift (WGS) oraz wariant zrównoważonego paliwa lotniczego (SAF) metodą Fischera–Tropscha. Kluczowe wskaźniki efektywności obejmują całkowitą sprawność energetyczną, poziomowy koszt paliwa (LCOF), potencjał tworzenia efektu cieplarnianego (GWP) oraz wskaźnik wyczerpywania zasobów kopalnych (FDP).

We wszystkich ścieżkach główną dźwignią pozostaje integracja wokół elektrolizera stałotlenkowego (SOEC). System biomasa → metanol, uzupełniony o magazynowanie energii w sprężonym powietrzu i cieple, zamienia przejściowe strumienie ciepła odpadowego w stabilną produkcję biometanolu i osiąga ok. 95% sprawności, koszt ok. 602 USD/t oraz GWP rzędu 0,135 kgCO$_2$eq/kg paliwa. W przypadku poligeneracji opartej na gazyfikacji, współwytwarzającej substytut gazu ziemnego oraz biometanol przy skoordynowanym zarządzaniu tlenem i CO$_2$, uzyskano ok. 82% sprawności, koszt ok. 961 USD/t, GWP ok. 0,167 kgCO$_2$eq/kg paliwa oraz FDP ok. 0,0345 kg ropy ekw./kg paliwa. Nakłady inwestycyjne koncentrują się na elektrolizerze i pętli syntezy. Konfiguracja biogaz → metanol zasilana energią wiatrową, z odzyskiem chłodu LNG i turbiną tlenową, osiąga GWP ok. 0,206 kgCO$_2$eq/kg paliwa oraz FDP ok. 0,042 kg ropy ekw./kg paliwa.

Dla amoniaku wyniki zależą od konstrukcji układu WGS oraz zakresu pracy elektrolizera. Preferowany jest wariant biomasa → amoniak z przeciwprądowym, membranowym reaktorem WGS, który osiąga ok. 54,6% sprawności, koszt 513 USD/t oraz GWP ok. 0,175 kgCO$_2$eq/kg paliwa dzięki lepszemu odzyskowi wodoru i zintegrowanemu zarządzaniu wodorem, tlenem i azotem.

Ścieżka zrównoważonego paliwa lotniczego uwidacznia kompromisy charakterystyczne dla paliw silnie zelektryfikowanych: sprawność elektryczna wynosi ok. 56,2%, koszt reprezentatywny ok. 1 893 USD/t, a GWP 0,464 kgCO$_2$eq/kg paliwa. Sekcje elektrolizera i syntezy dominują w strukturze nakładów inwestycyjnych. Kluczowe jest źródło energii elektrycznej: zasilanie wiatrowe wyraźnie poprawia wskaźniki środowiskowe, istotnie obniżając GWP i FDP względem polskiej sieci, podczas gdy obecne ceny energii z sieci pozostają korzystniejsze ekonomicznie.

Podsumowując, reguły optymalizacji projektowej są następujące: preferowanie wysokotemperaturowych SOEC tam, gdzie możliwa jest integracja cieplna; dla amoniaku – stosowanie przeciwprądowego, membranowego układu WGS; odzysk chłodu LNG i wykorzystanie turbin tlenowych tam, gdzie priorytetem jest odciążenie sieci oraz recyrkulacja spalin; współwytwarzanie paliw gazowych i ciekłych w celu ograniczenia ryzyka związanego ze zmiennością cen energii elektrycznej; oraz priorytetowe traktowanie energii odnawialnej w sytuacji dominacji kryteriów środowiskowych.

Słowa kluczowe:

Optymalizacja, energetyka wodorowa, analiza cyklu życia (LCA), analiza techno-ekonomiczna, biopaliwa, CCUS (wychwytywanie, wykorzystanie i składowanie CO_2).

Table of Contents

Nomenclature

4SCP	Four stage compressors	PP	Payback period, years
A	Active area, m^{2}	P^{0}	Partial pressure, bar
ANS	Annual net saving, $	$\dot{Q}$	Heat transfer, kW
BtA	Biomass-to-ammonia	Q_{0,H_2}	Hydrogen permeability (kmol m^{-1} h^{-1} kPa$^{-0.5}$)
C	Cost of equipment, $	R	Inflation rate / Universal gas constant (kJ kgmol^{-1} K^{-1})
$C_{i,base}$	Capital cost of equipment i at reference year	RF	Ratio factor
		RDF	Real discount factor
$C^{*}_{cap,i}$	Capital cost of equipment i at the current year	RES	Renewable energy sources
$C_{op,i}$	Operating cost of quantity i	r_{NH_3}	Reaction rate (kmol kg^{-1} h^{-1})
CAES	Compressed air energy storage	RWGS	Reverse water gas shift
CO	Co-current	S	Size of components
CC	Counter-current	SBR	Steam-to-biomass ratio
Comp	Compressor	SUP	Superheater
CRF	Capital recovery factor	SS	Sewage sludge
d	Diameter (m)	TCI	Total capital investment, $
D^{eff}	Diffusion, m^{2}/s	TCC	Total capital cost
e^{-}	Electron	TOC	Total operating cost
ER_{O_2}	O$_2$-equivalence ratio	U	Overall heat transfer coefficient, W/m^{2}K
E_{act}	Energy of activation, J/mol	V	Voltage, V
ECO	Economizer	$\dot{W}$	Electricity rate, kW
Eq	Equivalent	WGSR	Water gas shift reaction
EVA	Evaporator	y_i	Mole fraction of species i
f	Scale factor	z	Flow direction (m)
F	Constant of Faraday, °C/mol	$\dot{Z}$	Cost rate of components, $/h
FCI	Fixed capital investment, $	***Greek letters***	
FG	Flue gas	δ	Thickness, m
GT	Gas turbine	η	Efficiency, %
HRSG	Heat recovery steam generation	γ	Factor of pre-exponential, $\frac{\mathrm{A}}{\mathrm{m}^{2}}$
HX	Heat exchanger	φ	Operating and maintenance factor / Consumption rate of quantity
i	Current density (A cm^{-2}) / interest rate	ρ_b	Bulk density (kg m^{-3})
IF	Inflation factor	ρ_{cat}	Catalyst density (kg m^{-3})
J	Current density, A/m^{2}	Δ	Difference
k_b	Kinetic rate constant for backward reaction (kmol m^{-3} h^{-1} bar$^{0.5}$)	τ	Operating hours
k_f	Kinetic rate constant for forward reaction (kmol m^{-3} h^{-1} bar$^{-1.5}$)	***Subscripts***	
K_{eq}	Equilibrium constant (-)	a	Anode
LCA	Life cycle assessment	act	Activation
LCOA	Levelized cost of ammonia, $/tonne	c	Cathode
LHV	Low heating value, kJ/kg	CP	Compressor
LCOF	Levelized cost of fuel, $/tonne	conc	Concentration
M	Mixer	en	Energy
MEEP	Minimum energy efficiency point	e	Electrolyte
MSU	Methanol synthesis unit	i	Anode, cathode, and electrolyte
n	Number of transferred electrons, 2 / plant's lifetime (year)	N	Nernst equation
N	Cells number	Ohm	Ohmic
NGT	Natural gas turbine	REB	Reboiler
NPV	Net Present Value, $		
P	Pressure, bar		
PtA	Power-to-ammonia		

1. Introduction

Climate change driven mainly by greenhouse gas (GHG) emissions remains a critical threat to sustainable development. In the EU, emissions decreased overall between 1990 and 2022, reaching 3.2 billion tonnes of CO_2 equivalent, or 31% below 1990 levels. The EU has committed to reduce emissions by 55% by 2030, 90% by 2040, and achieve net-zero by 2050. As shown in Fig. 1.1, the largest sources are energy-producing industries (27%), transport (26%), and fuel combustion in other sectors (25%), land use and forestry offset about 7% of emissions. In Fig. 1.1, Poland's emission profile in 2022 shows land use acting as a small sink (−9.5%), while the energy industry remains the dominant contributor at 45.7%, followed by transport (18.8%), fuel combustion by other users (19.6%), agriculture (8.7%), industry (6.1%), and waste management (1.1%). These figures indicate that deep decarbonization of Poland's energy industry is crucial to achieving national and EU climate targets [1].

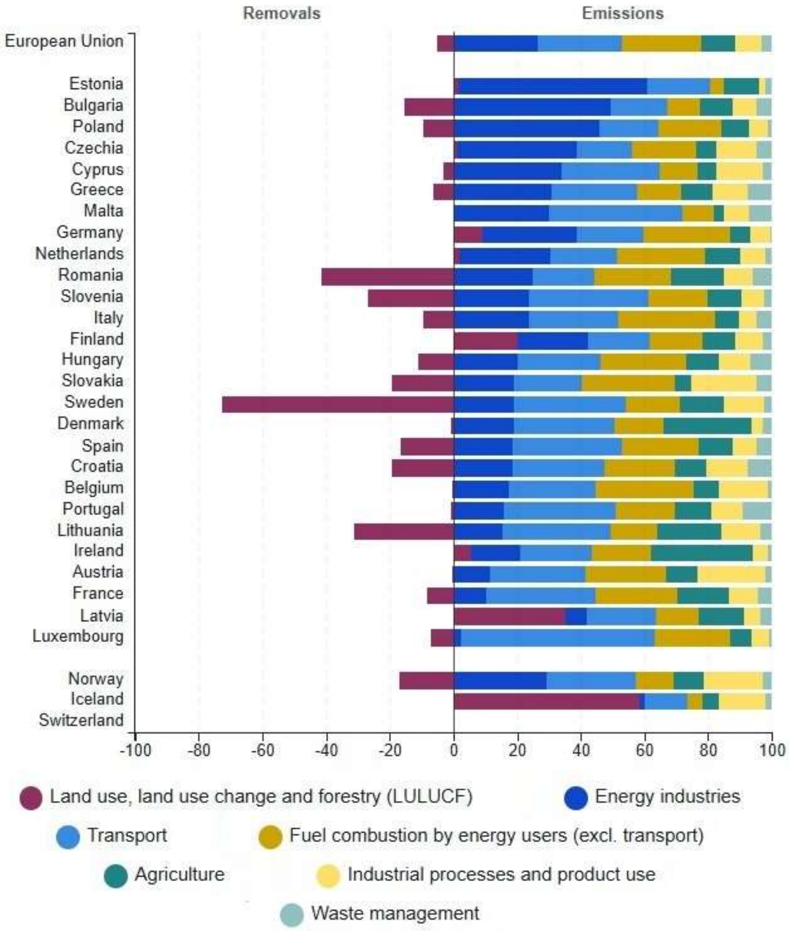

Fig. 1.1. Share of greenhouse gas emissions and removals by sector in 2022 [1].

In this regard, under the European Climate Law, the EU goal is to cut net GHGs by at least 55% by 2030 and reach climate neutrality by 2050. The EU 2030 mitigation strategies include [2]:

- A tighter EU Emissions Trading System (ETS) delivering −62% vs 2005.
- The Effort Sharing Regulation requiring −40% vs 2005 in transport, buildings, and agriculture.
- The Renewable Energy Directive (RED III) mandating +42.5% renewables in final energy.

- A binding energy-efficiency target of −11.7% vs 2020 projections.
- A land use net-removal target of 310 $MtCO_2eq$ in 2030.

In which, the first and third strategies have the largest contributions. The work plan of the first strategy called EU ETS includes [2]:

- Coal/lignite retirement.
- Renewable energy storage build-out.
- Grid reinforcement and demand response.
- Flexible gas turbines prepared for biomethane, H_2, and carbon capture.
- In steel, shift basic furnace toward green H_2 and renewable energy.
- In cement, lower clinker factor.
- Enhance carbon capture pilots.
- In chemicals and refining, electrify steam/heat and replace grey H_2 with renewable H_2
- In aviation, ramp sustainable aviation fuels including e-kerosene.
- In shipping, pilots with e-methanol/green ammonia.

As listed above, hydrogen energy recurs across virtually all ETS sectors. The third mitigation strategy called renewables share sets the parallel requirement to scale wind, solar and other renewables, which both decarbonize power directly and provide the zero-carbon electricity needed to produce renewable hydrogen. Consequently, rapid renewable energy deployment and green hydrogen production and use are the most decisive, system-level lever to deliver the EU's 2030 climate objectives.

1.1. Renewable energy

The EU's binding renewable-energy targets, policies, and funding mechanisms set the context and constraints. Within the EU, the energy mix is steadily moving away from polluting fossil fuels and toward renewable energy sources such as wind, solar, and hydro power, alongside nuclear energy. As shown in Fig. 1.2, renewable energy produced 46% of power demand in the EU in 2023. Nuclear energy followed with 28.6%, offering a stable, low-carbon option while solid fuels (including coal) accounted for 16.6%, natural gas for 5.3%, and crude oil for just 3.4%, demonstrating a clear shift away from high-emission sources to renewables.

In Poland, however, renewables accounted for 25.6%. This comparison underscores how critical it is for Poland to accelerate its transition toward renewable energy. Increasing the share of renewables would not only align the country with EU climate targets but also reduce its dependence on carbon-intensive sources, improve air quality, and promote long-term energy security. As EU policies and funding mechanisms support green energy infrastructure, Poland has a unique opportunity to modernize its energy sector and contribute to a healthier, more sustainable Europe [1].

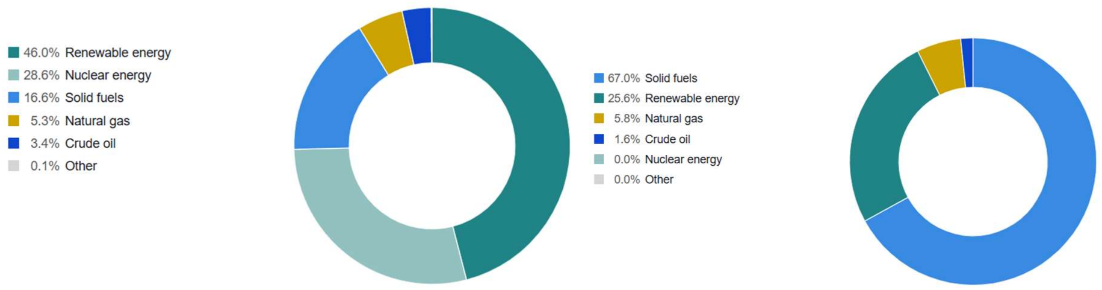

a) EU b) Poland

Fig. 1.2 Share of energy production by source in 2023 [1].

1.2. Biomass Conversion

Bioenergy is a key clean hydrogen pathway and supplies carbon- and energy-rich streams essential for low-carbon fuels. This section clarifies the feedstocks, co-products, and integration points that optimization of hydrogen-based polygeneration systems leverages. Main biomass conversion plants are divided into anaerobic digestion and biomass gasification.

Anaerobic digestion, shown in Fig. 1.3, converts wet organic feedstocks such as livestock manure, wastewater biosolids, food waste, and other organics including fats, oils, greases, and crop residues, processed singly or in co-digestion, into two saleable streams: biogas and digestate. The raw biogas typically contains about 50–75% CH_4 with CO_2, water vapor, H_2S, and trace gases. it can be combusted on site for heat, electricity, or cooling, or upgraded by removing CO_2, H_2S, and moisture to produce renewable natural gas (RNG) compatible with pipeline injection, suitable for compression/liquefaction as vehicle fuel, and usable as a platform gas for advanced energy carriers and biochemicals, while co-produced CO_2 from upgrading may be valorized in controlled-environment agriculture or other markets where purity standards are met. The digestate leaving the digester is a nutrient-rich slurry that is commonly separated into solid and liquid fractions to maximize value: the solids, after dewatering and conditioning, are used as animal bedding, organic fertilizer or compost, soil amendments, or as feedstock for bio-based materials (e.g., building products and bioplastics components). The liquid fraction is applied to fields as a fertilizer or used for crop irrigation following appropriate treatment, with optional nutrient-recovery operations (e.g., ammonia stripping or struvite precipitation) producing concentrated, transportable N/P fertilizers. Across these pathways, electricity and heat generation, vehicle fuel/RNG supply, horticulture products, organic fertilizers, animal bedding, bio-materials, and irrigation, AD can generate direct revenues and significant cost offsets (avoided bedding purchases, displacement of synthetic fertilizers, tipping fees for waste handling), thereby improving both the project economics and net environmental performance while advancing circular nutrient management and renewable energy deployment [3].

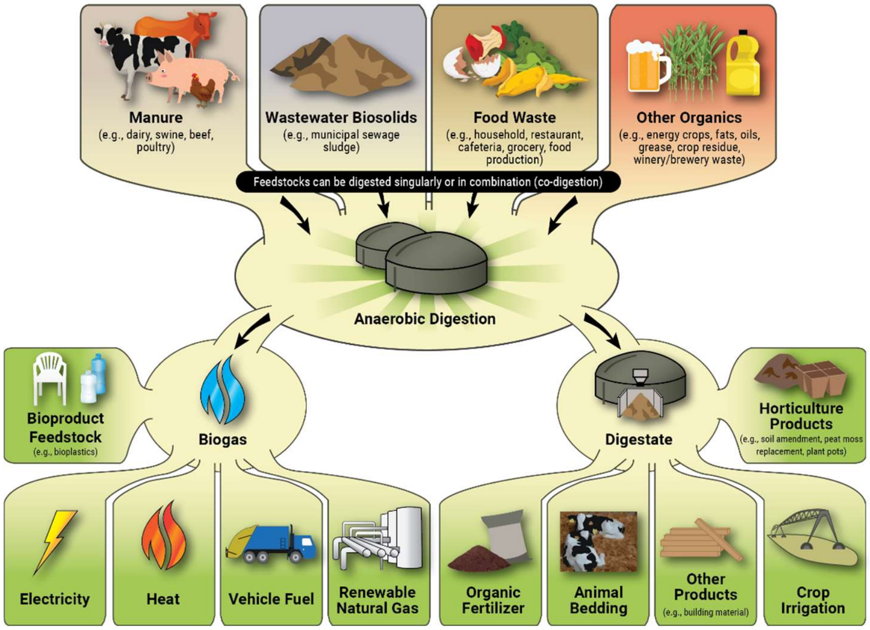

Fig. 1.3 Feedstocks and applications of anaerobic digestion plant [3].

The gasification system illustrated in Fig. 1.4 demonstrates a complete waste-to-energy conversion process with a strong focus on hydrogen-rich syngas production and its applications in power systems, fuels, and chemicals. The process begins with the intake of diverse feedstocks, including municipal solid waste (MSW), industrial waste, general organic waste, and biomass such as agricultural residues and wood chips. These materials are rich in carbon and hydrogen, making them suitable for syngas production through thermal decomposition. Within the gasifier, under limited oxygen or air with or without steam, the feedstocks undergo drying, pyrolysis, combustion, and reduction stages. This thermochemical breakdown results in the formation of syngas, a combustible mixture primarily composed of hydrogen (H_2), carbon monoxide (CO), methane (CH_4), and carbon dioxide (CO_2). By optimizing operating conditions, particularly by using steam as the gasifying agent, the hydrogen content in syngas can be enhanced through water-gas shift reactions. Following gasification, the syngas passes through a critical gas cleanup and cooling stage to remove tar, particulates, acid gases, and heavy metals. This purification is essential for maximizing hydrogen usability, especially in high-efficiency systems like fuel cells. The clean hydrogen-rich syngas can then be utilized in various applications. For power generation, it can fuel internal combustion engines, gas turbines, or be fed into hydrogen fuel cells to generate electricity with high efficiency and low emissions. In the biofuels sector, hydrogen from syngas is essential for Fischer–Tropsch synthesis to produce synthetic diesel and jet fuel, as well as for methanol, ethanol, and ammonia production. Additionally, hydrogen serves as a valuable feedstock in industrial chemical processes, including hydrogenation and polymer synthesis. Altogether, this gasification platform offers a robust pathway for transforming waste into high-value hydrogen, reinforcing its role in decarbonizing power, transport, and chemical sectors in alignment with the global hydrogen economy [4], [5].

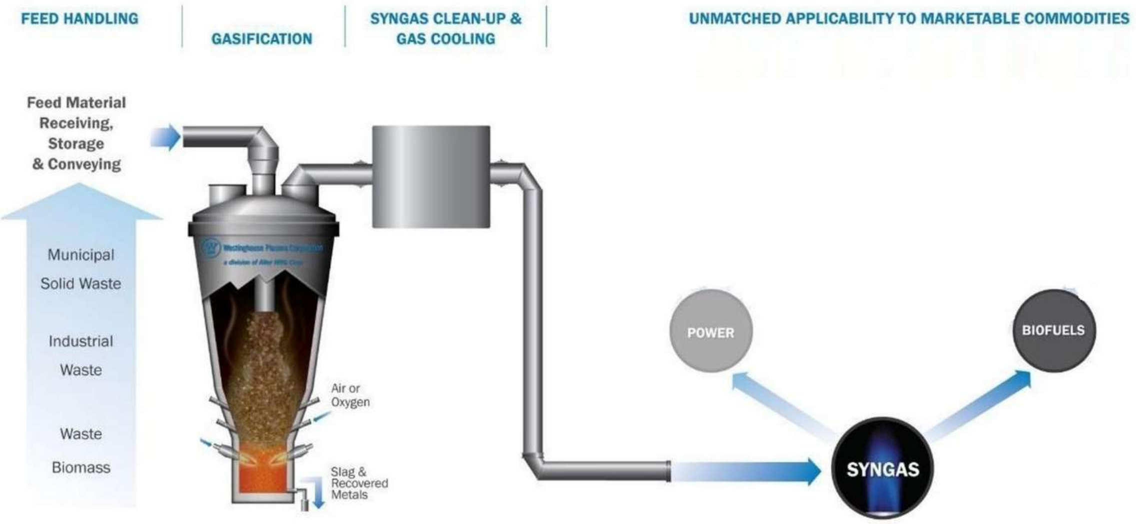

Fig. 1.4 Scheme of a gasification process [5].

1.3. Hydrogen production

Hydrogen energy becomes a strategic pillar of EU decarbonization, linking large-scale renewable integration with deep emissions cuts especially in hard-to-abate sectors. Fig. 1.5 shows the projections of hydrogen production methods across 100 years. In 2020, production is dominated by fossil routes (80%), while clean routes are marginal. Deeper into the century the clean share becomes 100%, with electricity expanding to roughly 50%, gas-CCS holding 25%, coal-CCS shrinking to 3%, and bioenergy with/without CCS holding 20%. In gas- or coal-based hydrogen with CCS, the hydrogen is produced for use, while the associated CO_2 emissions from syngas and/or flue gases are the streams that are captured, conditioned, transported, and permanently stored to minimize life-cycle impacts.

To achieve net-zero emissions, hydrogen production should be scaled up via pathways based on renewable electricity and bioenergy. Practically, this means targeting more than 60% electrolytic hydrogen by the mid-2030s and more than 80% by 2050, with the balance 20–30% supplied by bio-hydrogen while keeping unabated fossil at 0%. Electrolysis powered by renewables is technologically mature, which directly links H_2 scale to renewable build-out and to flexible operation to absorb variable wind and solar. Bio-H_2 with CO_2 capture complements this by delivering dispatchable output and durable removals to counter residual emissions elsewhere, provided strict sustainability and biomass-availability constraints are observed.

To sum up, the figure’s trajectory already points to a clean system. a net-zero-aligned strategy doubles down on the two cleanest levers, renewable-powered electrolysis and biomass with CCS.

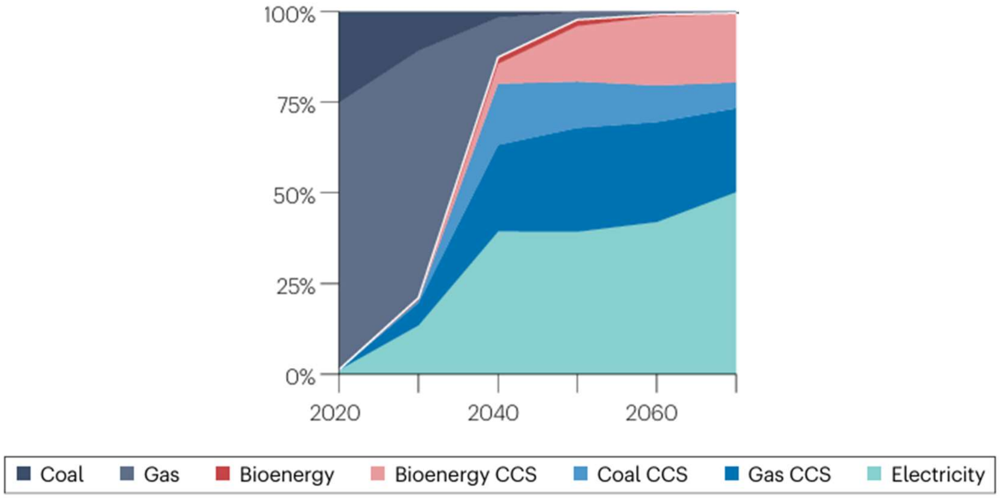

Fig. 1.5 Projections of hydrogen production methods to limit global warming to below 1.5 °C [6].

1.4. Hydrogen production using electrolysis cells

This section follows from the policy and system framing by detailing the electrolysis technologies that physically enable the hydrogen supply underpinning the polygeneration pathways. By comparing alkaline (AEL), proton exchange membrane (PEMEL), and solid oxide electrolyzer (SOEL) on efficiency, dynamics, integration potential, and cost, it provides the technical and parametric basis for subsequent optimization, design choices, and environmental analysis across the proposed hydrogen-centered systems. As shown in Fig. 1.6, electrolyzer converts electrical energy into chemical energy by splitting water into hydrogen and oxygen under direct current. At the cell level, anode and cathode are separated by a liquid electrolyte or solid membrane that conducts ions (H^+ or OH^-) while limiting hydrogen and oxygen crossover. porous transport layers and bipolar plates manage reactant distribution, bubble removal, current collection, and mechanical support. Multiple cells are clamped in series to form a stack, with spacers, gaskets, frames, and end plates ensuring electrical insulation, hydraulic sealing, and manifolded flows. Surrounding this, the balance conditions inputs and outputs: AC power is transformed and rectified to regulated DC, deionized water is supplied and cooled, and product gases are separated. Prior to compression and storage, the hydrogen stream is catalytically deoxygenated and then dried, while oxygen is vented or valorized. In operation, purified water is delivered to the electrodes through flow fields, ions traverse the electrolyte, and the membrane maintains product purity. Although water electrolysis has been known since 1800, advances in catalysts, membranes, and power electronics now enable efficient, continuous production of high-purity hydrogen from renewable electricity [7].

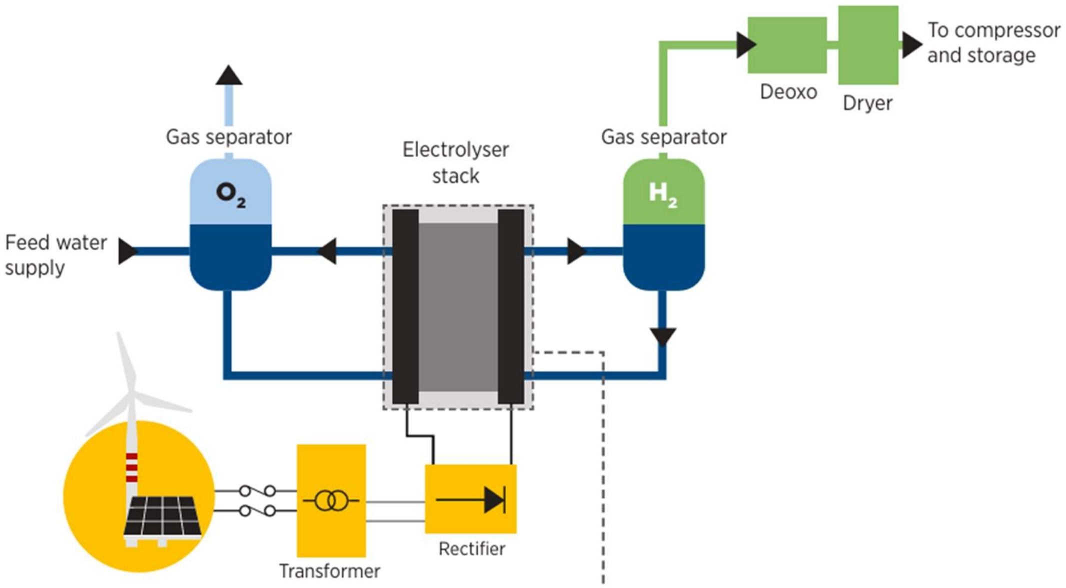

Fig. 1.6. System level diagram of an electrolysis cell [7].

According to Fig. 1.7, alkaline electrolysis is the most mature option, with the lowest specific investment and maintenance costs and many suppliers (single-stack units up to 6 MW). It typically operates at modest current densities (0.25–0.45 A/cm^2) with 55–75% LHV efficiency. Designed historically for steady, stationary duty, AEL requires adaptation for highly dynamic operation and has a limited turndown (20–25%) to avoid H_2/O_2 cross-contamination. cold starts are slower, though once at temperature load steps are sub-second.

Proton exchange membrane electrolyzer have advanced rapidly into the MW class (pilot plants up to 6 MW. several vendors with MW-scale stacks). Their strengths are compactness via high current density (1.0–2.0 A/cm^2, extendable), pressurized operation, short start-up (especially from cold), and stable operation over the full load range, enabling fast grid-responsive service. Efficiency is broadly comparable to AEL (50–80% LHV), with a tendency to decline at very high current densities as capital cost per area falls [8].

Solid-oxide electrolysis remains pre-commercial (early pilots), but operates at high temperature with steam, achieving the highest efficiencies. Beyond efficiency, SOEC can run reversibly (electrolyzer/fuel-cell) and co-electrolyze H_2O and CO_2 to produce syngas, opening direct e-fuel routes. The key development needs are durability, cycling stability, and pressurized operation under flexible duty [8].

For comparison, AEL offers the lowest upfront cost but is constrained in turndown and footprint. PEMEL delivers compact, pressurized, highly dynamic operation at higher current densities with similar efficiency to AEL. SOEC, however, is intrinsically better where high-temperature heat or steam is available: it cuts electricity consumption via endothermic operation, valorizes industrial waste heat, and enables reversible and co-electrolysis pathways that integrate directly with e-fuel and industrial processes. As manufacturing scales and durability improves, these system-level advantages position SOEC as the superior choice for lowest-energy, deeply integrated green-hydrogen and syngas production, while PEMEL and AEL remain pragmatic near-term choices for high-cycling and low-CAPEX baseload applications, respectively [8].

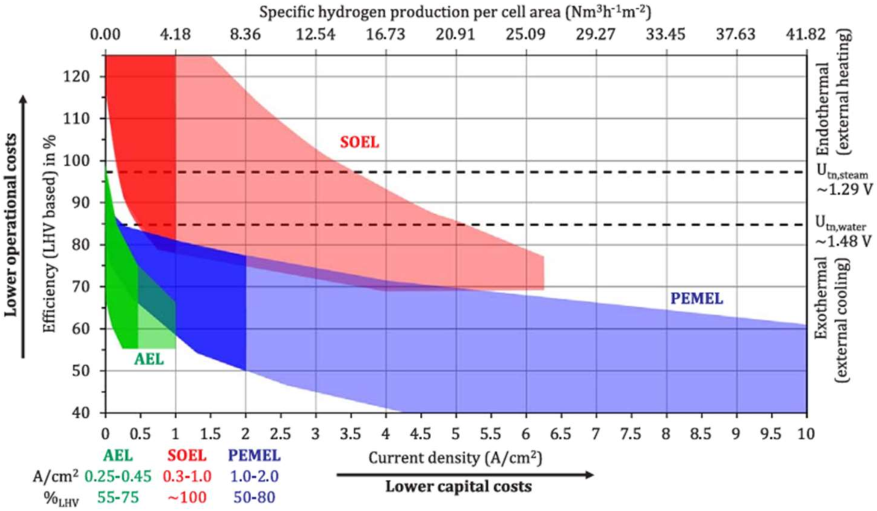

Fig. 1.7 Comparison of thermo-economic performance of three electrolysis cells [8].

High temperature electrolyzer are devices designed for electrochemical energy conversion [9]. For this purpose, they use electricity and heat supplied in the form of steam. High-temperature electrolyzer can use hydrogen H^+ or oxygen O_2^- ions as charge carriers [10], [11]. Many studies have been done on the use of high-temperature electrolysis cells. For example, Schiller et al. [12] created an experimental setup using SOEC to generate hydrogen. In their operating system, the SOEC stack needs 1.65 kWh of electricity, which can produce 1600 L of hydrogen in 4 h. From a thermodynamic point of view, the use of a high-temperature heat source is crucial, as it reduces power demand and enhances efficiency. Thus, this system takes advantage of solar heat to generate steam. Their unit includes a solar simulator, a steam generator, an accumulator, and a SOEC stack. The amount of steam generated in this unit is 5 kg/h, of which 0.58 kg/h is mixed with 10% of hydrogen recirculated from the product, then the mixture enters a SOEC with 12 cells. They concluded that 93% electrical efficiency could be achieved when a system operates at the steam temperature of 770 °C with a current density of 1.25 A/m^2 and a steam conversion rate of 70%. As it results from experimental and theoretical studies it can be profitable to benefit from high-temperature electrolysis cells instead of low-temperature ones, and to employ the exothermic condition to decrease the need for additional heat for the SOEC and mix some part of hydrogen with steam entering the SOEC. Recently, Jolaoso et al. [13] indicated that the SOEC system utilizes the steam generated from the flue gas as input and can be seamlessly integrated with various power production units, such as coal and natural gas-fired power plants. To assess the viability and environmental impact of this novel technology, a comprehensive levelized cost of hydrogen and a technoeconomic analysis have been conducted. The results show that the SOEC system achieves an efficiency of 97.4% and a thermal-to-hydrogen efficiency of 56.3%, allowing a daily production of 242400 kg of hydrogen in a cost range of \$2.9 to \$3.5 per kilogram of hydrogen.

1.5. Hydrogen storage challenges

Hydrogen's storage and safety constraints make direct hydrogen logistics sub-optimal, thereby prioritizing conversion into denser, infrastructure-compatible energy carriers. Optimization targets power-to-X and biomass-to-X polygeneration pathways, where hydrogen is utilized immediately to produce fuels/chemicals that reduce system risk while enabling deep decarbonization. Hydrogen's physical properties make bulk storage and logistics intrinsically challenging and safety-critical. It forms flammable mixtures across a very wide concentration range in air (4–75 vol %) and has a very low ignition energy, so small leaks can ignite easily. These fundamentals drive strict design and operational controls for any storage installation [14]. In practice, compressed-gas storage commonly operates at 35–

70 MPa, while liquid hydrogen requires cryogenic handling with boil-off losses that are difficult to eliminate, all of which necessitate venting systems and raise hazard potential. Beyond flammability and cryogenics, materials degradation is a persistent risk: exposure to high-pressure hydrogen can embrittle pipeline and vessel steels, reducing ductility and integrity under load. These hazards are reflected in regulatory frameworks that impose specialized siting, separation distances, venting, bonding/grounding, and equipment-qualification requirements for both gaseous and liquefied hydrogen systems—underscoring the non-trivial safety burden of H_2 storage. Finally, leakage matters for climate, too: hydrogen may be an indirect greenhouse gas, and value-chain emissions can erode near-term climate benefits if not tightly controlled [15].

Given these constraints, using hydrogen through power-to-X (PtX) or biomass-to-X (BtX) pathways is often more practical and safer from a storage/logistics standpoint. Converting hydrogen (from renewable electricity or biomass-derived syngas/biogas) into bioproducts yields energy carriers that are denser, storable under milder conditions, and compatible with existing tanks, pipelines, and bunkering infrastructure. Leading analyses note that derivatives are easier to transport over long distances and integrate into today's systems. In short, where direct on-site hydrogen use is not feasible, PtX or BtX vectors shift risk from high-pressure/cryogenic/hydrogen storage to better-understood chemical logistics, while still enabling deep decarbonization in fuels, chemicals, and hard-to-abate sectors [16].

1.6. Hydrogen applications

This section defines the major, near-term demands for hydrogen utilization to target polygeneration configurations. Hydrogen applications justify the case studies and set the optimization objectives. Table 1.1. displays the main hydrogen applications in industries. Its necessary applications are reported below:

- Refining and hydrogenation: Replace fossil-derived grey H_2 with green H_2 in hydrocracking and desulfurization.
- Fertilizer/ammonia: Ammonia (NH_3) is generated from N_2 and H_2 via Haber–Bosch for fertilizers and as a potential H_2 carrier/fuel.
- Methanol platform: Low-carbon H_2 and biogenic/captured CO_2 produce methanol (CH_3OH), a key intermediate for chemicals and an emerging transportation fuel.

There are some other possible applications of hydrogen listed below.

- Long-haul shipping and aviation: Hydrogen enables drop-in or near-drop-in fuels via power and biomass to X (PBtX).
- Chemical feedstocks: Substitute grey H_2, co-electrolyze H_2O/CO_2 to syngas for carbon containing products.
- Primary steel: Direct-reduced iron with H_2, coupled with electric arc furnaces.
- Long-duration energy storage: Power-to-hydrogen via electrolysis and storage.
- Biogas upgrading: Inject H_2 and hydrogenate CO_2 in raw biogas to raise CH_4 content (catalytic/biological methanation), producing pipeline-grade renewable methane.

As can be seen in Table 1.1 and its description above, refining, hydrogenation, fertilizer/ammonia, methanol, shipping, aviation, chemical feedstocks, biogas upgrading are the main applications of hydrogen for feedstocks conversion and hard-to-electrify segments via PtX and BtX.

Table 1.1. Hydrogen applications in different industries [6].

Primary alternative	Necessary	Possibly
Biomass	Refining	Shipping

Biogas	Hydrogenation	Aviation
CO_2 capture and storage (CCS)	Ammonia	Chemical feedstock
Electricity	Methanol	Steel plant
Batteries	Fertilizer	Long-duration energy storage
		Biogas upgrading

1.6.1. Power and biomass to methane

Power and biomass to methane is one of the hydrogen application in which electrolytic H_2 and O_2 integrates with biomass conversion to produce methane from biogenic CO/CO_2. Biomethane production is a single, integrated chain in which biomass conversion supplies a syngas that is cleaned, compressed, and fed to a fixed-bed methanation unit operated at 350 °C. to meet natural-gas-grid specifications, the synthesis is run with non-stoichiometric feeds. Biomass-to-methane (BtM), where H_2 contained in syngas limits conversion and unreacted CO_2 is captured downstream. and power-to-methane (PtM), where surplus renewable electricity produces additional H_2 via electrolysis and the co-produced O_2 is valorized as a steam-oxy gasifying agent, enriching carbon oxides and avoiding N_2 dilution. Water condensed after methanation can be recycled to electrolysis. Cold-gas efficiency of the PBtM process is found to be 63-77%.

Under 2022 market conditions, PtM becomes cost-competitive against natural gas part or most of the year, while all concepts provide grid-injectable biomethane and a pathway for long-duration energy storage using existing gas infrastructure [17].

1.6.2. Power and biomass to methanol

Renewable H_2 enables CO_2-to-methanol synthesis, a core PBtX pathway for polygeneration optimization. Methanol is produced by directly hydrogenating captured CO_2 with renewable H_2 over a Cu/Zn/Al/Zr catalyst at 250 °C and 50 bar with recycle control to an optimal stoichiometric number and downstream distillation to 99% purity. relative to a syngas-route baseline, the simplified CO_2 to methanol scheme eliminates energy-intensive CO/CO_2 separation and shift steps, raising process energy efficiency and carbon efficiency while cutting utility use. Its carbon efficiency reaches 96%, and the minimum selling price is 0.94 $/kg in the base case, indicating potential market-level competitiveness. When CO2 is biogenic from biomass conversion plants, the same unit operations define biomethanol with the same performance envelope but better environmental impacts [18].

1.6.3. Power and biomass to ammonia

Ammonia is a key product in hydrogen applications where electrolytic or biomass-derived H_2 is coupled with air separation and Haber–Bosch reactor to yield ammonia. Ammonia synthesis is implemented as a Haber–Bosch fixed-bed reactor at 370 °C and 30 bar where nitrogen separated from air and hydrogen produced react to form NH_3. The configuration constitutes power-to-ammonia when using electrolysis. Conversely, sourcing H_2 from biomass conversion systems with air separation for N_2 constitutes biomass-to-ammonia [19].

1.6.4. Power and biomass to jet fuel

In the process of jet fuel production, electrolytic H_2 and O_2 integrate with biomass conversion and Fischer–Tropsch reactor. It directly supports the thesis by motivating polygeneration designs that optimize efficiency, product yields, and process integration for hydrogen-centric systems. Power-and-biomass-to-jet fuel systems comprise an integrated thermochemical chain in which biomass is oxygen-blown in a gasifier at 1400 °C and 30 bar to syngas, followed by gas cleaning, reverse water gas shift

(RWGS) reactor, acid-gas removal, and Fischer–Tropsch synthesis in a slurry bubble column reactor with Co-catalyst at 230 °C, 20 bar, and a H_2/CO ratio of 2.1. the FT liquids (C_5^+) are then hydro processed to the kerosene (C_8–C_{16}) jet-fuel cut. PBtX augments BtX with renewable electrolysis, using O_2 from the electrolyzer as the gasification oxidant, displacing air separation, and H_2 to raise the H/C ratio of syngas and drive RWGS, which lifts carbon efficiency from 40% (BtX) to 67–97% with product yields twice higher [20].

1.7. Summary

In summary, while power-to-methane (PtM) is technologically well-resolved and widely studied, offering grid-injectable synthetic natural gas for long-duration storage and integration with electrolysis/oxygen-blown biomass gasification, its role is largely confined to gaseous energy services.

This thesis, however, will focus on liquid fuels production via power-and-biomass-to-liquid (PBtL) processes. Many industries, especially aviation, shipping, and heavy transport, still rely on liquid fuels which behave like conventional fuels yet can approach carbon-neutrality when the emitted CO_2 is circularly reused. This is an emerging but promising bridge from variable renewables to hard-to-electrify sectors. Transport of liquid fuels leverages existing global liquid chemical/fuel logistics. Within PBtL, it is important to note [18], [19], [20]:

- Biomethanol's role as a versatile platform chemical and energy feedstock gateway to formaldehyde, acetic acid, and as a liquid energy carrier for transport and power sectors. Methanol also enables downstream conversion to dimethyl ether (DME) or to light olefins, broadening decarbonization options across fuels and chemicals while valorizing captured CO_2.
- Ammonia production retains the Haber–Bosch synthesis block while enabling carbon-lean hydrogen sourcing. Ammonia's high volumetric hydrogen density and ease of liquefaction make it an attractive hydrogen carrier and seasonal energy vector, alongside established and emerging applications in fertilizers, refrigeration, and low-carbon power generation
- These FT jet fuels are drop-in hydrocarbons suitable for aviation and co-produced diesel/Nafta, addressing long-distance transport where high volumetric energy density and compatibility with existing combustion hardware are critical

1.8. State of the Art

This section reviews the state of the art in hydrogen-based routes for biomethanol, ammonia, and biojet fuel production, with emphasis on how different systems shape plant efficiency, levelized cost, and life-cycle impacts. It synthesizes advances in process intensification alongside emerging evidence from techno-economic and environmental analysis.

1.8.1. State of the Art in biomethanol production

This section surveys prior work on hydrogen-enabled biomethanol pathways to understand how H_2 integration affects efficiency, cost, and environmental performance of biofuel systems. It identifies progress and gaps to motivate the optimization framework and case studies developed in this thesis. Several researchers have studied power-to-methanol plants using electrolysis cells. In this regard, Su et al. [21] presented a new system for methanol production, integrating hydrogen obtained via water electrolysis with CO_2 separated from a gas plant. The research demonstrated that units producing renewable methanol utilize 1.045 times more power than traditional systems. Furthermore, traditional methanol synthesis generates three times more greenhouse gas emissions compared to renewable methanol systems. Subsequently, Moioli et al. [22] examined the technological, environmental, and economic aspects of methanol production through CO_2 hydrogenation, employing hydrogen obtained from proton exchange membrane electrolysis and CO_2 sourced from natural gas fields. They discovered that integrating hydrogen production with methanol synthesis, both before and after incorporating a heat exchanger network, resulted in overall energy efficiencies of 48.39% and 55.16%, respectively. Economically, methanol production costs were estimated at 1040.17 and 1669.56 $/tonne for scenarios including photovoltaic grids and batteries. Environmentally, the total CO_2-equivalent emissions were recorded at 0.244 and -0.016 kg/MJ of methanol for the photovoltaic grid and battery scenarios, respectively.

CO_2 emissions from fossil fuels, trapped for millions of years, increases atmospheric CO_2 levels. However, biogenic CO_2 originates from organic matter. Plants absorb CO_2 through photosynthesis. Then, biogenic CO_2 can be combined with green hydrogen to produce biomethanol, offering a pathway to mitigate climate change [23]. Accordingly, Hernandez et al. [24] aimed to identify the most suitable organic waste to produce various biofuels integrated with biogas reforming. Their optimal biomass was found to be sludge to produce cost-effective fertilizer. Nugroho et al. [25] conducted techno-economic and life cycle assessments of two biomethanol plants based on anaerobic digestion or gasification of biomass. They found that the production of methanol from biogas is more cost-effective and environmentally friendly compared to that of gasification technology. Rinaldi et al. [26] presented an in-depth analysis of the techno-economics of a biogas-to-methanol process through steam reforming. Their process was specifically designed to treat biogas derived from the anaerobic digestion of municipal solid waste. The optimal plant configuration was determined to be one in which carbon dioxide separation occurred upstream of the reformer. In the baseline scenario, their configuration yielded a carbon and fuel efficiency of 51.4% and 72.2%, as well as a levelized cost of methanol of 378 €/t. Reducing the pressure of the methanol reactor to 50 bar resulted in nearly constant methanol production but substantially lower overall costs, with a levelized cost of methanol of 357.7 €/t. Fedeli et al. [27] explored the synthesis of biomethanol using the biogas reforming method. The results of environmental analysis revealed a reduced carbon footprint associated with biomethanol technology compared to the simple production of biomethane by CO2 capture and a biogas-based combined heat and power system based on biogas. Furthermore, a thorough analysis of capital expenditure and operating expenditure demonstrated the economic viability of the biomethanol plant. Furthermore, there are several works that aim to assess production of methanol using high-temperature electrolyzer and a biomass gasification unit. As an example, Rivera-Tinoco et al. [28] compared SOEC and PEM electrolyzer to produce methanol in terms of their economics. In their comparison, SOEC has higher capital investment costs, while PEM electrolyzer has higher operating and maintenance costs. The unit cost of methanol using the SOEC and PEM electrolyzer is, respectively, 15 and 2.5 times higher than the market price of methanol. Therefore, some important improvements are necessary for electrolysis systems to make them profitable. Furthermore, Lonis et al. [29] analyzed an integrated system for the generation of methanol using hydrogen produced in SOEC. In their system, simple thermal integration and thermal energy storage (TES) are considered to transfer the extra heat from the SOFC to the methanol synthesis unit (MSU) and SOEC. Their overall efficiency improved from 27.58 to 32.93% by introducing a TES. Chen et al. [30] has conducted a comparative economic and environmental study of a solar and biomass-based methanol generation unit. Their work includes three configurations to produce methanol, namely a conventional coal driven system, a solar-based coal gasification unit, and a solar-biomass-based CO2 hydrogenation plant. Their results show that the environmental impacts of a solar-biomass-driven CO2 hydrogenation method are 57.5% less than that of a basic coal-fueled unit, making the third system a negative greenhouse gas (GHG) emission system. However, the third system is five times more expensive than the basic one, while the second system can be economically feasible by considering the carbon tax level until 2030. Wang et al. [31] validated a co-electrolyzer of H2O and CO2 by isothermal 6000 h SOEC stack for a quasi-2D modeling. They compared four power-to-X technologies, namely methane, methanol, dimethyl ether, and gasoline, from a techno-economic viewpoint. Their results revealed that the efficiencies based on higher heating values (HHV) continuously decreased from 94% for SOEC to 64% for power-to-gasoline. In addition, Ali et al. [32] investigated a novel biomethanol generation system that benefits from a biomass gasification unit and a solid oxide electrolysis cell (SOEC). Their system benefits from oxygen produced in the SOEC that is supplied to the gasifier and the autothermal reformer (ATR). Their combined system had a thermal efficiency of 72.08%, while the same system achieved an efficiency of 55.7% without a SOEC. As an improvement, they could recover the low-grade waste heat from the methanol synthesis unit (MSU). Then, Zhang and Desideri [33] economically optimized a power-to-methanol system that included CO2 and H2O co-electrolysis in a SOEC. Power-to-methanol systems can tackle some obstacles such as a considerable amount of energy storage and carbon capture and utilization. In their new co-electrolyzer, steam, CO2, and some hydrogen produced enter the cathode, and some of the produced O2 enters the anode. The proposed system achieved a high energy efficiency of 72% but is not cost-effective due to factors such as the high price of the SOEC stack, short lifetime of the stack, and high unit cost of power. Bos et al. [34]designed a novel wind-powered electrolysis that provides hydrogen to a methanol plant to which CO2 is added from direct air capture. They showed that CO2 air capture, electrolysis and methanol synthesis systems are responsible for 50%, 45%, and 5% of capital investment costs, respectively. Subsequently, Im-orb et al. [35] analyzed a biomass-based methanol production unit in which O2 is the gasification and partial oxidation agent. Their proposed system contains three gas pressure swing adsorption units (PSA) and a ZnO filter for H2S removal. They stated that the recycling of CO2 into the gasifier is not an efficient method and when gasifying temperature and the equivalence ratio are 750 °C and 0.25, the efficiency of the system will be maximized. Ishaq and Dincer [36] introduced a new concept for generating methanol and hydrogen using wind energy. The proposed approach uses industrial carbon emissions to produce methanol. The design of the system consists of several key components including wind turbines, a water electrolysis cell, a methanol production system, and a distillation unit. The overall efficiency of the system is evaluated as performance indicators, resulting in an exergy efficiency of 38.2% and an energetic efficiency of 39.8%. It should be noted that this integration produced 1648 tonne/yr of methanol and reduced annual CO2 emissions by 2999 tons. A techno-economic analysis (TEA) of a novel solar tower-based methanol generation system has been done by Monnerie et al. [37]. Their new system produces H2 and CO using a solar thermochemical plant for a CO2-free methanol synthesis unit. They modeled a case study for Almeria, Spain, in which the unit cost of methanol is found to be 1.14 €/L. Qin et al. [38] performed a techno-economic and environmental investigation of a coal and biomass co-gasification system to produce methanol by benefitting from the solar hydrogen generator. They showed that the addition of biomass to coal and solar-based hydrogen production deteriorates efficiency and cost objectives. However, they lead to a reduction of GHG emissions by 24.34%. Then, Ostadi et al. [39] examined three methods to increase methanol production utilizing hydrogen generated from water electrolysis, natural gas pyrolysis, or a combination of both processes. The use of hydrogen produced through natural gas pyrolysis showed the potential for greater economic attractiveness compared to that of electrolytic hydrogen produced using renewable electricity. Incorporating hydrogen into the methanol production process enhances carbon conversion efficiency by approximately a factor of two, increasing it from 44% to 94%. Considering an electrolyzer cost of 1000 $/kW, an electricity price of 50 $/MWh, a natural gas price of 5 $/GJ, and a carbon black selling price of 100 $/tonne, the design involving natural gas pyrolysis yields the lowest cost to produce methanol. Based on their analysis, the price of methanol could range from 300 to 1000 $/tonne. Their research involved significant consumption of fossil fuels during natural gas pyrolysis and use of electricity in the air separation unit.

As a result, some amounts of CO2 are emitted to the environment. Furthermore, they could harness the waste heat from the biomethanol synthesis unit.

1.8.2. State of the Art in energy storage integrated hydrogen utilization

This section surveys hybrid hydrogen and energy storage systems using high-temperature electrolysis integrations which motivate design choices that co-utilize waste heat and storage to boost efficiency, economic, and environmental performance. In addition to pumped storage installations, which currently most often perform this function, installations using hydrogen as an energy carrier and compressed air energy storage installations (CAES) are becoming increasingly popular. Both technologies have numerous advantages, but also certain disadvantages. This system presents the idea of hybridizing an installation using hydrogen as an energy carrier and a CAES installation to improve the efficiency of the installation and increase its operational flexibility.

Hydrogen in the biomethanol production system integrated with energy storage is produced via high temperature electrolyzer. It is therefore also possible to integrate high-temperature processes such as gasification, or fuel synthesis with this type of electrolyzer, because the heat generated during these processes can be used to reduce the energy demand of the electrolyzer [40]. This combination may offer great benefits when one of the processes is highly exothermic while the other requires significant amounts of heat. An important aspect of the discussed technology is the thermal integration of processes, which assumes maximum energy use within a closed loop of the installations and connects individual system chains. The concept therefore increases energy efficiency and decreases emissions of the system. Despite the fact that high-temperature electrolysis is not as mature technology as that used in low-temperature electrolysis process in proton exchange membrane and alkaline devices, which are mainly considered for design process of power to gas and power to gas to power installations [41], [42], however, many currently conducted studies indicate that high-temperature electrolyzer have greater potential for development and the possibility of cooperation with many energy installations of various types [11], [43].

The hybridization of energy storage systems is gaining popularity due to the implementation of a closed-cycle economy policy, which reinforces the need to maximize the energy potential of available energy carriers. In Table 1.2, recent articles on hybrid compressed air energy storage systems are presented.

Table 1.2. Recent articles on hybrid compressed air energy storage systems.

Reference	System variant	Cooperative system	Integration method
Ran et al [44]	Adiabatic	Solar thermal collector	Thermal oil as a circulating medium in the STC used in the process of heating air during the discharge phase
Kowalczyk [45]	Diabatic	Thermal Energy Storage, Gas Turbine, Turboexpander	Exhaust-air heat exchanger
Zheng et al [46]	Adiabatic	Reverse Osmosis desalination	The energy generated from the CAES expanders is used to power the reverse osmosis process
Wu et al [47]	Diabatic	Thermochemical Energy Storage	During the discharging stage, compressed air is released to oxidize cobalt monoxide
Houssainy et al [48]	Adiabatic	Low- and High Temperature Thermal Energy Storage	The system includes a low- and elevated temperature heat storage tank

Bartela [49]	Diabatic	Hydrogen utilization system and methanation reactor	The system assumes the use of a heat exchanger that integrates the CAES and Power to SNG systems

1.8.3. State of the Art in ammonia production

This section surveys the techno-economic and environmental state of green and biomass-based ammonia to optimize hydrogen-based polygeneration systems to define realistic design constraints and targets for the ammonia case studies. Ammonia is conventionally produced by converting natural gas to hydrogen via steam-methane reforming with a subsequent water–gas shift, followed by synthesis in the Haber–Bosch loop. Because this route relies on fossil natural gas, its cradle-to-gate footprint is about 2.6 $kgCO_2eq/kgNH_3$. As the world's second most-produced chemical, ammonia consumes roughly 2% of global fossil energy and releases over 420 Mt of CO_2 annually [50]. Market price of fossil ammonia is reported as 585 \$/tonne in February 2025 [51]. Considering the increase in global demand for ammonia because of its application in hydrogen energy storage and decarbonization, it seems necessary to shift from traditional production processes to more sustainable and green ones [52]. Hence, renewable-source-based routes should be considered to produce green hydrogen for ammonia synthesis units. Water electrolysis and biomass gasification, as two promising alternatives, are introduced for green hydrogen production via renewable electricity [53], mainly provided by solar and wind energies [54].

Techno-economic analysis and life cycle assessment of hydrogen energy systems is gaining lots of attention [55]. In this concept, economic and environmental analyses of an ammonia synthesis unit equipped with a proton electrolyte membrane electrolyzer cell revealed that the proposed plant, with a net present value and payback time of 40 M\$ and 4-6 years, respectively, could be a potential alternative route for green ammonia [56]. Generally, the cost of ammonia production through electrolysis technology strongly depends on the cost of renewable electricity [57]. For instance, the levelized cost of ammonia (LCOA) in the USA, where electrolyzer rely heavily on grid electricity, is 1.05 $\$/kg_{NH3}$. However, when LCOA is subsidized by selling electricity, LCOA decreases to 0.58 $\$/kg_{NH3}$ [58]. A comprehensive economic study on green ammonia production, based on electrolyzer technology and wind and solar energy for 350 locations in 70 countries, was made by [59]. The techno-economic investigation showed an LCOA of 473 \$/ton, which was predicted to drop to 310-350 \$/ton by 2030. However, Cesaro et al. [60] predicted an LCOA lower than 400 \$/ton for many locations in 2040 and less than 300 \$/ton as an optimistic case. An economic study was conducted to find the appropriate water electrolysis technology for the green ammonia plant. At the lowest electricity price and the highest learning rate, the alkaline electrolyzer was found to be the most cost-effective type with an LCOA of 174 \$/ton in 2045, while at the highest electricity price and highest learning rate, the solid oxide electrolyzer showed the best economic performance with an LCOA of 709.6 \$/ton [61]. Qi et al. [62] proposed a co-production of electricity and green ammonia with an LCOA of 360.74 €/ton (426.76 \$/ton) by integrating a solid oxide electrolyzer with liquid air energy storage. A comparative study in China has shown that producing green ammonia has a levelized cost of 820 \$/ton, which is approximately twice as much as producing grey ammonia [63]. The global potential of green ammonia plants based on photovoltaic-wind sources integrated with alkaline electrolyzer was techno-economically studied [64]. The results showed that LCOA could reach 260–290 €/ton (297-331 \$/ton) in 2050 from 440–630 €/ton (502-719 \$/ton) in 2020. Campion et al. [65] reported a PtA energy efficiency of 47%–48% and 52%–54% for alkaline electrolyzer-based system and solid oxide electrolyzer-based system, respectively. Also, the lowest LCOA of 842 €/ton (887 \$/ton) was obtained using an alkaline water electrolyzer powered with solar PV. In a recent study [66], the potential of

Australia, with its high capacity in solar and wind resources, was investigated to develop a cost-competitive green ammonia plant. The modelling results showed an LCOA of AU$756/ton and AU$659/ton in 2025 and 2030, respectively.

As mentioned earlier, biomass gasification is an alternative pathway to produce green hydrogen for ammonia production. Unlike water electrolysis, which produces pure H_2, a mixture of H_2, CO, and CO_2 is obtained in biomass gasification. First, the biomass gasification unit is coupled with a water-gas-shift (WGS) reactor to increase H_2 concentration. Then, to purify hydrogen and remove CO_2 content, which is poisonous for ammonia reaction catalyst, the high-content hydrogen stream passes through amine-based acid gas cleaning and methanation units [67]. The economic feasibility of an ammonia synthesis unit integrated with biomass gasification was compared with a standalone ammonia production case [68]. According to the results, LCOA was obtained at 458 and 523 €/ton (608 and 695 $/ton) for integrated and standalone production cases, respectively. In a similar study, an LCOA of 743 to 748 $/ton was reported by [69] by investigating the effect of three different gasification feedstocks. A techno-economic comparative study between two green ammonia plants and a conventional methane-based case was performed. The results showed that the power-to-ammonia (PtA) case could reach the highest energy efficiency of over 74%. Also, the LCOA for the biomass-to-ammonia (BtA) case was achieved at 450 $/ton, competitive with the methane-to-ammonia case with an LCOA of 400 $/ton [67]. In a case study in Portugal, a net present value and payback time of 3714 k€ (4394 k$) and 4.6 years were reported for a small-scale biomass-to-ammonia plant [70]. Some recent publications have analyzed biomass-to-ammonia-to-power (BtAtP) and power-to-ammonia-to-power (PtAtP) concepts thermodynamically [71] and techno-economically [72].

1.8.4. State of the Art in biojet fuel production

This section reviews state-of-the-art biojet fuel pathways, emphasizing subsystem integration, conversion efficiencies, costs, and life-cycle impacts. By synthesizing these findings, it pinpoints key design levers and remaining gaps that guide the optimization of hydrogen-enabled polygeneration routes for sustainable aviation fuel (SAF). Several studies have discussed power-and-biomass-to-liquid (PBtL) plants with electrolysis. Researchers from the National Energy Technology Laboratory (NETL), US, [73] focused on the production of Fischer-Tropsch jet fuel using coal and biomass to liquid (CBTL) process, evaluating both technical feasibility and compliance with the Energy Independence and Security Act (EISA) of 2007 greenhouse gas (GHG) emissions requirements. The novelty lies in analyzing twenty scenarios that combine coal and varying levels of biomass, including innovative biomass pretreatments such as torrefaction, to achieve reductions in greenhouse gas (GHG) emissions of up to 62.1% compared to conventional jet fuel. The results show that the efficiency of jet fuel production reaches 53.2%, with the global warming potential (GWP) ranging from 33.52 to 72.83 g CO_2e/MJ and required selling prices (RSP) ranging from $ 127 to $ 146 per barrel (approximately $ 0.92/L). Rafati et al. [74] conducted a techno-economic analysis of Fischer-Tropsch liquid fuel production from biomass gasification, demonstrating overall thermal efficiencies ranging from 41.3% to 45.5%. Cobalt-based FT processes achieved slightly higher efficiency. Co-feeding biomass and natural gas, each 200 MW_{th}, improved economic viability, reducing production costs from 28.8 $/GJ for biomass-only processes to 19–20 $/GJ while increasing liquid FT yields by 36%. Xu modeled a hybrid system that combined solid oxide electrolysis cells with Fischer-Tropsch synthesis, producing hydrocarbons with C5+ (pentane, hexane, heptane, and heavier hydrocarbons) fractions reaching 22%. The system demonstrated a significant reduction in electricity demand (up to 80% at elevated temperatures), highlighting its potential for efficient CO_2 utilization and low-carbon fuel production. Comidy et al. [75] evaluated the feasibility of producing liquid fuel on aircraft carriers using innovative technologies such as seawater acidification and Fischer-Tropsch synthesis. The analysis identifies three production pathways, including the integration of a reverse water gas shift reactor (RWGS) with an alkaline electrolyzer, solid oxide electrolyzer, and co-electrolyzer. Fuel costs ranged from 1.91 to 4.49 $/L, and carbon reductions during the life cycle were 82 to 86% compared to conventional aviation fuel. Guimar et al. [76] investigated the integration of biomass-to-liquid technology (BtL) with existing sugarcane ethanol facilities in Brazil, focusing on producing advanced biofuels through gasification and Fischer-Tropsch synthesis. It highlighted significant economic and technical challenges, such as high capital expenditures (over 30% of production costs) and low conversion efficiency (only 15% of carbon in biomass is transformed into fuels), while showing potential for economic feasibility with an internal rate of return (IRR) reaching 20% under optimal scenarios. Hillestad et al. [77] evaluated a process for PBtL integration that utilizes hydrogen from renewable energy sources to enhance the carbon efficiency of BtL fuel production. Innovation increased carbon efficiency from 38% to more than 90%, enabling a 2.4-fold increase in fuel production using the same biomass, with a specific power demand of 11–12 kWh/L. The levelized cost of producing biofuel with PBtL technology was estimated at 1.7 $/L, approximately 30% less than conventional methods. Dossow et al. [20] investigated an advanced PBtL process that combined biomass gasification, Fischer-Tropsch synthesis, and electrolysis, achieving carbon efficiencies of 67%-97% and fuel-biomass ratio yields up to 0.574. The key subsystems included oxygen-blown entrained flow gasification, sour water-gas-shift reactors, and solid oxide electrolysis. Cinti et al. [78] explored the integration of a solid oxide electrolyzer with a Fischer-Tropsch process to produce synthetic fuels. When comparing three system configurations, it demonstrated reductions of up to 73% in water consumption and 51% in CO_2 consumption, while achieving daily fuel production of one barrel (159 L) with a Fischer-Tropsch energy efficiency of 52.7%. Lee et al. [79] evaluated the global warming potential (GWP) of municipal solid waste (MSW)-derived fuels produced through gasification and Fischer-Tropsch (FT) processes, finding GWP values ranging from 80 to 105 g CO_2e/MJ. Implementing carbon capture and sequestration (CCS) significantly reduced the global warming potential (GWP) to as low as 36 gCO_2e/MJ. Recently, Almena et al. [80] investigated the environmental and economic performance of sustainable aviation fuel (SAF) produced by Fischer-Tropsch synthesis using forest residues integrated with carbon capture and storage (CCS) technology. Life cycle assessment (LCA) reveals that the production of Fischer-Tropsch synthetic paraffinic kerosene with carbon capture and storage (CCS) results in well-to-wake fossil emissions of 21.6 gCO_2eq/MJ while also achieving a net negative carbon flux of -20.0 gCO_2e/MJ when accounting for biogenic carbon sequestration. The blend of FT synthetic paraffinic kerosene with conventional jet fuel reduces fossil emissions by 37%, although the net carbon flux turns positive (30.9 gCO_2e/MJ) due to the blend. Economically, SAF production remains more costly than conventional fuels, but integrating CCS improves the carbon offset potential, significantly contributing to emission reduction targets, especially within the UK aviation sector. Michaga et al. [81] evaluate the environmental and economic feasibility of producing SAF from forest residues using the Fischer-Tropsch (FT) process integrated with bioenergy with carbon capture and storage (BECCS). Life cycle assessment (LCA) indicates that the BECCS configuration achieves significant environmental benefits, with a global warming potential (GWP) of -121.83 g CO_2eq/MJ of jet fuel. In contrast, the scenario without CCS shows a positive GWP of 15.51 gCO_2eq/MJ. Economically, incorporating CCS increases the minimum jet fuel selling price (MJSP) from 3.03 to 3.27 £/kg (5.10 to 5.51 $/L). Although SAF production remains costlier than conventional jet fuel, CCS integration enhances the process's environmental sustainability. Vela-Garca et al. [82] evaluated the environmental life cycle and economic performance of the production of biojet fuel from oleaginous crop residues using two thermochemical routes: Alcohol-to-Jet (ATJ) and hydro-processed esters and fatty acids (HEFA). Life cycle assessment (LCA) revealed a global warming potential (GWP) of 75 gCO_2eq/MJ for the ATJ process and 18 g CO_2eq/MJ for the HEFA process. These emissions are significantly lower than those from jet fuel derived from petroleum. Economically, the minimum bio jet fuel selling price ranges from 1.01 $/kg for HEFA to 1.43 $/kg for ATJ, with HEFA demonstrating better cost efficiency due to higher yields and simpler processing.

This review identifies cross-cutting research gaps in hydrogen-enabled biomethanol, ammonia, and biojet fuel pathways, particularly when co-integrated with thermal and compressed-air energy storage. Thermodynamically, integration of gasification, high-temperature electrolysis, and synthesis loops remain underdeveloped, with limited attention to efficiency enhancement by co-generation of liquid and gaseous fuels. Novel systems should focus on utilization of heat, oxygen, and CO_2. Techno-economic studies commonly assume steady operation and overlook flexibility valuation, revenue stacking (e.g., grid services, oxygen and heat monetization). Life-cycle assessments are heterogeneous in system boundaries and treatment of biomass sustainability. There are limited studies to compare LCA results by changing allocation strategies and sources of electricity. Pathway-specific needs include heat recovery of fuel synthesis units for carbon-utilization, surplus biofuels production, and tail-gas recycling for PBtL systems, and unified comparisons of energy, techno-economic, and LCA results with similar works. A coherent research agenda is to integrate CAES/TES energy storage systems, waste heat recovery, and synthesis units; and report harmonized KPIs of fuel capacity, energy efficiency, LCOF, and life cycle impacts to optimize hydrogen based polygeneration systems.

2. Motivation and scope of the thesis

2.1. Motivation

As variable renewable electricity penetrates power systems, process industries require pathways that can convert intermittent power into storable, value-added products while minimizing cost and environmental footprints. Hydrogen energy is pivotal in this transition as it enables deep process integration across electrolysis, biomass conversion, synthesis, and utilities. However, most prior assessments treat these units in isolation rather than as integrated polygeneration systems. This thesis is motivated by the premise that, at plant scale, coordinated use of hydrogen, oxygen, heat, and power, together with surplus energy storage and waste heat-recovery options, can unlock system-level advantageous unreachable by analysis of single components alone. To sum up, it is possible to increase efficiency, reduce costs, and avoid environmental footprints by design optimization of hydrogen utilization, biomass conversion, oxygen management, fuel synthesis, and utility subsystems.

2.2. Scope

The thesis develops and evaluates hydrogen-based polygeneration configurations for liquid biofuels production with a focus on biomethanol, ammonia, and bio-jet fuel. The work is model-based and encompasses:

- Building steady-state models for biomass digestion/gasification, alkaline and solid-oxide electrolysis, water–gas shift, CO_2 capture/recycle, methanol and ammonia synthesis, jet-fuel upgrading, and distillations.
- Representation of oxy-fuel gas turbines for power generation, LNG regasification for heat recovery, and energy recovery from compressed-air/thermal energy storage (CAES/TES).
- Thermodynamic analysis, heat integration, and energy efficiency calculations.
- Levelized cost metrics and cradle-to-gate life-cycle indicators for wind-powered systems, and benchmarking with Poland electricity mix.
- Design optimization and sensitivity analysis according to efficiency, cost, and emissions. robustness to electricity price and performance variability.

Across five new proposed polygeneration systems, the thesis seeks the best design for hydrogen utilization.

2.3. Hypothesis

To operationalize the thesis question, this subsection formulates testable hypotheses on how specific integration levers shape efficiency, cost, and environmental outcomes. These hypotheses structure the modeling and optimization tasks and define the metrics used to evaluate the eight proposed configurations. The thesis tests the following hypotheses: each phrased as a possibility enabled by process integration. Together they reflect the best choice for hydrogen use and the conducted energy, economic, environmental, and sensitivity analyses.

- It is possible to increase overall energy efficiency of plants by adopting high-temperature electrolysis.
- It is possible to improve plant performance by coupling oxy-fuel gas turbine and LNG cold-energy recovery.
- It is possible to manage oxygen utilization among subsystems.

- It is possible to raise production capacity by integrating CAES/TES energy storage systems.
- It is possible to improve techno-economic indicators through co-production of biofuels and natural gas.
- It is possible to decrease environmental footprints by powering the plant with wind energy instead of Poland electricity mix.

These hypotheses are evaluated across the eight proposed configurations. The intended outcome is to find which integration effectively increases efficiency, decreases cost, and reduces environmental impacts in hydrogen-driven polygeneration systems.

3. Process modeling of subsystems for hydrogen utilization

This section builds the transparent, equation-based models of all hydrogen-utilization subsystems that underpin the optimization of polygeneration systems. These validated models and assumptions provide the quantitative basis to evaluate the thesis hypotheses on how specific integration levers affect efficiency, cost, and environmental performance. The methodology employed for the energy analysis is thoroughly discussed. A comprehensive overview of the analytical approach is presented, including all relevant equations, modeling techniques, and computational procedures. Additionally, the underlying assumptions adopted throughout the analysis are clearly stated to ensure transparency and reproducibility. In this section, the methodology is presented for all the main subsystems present in the analysed later solutions. Main input data and assumptions of the proposed subsystems in this chapter are reported in Appendix.

3.1. Water electrolysis

Physics-based models for alkaline and solid-oxide electrolysis are modelled in Aspen Plus, to quantify hydrogen/oxygen production, voltage losses, and heat/power demands across operating conditions. These models provide the parametric backbone for optimizing hydrogen-centric polygeneration and for validating outcomes against literature data. Among the water electrolysis technologies, the alkaline type is known as the most mature commercially-available technology to produce hydrogen on a large scale. A typical alkaline cell is composed of a pair of electrodes (cathode and anode) separated by a porous diaphragm filled with an aqueous alkaline electrolyte solution [83]. Water splitting occurs at the cathode to form hydrogen through a reduction reaction, while oxygen molecules are generated at the anode. These half-reactions are called hydrogen/oxygen evolution reactions and are described as follows, respectively [84]:

Cathode half-reaction:

$$2\mathrm{H_2O(l)} + 2\mathrm{e^-} \rightarrow \mathrm{H_2(g)} + 2\mathrm{OH^-(aq)} \tag{3.1}$$

Anode half-reaction:

$$2\mathrm{OH^-(aq)} \rightarrow \frac{1}{2}\mathrm{O_2(g)} + \mathrm{H_2O(l)} + 2\mathrm{e^-} \tag{3.2}$$

In this thesis, the alkaline electrolysis operation is simulated using a model to predict the electrolysis operating voltage and determine the hydrogen and oxygen production rates at different operating conditions. The cell operating voltage and stack electrical power are calculated as follows:

$$V_{\mathrm{cell}} = V_{\mathrm{rev}} + \eta_{\mathrm{act}} + \eta_{\mathrm{ohm}} \tag{3.3}$$

$$W_{\mathrm{stack}} = i \cdot A_{\mathrm{cell}} \cdot N_{\mathrm{cell}} \cdot V_{\mathrm{cell}} \tag{3.4}$$

where, i, V_{rev}, η_{act}, and η_{ohm} are current density, reversible voltage, activation overpotential, and ohmic overpotential, respectively. Also, the following equations show hydrogen and oxygen production rates:

$$H_{2\,\mathrm{production}} = \frac{i \cdot A_{\mathrm{cell}} \cdot N_{\mathrm{cell}}}{n \cdot F} \cdot \eta_{\mathrm{F}} \tag{3.5}$$

$$O_{2\,\mathrm{production}} = \frac{i \cdot A_{\mathrm{cell}} \cdot N_{\mathrm{cell}}}{2 \cdot n \cdot F} \cdot \eta_{\mathrm{F}} \tag{3.6}$$

A detailed description of how to calculate above-mentioned equations is given in [84]. The experimental data are used to evaluate the accuracy of the alkaline electrolyzer electrochemical model. Fig. 3.1 compares cell voltage results between the theoretical model developed in this work and experimental values of ref. [85]. As can be seen, the electrochemical model accurately estimates cell voltage at different current densities and temperatures.

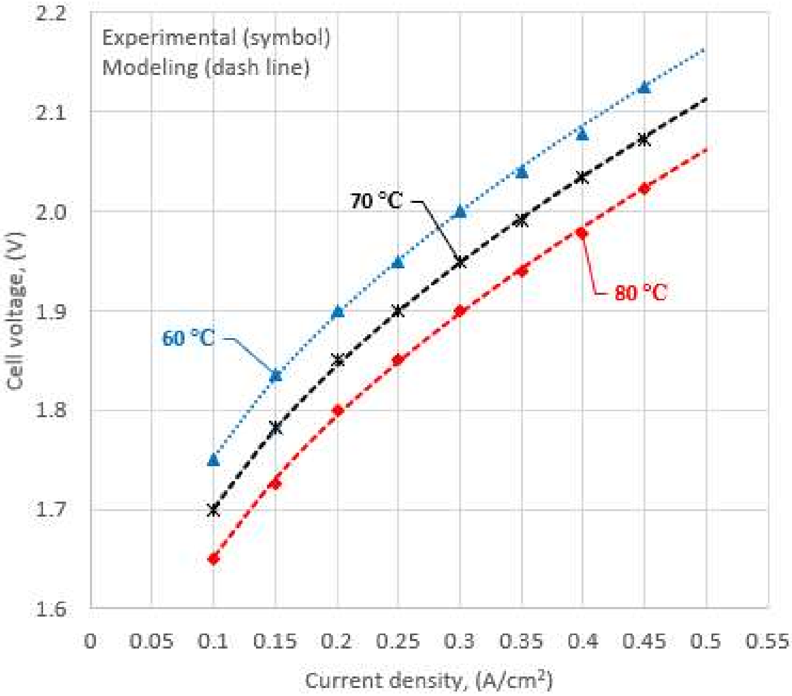

Fig. 3.1. Validation of the alkaline electrolyzer electrochemical model [85].

Fig. 3.2 shows a detailed schematic diagram of the solid oxide electrolysis cell (SOEC) subsystem. Water in state 39 passes through a series of heat exchangers, where it is converted into superheated vapor at state 42. Additional water from the phase separator (SEP 2) is then introduced, decreasing its temperature. Then, part of hydrogen and water (state 45) is mixed with vapor (state 44), and the mixture enters the SOEC stack, which needs additional input of heat and power. In the SOEC stack, 60% of water is converted to hydrogen and oxygen. After that, oxygen (state 48) is separated from the mixture in a separator (SEP 1) and is supplied to the gasifier and gas turbine units. Finally, the hydrogen cooler transfers heat to the economizer (ECO 2) in the gasification subsystem, and the separated hydrogen goes to the methanol synthesis unit.

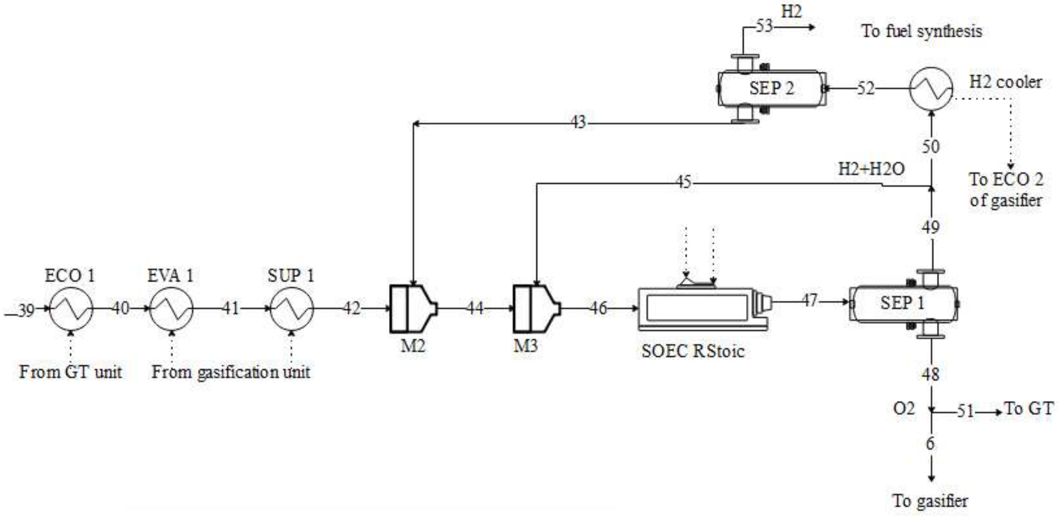

Fig. 3.2 Schematic diagram of the solid oxide electrolysis cell (SOEC) subsystem

All components of the proposed system were modeled using Aspen Plus. SOEC needs additional calculations that were written in the calculator of the Aspen Plus. The potential of the SOEC process was calculated by the following equation [86]:

$$V_{\mathrm{Cell}} = V_{\mathrm{N}} + V_{\mathrm{Ohm}} + V_{\mathrm{act,a}} + V_{\mathrm{act,c}} + V_{\mathrm{conc,a}} + V_{\mathrm{conc,c}} \tag{3.7}$$

The V value refers to the voltage and the subscripts N, Ohm, act, conc, a, c are the Nernst, Ohmic, activation, concentration, anode, and cathode, respectively.

The equilibrium voltage can be found by the Nernst equation as follows [86], [87]:

$$V_{\mathrm{N}} = V_{0,\mathrm{N}} + \left(\frac{RT}{2F}\right) \cdot \ln\left[\frac{P^0_{\mathrm{H_2}}\sqrt{P^0_{\mathrm{O_2}}}}{P^0_{\mathrm{H_2O}}}\right] \tag{3.8}$$

$$V_{0,\mathrm{N}} = -0.000281\,T + 1.2771 \tag{3.9}$$

In the above equations, N refers to the constant of Nernst equation, R is the ideal gases constant, T is the stack temperature, F is the Faraday's constant, and the P^0 is the partial pressure.

The ohmic polarization can be written as follows [88]:

$$V_{\mathrm{Ohm}} = J(\rho_{\mathrm{a}}\delta_{\mathrm{a}} + \rho_{\mathrm{c}}\delta_{\mathrm{c}} + \rho_{\mathrm{e}}\delta_{\mathrm{e}}) \tag{3.10}$$

In which J is the current density, δ is the thickness, and a, c and e refer to the anode, cathode, and electrolyte, respectively. The other unknown parameters can be calculated using the equations [88]:

$$\rho_a = 0.0000298\exp\left(\frac{-1392}{T}\right) \tag{3.11}$$

$$\rho_c = 0.0000811\exp\left(\frac{600}{T}\right) \tag{3.12}$$

$$\rho_e = 0.0000294\exp\left(\frac{10350}{T}\right) \tag{3.13}$$

The activation overpotential of the cathode and anode is calculated as below [88]:

$$V_{act,i} = \left(\frac{RT}{F}\right) \cdot \mathrm{Ln}\left[\left(\frac{J}{2J_{0,\mathrm{i}}}\right) + \sqrt{1 + \left(\frac{J}{2J_{0,\mathrm{i}}}\right)^2}\right] \tag{3.14}$$

$$J_{0,\mathrm{i}} = \gamma_{\mathrm{i}} \cdot \exp\left(-\frac{E_{\mathrm{act,i}}}{RT}\right) \tag{3.15}$$

where, R is ideal gases constant, T is the stack temperature, F is the Faraday constant, J is the current density, γ is the pre-exponential factor, E_{act} is the activation energy, and i refers to the anode or cathode.

According to Ref. [88], [89], the concentration overpotential of the anode and cathode can be found from the following equations:

$$V_{\mathrm{conc,c}} = \left(\frac{RT}{2F}\right) \cdot Ln \left[\frac{1 + \frac{JRT\delta_c}{2FD_{\mathrm{c}}^{\mathrm{eff}} P_{\mathrm{H_2}}^{0}}}{1 - \frac{JRT\delta_{\mathrm{c}}}{2FD_{\mathrm{c}}^{\mathrm{eff}} P_{\mathrm{H_2O}}^{0}}} \right] \tag{3.16}$$

$$V_{conc,a} = \left(\frac{RT}{2F}\right) \cdot Ln \sqrt{1 + \frac{JRT\delta_a}{4FD_{\mathrm{a}}^{\mathrm{eff}} P_{\mathrm{O_2}}^{0}}} \tag{3.17}$$

In the written equations, δ refers to the thickness, $D_{\mathrm{a,c}}^{\mathrm{eff}}$ are the effective diffusion of the anode and cathode, and P_{i}^{0} is the partial pressure.

To determine the number of cells needed for the SOEC stack, the hydrogen mole flow must first be obtained using Aspen Plus. Based on this, the following equations are applied to calculate the power demand and the heat demand [90], [91]:

$$N_{\mathrm{Cell}} = \frac{2F\dot{n}_{\mathrm{H_2}}}{JA_{\mathrm{Cell}}} \tag{3.18}$$

$$\dot{W}_{\mathrm{SOEC}} = JA_{\mathrm{Cell}} N_{\mathrm{Cell}} V_{\mathrm{Cell}} \tag{3.19}$$

$$\dot{Q}_{\mathrm{SOEC}} = \dot{n}_{\mathrm{e}} h_{\mathrm{e}} - \dot{n}_{\mathrm{i}} h_{\mathrm{i}} - \dot{W}_{\mathrm{SOEC}} \tag{3.20}$$

where $\dot{n}_{\mathrm{H_2}}$ is the mole flow rate of generated hydrogen in (mol/s), *N* and *A* refer to the number and area of the cell, respectively. Additionally, $\dot{W}_{\mathrm{SOEC}}$, $\dot{Q}_{\mathrm{SOEC}}$, h, i, and e are power demand, the heat demand, enthalpy, inlet and outlet, respectively.

The model built for this study was validated using data from the literature. The results of the mass flow rate in Aspen Plus are reported and compared with ref. [87] in Table 3.1. The SOEC stack is validated by comparison with Ref. [91], shown in Fig. 3.3. Based on the results shown, it can be stated that there is good agreement between the present study and the results of the references mentioned above.

Table 3.1. Comparison of the SOEC mass balance results between present study and ref. [87]

		$\dot{m}$ *(kmol/h)* *(1023 K and* one *bar)*
Ref. [87] states	Present work	Ref. [87]
8	644.00	644.49
9	772.00	771.75
10	979.00	978.75
11	207.00	207.00
14	127.00	127.27
15	644.00	644.49
17	230.00	230.49
Pure H2	414.00	414.00

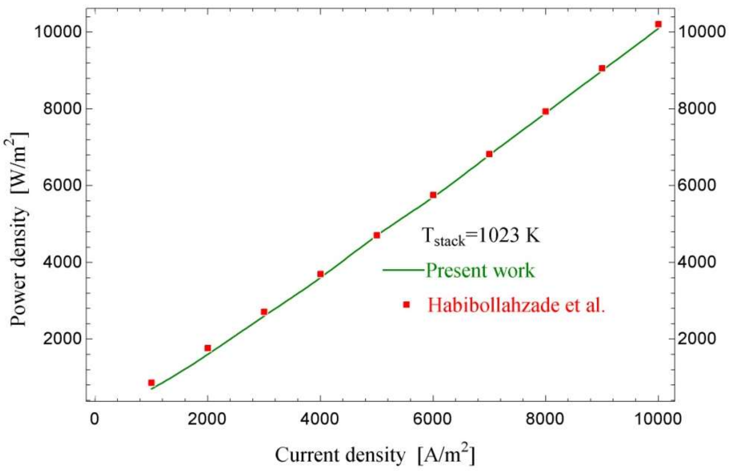

Fig. 3.3. Comparison of the results of SOEC modeling between the present study and ref. [91]

3.2. Anaerobic digestion unit

This subsection describes an anaerobic digestion unit for biogas production. It underpins the polygeneration optimization by defining feed–utility interfaces, heat recovery, and CO₂ utilization. Fig. 3.4. outlines an energy-integrated anaerobic digestion system with thermal pretreatment. The incoming feedstock first recovers heat from the warm digestate in heat exchanger 1, then is pressurized by pump 1 (P1) and brought to its target temperature in heat exchanger 2 (HX2). The slurry then enters a thermal pretreatment tank (TPT), which can be supplied with low-grade heat recovered from the CO₂ cooler to reduce external utility demand. After pretreatment, pump 2 (P2) transfers the material to the anaerobic digester, where it is converted into biogas and digestate. The digestate returns through heat exchanger (HX1) to release residual heat before discharge, closing the heat-recovery loop. Meanwhile, the produced biogas is conditioned in a gas-treatment unit, dehumidified using a cooling-water chiller, and finally upgraded for downstream use. It is worth noting that the experimental data of sewage sludge used in this work is collected from a wastewater treatment plant in Tabriz, Iran [92]. Subsequent calculations are carried out in EES, and the underlying assumptions are documented in Tables A.3 and A.4 of Appendix.

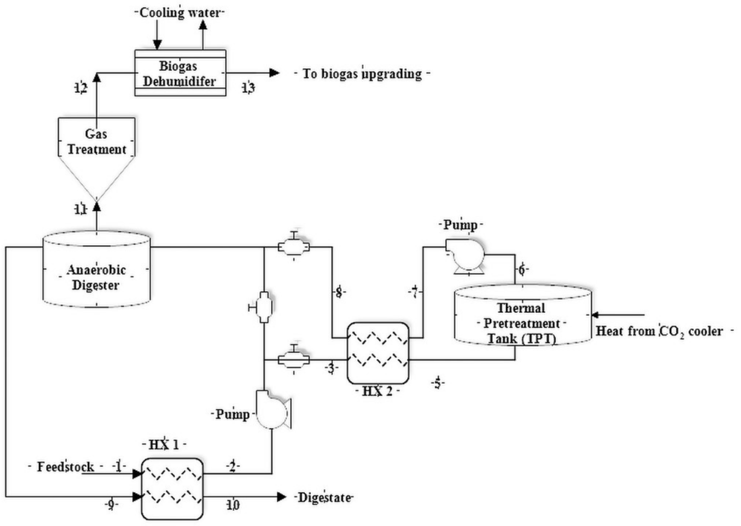

Fig. 3.4. Schematic diagram of the anaerobic digestion plant.

3.3. Biogas upgrading unit

This subsection presents water-scrubbing as the reference biogas-upgrading route, aligning with its dominant industrial use and simplicity. Biomethane/CO_2 interface is defined for PBtX integration and CO_2 capture and utilization (CCU) is involved in hydrogen-based polygeneration systems. There are various techniques for biogas upgrading, among which the most used is called water scrubbing. As shown in Fig. 3.5, water scrubbing is the dominant upgrading option with 35%, followed by chemical absorption and membranes at 21%. Pressure swing adsorption (PSA) accounts for 17%, physical absorption for 5%. These numbers justify prioritizing water scrubbing as the reference technology in this thesis.

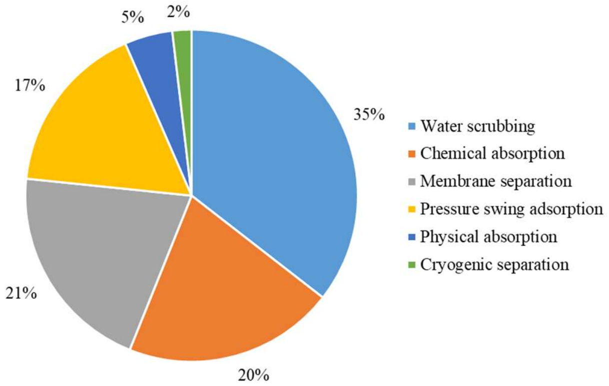

Fig. 3.5. Biogas upgrading methods [93].

Fig. 3.6. shows a water-scrubbing biogas-upgrading unit with closed-loop solvent regeneration. Raw biogas is compressed in two stages with intercooling and fed to the base of a packed absorber. Lean water enters at the top of the absorber from the recirculation loop, dissolving CO_2 (and part of H_2S) counter-currently, while purified biomethane exits overhead. CO_2-rich water from the absorber bottom is flashed/held before being sent to a CO_2 stripper, where a small stream of compressed air strips the dissolved CO_2 and is released as off-gas exit. The regenerated water returns to the loop, with minor make-up water supplied via a water pump. The system is simple, solvent-free (water only), and designed for stable grid-grade biomethane production with low operational complexity. This model is developed in Aspen Plus software, and the main assumptions are reported in Table A.5 of Appendix.

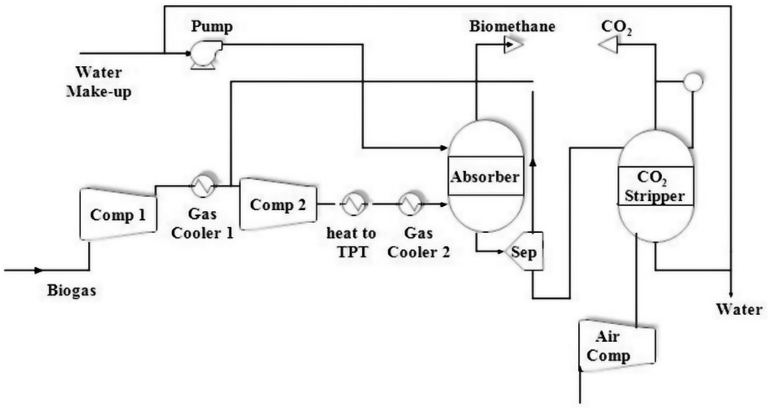

Fig. 3.6 Biogas upgrading used in the proposed system.

3.4. Biomass gasification

This subsection develops and validates the steam–oxygen biomass gasification model that sets syngas quality, heat duties, and O_2/steam splits for downstream fuel synthesis. It is essential to the hydrogen-centric polygeneration optimization and to testing hypotheses on O_2 management, efficiency, and process integration. Fig. 3.7 shows a detailed configuration of the biomass gasifier flowsheet built in Aspen Plus. Biomass first enters a decomposition unit where solids are converted into a mixture of vapor, liquid, and solid by transferring heat to a pyrolysis unit. Wood is heated in an oxygen-free pyrolysis, where the supplied heat drives endothermic depolymerization and cracking of solids. The resulting primary volatiles exit the particles and, upon cooling, partition into condensable liquids and permanent gases, while a carbon-rich char remains. These pyrolysis products then feed the downstream gasification/combustion steps. The decomposed biomass (stream 19) enters a water separator to which cold and compressed oxygen is added. The remaining oxygen is added to the gasifier and combustor. Water and ash are separated from decomposed biomass. Then, dry biomass is supplied to the combustor. After that, stream 20, which contains mostly carbon, hydrogen, and oxygen, enters a carbon separator. Hydrogen and oxygen coolers generate steam, which is fed into the gasification system. The carbon separator distributes carbon to the pyrolysis, gasifier, and combustor, and heat is continuously transferred from pyrolysis to the gasifier and combustor, and a small amount of heat is lost in the combustor. Subsequently, the output streams from the pyrolysis, the gasifier, and the combustor are mixed and enter the solids separator. Separated gases transfer heat to the steam generator (EVA 1 and SUP 1). Finally, dry and clean syngas is produced after removal of water, H_2S, and HCL [94].

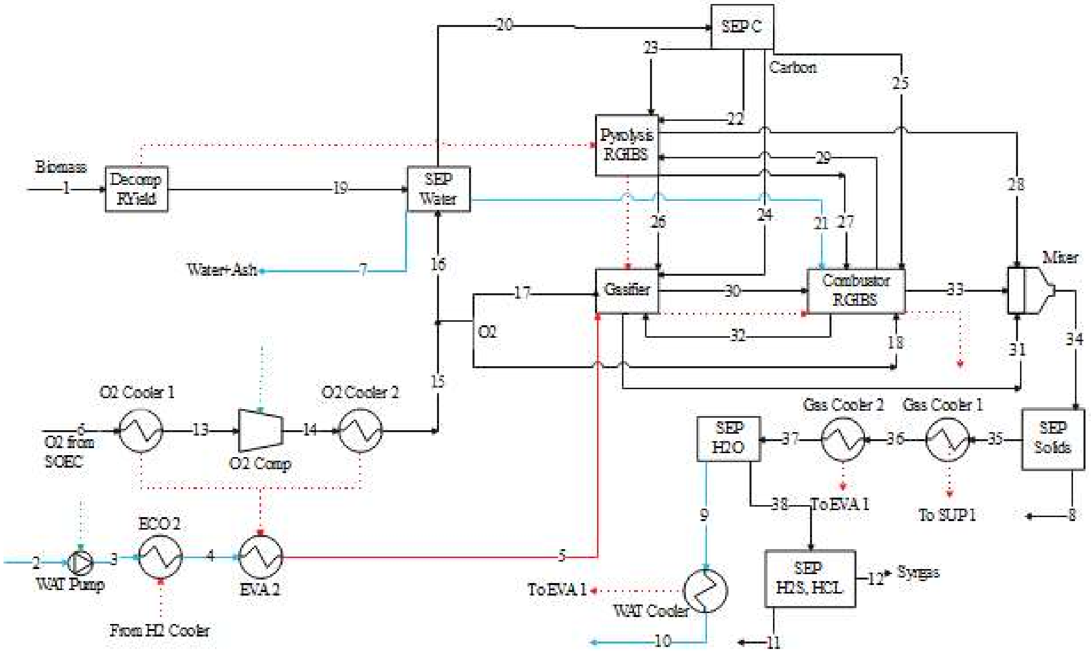

Fig. 3.7 Schematic diagram of the biomass gasification subsystem using steam and oxygen as gasification agents.

Biomass gasification is considered a prominent thermochemical conversion method with high energy efficiency for generating clean syngas [95]. Steam, air, oxygen, and oxygen-enriched air are generally utilized as gasification agents, resulting in different heating values and syngas ratios [96]. Steam gasification is a favorable route to produce syngas with a high heating value and a high H_2 content. However, steam gasification is an endothermic reaction that requires a thermal source, increasing gasification cost [97]. Alternatively, air or pure oxygen can be added to the gasifier to provide the heat necessary for steam gasification. In air gasification, syngas with high nitrogen content and, consequently, low heating value is produced, while in oxygen gasification, syngas with medium heating value is achieved. However, it requires an oxygen-producing unit, increasing energy consumption and cost [98]. In this study, the steam-oxygen mixture is considered as a gasification agent because pure oxygen internally is generated in the electrolyzer or the air separation unit. In the system for ammonia production, CO_2 capture is easily possible through compression and condensation of flue gas in the absence of nitrogen. A Gibbs reactor is selected to simulate the biomass gasification process, and the steam-to-biomass ratio (*SBR*) and O_2-equivalence ratio (ER_{O_2}) are considered as input variables, which are defined as follows [99]:

$$SBR = \frac{\dot{m}_{\mathrm{steam}}}{\dot{m}_{\mathrm{biomass,db}}} \tag{3.21}$$

$$ER_{O_2} = \frac{\dot{m}_{\mathrm{oxygen}}}{\dot{m}_{\mathrm{oxygen,st}}} \tag{3.22}$$

where, $\dot{m}_{\mathrm{I}}$ refers to the mass flow rate of component i, and index db indicates dry basis. Also, $\dot{m}_{\mathrm{oxygen,st}}$ denotes the mass flow rate of pure oxygen for a complete biomass combustion reaction, derived from the stoichiometry of the following oxidation reaction [100]:

$$\mathrm{C_XH_YO_Z} + \left(\mathrm{X} + \frac{\mathrm{Y}}{4} - \frac{\mathrm{Z}}{2}\right)\mathrm{O_2} = \mathrm{XCO_2} + \frac{\mathrm{Y}}{2}\mathrm{H_2O} \tag{3.23}$$

Table 3.2 shows that the syngas mole fractions from the present work are virtually identical to those reported in Ref. [101] for O_2–steam gasification of wood, with a mean absolute difference of nearly-zero percentage points across species, thereby confirming the fidelity of the gasifier sub-model under the validated operating regime.

Table 3.2. Comparison of the molar fractions of syngas produced in the gasifier between the present study and Ref. [101]

Component	Present model	Ref. [101]
CO_2 (%)	26.9914	26.9910
N_2 (%)	0.6443	0.6440
H_2 (%)	32.8415	32.8420
CO (%)	31.6988	31.6990
CH_4 (%)	7.8241	7.8240

3.5. Ammonia synthesis subsystem

This subsection specifies the Haber–Bosch synthesis model that closes the ammonia loop for both PtA and BtA pathways. It provides the assumptions and integration levers needed to optimize hydrogen-centric polygeneration and test hypotheses on efficiency and cost. Currently, the exothermic Haber-Bosch process is the main industrial method for ammonia production. As shown in Fig. 3.8, the Haber-Bosch reactor consists of two adiabatic catalytic beds with a fractional nitrogen conversion (25–35%) through each catalytic bed. Firstly, mixture of hydrogen and nitrogen is fed to the synthesis loop at a molar ratio of 3:1, and ammonia is synthesized through the following equilibrium reaction [67]:

$$3\mathrm{H_2} + \mathrm{N_2} \leftrightarrow 2\mathrm{NH_3} \tag{3.24}$$

The adiabatic catalytic beds of the reactor are modeled by the Plug reactor with the Temkin–Pyzhev kinetic model [67]:

$$r_{\mathrm{NH_3}} = \frac{2f}{\rho_{\mathrm{cat}}}\left(k_{\mathrm{f}}\frac{p_{\mathrm{N_2}}p_{\mathrm{H_2}}^{1.5}}{p_{\mathrm{NH_3}}} - k_b\frac{p_{\mathrm{NH_3}}}{p_{\mathrm{H_2}}^{1.5}}\right) \tag{3.25}$$

$$k_{\mathrm{f}} = 1.79 \cdot 10^{-4} \exp\left(-\frac{87090}{RT}\right) \tag{3.26}$$

$$k_b = 2.57 \cdot 10^{16} \exp\left(-\frac{198464}{RT}\right) \tag{3.27}$$

where, f, ρ_{cat}, and P_I are correcting factors (4.75), catalyst bulk density, and partial pressure of components, respectively.

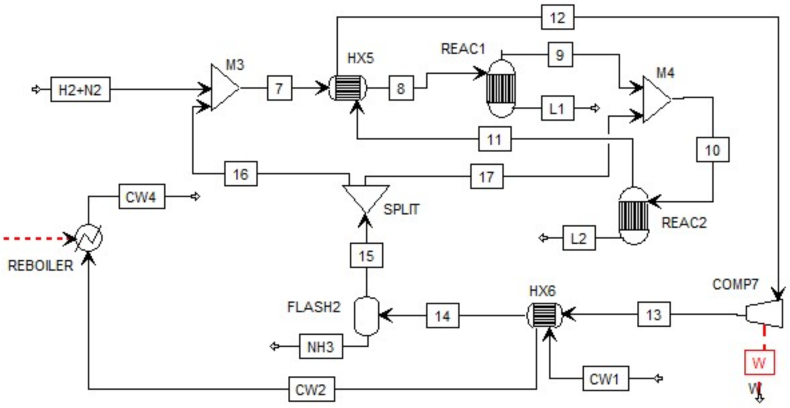

Fig. 3.8. Ammonia synthesis scheme.

3.6. Methanol synthesis unit

This subsection specifies and validates the CO₂ hydrogenation for methanol production establishing the mass/energy balances, recycle strategy, and heat-integration levers central to PBtX. It directly supports the thesis hypothesis by quantifying how biofuel synthesis affects efficiency, cost, and environmental performance in hydrogen-based polygeneration. In the methanol synthesis unit (Fig. 3.9), three streams are mixed to provide the feed for CO_2 hydrogenation: flue gas (55) from the WGSR (55), hydrogen from the SOEC (53), and syngas from the gasification unit (12). All streams are compressed and mixed using four-stage compressors. The waste heat is recovered and used primarily by the LNG regasification unit. These streams are also combined with the recirculating gas (stream 61) and directed to the methanol reactor and its heater. Gases leaving the reactor provide thermal energy to preheat the methanol-water mixture entering the distillation column. Subsequently, the gases are cooled and routed to the drum and flash separators, where gas and liquid phases are separated. The purity of biomethanol at this stage is approximately 99.5%. The liquid part (stream 72) is fed to the distillation column for further production of biomethanol and water. Finally, the gaseous fraction (stream 80) is compressed and recycled back to the inlet streams of hydrogen, syngas and flue gases produced in the SOEC, gasifier, and WGSR, respectively. The verification of the methanol generation unit is reported in Table 3.3 in which the temperature, molar flow rate and composition of each stream are compared to Ref. [102].

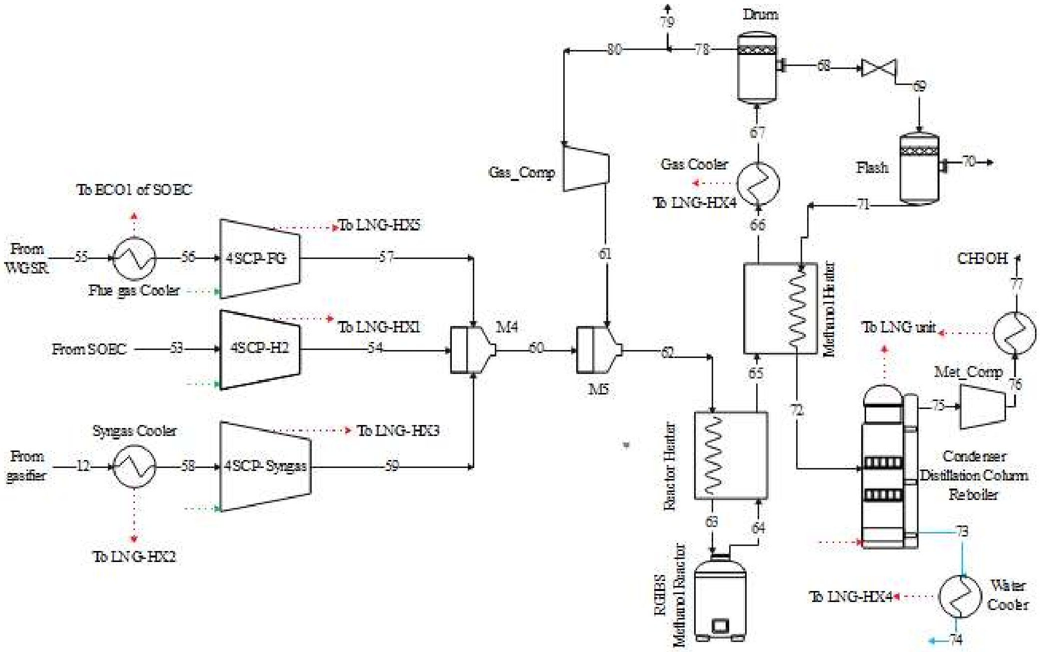

Fig. 3.9 Schematic diagram of the methanol synthesis unit (MSU) subsystem

Table 3.3. Comparison of the stream properties of the methanol synthesis unit between the present study (PS) and ref. [102]

Stream	*T (K)* [102]	*T (K)* (PS)	$\dot{n}$ (mole/s) [102]	$\dot{n}$ (mole/s) (PS)	CO [102]	CO (PS)	CO_2 [102]	CO_2 (PS)	H_2O [102]	H_2O (PS)	H_2 [102]	H_2 (PS)	CH_3OH [102]	CH_3OH (PS)
CO_2	303.2	303.2	0.38	0.38	0.00	0.00	1.00	1.00	0.00	0.00	0.00	0.00	0.00	0.00
H_2	353.0	353.0	1.13	1.13	0.00	0.00	0.00	0.00	0.00	0.00	1.00	1.00	0.00	0.00
Reactor outlet	551.1	551.1	9.12	9.07	0.04	0.04	0.12	0.13	0.04	0.04	0.76	0.74	0.04	0.04
Water	372.8	373.02	0.36	0.36	0.00	0.00	0.00	0.00	1.00	0.99	0.00	0.00	0.00	0.01
Distillation outlet	337.3	337.99	0.35	0.35	0.00	0.00	0.00	0.00	0.00	0.01	0.00	0.00	0.99	0.99
CH_3OH	313.2	313.20	0.35	0.35	0.00	0.00	0.00	0.00	0.00	0.01	0.00	0.00	1.00	0.99

3.7. Power and natural gas production subsystem

Cold-energy recovery of LNG, oxy-fuel gas turbine, and water gas-shift reactor subsystems co-produce power, natural gas, and flue gases stream for the methanol production, an integration core to hydrogen-centric polygeneration systems. It directly tests the hypotheses that coupling oxy-fuel combustor with LNG cold recovery and flue-gas shifting can lift overall efficiency, lower costs, and improve environmental performance.

The schematic diagram of the power and natural gas production subsystem is presented in Fig. 3.10. It includes a liquified natural gas (LNG) cold-energy recovery unit, a fuel-rich fired gas turbine, and a water gas shift reactor (WGSR). In this system, LNG is pumped and heated by five heat exchangers that recover waste heat from the methanol synthesis unit. After reaching high pressure and temperature, natural gas stream enters a natural gas turbine and stream 88 is reheated by the methanol cooler. This process produces a large amount of gaseous natural gas, a portion of which is compressed and supplied to the combustor. The surplus oxygen from the SOEC is compressed to 35 bar and 750 °C by a four-stage compressor. Additionally, a large amount of CO_2 is supplied to the combustion chamber after being pumped to 35 bar and heated by the oxygen compressor coolers. The combustion gases generate electricity in the gas turbine and subsequently are cooled in the heat recovery steam generator (HRSG). The steam produced in the HRSG is mixed with the flue gases to increase the H_2O content of the mixture. Finally, a high amount of H_2O leads to a high amount of H_2 after the water gas shift reactor, and some part of CO is converted into CO_2, providing feedstock for further biomethanol production using the CO_2 hydrogenation process.

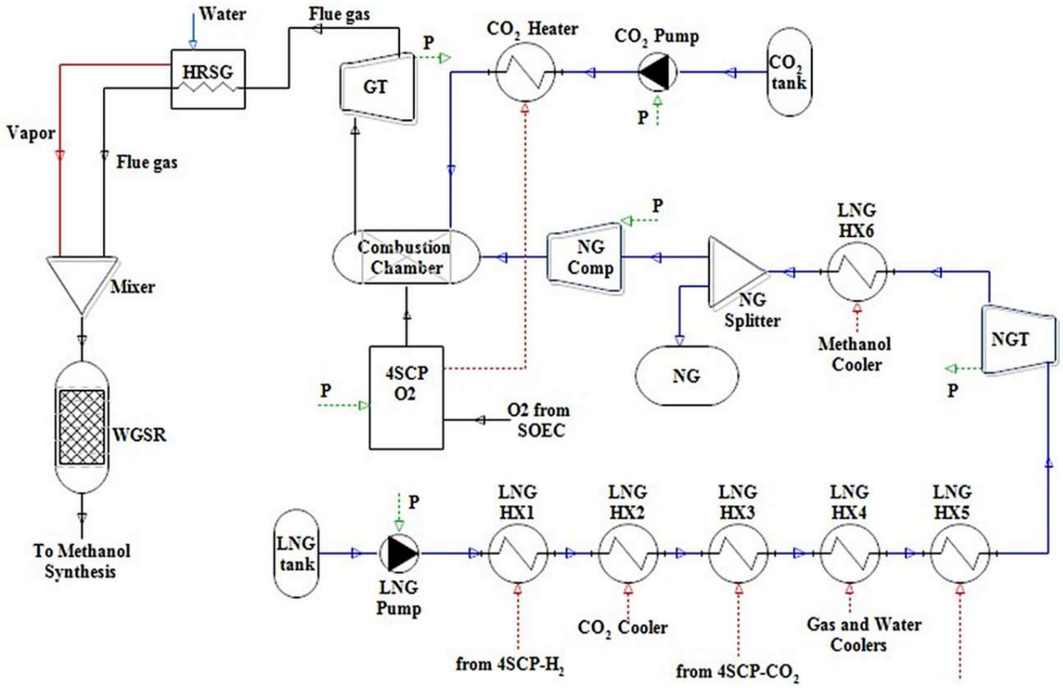

Fig. 3.10 Schematic diagram of the power and natural gas production subsystem

In industry, the water-gas-shift reaction is typically conducted in two series of adiabatic reactors: a high-temperature shift (HTS) reactor operating at 300–450 °C, and a low-temperature shift (LTS) reactor operating at 200–250 °C, to maximize CO conversion. However, complete CO conversion can be achieved in a single water-gas-shift membrane reactor at high temperatures by extracting hydrogen from the reaction mixture [103]. In this regard, a high-temperature water gas-shift membrane reactor is considered an effective option for purifying hydrogen produced by the gasification unit. Equation (10) shows the water-gas-shift reaction:

$$\mathrm{CO(g)} + \mathrm{H_2O(g)} \leftrightarrow \mathrm{H_2(g)} + \mathrm{CO_2(g)} \tag{3.28}$$

The commercial catalysts for HTS reaction are based on Fe-Cr. At high temperatures, the reaction rate over the Fe-Cr catalyst can be expressed by the power-law model as follows [104]:

$$r_{\mathrm{WGS}} = 10^{0.659} exp\left(\frac{-8800}{RT}\right) P_{\mathrm{CO}}^{0.9}\, P_{\mathrm{H_2O}}^{0.31}\, P_{\mathrm{CO_2}}^{-0.156}\, P_{\mathrm{H_2}}^{-0.05} \left(1 - \frac{P_{\mathrm{CO_2}} P_{\mathrm{H_2}}}{P_{\mathrm{CO}} P_{\mathrm{H_2O}} K_{\mathrm{eq}}}\right) \tag{3.29}$$

Where R is called ideal gases constant, T is temperature, and P is the partial pressure of different components. In this equation, K_{eq} is the equilibrium constant. The WGS membrane reactor is modeled using a 1-D pseudo-homogenous mathematical approach under isothermal and isobaric conditions at co-current and counter-current modes. For the reaction P_{in} side (shell side), the mass balance of components is described as follows [105]:

$$\frac{dF_{\mathrm{i,r}}}{dz} = \pm A_{\mathrm{c}} r_{\mathrm{WGS}} \rho_{\mathrm{b}} \tag{3.30}$$

where negative and positive signs refer to reactants and products, respectively. For the tube side (permeation side), the mass balance of hydrogen is described as follows [105]:

$$\frac{dF_{\mathrm{H_2,P}}}{dz} = \pi d_{\mathrm{te}} J_{\mathrm{H_2}} \tag{3.31}$$

where, $J_{\mathrm{H_2}}$ indicates hydrogen permeation flux and is calculated based on Sievert's law [105]:

$$J_{\mathrm{H_2}} = \frac{Q_{0,\mathrm{H_2}} \exp\left(\frac{-E_{\mathrm{H_2}}}{RT}\right)}{\delta_{\mathrm{m}}} \left(\sqrt{P_{\mathrm{H_2,r}}} - \sqrt{P_{\mathrm{H_2,P}}}\right) \tag{3.32}$$

In the previous equations, A_c, ρ_b, d_{te}, Q_0, E_{H2}, and δ_m are called cross sectional area, bulk density, external tube diameter, preexponential factor, activation energy of hydrogen permeability, and palladium thickness, respectively, given in ref. [105]. The boundary conditions are as follows [105]:

For both modes, at flow direction $z = 0$: $F_{\mathrm{I,r}} = F_{\mathrm{I,in}}$, i = CO, H_2O, H_2, and CO_2.

For co-current mode: at $z = 0$: $F_{\mathrm{H_2,P}} = 0$ and for counter-current mode: at $z = \mathrm{L}$: $F_{\mathrm{H_2,P}} = 0$.

To validate the mathematical model of the WGS membrane reactor, the theoretical values of CO conversion and H_2 recovery were compared with experimental data reported by Augustine et al. [106]. Table 3.4 presents this comparison for steam-to-carbon ratios of 1.6 and 2.6 at temperatures of 400, 450, and 500 °C. As shown, at 450 °C, the operating temperature of the WGS membrane reactor in this study, the proposed model shows an acceptable accuracy with relative errors of 0.4 and 5% for CO conversion and H_2 recovery, respectively.

Table 3.4. Comparison between the theoretical data for CO conversion and H2 recovery with those of ref. [106].

Temperature (°C)	S/C = 1.6				S/C = 2.6			
	X_WGS (%)		Y_H_2 (%)		X_WGS (%)		Y_H_2 (%)	
	Ref. [106]	This study	Ref. [106]	This study	Ref. [106]	This study	Ref. [106]	This study
400	95.94	97	76.80	76.67	96.42	98.13	57.09	62.92
450	97.27	96.76	82.96	83.53	98	97.6	73.72	70.03
500	96.79	95.28	84.76	84.89	97.82	97.22	76.74	76.58

3.8. Air separation unit

This subsection defines the air separation block that supplies high-purity O_2 and N_2, with explicit energy use and purity constraints, so the optimization can test oxygen utilization in gasification and combustor and secure N_2 for ammonia synthesis, quantifying its impact on system efficiency, cost, and life-cycle performance. Cryogenic air separation unit is the main industrial method for nitrogen and oxygen production in high volume and purity. Many research studies have been conducted to develop new configurations for cryogenic air separation units and reduce the overall energy consumption and capital cost of ASUs [107]. In the present study, a black-box model developed in [67] is adopted to simulate ASU to simplify flow sheet simulation and reduce unnecessary calculations by considering the key operating conditions and energy consumption. The oxygen purity is 99.5% at an operating pressure of 1 atm, and ASU's energy consumption is 160 kWh/tonne of pure O_2 [67].

3.9. Compressed air and thermal energy storage systems

This thesis aims to recover waste heat of energy storage systems for being used in the biomethanol production plant. Therefore, the energy storage system itself is not modeled in this thesis. Instead, experimental data are collected from the group for energy storage technologies (GEST) at the Silesian

University of Technology led by Prof. Bartela [108]. This directly serves the hypotheses that integrating waste heat of energy storage system can boost efficiency and flexibility in hydrogen-based polygeneration. Detailed assumptions and methodology of the energy storage systems are reported in ref. [108], [109].

Fig. 3.11 shows the scheme of the energy storage system applied for the analysis. In the compressed air energy storage (CAES), the electricity generated by turbines is used to drive a two-stage air compressor, which compresses gas from ambient pressure to the compressed air reservoir. The operation of the compressors is assumed to achieve a maximum air temperature after the second stage at 400 °C. This assumption is based on the temperature of the thermal energy storage (TES) tank required for the adiabatic CAES system. Crucial from the perspective of the system discussed is the management of waste heat from the heat exchange between the compressors as indicated in Fig. 3.11. In conventional CAES installations, the heat from the interstage heat exchanger is lost to the environment and the efficiency of the adiabatic CAES is found to be 70%. In this thesis, however, the proposed heat recovery contributes to overall efficiency enhancement.

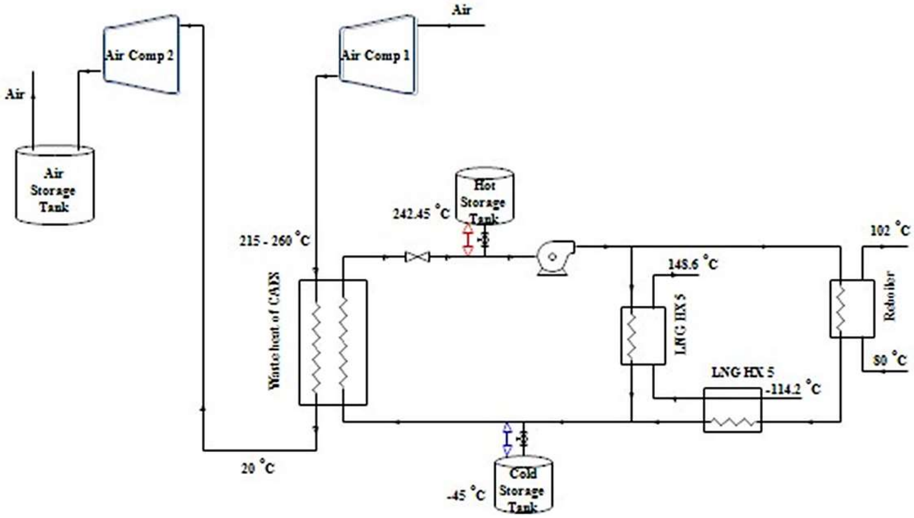

Fig. 3.11 Schematic diagram of CAES and thermal energy storage (TES) for stable heat recovery.

3.10. Biojet fuel production system

This subsection formalizes the biojet fuel production process, quantifying how H_2 and syngas are conditioned and upgraded into jet-fuel range hydrocarbons. It underpins the polygeneration optimization by exposing key levers, H_2/CO ratio control, recycle strategy, heat recovery, and hydrocracking severity, that govern efficiency, product yields, energy use, and life cycle impacts in hydrogen-enabled PBtL. Biojet fuel production consists of four main stages namely, reverse water gas shift (RWGS) reactor, the Fischer-Tropsch (FT) reactor, distillation towers, and hydrocracking. As shown in Fig. 3.12, a mixture of flue gases, hydrogen, and syngas is used in the shift process. The equilibrium is intentionally shifted toward greater CO formation by removing H_2O, which is separated from the gas stream by condensation. After dehydration, the syngas is reheated to 800 °C, the operating temperature of the shift reaction. At this stage, the CO concentration increases to a level that achieves the desired hydrogen-to-CO ratio of 2. After generating syngas with optimized composition in the shift reactor, the next step involves synthesizing jet fuel using the low-temperature Fischer–Tropsch (FT) synthesis. This industrial process operates effectively typically within a range of 180 °C to 250 °C, facilitating the hydrogenation of CO molecules. Through this process, methylene intermediates are formed, which serve as the building blocks for creating hydrocarbon chains of varying sizes [110], [111].

Since water is a byproduct of the Fischer–Tropsch synthesis, a water-removal step is integrated upstream of the FT reactor to enhance hydrocarbon yield. This dehydration is achieved through flash condensation, utilizing cooling techniques like those employed before the shift reactor. The low-temperature FT process considered in this study follows a chain propagation mechanism, with product distribution patterns of olefins and paraffins described by Song et al. [112] and Todic et al. [113], respectively. To produce jet fuel within the desired specifications, the carbon chain lengths typically range from C_5 and C_{16}, corresponding to the composition of naphtha and kerosene fuels [114]. Therefore, the process temperature is selected to favor chain propagation factor that maximizes jet fuel output. Based on this criterion, an optimal operating temperature of 185 °C is identified. Operating at this reduced temperature not only increases selectivity for target hydrocarbons but also reduces catalyst degradation.

As shown in Fig. 3.12, once the Fischer–Tropsch synthesis is complete, the initial product separation is conducted using a three-phase separator, based on vapor-liquid-liquid equilibrium analysis at the FT operating pressure and a temperature of 35 °C. In this step, the gaseous phase is recycled back to the RWGS reactor, while the condensed hydrocarbons are separated from the aqueous phase. The resulting hydrocarbon liquid stream then undergoes further separation in four distillation columns.

For the distillation column design, shortcut methods are employed to estimate the required number of theoretical stages and calculate condenser and reboiler energy duties, based on the specified separation targets for light and heavy components. One of the most important assumptions is the reflux ratio, defined as the ratio of liquid returned to the column top (reflux to the distillate product withdrawn from the top. The first stage of distillation removes lighter components- primarily C_1 to C_4 - ensuring 95% recovery of C_4 in the overhead stream and limiting the C_6 content in the bottoms to 4%. The next distillation step isolates the jet fuel fraction (C_5–C_{16}), targeting 90% C_{16} recovery in the distillate and a maximum of 10% C_{17} in the bottoms. This procedure segments the hydrocarbons into three streams: a light gas fraction (C_1–C_4), the desired jet fuel range (C_5–C_{16}), and a residual heavy wax stream (C_{17+}).

The wax stream, rich in long-chain hydrocarbons, is then upgraded through hydrocracking, a catalytic process that is enhanced by the addition of hydrogen. This step, carried out at 319 °C and 3.5 bar, follows experimental guidelines presented by Calemma et al. [115] to improve jet fuel yield. Finally, a second distillation - applied using the same recovery principles - separates the upgraded products into refined jet fuel, light gases, and any remaining heavy waxes.

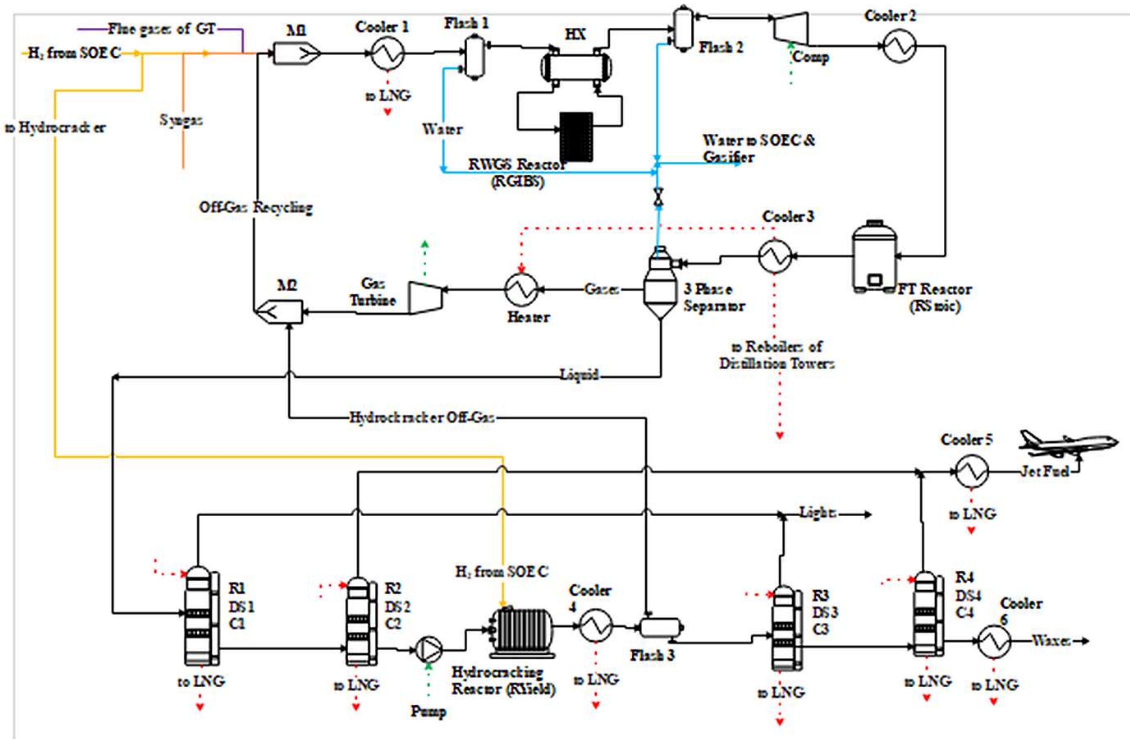

Fig. 3.12. Detailed flowsheet of the subsystem for bio jet fuel production.

In Fischer–Tropsch synthesis modeling, the process is governed by the chain growth probability, represented by α. This parameter determines the distribution of hydrocarbon products and controls the selectivity toward different chain lengths. It can be calculated using the following equation:

$$\alpha = \left(a_1 \frac{y_{CO}}{y_{H2} + y_{CO}} + a_2\right)\left(1 - 0.0039(T - 523\ K)\right) \tag{3.33}$$

According to Song et al. [116], the coefficients a_1 and a_2 take values of 0.2332±0.0740 and 0.6330±0.0420, respectively. The H_2 to CO molar ratio is fixed at 2 [117]. Under this constant ratio, the chain growth probability becomes dependent solely on the reaction temperature.

In FT synthesis, the molar fraction of hydrocarbons with chain length is obtained from the chain growth probability, as expressed below.

$$y_{Cn} = \alpha^{N-1}(1 - \alpha) \tag{3.34}$$

Here, N represents the carbon atom count, and the molar yields of olefins (y_O) and paraffins (y_P) show an exponential dependence on the chain length [113].

$$\frac{y_O}{y_P} = \exp\left(-\frac{\Delta e}{RT} N\right) \tag{3.35}$$

In this expression, Δe denotes the variation in activation energy, quantified as 1.1 kJ/mol for each carbon atom, while R refers to the universal gas constant. The model accounts for olefins up to C_{16}, while paraffins are considered for chain lengths extending to C_{30}. The following strongly exothermic reaction can summarize the overall process [118]:

$$n\,CO + (2n + 1)\,H_2 \rightarrow C_nH_{2n+2} + n\,H_2O \qquad \text{Parafins} \quad 1 \leq n \leq 30 \tag{3.36}$$

$$n\,CO + (2n)\,H_2 \rightarrow C_nH_{2n} + n\,H_2O \qquad \text{Olefins} \quad 1 \le n \le 16 \qquad (3.37)$$

In addition, the extent of reactant conversion needs to be defined. Following the approach of Campanario and Gutiérrez Ortiz [119], it is assumed that 90% of the CO fed into the reactor is transformed into fuel products. The allocation of this conversion across reactions is determined by the distribution of carbon chain lengths, with chains shorter than C_{16} further categorized into paraffins and olefins.

In the subsystem of biojet fuel production, the hydrocracking reactor is represented using the RYield model, with its outputs adjusted to align with the experimental findings reported by Calemma et al. [115].

Figures 3.13, 3.14, and 3.15 present the validation of the RWGS, FT, and hydrocracking reactor models, respectively, using Aspen Plus with the reference data of Paulsen et al. [118]. Carbon numbers (number of carbon atoms in different product fractions), ranging from 1 to 30, are paraffins, and from 31 to 45 are olefins. The results show strong agreement between the Aspen model and the reference values since both distributions follow a similar trend with minimal deviations. The peak mass fraction occurs around the carbon numbers 13-14, demonstrating that the model accurately predicts the product distribution of hydrocarbons in the reactors. Small variations between the two data sets can be attributed to model assumptions, kinetic parameters, or numerical approximations in the Aspen simulation. Overall, the verification confirms the reliability of the Aspen model in replicating the reactor performance, making it a useful tool for further analysis of the process.

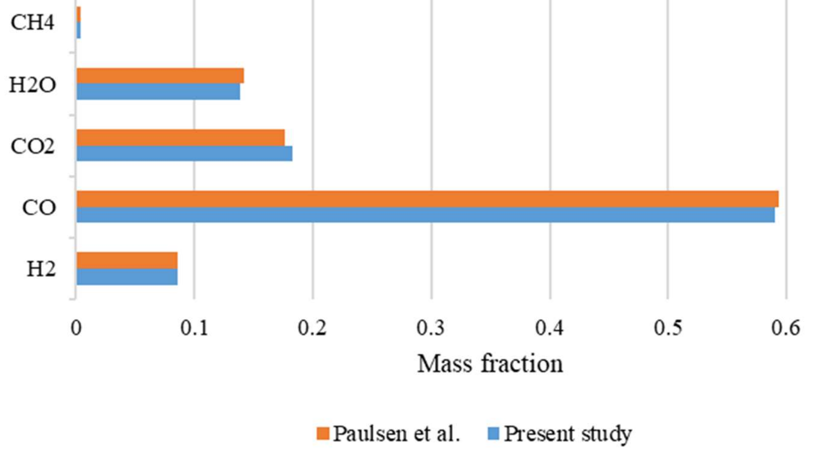

Fig. 3.13 Model verification of the RWGS reactor with the results of Paulsen et al. [118].

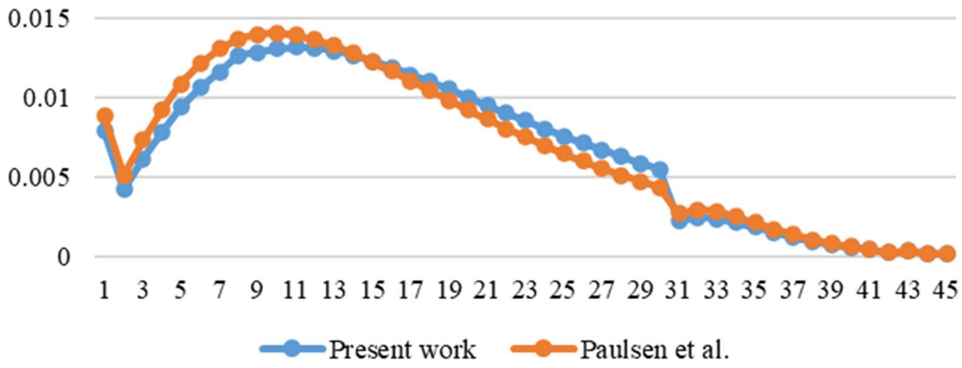

Fig. 3.14 Model verification of the FT reactor with the results of Paulsen et al. [118].

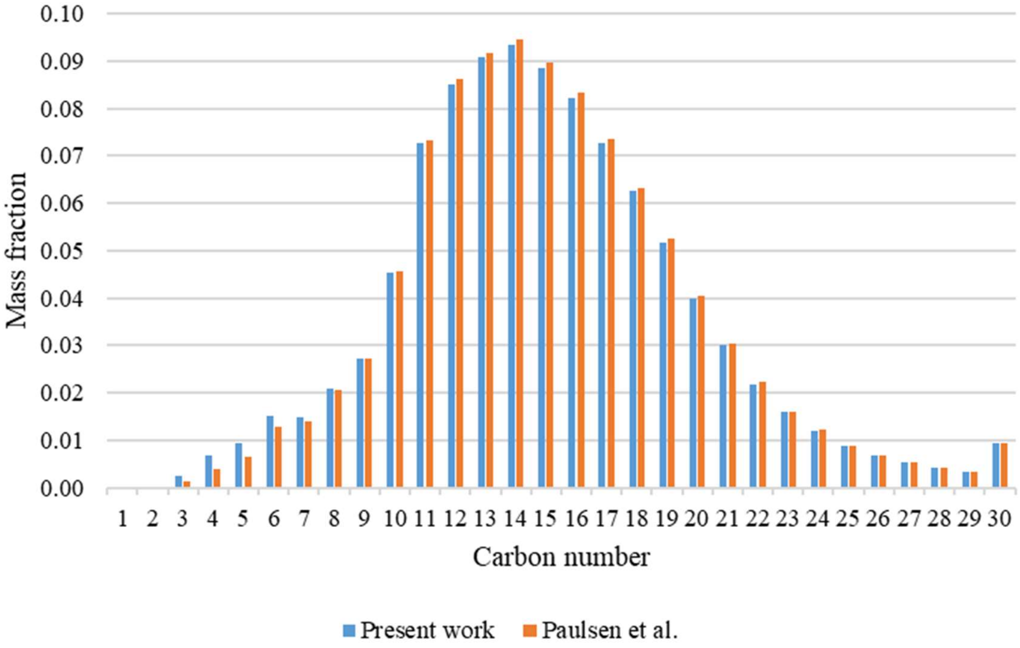

Fig. 3.15 Model verification of the hydrocracking reactor with the results of Paulsen et al. [118].

4. Techno-economic and life cycle assessment methodology

This chapter defines the techno-economic and life-cycle assessment framework that rigorously tests the hypotheses on optimizing hydrogen-enabled polygeneration systems. By fixing system boundaries, datasets, cost scaling, and performance indicators and by specifying scenario design, it turns the process models into transparent, reproducible decision metrics that link integration levers to quantified efficiency, cost, and environmental outcomes.

4.1. Techno-economic analysis

A techno-economic analysis is conducted to compare eight configurations from two viewpoints: the payback time and the levelized cost of fuel, as two useful functions to find the optimal operating points and facilitate the design of biofuels plants. Production expenses are adjusted using the Chemical Engineering Plant Cost Index (CEPCI), referencing data from 2023. The projections relied on discounting techniques, aligned with the standards provided by the United Nations Industrial Development Organization (UNIDO), and are based on computing the Net Present Value (NPV) [120].

This approach is employed because it offers a comprehensive and reliable framework for assessing the economic performance of a project over time. NPV is employed to account for the time value of money, recognizing that a dollar today is worth more than the same amount in the future. By discounting all future cash flows, both revenues and expenses, NPV helps determine whether a project generates more value than it costs, making it a solid indicator of profitability. On the other hand, the levelized cost of fuel (LCOF) serves as a standardized metric that spreads the total discounted costs over the discounted production output, yielding a cost per unit (e.g., \$/L or \$/GJ). This allows for easy comparison between different technologies or systems, even when their operational lifespans or cost structures differ. While NPV reveals whether an investment is financially viable on a broader scale, LCOP shows how cost-effective the system is at the unit level and can help identify the break-even selling price. Together, NPV and LCOP offer both high-level investment insight and detailed cost competitiveness, enabling sound economic decision-making [121].

In techno-economic analysis, purchased-equipment costs are typically estimated by scaling from a known reference size using a cost–capacity (power-law) relation and then updating to the target year with a cost index [122]. If the equipment cost equations do not match the capacity of the proposed system, they should be scaled accordingly. To estimate the equipment expenses for the proposed process units, an appropriate calculation can then be applied [92]:

$$C = C_0 \cdot \left(\frac{S}{S_0}\right)^f \tag{4.1}$$

Symbols f, S_0, C_0, S, and C denote the scaling factor, reference size, reference cost, updated size, and estimated cost, respectively. These symbols are also used in Table 4.1.

The reference year for different equations is shown in Table 4.1. To update the cost rates to the current year (2023), following equation should be applied [123]:

$$C_{2023} = C_{\text{Ref}} \cdot \frac{CEPCI_{2023}}{CEPCI_{\text{Ref}}} \tag{4.2}$$

Here, CEPCI_{2023} is valued at 800.6, and CEPCI of the reference years are reported in ref [124].

In economic analysis, the fixed capital investment (FCI) is initially calculated from the base equipment costs (C). However, equipment costs alone do not account for all capital expenses (e.g., installation, piping, instrumentation, electrical, building structures, land, engineering, contingency, etc.). To capture these additional direct and indirect costs, empirical multipliers known as ratio factors (RFs) are applied to the base equipment cost. In short, RFs provide a practical shortcut to estimate the hidden parts of capital expenditure beyond the purchase of major process equipment. The sum of all these factors (RF_{tot}) is then applied to FCI to determine the total capital investment (TCI) [125]:

$$RF_{tot} = \sum RF_{\mathrm{i}} \tag{4.3}$$

$$FCI = \sum C_{\mathrm{i}} \tag{4.4}$$

$$TCI = FCI\ (1 + RF_{\mathrm{tot}}) \tag{4.5}$$

The fixed capital investment is abbreviated as FCI. Equipment costs for individual units, represented by C, are listed in Table 4.1. To calculate the total capital investment costs, the ratio factors (RF) for each component are provided as follows [125].

- Installation of purchased equipment: 0.39
- Instrumentation and controls: 0.26
- Piping: 0.31
- Electrical system: 0.10
- Buildings: 0.29
- Yard improvements: 0.12
- Service facilities: 0.55
- Engineering and supervision: 0.32
- Construction expenses: 0.34
- Legal expenses: 0.04
- Contractor's fee: 0.19
- Contingency: 0.37

The total product cost (TPC) is then determined using the equation provided below.

$$TPC = C1 + C2 + C3 + C4 + C5 + C6 + C7 \tag{4.6}$$

In which C1 to C7 are defined below, and their values are reported in Table 4.2.

- C1: Utilities and raw materials
- C2: Operation and maintenance
- C3: Royalties and patents
- C4: Depreciation
- C5: Insurance and local taxes
- C6: Overhead costs of the plant
- C7: General expenditure

The net present value (NPV) of the proposed plants can be calculated using the following set of equations [126]:

$$AI = AI_{NG} + AI_{SAF} \tag{4.7}$$

$$ANS = AI - TPC \tag{4.8}$$

$$PP = \frac{TCI}{ANS} \tag{4.9}$$

$$IF_i = (1 + R/100)^{-i} \qquad i = 1, N \tag{4.10}$$

$$RDF_i = (1 + RIR/100)^{-i} \qquad i = 1, N \tag{4.11}$$

$$NPV_i = -TCI + \sum_{i=1}^{N} ANS_\mathrm{i}\, RDF_\mathrm{i}\, IF_\mathrm{i} \tag{4.12}$$

In this study, *AI* refers to annual income, *ANS* to annual net savings, and *PP* to the payback period. Similarly, *IF* represents the inflation factor, *RDF* the real discount factor, *R* the inflation rate, *RIR* the real interest rate, and *N* the system's operational lifetime.

Levelized cost of fuel (LCOF) is the discounted-average cost to produce one unit of fuel over a plant's lifetime. It is computed as the net present value (NPV) of all expenditures (capital and operating), minus the NPV of by-product revenues and credits, divided by the NPV of fuel output. Typical units are \$/tonne of product. energy-normalized variants such as \$/GJ or \$/L are also used. By-product revenues can include sale of co-produced gases/liquids, heat, electricity exports, or environmental credits (e.g., CO_2 offtake), and should be treated consistently with the chosen system boundary and price basis [125]:

$$CRF = \frac{RIR(1 + RIR)^n}{(1 + RIR)^n - 1} \tag{4.13}$$

$$LCOF = \frac{\left(FCI \cdot CRF + TPC - AI_{Byproducts}\right)}{\dot{m}_F \cdot \tau} \tag{4.14}$$

The notations *CRF*, n, and *RIR* correspond to the capital recovery factor, the operational lifetime of the system, and the real interest rate, respectively. The real interest rate (RIR) is obtained by calculating the difference between the inflation rate (*R*) and the discount rate (*DR*). In addition, $\dot{m}$ represents the mass flow rate of the main fuel, while τ denotes the 8000 h of full load hours [127].

Table 4.1. The capital expenditure (CAPEX) details for the proposed systems.

Component	Parameter	Reference year	Ref.
Biomass gasification	$C_0 =$ 0.3 M€ S_0 = 220 kg/h f = 0.75	2011	[128]
Syngas cleaning	$C_0 =$ 38 M€ S_0 = 37 kg/s f = 0.7	2011	[128]
SOEC electrolyzer	$C_0 =$ 2.31 M€ S_0 = 1000 kW f = 0.907	2019	[118]
Fischer-Tropsch reactor	$C_0 =$ 2385 \$ S_0 = 1 m3/h of inlet gases f = 1	2010	[118]
Distillation towers of biojet fuel production	$C_0 =$ 8.2 M\$ $S_0 =$ 6.6245 m3/h of inlet fluid f = 0.51	2007	[118]
RWGS reactor	$C_0 =$ 32 M\$ S_0 = 43000 kg/h of inlet gases f = 0.65	2017	[118]
Hydrocracking reactor	$C_0 =$ 15.65 M\$ $S_0 =$ 6.6245 m3/h of inlet fluid f = 0.719	2007	[118]

Hydrogen compressor	$C_0 = 5.7$ M€ $S_0 = 10$ MW $f = 0.67$	2010	[125]
Oxygen compressor	$C_0 = 18.1$ M\$ $S_0 = 13.2$ MW $f = 0.85$	2002	[125]
Carbon dioxide and flue gas compressors	$C_0 = 12.9$ M\$ $S_0 = 13.2$ $f = 0.85$	2002	[125]
WGS reactor	$C_0 = 2.7$ M\$ $S_0 = 150$ kg/s $f = 0.5$	2010	[129]
Methanol reactor	$C_0 = 7$ M\$ $S_0 = 87.5$ tonne/h of methanol $f = 0.6$	2001	[125], [130]
Distillation tower of methanol production	$C_0 = 15.1$ M\$ $S_0 = 87.5$ tonne/h of methanol $f = 0.7$	2001	[125], [130]
Pretreatment tank	$C_0 = 575621.55$ \$ $S_0 = 3000$ m^3 $f = 0.8$	2016	[92]
Ammonia synthesis unit	$C_0 = 215$ M\$ $S_0 = 1800$ tonne/day $f = 0.7$	2022	[84]
Air separation unit	$C_0 = 141$ M\$ $S_0 = 52$ kg/s of O_2 $f = 0.5$	2007	[131]
Anaerobic digestion	$C_{AD} = 9320000 \cdot m_{Biomass}{}^{-0.55}$ C_{AD} (\$), $m_{Biomass}$ (kg/h)	2016	[132]
Air and biogas compressors	$\log_{10} C_{CP} = 5.0355 - 1.8002 \log_{10} \dot{W}_{CP} + 0.8253(\log_{10} \dot{W}_{CP})^2$ $C_{CP}(\$), \dot{W}_{CP}\ (kW)$	2017	[133]
Stripper	$\log_{10} C_{str} = 3.4974 + 0.4485 \log_{10} V_{str} + 0.1074(\log_{10} V_{str})^2$ $C_{CP}(\$), V_{str}$ (m^3)	2017	[133]
Absorber	$\log_{10} C_{abs} = 3.4974 + 0.4485 \log_{10} V_{abs} + 0.1074(\log_{10} V_{abs})^2$ $C_{abs}(\$), V_{abs}$ (m^3)	2017	[133]
Gas turbines	$C_{GT} = \left(-98.328 \cdot Ln\left(\dot{W}_{\mathrm{GT}}\right) + 1318.5\right) \cdot \dot{W}_{\mathrm{GT}}$ C_{GT} (\$), $\dot{W}_{\mathrm{GT}}\ (kW)$	2004	[134]
Heat recovery steam generator (HRSG)	$C_{HRSG} = 6570\left(\frac{\dot{Q}_{HRSG}}{LMTD_{HRSG}}\right)^{0.8} + 21276\dot{m}_{steam} + 1184.4m_{gas}{}^{1.2}$ C_{HRSG} (\$), $\dot{m}_{\mathrm{HRSG}}\ \left(\frac{kg}{s}\right)$	1995	[135]
LNG heat exchangers	$C_{LNG,hx} = 32800 \cdot f_m f_p \left(\frac{A}{80}\right)^{0.68}$ $f_p = 1.5$ for operating pressure of 0.7-5 MPa $f_m = 3.4$ for high grade stainless steel	2005	[136]

	$A = \frac{\dot{Q}}{U \cdot \Delta T_{\mathrm{LMTD}}}$		
Combustion chamber	$C = \frac{46.08\, m_{in}}{0.995 - \left(\frac{P_{out}}{P_{in}}\right)} (1 + \exp(0.018\, T_{out} - 26.4))$ m(kg/s) and T(K)	1995	[137]
Alkaline electrolysis unit	$C_{ALE} = 840 \cdot \dot{W}$ $\dot{W}(kW)$	2022	[84]
WGS membrane reactor	$C_{WGS} = Cr + Cm + Cc$ $Cr = FP \cdot 5774 \left(\frac{V_{WGS}}{0.104}\right)^{0.59}$ $Cm = FP \cdot 3570 A_{mem}$ $Cc = 10^5 \cdot V_{cat}$ $FP = 1.62 + 1.47\, B$ $B = 0.5146 + 0.6838 \log P + 0.297 (\log P)^2 + 0.0235 (\log P)^6 + 0.002 (\log P)^8$ $A(m^2), V(m^3), P(bar)$	2023	[138] [139]
Pump	$705.48 \cdot \dot{W}^{0.71} (1 + \frac{0.2}{1 - \eta_{pump}})$ $\dot{W}(kW)$	2015	[140]
€ to $ exchange rate	1.056	-	[141]

Table 4.2. Operating expenditure (OPEX) details to determine total product costs (TPC).

Item	Value	Ref.
C1-Raw materials and utilities		
Price of input electricity	0.05 €/kWh	[142]
Price of input CO_2	0.0173 $/kg	[143]
Price of sewage sludge	0	[92]
Price of input heat	9.64 €/GJ	[144]
LNG price	8.303 $/GJ	[145]
Price of woody biomass	0.05 $/kg	[146]
Price of electricity in the Polish energy mix	61 €/MWh	[147]
Price of onshore wind energy in Poland	83 €/MWh	[148]
Water price	0.232 $/m^3	[149]
KOH price	0.82 $/kg	[84]
Plant lifetime	25 years	[150]
Operating hours per year	8000 h	[151]
C2-Operating and maintenance		
Labor cost	For a 435 MW$_{th}$ plant based on LHV of dry biomass: One process manager (161.7 k$/yr) An operating manager (88.2 k$/yr) Two engineers (95 k$/yr) 24 operators (58.8 k$/yr) Three supervisors (66.2 k$/yr) 9 building operators (36.8 k$/yr)	[77]
Supervision	20% of labors’ salary	[152]

Maintenance and repairs	6% of fixed capital investment (FCI)	[152]
Maintenance supplies	15% of maintenance and repairs	[152]
Laboratory charges	15% of labors' salary	[152]
C3-Patents and royalties		
Patents and royalties	1% of total product costs (TPC)	[152]
C4-Depreciation		
Salvage	5% of fixed capital investment (FCI)	[152]
Lifetime	25 years	[152]
Depreciation cost	$\frac{\text{FCI} - \text{Salvage}}{\text{Lifetime}}$	[152]
C5-Local taxes and insurance		
Local taxes and insurance	3% of fixed capital investment	[152]
C6-Plant overhead costs		
Plant overhead costs	60% of (labors' salary, supervision, and maintenance and repairs)	[152]
C7-General expenses		
Administration	5% of total product costs	[152]
Marketing	5% of total product costs	[152]
Research and development	4% of total product costs	[152]

Table 4.3. Details of the techno-economic analysis to calculate the net present value (NPV).

Item	Value	Ref.
Inflation rate, R	5%	[126]
Discount rate, DR	8%	[126]
Biomethanol selling price	1.1 $/kg	[152]
Natural gas selling price	0.85 $/kg	[153]
Selling price of biojet fuel	1.26 $/L	[77]
Selling price of wax and light hydrocarbons	0.78 $/kg	[154]
Green ammonia selling price	0.95 $/kg	[155]
CO_2 selling price	0.03 $/kg	[67]
Oxygen selling price	0.177 $/kg	[67]

4.2. Life cycle assessment

Life Cycle Assessment is a systematic approach used for evaluating the potential environmental impacts associated with a product system across all stages of its life cycle [156]. It is an established methodology with published ISO standards 14040 and 14044 [33].

The goal of this section is to perform a comprehensive life cycle environmental assessment of the hydrogen utilization systems to produce biofuels, with a specific focus on structural optimization of the systems to achieve nearly zero greenhouse gas (GHG) emissions connected with climate change or global warming potential (GWP) impact categories. Another important category is consumption of resources, especially fossil ones. This work targets researchers and professionals engaged in Life Cycle Assessment (LCA) and hydrogen-based technologies.

The functional unit is defined as 1 kg of biofuels or 1 kg of input biomass, which provides a consistent basis for comparing environmental impacts.

Generally, the system boundary encompasses all relevant upstream and conversion processes, including:

- Biomass Conversion
- Hydrogen production and utilization
- Electricity and natural gas supply
- Fuel synthesis

Life cycle inventory (LCI) data is collected from validated sources, including Aspen Plus process simulation models and the Ecoinvent 3.11 database. Validation of subsystem data is conducted through comparison with existing literature to ensure reliability and accuracy [156].

This thesis explores different renewable energy scenarios, focusing on the use of wind energy and the Poland electricity mix. Assumptions regarding the type and proportion of renewable sources are explicitly stated. Biomass used in the proposed hydrogen energy systems is considered as sewage sludge for biogas plants or woody chips for gasification processes. Geographical boundary is considered Poland.

A lifespan of 25 years is assumed for all proposed systems. It should be noted that this thesis focuses on cradle-to-gate LCA study, mainly considering the process itself. Therefore, impact of infrastructures (pipes, material extraction, and disposal) are excluded because of 25 years of lifespan.

As presented in Table 4.4, attributional LCA is particularly well-suited for process engineering applications because it relies on average data and existing technologies, which reflect the actual performance of current industrial systems. This aligns closely with how engineers design, optimize, and benchmark processes, where consistency and real-world feasibility are essential. Attributional LCA provides a stable and reproducible framework, enabling engineers to make decisions based on well-defined system boundaries and established datasets, without needing to account for broader economic or behavioral shifts. Its simplicity allows for effective environmental hotspot identification, material selection, and incremental improvement within the boundaries of a controlled system.

In contrast, consequential LCA is designed to model system-wide environmental consequences of a decision, including indirect effects such as market responses, supply shifts, and policy impacts. It is more appropriate for strategic, policy-level assessments such as evaluating the potential impacts of carbon taxes, mandates, or large-scale changes in consumer behavior. However, this approach involves complex modeling assumptions such as predicting marginal technologies and market substitutions, which introduces higher levels of uncertainty and data sensitivity. These features make consequential LCA less practical for day-to-day engineering tasks but more powerful for assessing long-term or economy-wide changes.

Table 4.4. Comparison of the attributional and consequential LCA.

Attributional LCA	Consequential LCA
Better for engineering needs by focusing on average and current technologies based on average production data [157]	Appropriate for policy or systemic decision-making [158]
Simplicity, reproducibility, and stability, more practical for design. No complex modeling of indirect effects [159]	Modeling economic consequences of changes in demand or policy and broader system interactions [160]
Fewer assumptions, no systemic responses, and easier to replicate [161]	Higher uncertainty due to reliance on economic and market models [162]
Well-suited for hotspot identification [163]	Depending on marginal effects and future market dynamics, complexity [164]
Widely used in industry due to compatibility with existing LCA tools and data	Broader system knowledge, more difficult to apply in controlled engineering environments, where simplicity and certainty are valued [165]

4.2.1. Consequential LCA using Impact 2002+

Firstly, this thesis models the study with long-term consequential LCA (CLCA) in SimaPro v10.2. In practice, the processes are paired with ecoinvent's "substitution, consequential, long-term" system so that marginal linking and substitutions are applied consistent with ISO goal-and-scope guidance and ILCD recommendations for decision-oriented to avoid harmful products and use value-added products. SimaPro provides direct access to this consequential model and current Ecoinvent v3.11 [166]. For impact assessment, IMPACT 2002+ is selected as a mature hybrid method that connects midpoints to four damage/endpoint areas: human health, ecosystem quality, climate change, and resource use, and is implemented natively in SimaPro, supporting decision-oriented synthesis [167]. This method is chosen because [168]:

- IMPACT 2002+ yields damage-level results suited to cross-category trade-offs common in waste management and energy systems.
- The decision context is long-term, e.g. 25 years.
- System-wide transformation falls under macro decision support where background markets adapt over time.
- CLCA links changes to marginal suppliers and resolves multifunctionality by system expansion/substitution rather than burden-sharing.

Therefore, this research aims to evaluate and compare the environmental impacts across various hydrogen utilization scenarios. It is important to highlight that future advancements, market dynamics, and other factors influencing environmental sustainability were taken into consideration. Additionally, biofuels production using hydrogen as an energy carrier is expected to lead to structural shifts in background systems, which lie beyond the scope of current decision-making processes. According to the international reference life cycle data guidebook, this places the present study in scenario B, or the meso/macro level [169]. Decisions that have a macro-level impact on background systems were modeled using long-term consequential life cycle assessment. System expansion is used in consequential life cycle assessment modeling to solve multifunctionality problems. Marginal goods or technologies are used in place of the products, rather than sharing the environmental consequences among them. Carbon dioxide collection, methanol synthesis, anaerobic biomass digestion, electrolysis cells, and product replacement with marginal equivalents were among the system limits.

A variety of datasets were used in this investigation, including both historical and operational data. The Ecoinvent database 3.11 was used to retrieve historical data on energy and chemical output. Additional process cycles were simulated using Aspen Plus, and operational data on the mass and energy dynamics of the biogas plant were provided in ref. [92]. The next subsections describe in greater detail the methods and assumptions applied to wastewater sludge treatment. The Impact 2002+ approach was used to do the LCIA at the endpoint level in this study, which covered damage and climate change categories. The approach is pertinent to this investigation as it is widely used in the assessment of waste valorization scenarios [170], [171].

For marginal technologies and products, even little changes in demand have a significant effect. As demand rises, they are expected to emerge as the most adaptable and well-liked choices in the future. Table 4.5 lists the marginal technologies and items that were discovered across a ten-year time span using the Weidema et al. [172] approach.

Table 4.5. Life Cycle Assessment Details in SimaPro Software.

Electricity input	The system uses electricity generated from onshore wind turbines with a capacity of 1-3 MW. These turbines are connected to a high-voltage network in Poland, and the assessment follows a consequential approach.
Water input	The source of water is natural, with no additional modifications or treatments applied.
Heat input	Heat is supplied from a combination of local sources, including small-scale and central facilities, co-generation plants, and biogas production within Poland. This is also evaluated using a consequential approach.
Liquified natural gas input	The liquefied natural gas is sourced from the global market, using a consequential system model for assessment.
CO_2 usage	The carbon dioxide used in the system comes from the global market for liquid CO_2, and its utilization follows a consequential system approach.
Avoided product—natural gas	The system accounts for the displacement of high-pressure natural gas in Poland. The market for this gas and its assessment is based on consequential modeling.
Avoided product—biomethanol	Methanol, produced globally, is the avoided product in this system, with a consequential global market assessment applied.
Avoided product—oxygen	The system avoids the production of liquid oxygen, which is sourced from the global market and evaluated under a consequential framework.

4.2.2. Attributional LCA using ReCipE 2016

To enable a transparent comparison between LCA allocation methods, this thesis first applies a consequential LCA (CLCA) with IMPACT 2002+ to consider long-term, market-mediated consequences of the decision context. IMPACT 2002+ was an appropriate, widely used LCIA at that time, linking 14 midpoint categories to four damage endpoints. This section now complements the CLCA by reporting an attributional LCA (ALCA) that characterizes the average allocation of the products under current technology and supply mixes, using the state-of-the-art ReCiPe 2016 Midpoint (H) method for impact assessment in SimaPro. ReCiPe 2016 offers updated, harmonized characterization factors across a comprehensive set of midpoint impact categories, improved modelling. Choosing midpoints further reduces value-laden aggregation and facilitates comparison with contemporary studies. Presenting ALCA results alongside the earlier CLCA allows testing the sensitivity of conclusions to allocation versus system expansion/substitution choices, enhances reproducibility under ISO 14040/14044, and aligns with current best practice for reporting both decision-consequences (CLCA) and attributional baselines (ALCA) [173].

All impact categories related to industrial processes are considered, as shown in Table 4.6. In this table, particular focus is given to climate change, alongside non-climate-related categories, including human toxicity, ionizing radiation, and terrestrial ecotoxicity. Additionally, resource-related impact categories, such as fossil fuel depletion, are also considered.

This study presents a current scenario that reflects the most recent technological advances adopted by bio-jet fuel and natural gas production. In addition, energy sources based on fossil fuels (Poland's electricity mix) and renewable sources (wind turbines) are compared for all investigations. Moreover, the design parameters are reported in mass/energy results of each chapter. Table 4.7 also reports the selection of the input data in SimaPro.

Table 4.6. Impact categories of the Recipe 2016 method [174]

Impact category	Unit	Abbreviation	Impact category	Unit	Abbreviation
Global Warming	kg CO_2 eq	GWP100	Freshwater ecotoxicity	kg 1.4-DCB	FETP

Stratospheric ozone depletion	kg CFC11 eq	ODP	Marine ecotoxicity	kg 1.4-DCB	METP
Ionizing radiation	kBq Co-60 eq	IRP	Human carcinogenic toxicity	kg 1.4-DCB	HTP
Ozone formation, Human health	kg NOx eq	OF-HH	Human non-carcinogenic toxicity	kg 1.4-DCB	HTP
Fine particulate matter formation	kg PM2.5 eq	PMFP	Land use	m^2a crop eq	LU
Ozone formation, Terrestrial ecosystems	kg NOx eq	OF-TE	Mineral resource scarcity	kg Cu eq	MDP
Terrestrial acidification	kg SO_2 eq	TAP	Fossil resource scarcity	kg oil eq	FDP
Freshwater eutrophication	kg P eq	FEP	Water consumption	m^3	WC
Marine eutrophication	kg N eq	MEP			
Terrestrial ecotoxicity	kg 1.4-DCB	TETP			

Table 4.7. Input data sets from Ecoinvent 3.11 for the modeled system in Poland.

Component	Assumption
Wind energy	Electricity, high voltage | electricity production, wind, >3MW turbine, onshore | Cut-off, System
Polish electricity mix	Electricity, high voltage | production mix | Cut-off, System 36.1% coal, 32.6% oil, 16.2% natural gas, 3.4% solar-wind, and 11.7% biofuels [175]
CO_2	carbon dioxide, liquid | market for | Cut-off, System
Biomass	Pulpwood, softwood, measured as solid wood under bark | softwood forest, spruce, sustainable forest management | Cut-off, System
Wastewater of syngas cleaning	Wastewater from plywood production | treatment of, capacity 5E9l/year | Cut-off, System

4.3. Overall key performance indicators

First and foremost, fuel production capacity establishes plant scale mass/energy balances and sizing. It lets comparison of configurations on a common functional basis and check that optimal designs still meet targeted output levels of fuel production. It is a primary performance indicator in the proposed hydrogen utilization systems. It quantifies the sustained rate at which saleable fuel can be produced under defined operating conditions, and it anchors whether a facility is considered small-, medium-, or large-scale within its specific industry context. Beyond simple throughput, capacity shapes design choices, cost structure, and environmental performance [176].

The energy efficiency of each subsystem captures the thermodynamic benefit of integration levers. It is the primary physics-based indicator linking design choices to lower material consumption per unit product, central to optimization. It is evaluated by calculating the ratio of the energy content in the output streams to that of the corresponding input streams [177]:

$$\eta_{en} = \frac{(\dot{m} \cdot LHV)_{\mathrm{P}}}{\dot{W}_{\mathrm{in}} + (\dot{m} \cdot LHV)_{\mathrm{F}}} \tag{4.15}$$

In these equations $\dot{m}$, LHV and $\dot{W}_{\mathrm{in}}$ represent the mass flow rate, lower heating value, and power demand of the subsystems. Additionally, the subscripts P and F show the products and fuels of each subsystem. In this equation, the chemical energy of useful products such as fuels is divided by the chemical energy of the input streams. Losses and inefficiencies are considered here (including waste streams of tars and ash in the gasification process, CO_2 emissions from methanol synthesis, and waste heat from combustion and pyrolysis).

Levelized cost of fuel (LCOF) gives a discounted, per-unit cost that is comparable across pathways, scales, and scenarios. It is the core economic objective for selecting polygeneration designs that are not only efficient but also market competitive. It is the discounted-average cost to produce one unit of fuel over a plant's lifetime. It is computed as the net present value (NPV) of all expenditures (CAPEX and OPEX), minus the NPV of by-product revenues and credits, divided by the fuel capacity. Typical units are \$/tonne of product. energy-normalized variants such as \$/GJ or \$/L are also used. By-product revenues can include sale of co-produced gases/liquids, heat, electricity exports, or environmental credits (e.g., CO_2 offtake), and should be treated consistently with the chosen system boundary and price basis [125]:

$$LCOF = \frac{\left(FCI \cdot CRF + TPC - AI_{Byproducts}\right)}{\dot{m}_{\mathrm{F}} \cdot \tau} \tag{4.16}$$

In which $\dot{m}$ represents the mass flow rate of the main fuel, while τ denotes the 8000 h of full load hours. In addition, *FCI, CRF, TPC*, and *AI* refer to fixed capital investment, capital recovery factor, total product cost, and annual income, respectively. These parameters are defined in the section for techno-economic analysis.

From an environmental perspective, global warming potential (GWP) quantifies climate performance of each configuration on a consistent cradle-to-gate basis, testing whether integration choices deliver decarbonization aligned with EU targets and validating trade-offs when cost and efficiency pull in other directions. It is a key performance indicator that quantifies the contribution of life-cycle greenhouse-gas emissions to climate change. It is typically reported as GWP_{100} in $kgCO_2eq/kgFuel$, aggregating all emitted gases into carbon-dioxide equivalents over a 100-year time horizon [178]:

$$GWP_{100} = \sum m_i CF_i \tag{4.17}$$

Where, m_i is the mass of gases in the inventory and CF_i is the ReCiPe-implemented characterization factor.

Fossil resource scarcity, also called fossil depletion potential (FDP) tracks reliance on fossil inputs displaced by hydrogen and biomass integration. It complements GWP by reflecting energy security and resource sustainability, ensuring the chosen designs reduce both emissions and fossil dependence. It is a key LCA indicator that quantifies the use of fossil resources. In ReCiPe 2016, extracted fossil carriers (e.g., crude oil, natural gas, hard coal) are converted to oil-equivalent mass using the method's fossil fuel potential (FFP) characterization factors and summed. Results are typically reported as kgoileq/kgFuel [179]:

$$FDP = \sum R_j CF_j \tag{4.18}$$

Where R_j is the quantity of fossil resources and CF_j is based on the ratio of the carrier's higher heating value (HHV) to that of crude oil.

Next five chapters examine hydrogen-based polygeneration systems selected to prioritize liquid energy carriers for hard-to-electrify sectors while exploiting deep process integration enabled by electrolytic hydrogen and oxygen. Whereas power-to-gas (PtG) is technologically mature for long-duration storage yet largely confined to gaseous energy services, power-and-biomass/biogas-to-liquid

(PBtL) fuels provide drop-in products compatible with existing logistics and combustion infrastructure. Accordingly,

- Chapter 5 analyzes two biogas-to-methanol plants, which integrate anaerobic digestion and biogenic CO_2 with green H_2 to produce biomethanol. The improved case integrates power and natural gas production with the base case.
- Chapter 6 presents biomass-to-methanol system with power and natural gas production, which couples oxygen-blown gasification with solid oxide electrolyzer to raise biomethanol and natural gas capacity.
- Chapter 7 integrates biomass-to-methanol with energy storage systems, which recovers waste heat from CAES/TES systems to the biomethanol plant to enhance energy efficiency.
- Chapter 8 describes three power-to ammonia and biomass-to-ammonia cases, which retain Haber–Bosch reactor while sourcing green hydrogen and leveraging electrolyzer O_2, with CO_2 capture, to produce easily liquefied hydrogen carrier suited to seasonal storage.
- Chapter 9 proposes a biomass-to-jet fuel system, which converts biogenic syngas to drop-in sustainable aviation fuel (SAF) for long-distance transport demanding high volumetric energy density with co-produced natural gas.

Collectively, these systems span woody biomass or sewage sludge feedstocks and baseline versus storage-enhanced operability, and were chosen to demonstrate, within comparative scenarios, how hydrogen-based polygeneration units can increase efficiency, decrease LCOF, and reduce LCA impacts.

5. Power and biogas to methanol

This section establishes the cases for biomethanol production that this thesis optimizes against, providing the reference mass/energy balances, techno-economic, and environmental baselines. By explicitly revealing the integration gaps, it defines where polygeneration levers can lift efficiency, cut cost, and reduce impacts in hydrogen-enabled methanol production.

5.1. Basic biogas-to-methanol system

The base case of biomethanol production couples high-temperature electrolysis, chosen for its superior efficiency and heat-integration potential, with an anaerobic-digestion biogas plant that valorizes wastes and improves environmental outcomes. Together they convert low-value residues and renewable power into biomethanol and biomethane, a high-value platform fuel/chemical, providing a pragmatic reference for later optimization. The proposed plant in Fig. 5.1 produces biomethanol using wind electricity or Poland electricity mix as the primary energy sources. Sewage sludge first undergoes thermal pretreatment at 90 °C to enhance degradability, which needs some additional input of thermal energy. Thermal treatment effectively dissolves contaminants of sludge like heavy metals and organic pollutants, serving as a pretreatment method that significantly boosts its potential for biogas production [180]. Then, sewage sludge is directed to the anaerobic digester, 10% of which is converted to biogas, while 90% of which is digestate. Under thermophilic condition, biogas is produced at 1.5 bar and 55°C. In Fig. 5.1, biogas is upgraded to CO_2 and biomethane.

Various techniques are available for the removal of carbon dioxide from biogas, including cryogenic upgrading, scrubbing, chemical adsorption, and pressure swing adsorption. These biogas upgrading technologies and plants demonstrate high efficiency, achieving biomethane recovery rates of 95% to 99%, among which, water scrubbing is preferred for its simplicity in operation and low cost [93]. In this subsystem, biogas and water enter the absorber, producing biomethane from top of the column. Then, the solvent is directed into the stripping column, which functions at 30°C and 1.16 bar for regeneration. Air serving as a stripping gas is introduced at the bottom of the stripper column at 30°C. The solvent (water) is then cycled back to the absorption column. Finally, the methanol synthesis unit receives the CO_2 produced by the stripper, where it is mixed with H_2 from a solid oxide electrolyzer, compressed to 51 bars, and converted to methanol in a reactor loop. Biomethanol is then sent to a distillation column. A modest reboiler duty is supplied, and biomethanol of 99% purity is obtained. Process water from distillation is recycled as feed to the electrolyzer. Waste heat of H_2/O_2 coolers is used to generate steam for the electrolyzer.

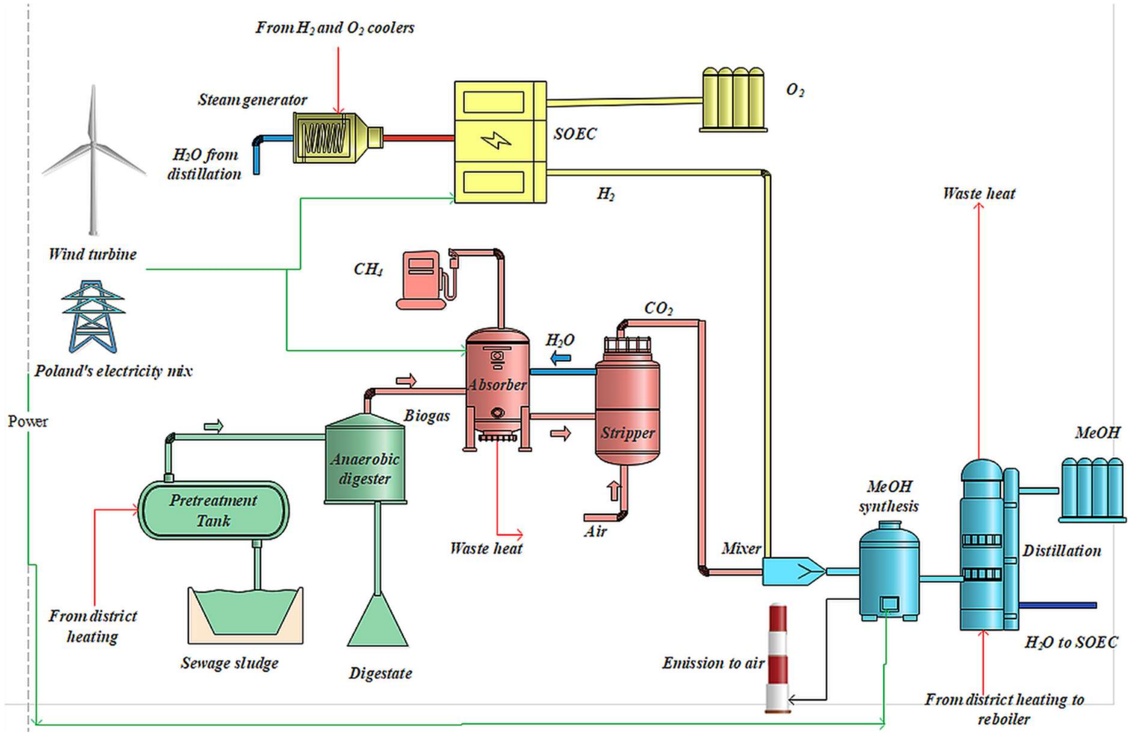

Fig. 5.1 Base case for biomethanol production.

Base case limitations visible from Fig. 5.1 are as follows:

- The methanol synthesis loop rejects a large amount of waste heat that is simply dumped, with no recovery or cross-integration.
- Oxygen co-production in the SOEC is not utilized anywhere in the process. so, the base case requires O_2 compression and storage facilities, adding electricity demand and product costs.
- The base case exhibits weak thermodynamic integration and avoidable energy losses, signaling room for improvement via waste-heat recovery and O_2 utilization.

5.2. Improved biogas-to-methanol system with power and natural gas production

To optimize the base case for hydrogen utilization and biomethanol production, this thesis remedies two visible weaknesses of the base case, large unrecovered process heat and unutilized electrolytic O_2, by proposing the improved configuration shown in Fig. 5.2, which couples liquefied natural gas (LNG) regasification, an oxy-fuel gas turbine, and a water-gas-shift reactor (WGSR) into a single thermodynamically coherent scheme.

Liquified natural gas is increasingly important in meeting rising natural-gas demand because of its high LHV and reduced volume for efficient long-distance transport. Once regasified it serves multiple industrial applications, notably power generation and gas-supply operations [181], [182].

In Fig. 5.2, the methanol loop's low temperature waste heat is matched to LNG's deep cold energy during regasification, transforming what was rejected heat into useful duty, sharply reducing external utilities while enabling water-free natural gas production via closed heat exchanger network. a 10% of the produced natural gas then feeds an oxy-combustor that uses the SOEC's by-product O_2. Then, after being compressed to 35 bars, oxygen from the solid oxide electrolyzer is transferred to a fuel-rich combustor, which also heats and uses CO_2, playing a critical role specifically to lower the flame temperature. To further decrease the flame temperature of the combustor to 1200 °C before entering the gas turbine, a cooler is installed downstream of the combustor because after the fuel-rich combustion, the flame temperature is very high causing lower efficiency and thermal stress to gas turbines [183]. Output heat of the gas turbine's intercooler is used in the steam generator of solid oxide electrolyzer. Oxy-gas turbine generates power, decreases total input electricity, and closes thermal loops. The flue gases leaving the gas turbine is usually lost to the environment, causing GHG emissions. However, gases are enriched by a water gas shift reactor in the improved cycle to enhance hydrogen content and reduce CO content making it suitable for CO_2 hydrogenation in biomethanol production. Then, rich flue gases are mixed with hydrogen from the electrolyzer and CO_2 from the biogas upgrading unit. In this way, exhaust gas recycling contributes to further hydrogen utilization and biomethanol production. Integration of LNG and gas turbine units with the base case could increase energy efficiency and fuel capacity while utilizing of O_2.

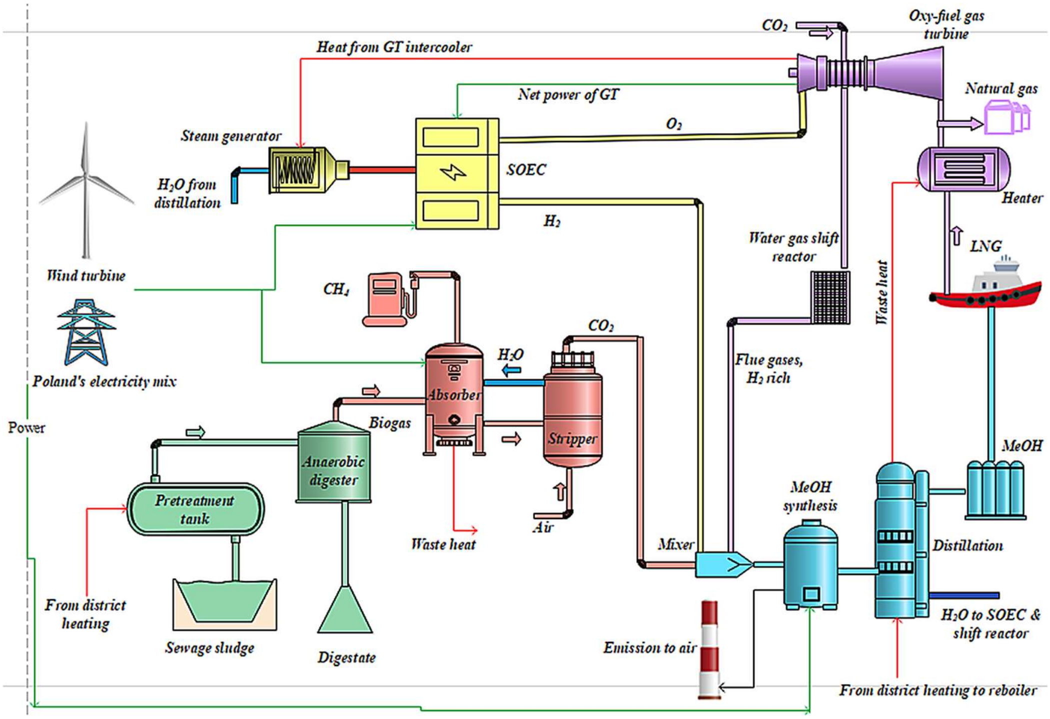

Fig. 5.2. Improved case of biogas based biomethanol and natural gas production.

Subsystems not explicitly described in the improved configuration, namely biogas generation and upgrading, are retained as in the base case. This chapter therefore compares the two biogas-based hydrogen-utilization schemes (base vs. improved) across energy performance, techno-economic metrics, and life-cycle impacts.

5.3. Thermodynamic results of the biogas-to-methanol plants

This subsection presents the evaluation of the proposed biogas-to-methanol systems using hydrogen energy from key perspectives of energy efficiency and production capacity. The analysis is supported by sensitivity analysis to assess the influence of critical parameters. Together, these results provide a comprehensive understanding of the system's potential within the broader context of biofuels development.

In Fig. 5.3, mass and energy results of the biogas-to-methanol system are presented. The system co-produces natural gas and bioethanol using sewage sludge as feedstock. About 30988 kg/h of sewage sludge enters pretreatment, which needs roughly 567 kW of heat. The anaerobic digester produces 30225.6 kg/h of digestate and directs raw biogas to water-scrubbing unit. The upgrading loop requires 94.65 kW of electricity, releases 58 kW of heat, and then splits the biogas into 240 kg/h of CH_4-rich gas and 381 kg/h of CO_2 from the stripper. Power is supplied by wind energy or by the Polish electricity mix, with the majority (748 kW) consumed by the electrolyzer. The electrolyzer consumes 260 kg/h of H_2O and produces 29 kg/h of H_2 and O_2. Oxygen feeds an oxy-fuel gas turbine, which delivers 288 kW of net power to SOEC and 119.5 kW of recoverable heat to the steam generator. A heater fed by LNG (2600 kg/h) recovers waste heat from the methanol synthesis unit. a water-gas shift reactor conditions the H_2/CO_2 stream for fuel synthesis. The methanol synthesis transfers 508 kW of process heat to LNG regasification and consumes 290 kW of electricity, plus 105.6 kW of district heat for refining, and produces 126 kg/h of methanol, where 293 kg/h of water is recycled to the SOEC and WGSR. In the stack, CO_2 emissions are found to be 3.8 kg/h biogenic and 6.4 kg/h fossil, with 2.16 kg/h of fossil CO emissions, while other substances are minor.

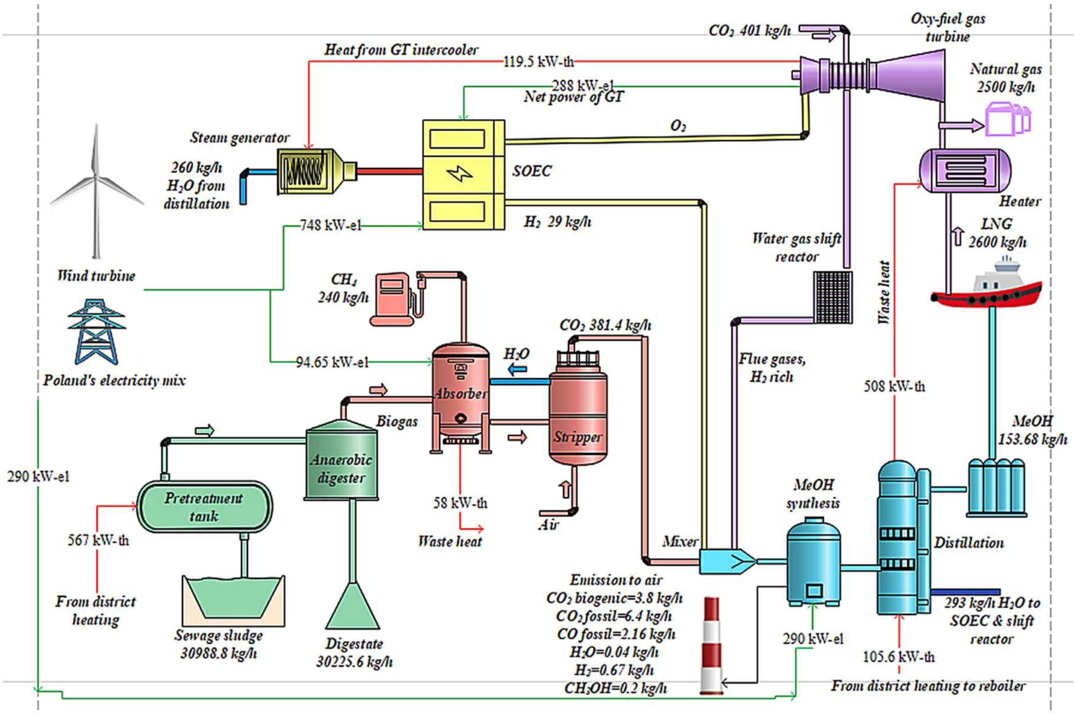

Fig. 5.3. Mass and energy results of the plant with LNG and gas turbine units.

In this thesis, a sensitivity analysis on the SOEC cell count is performed because its sizing is the primary lever that sets the plant's hydrogen supply and co-produced O_2, thereby controlling biomethanol throughput, power draw, and heat-integration opportunities. Varying the number of cells quantifies the capacity and efficiency trade-off. Comparing the base and improved cases reveals how integration guides optimal electrolyzer sizing for maximum fuel capacity at acceptable efficiency. The influence of the number of solid oxide electrolysis cells on biomethanol production capacity is illustrated in Fig. 5.4 (right). As the number of solid oxide electrolyzer cells increases, both the size of the electrolysis system and the hydrogen production rate grow, leading to higher biomethanol capacity. Notably, when the cell count rises from 180 to 280, biomethanol production increases significantly by 9.52% in the system without liquified natural gas and gas turbine cycles, and by 16.32% in the system with these cycles. The impact of solid oxide electrolyzer cell count on overall energy efficiency is depicted in Fig. 5.4. As the number of cells increases, the power consumption of the electrolyzer also rises, which reduces energy efficiency by 6.35% in the system without liquified natural gas and gas turbine cycles and by 1.04% in the system with these cycles. Consequently, the system integrating LNG and gas turbine cycles achieves improvements in both biomethanol production, reaching 1225 tonne/yr, and energy efficiency, reaching 84%.

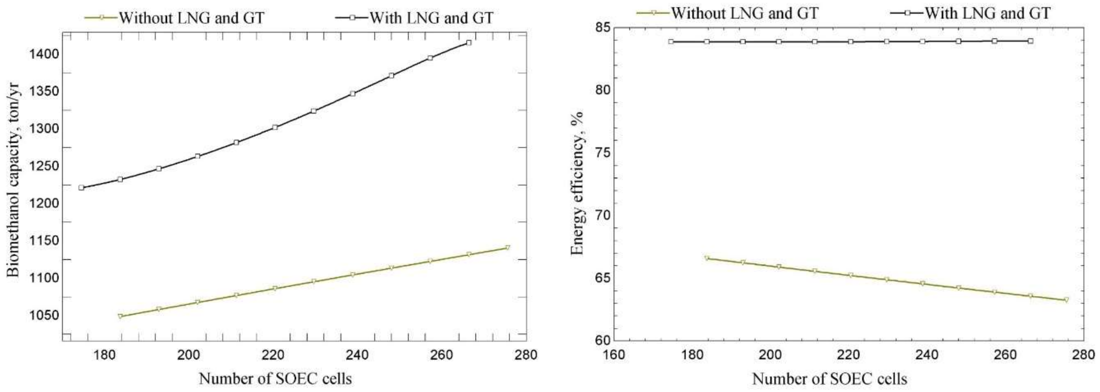

Fig. 5.4. The effect of the number of SOEC cells on the fuel capacity and energy efficiency of two proposed plants.

Additionally, the influence of methanol-reactor temperature because it is a first-order lever on equilibrium approach, recycling loading, and heat duties, hence it directly sets fuel capacity and system efficiency. Sensitivity over both cases shows how heat-integration maximizes biomethanol output and energy efficiency for optimal hydrogen utilization. The impact of raising the temperature of the methanol reactor from 200°C to 300°C on the production of biomethanol is shown in Fig. 5.5. Increasing the temperature enhances the reactor's capacity, boosting biomethanol output from 750 to 1200 tonne/yr without liquified natural gas and gas turbine units, and from 825 to 1500 tonne/yr with these units. This improvement stems from the improved conversion efficiency of input gases into liquid water and biomethanol within the reactor, resulting in a higher concentration of biomethanol at the reactor's exit. When the liquified natural gas and gas turbine cycles are integrated, the flue gases from the gas turbine cycle combine with hydrogen and CO_2 entering the methanol synthesis unit, enhancing the methanol generation system's capacity. Thus, the biomethanol production rate is increased when liquified natural gas and gas turbine cycles are employed.

Fig. 5.5 depicts the influence of methanol reactor temperature on energy efficiency, showing a clear upward trend. An increase in energy efficiency is the result of an increase in biomethanol capacity. Additionally, by increasing the temperature from 200 to 300 °C, the energy efficiency of the system without liquified natural gas and gas turbine units increases from 58% to 67%, and that of the system including liquified natural gas and gas turbine cycles increases from 82.5% to 84%. When the liquified natural gas and gas turbine cycles are involved, it is possible to produce 2500 kg/h of natural gas, electricity, and more biomethanol. Therefore, the energy efficiency of the system including the gas turbine and liquified natural gas units is much higher than that of the system without the liquified natural gas and gas turbine subsystems.

In summary, maximization of the temperature of the methanol reactor is deemed beneficial because it leads to an increase in both the biomethanol capacity and energy efficiency.

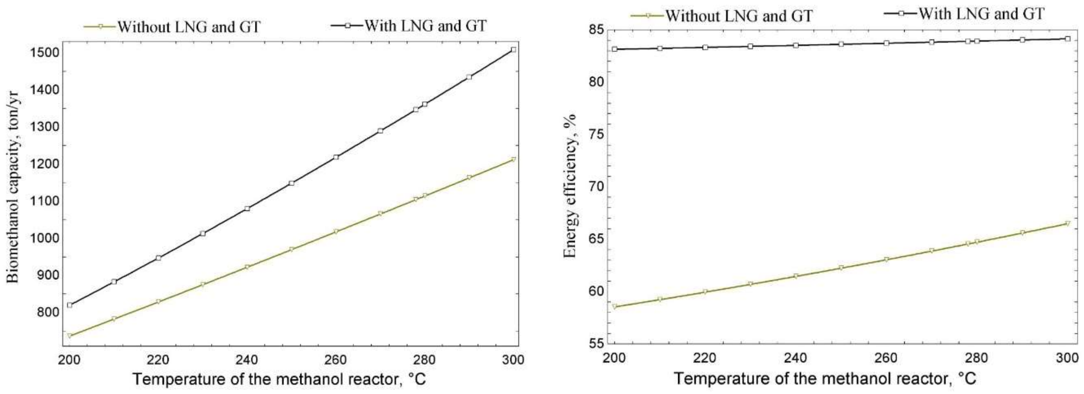

Fig. 5.5. Effect of methanol reactor temperature on two planned plants' biomethanol capacity and energy efficiency.

5.4. Techno-economic results of the biogas-to-methanol systems

This section reports the techno-economic analysis for both biogas-based methanol production systems because cost minimization via levelized cost of fuel (LCOF) is a core objective of this thesis. By quantifying cost drivers and comparing base vs. integrated designs, it identifies the configurations and setpoints that achieve optimal hydrogen utilization at the lowest unit cost.

Fig. 5.6 presents the results of analysis regarding the two dominant drivers of operating expenditure (OPEX), i.e. price of sewage sludge and electricity as prime movers of the plants, directly tied to the thesis goal of minimizing unit cost under real market variability. The cost-effective design ensures the optimal hydrogen utilization solution. Fig. 5.6 shows the impact of the price of wastewater sludge on the levelized cost of fuel. In the base case, the price of the sewage sludge was assumed to be 0. As the price increases from 0 to 0.2 $/kg, the LCOF increases by 35% in the system with liquified natural gas and gas turbine cycles, and from 700 to 3200 $/tonne in the system without these cycles. This occurs because wastewater sludge is one of the raw materials inputs to the proposed plants, thereby increasing operating and maintenance cost. Furthermore, the system with liquified natural gas and gas turbine cycles has a lower LCOF than the system without them, as it produces additional natural gas, which improves the annual income from sold products.

Fig. 5.6 (left) also illustrates the impact of the price of input electricity on the LCOF. In the base case, the price of input electricity was equal to 0.05 $/kWh. When the price of input power increases from 0.01 to 0.2 $/kWh, the LCOF increases from 550 to 650 $/tonne in the system with LNG and gas turbine cycles and from 600 to 1650 $/tonne in the system without them, as input electricity is one of the input utilities for the proposed plants, increasing the operating and maintenance cost. Furthermore, the system with liquified natural gas and gas turbine cycles has a lower LCOF than the system without them, as it produces additional natural gas, which improves the annual income of the sold products.

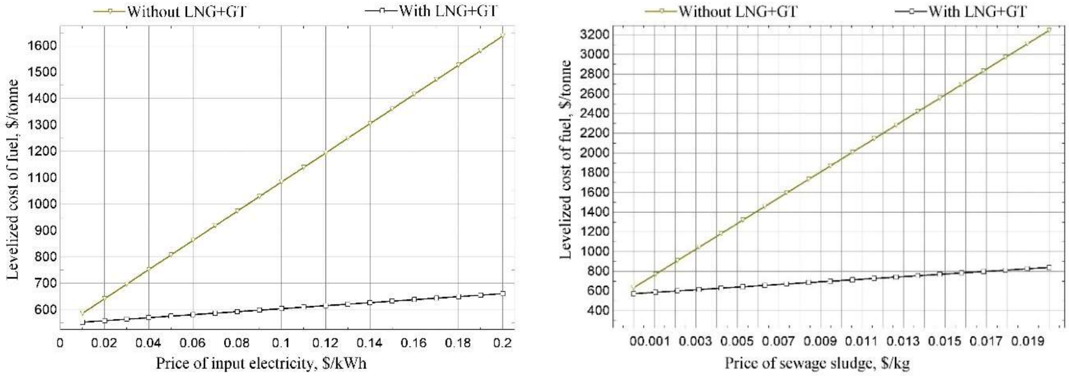

Fig. 5.6. Effect of the biomass and electricity prices on the levelized cost of fuel of two proposed plants.

Because investment viability is as critical as thermodynamic performance, a 25-year net present value (NPV) and payback time are calculated to quantify long-term value creation and capital recovery for each configuration. These metrics capture the benefits of integration versus added CAPEX, directly testing the thesis hypothesis that LNG and gas turbine coupling improves the revenues and deployment readiness of hydrogen-enabled polygeneration system. Fig. 5.7 presents the net present value and the payback time for systems with and without liquified natural gas and gas turbine units. The payback time of the system incorporating LNG-GT units is 3 years, whereas for the system without them it extends to 10 years. This difference arises from the fact that the system with LNG-GT can produce 2500 kg/h of natural gas, along with a higher volume of biomethanol, and compensate for a part of the input electricity. On the contrary, the system lacking LNG and gas turbine cycles does not generate electricity or natural gas, both of which are key marketable products. Over a span of 25 years, the NPV of the plant equipped with liquified natural gas and gas turbine cycles is projected to reach 140 M$, while that of the plant without these cycles is estimated at 20 M$.

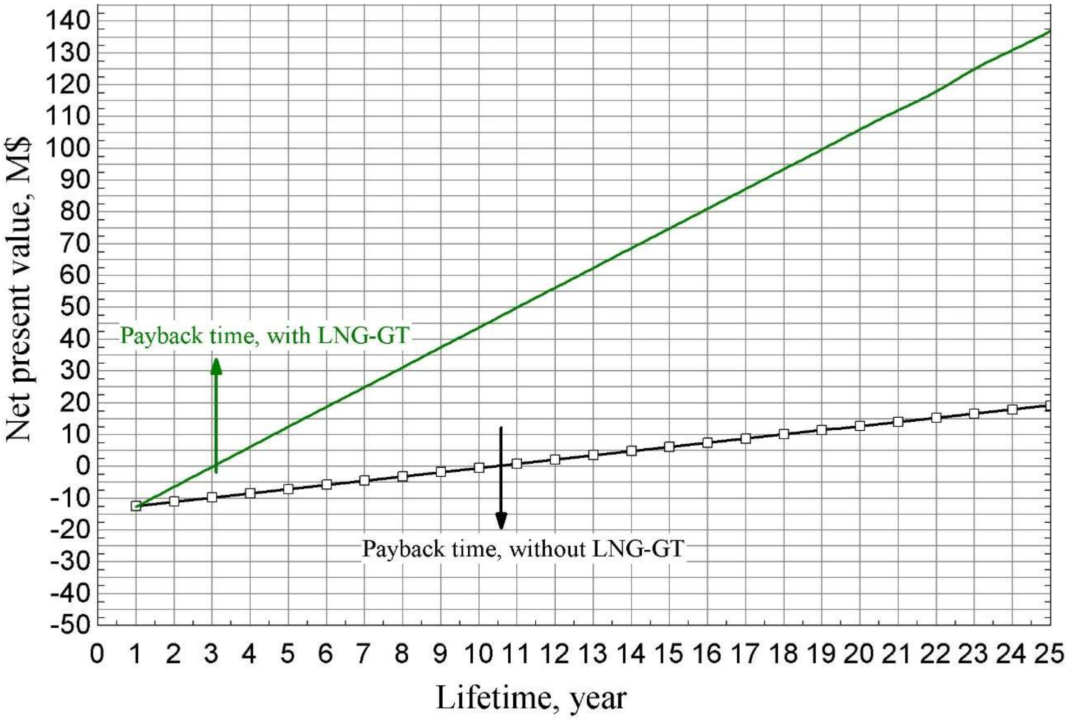

Fig. 5.7. The lifetime impact on the plant's NPV for with and without LNG-GT subsystems.

5.5. Consequential environmental results of the biogas-to-methanol systems

This thesis applies long-term consequential LCA in SimaPro v10.2 using ecoinvent's consequential "substitution, long-term" model to capture marginal suppliers and market adaptations. IMPACT 2002+ is chosen for damage-level results suited to 25-year, system-transforming decisions and for resolving multifunctionality via system expansion.

Fig. 5.8 and 5.9 quantify how integration of LNG and gas turbine impacts climate change and resource consumption under consequential LCA. They validate the hypothesis that energy integration can cut environmental impacts more than a base case. Fig. 5.8 and 5.9 present the results of the life cycle assessment performed in this study. In Fig. 5.8, particular attention is paid to the climate change category, comparing systems with and without liquefied natural gas (LNG) and gas turbine units. Both systems show net negative CO_2 emissions. This outcome may initially seem paradoxical, especially considering the positive CO_2 emissions associated with the input from liquified natural gas stream. However, on closer examination, it becomes evident that the production of natural gas within the system produces more pronounced negative carbon dioxide emissions. This is primarily because it eliminates the need to buy and import natural gas from other nations, like Norway, to Poland, hence reducing the carbon emissions that come with distribution and transportation. Consequently, despite the positive CO_2 emissions from the liquified natural gas input, the overall impact is mitigated by the system's reliance on domestically re-gasified natural gas. Consequently, the system that features liquified natural gas and gas turbine units achieves 53% reduction in CO_2 emissions compared to the system that without these components.

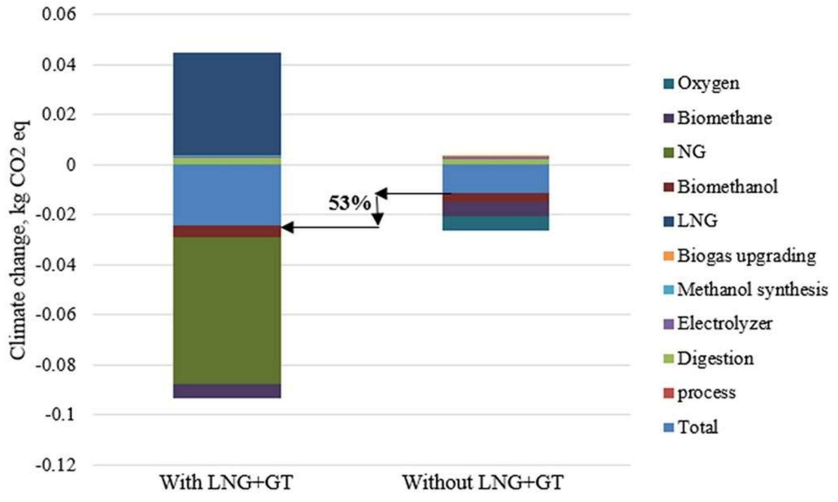

Fig. 5.8. Comparison of the values of climate change for with and without LNG and gas turbine subsystems.

In Fig. 5.9, attention is focused on the damage category of resources, comparing systems with or without liquefied natural gas and gas turbine units. Both systems exhibit negative resource consumption, a seemingly paradoxical outcome at first glance, especially given the positive resource utilization associated with the input liquified natural gas input stream. However, closer examination reveals that the production of natural gas within the system leads to more significant negative resource consumption. As before, this effect arises mainly from avoiding the need to import natural gas from other countries to Poland. Consequently, despite the positive consumption of resources consumption linked to LNG input, the overall impact is counterbalanced by the system's reliance on domestically re-gasified natural gas.

As a result, the inclusion of LNG and gas turbine units achieves a 70% reduction in resource use compared to the system without these components.

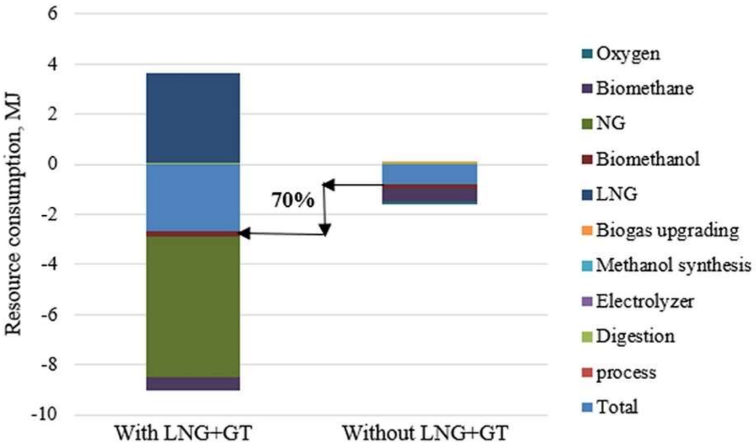

Fig. 5.9. Comparison of resource values for the plant with and without liquified natural gas and gas turbine subsystems.

Figures 5.10 and 5.11 are included to choose wind energy or Poland electricity in terms of environmental outcomes of hydrogen-enabled biomethanol production. In addition, these figures identify the environmental hotspots among different subsystems and products. Figure 5.10 presents a sensitivity analysis of climate change impacts across various power sources, considering the inclusion of liquified natural gas and gas turbine units. The results highlight significant differences depending on the energy source selected. For instance, when wind turbines are used as a renewable energy source, the total climate change impact is -0.02 kgCO$_2$eq/kgBiomass, indicating a net reduction in greenhouse gas emissions. Conversely, if Poland's electricity mix dominated by fossil fuels is employed, the total climate change impact rises to approximately +0.01 kgCO$_2$eq/kgBiomass, reflecting a net increase in emissions. Biofuel production capacities exhibit favorable life cycle assessment outcomes, primarily due to their ability to achieve negative CO$_2$ emissions. However, other subsystems contribute to increased global warming. Among these, the most notable contributors are natural gas capacities, which offset emissions and act as negative contributors, and the combined effects of the electrolyzer, liquified natural gas, and gas turbine units, which emerge as significant positive contributors to CO$_2$ emissions. This analysis highlights the critical influence of energy source selection on climate change impacts, emphasizing the potential benefits of integrating renewable energy technologies and biofuel systems to effectively mitigate greenhouse gas emissions.

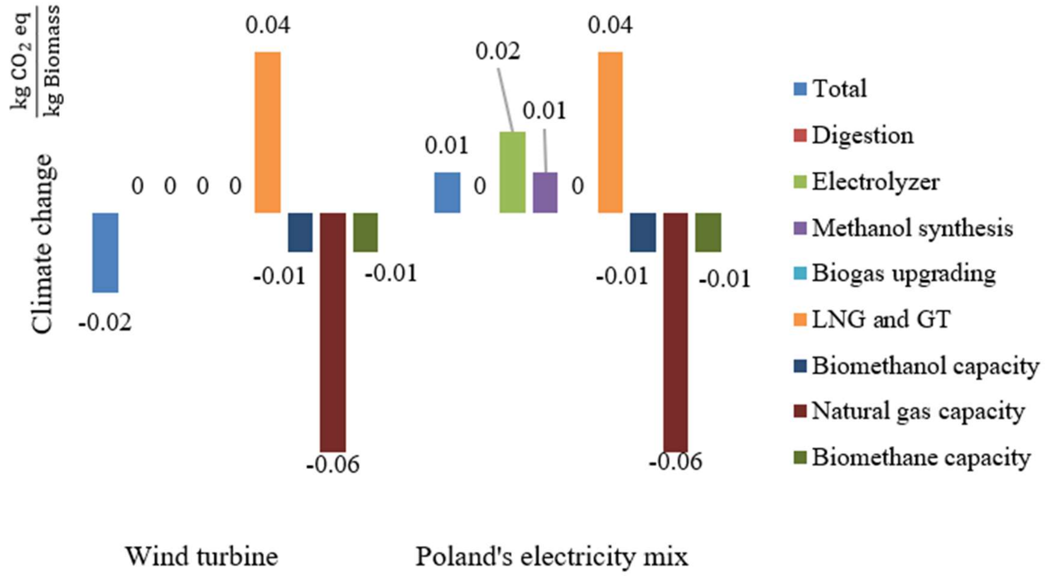

Fig. 5.10. Sensitivity analysis of climate change for different power sources with LNG and gas turbine units.

Figure 5.11 illustrates the resource consumption for two different power sources: wind turbines and Poland's electricity mix. In the wind turbine scenario, the total resource consumption is -2.69 MJ/kgBiomass, demonstrating a net reduction in resource use, while in Poland's electricity mix scenario, the total consumption rises to about -2.27 MJ/kgBiomass, reflecting a net increase. Natural gas capacity shows the most significant negative impact in both scenarios, at around -5.59 MJ/kgBiomass. Liquified natural gas and gas turbine units are the largest positive contributors in both scenarios, with +3.6MJ/kgBiomass. Overall, the wind turbine scenario demonstrates the potential for significant reductions in resource consumption compared to that of Poland's electricity mix.

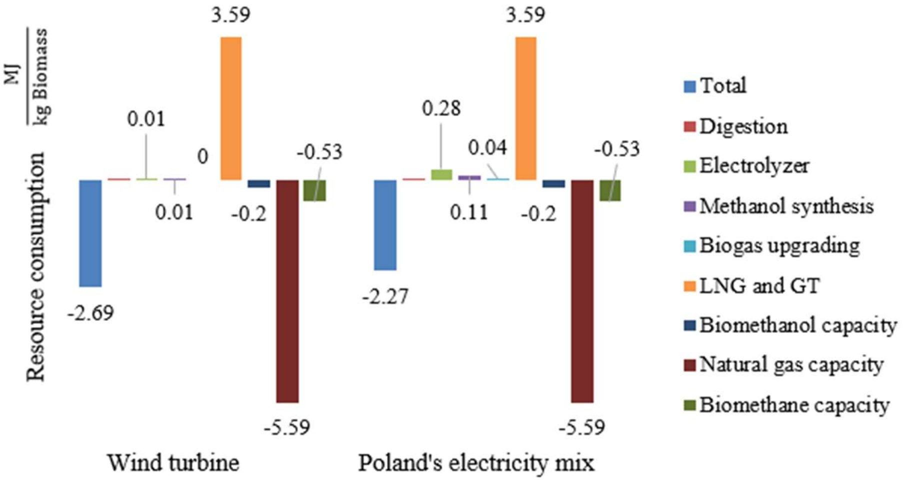

Fig. 5.11. Sensitivity analysis of resource consumption for different power sources with LNG and gas turbine units.

5.6. Attributional environmental results of the biogas-to-methanol systems

This thesis complements the consequential LCA by running an attributional approach with ReCiPe 2016 Midpoint (H) to quantify average burdens under current technologies and supply mixes, using updated, harmonized factors that improve comparability. Reporting ALCA alongside CLCA tests sensitivity to allocation vs. substitution, enhances reproducibility per ISO 14040/14044, and aligns with current best practice.

The detailed LCA breakdown reported in Table 5.1 ties directly to the thesis topic by pinpointing where environmental burdens arise inside the plant. By hotspot identification, it guides the optimization goals to lessen environmental impacts. The detailed LCA results presented in Table 5.1 provide a comprehensive overview of the environmental impacts associated with the biogas-to-methanol system. Among the various impact categories, global warming potential stands out with a total value of 0.205893 kgCO$_2$eq, where significant contributions come from the SOEC subsystem (0.079263 kgCO$_2$eq), followed by LNG-GT (0.042442 kgCO$_2$eq). Terrestrial ecotoxicity shows the highest overall impact at 2.197354 kg1.4-DCB, mainly driven by SOEC (1.133983 kg1.4-DCB) and LNG-GT (0.364107 kg1.4-DCB). Human non-carcinogenic toxicity also shows a high total impact of 0.135886 kg1.4-DCB, with SOEC (0.063526) and LNG-GT (0.111105) being major contributors. In the category of fossil resource scarcity, the total impact is 0.041494 kgoileq, led by SOEC (0.021683 kgoileq) and LNG-GT (0.008327 kgoileq). Water consumption amounts to 0.003334 m^3 in total, with SOEC again being the largest contributor at 0.002579 m^3. Overall, the SOEC and LNG energy recovery subsystems show the highest environmental burdens in several categories due to high electricity consumption of SOEC and LNG production and transport.

Table. 5.1 Detailed LCA results of the biogas-to-methanol system.

Impact category	Unit	Total	MeOH	LNG-GT	SOEC	CCS	Input heat	Wind energy
Global warming	kg CO2 eq	0.205893	0.041365	0.042442	0.079263	0.006017	0.006081	0.030725
Stratospheric ozone depletion	kg CFC11 eq	1.03E-07	0	8.47E-09	3.05E-08	2.31E-09	5.02E-08	1.18E-08
Ionizing radiation	kBq Co-60 eq	0.001024	0	0.000356	0.00042	3.19E-05	5.32E-05	0.000163
Ozone formation, Human health	kg NOx eq	0.000614	6.09E-05	4E-05	0.000234	1.77E-05	0.000171	9.06E-05
Fine particulate matter formation	kg PM2.5 eq	0.000322	0	3.04E-05	0.000171	1.3E-05	4.12E-05	6.64E-05
Ozone formation, Terrestrial ecosystems	kg NOx eq	0.000673	9.83E-05	4.09E-05	0.000246	1.87E-05	0.000174	9.53E-05
Terrestrial acidification	kg SO2 eq	0.000698	0	7.94E-05	0.00033	2.5E-05	0.000136	0.000128
Freshwater eutrophication	kg P eq	1.37E-05	0	1.6E-06	7.1E-06	5.39E-07	1.68E-06	2.75E-06
Marine eutrophication	kg N eq	6.55E-06	0	1.95E-06	3.05E-06	2.31E-07	1.33E-07	1.18E-06
Terrestrial ecotoxicity	kg 1.4-DCB	2.197354	0.000158	0.364107	1.133983	0.086084	0.173457	0.439566
Freshwater ecotoxicity	kg 1.4-DCB	0.000482	1.71E-07	5.74E-05	0.00028	2.12E-05	1.55E-05	0.000108
Marine ecotoxicity	kg 1.4-DCB	0.001638	5.83E-07	0.000136	0.00094	7.13E-05	0.000125	0.000364
Human carcinogenic toxicity	kg 1.4-DCB	0.022311	0	0.00049	0.014766	0.001121	0.000211	0.005724
Human non-carcinogenic toxicity	kg 1.4-DCB	0.135886	0.000202	0.011105	0.063526	0.004822	0.031605	0.024625
Land use	m2a crop eq	0.055883	0	0.000743	0.006157	0.000467	0.046129	0.002387
Mineral resource scarcity	kg Cu eq	0.003883	0	0.000156	0.002523	0.000192	3.45E-05	0.000978
Fossil resource scarcity	kg oil eq	0.041494	0	0.00827	0.021683	0.001646	0.00149	0.008405
Water consumption	m3	0.003334	0	0.00031	0.002579	6.74E-05	3.35E-05	0.000344

5.7. Summary of biogas-to-methanol plants

This summary ties the chapter back to the thesis aim by aggregating the quantitative evidence that each integration lever moves the system toward higher efficiency, lower cost, and lower life cycle impacts, while sensitivities reveal where the optimal condition lies. In conclusion, the subsystem results in decision-ready guidance for the best use of hydrogen in biogas-to-methanol plants.

- By enhancing temperature of methanol reactor, the system without LNG and gas turbine units sees an increase in efficiency from 58% to 67%, while the system with these cycles improves from 82.5% to 84%, showing that incorporating these cycles not only boosts biomethanol production but also increases overall energy efficiency.
- For systems without and with LNG-GT cycles, the ability to produce biomethanol improves by 9.52% and 16.32%, respectively, when the number of SOEC cells increases from 180 to 280.
- Economic analyses show that systems incorporating LNG and gas turbine cycles exhibit lower levelized costs of fuel and shorter payback periods, underscoring their economic viability and superiority over systems without these components.
- Consequential LCA demonstrates that the systems featuring LNG-GT units offer a significant reduction of 53% and 70% in the impacts of climate change and resource use, thus further advancing environmental sustainability.
- Attributional LCA based on wind energy and LNG-GT subsystems shows a GWP of 0.2058 kgCO2eq/kgFuel and an FDP of 0.0415 kgoileq/kgFuel.
- By comparing different power sources, the wind turbine scenario demonstrates the potential for significant reductions in climate change and resource consumption compared to those of Poland's electricity mix.

In general, the integration of liquified natural gas and gas turbine units into methanol and natural gas production systems represents a promising approach to improve performance, efficiency, and environmental sustainability while reducing the LCOF.

6. Biomass-to-methanol system using gasification

This chapter introduces some oxygen–steam biomass-to-methanol (BtM) route via wood gasification to test whether the integration gains proven for BtM with anaerobic digestion improve when the biomass pathway changes. Gasification delivers higher-LHV syngas and high-temperature component that can be tightly co-integrated with SOEC (shared heat, direct O_2 utilization in the gasifier), offering potential boosts in outcomes. Although experimental data are available only for the digestion case, the Aspen Plus gasification model is more controllable. Because most subsystems are implemented in Aspen Plus, gasification can be integrated, enabling improved result collection and more comprehensive sensitivity analysis. The improved biomethanol plant shown in the previous chapter can be systematically compared with improved configuration based on gasification on all KPIs to determine which pathway enables more optimal hydrogen utilization: digestion or gasification-based BtM.

6.1. Description of biomass-to-methanol system using gasification

The 3rd proposed system in this thesis shown in Fig. 6.1 integrates biomass gasification subsystem with SOEC cells, a methanol synthesis unit, and power and natural gas production subsystems. The mentioned units are combined with an LNG cold energy recovery to recover the waste heat of the methanol synthesis unit, use the surplus oxygen from the electrolyzer for the gas turbine cycle, compensate for some part of the input electricity, produce a large amount of natural gas, and generate further biomethanol. Biomass, heat and electricity are the prime movers used to produce biofuels. Specifically, oxygen from electrolyzer and steam are the gasification agents that allow syngas to be produced. Hydrogen generated in the solid oxide electrolyzer together with syngas produced enter the MSU to produce biomethanol. As shown in Fig. 6.1, the heat recovered from the gasifier cooling is provided to SOEC. It should be noted that the high temperature electrolyzer is endothermic in this study, so additional heat is needed. Furthermore, hydrogen and oxygen coolers provide thermal energy for the heat recovery steam generator (HRSG 2). The proposed cycle needs liquified natural gas (LNG) and CO_2 to generate natural gas and more biomethanol. In the proposed system, the LNG regasification unit recovers the waste heat of the methanol synthesis unit (MSU) to generate electricity and natural gas. Then, a part of natural gas is directed to a gas turbine that uses the excess oxygen from the electrolyzer and CO_2. Additionally, a water gas shift reactor (WGSR) is used to enhance hydrogen and diminish CO in the flue gas, which is added to syngas and hydrogen for generation of additional biomethanol.

6.2. Thermodynamic results of the biomass-to-methanol system using gasification

This section reports the core thermodynamic balances for the gasification-based BtM plant to pinpoint the dominant levers that drive performance. The results provide the quantitative baseline for subsequent sensitivities and TEA/LCA trade-offs, guiding how to best allocate hydrogen, heat, and oxygen in the polygeneration design. This section presents the primary results of the proposed biomass-to-methanol system modeled in Aspen Plus software, which are reported in Table 6.1, Fig. 6.2, and Fig. 6.3. As shown in Fig. 6.2, the SOEC stack has by far the highest power consumption of 75%, confirming that it is necessary to improve the electrolysis cell. Some components, such as the syngas compressor, the gasification oxygen compressor, and LNG pump have low work consumption sharing 1% of the overall power consumption. It is noteworthy that some other equipment is not reported in this pie chart since they have nearly zero work consumption.

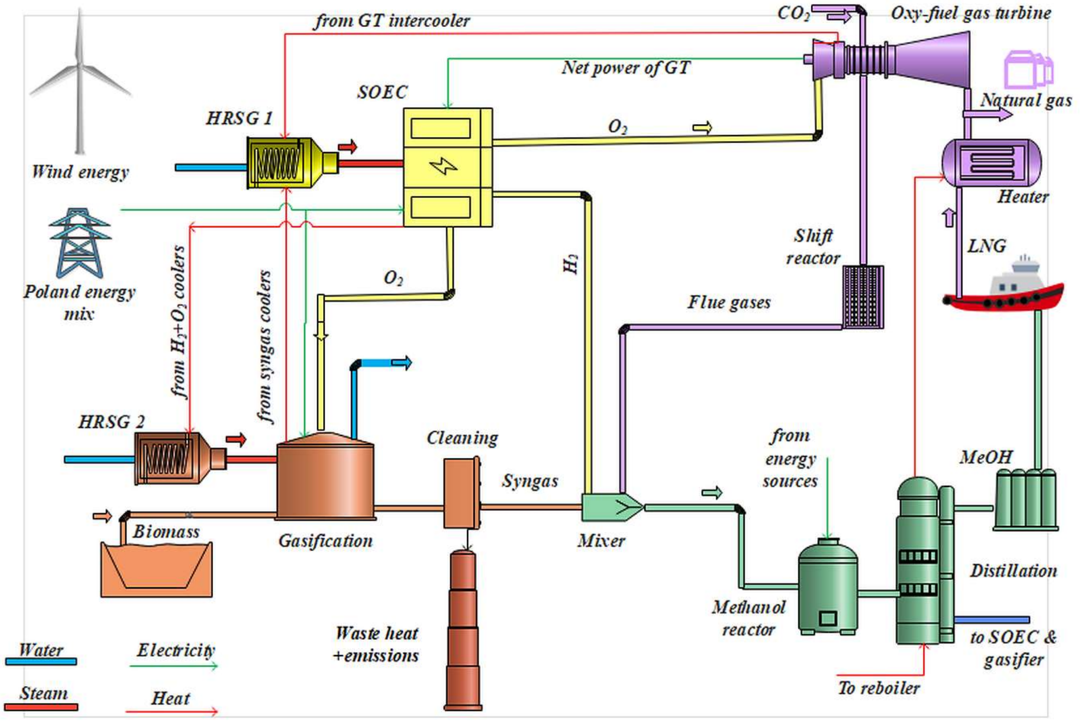

Fig. 6.1 Schematic diagram of the proposed cycle to produce natural gas and biomethanol using biomass gasification.

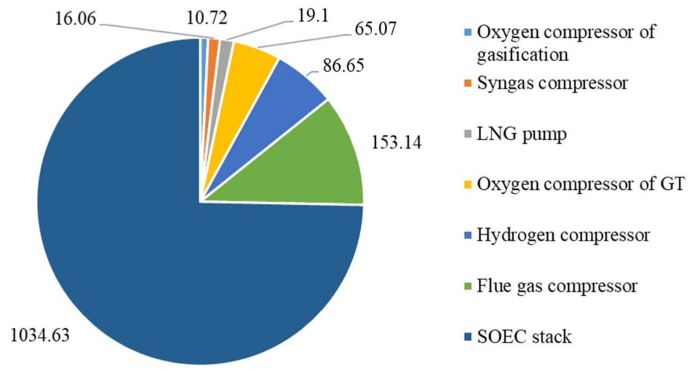

Fig. 6.2. Power consumption of the components of the proposed cycle in kW.

According to the information presented in Table 6.1, there is a notable disparity between the production of natural gas and biomethanol. The reason for this discrepancy lies in the fact that the natural gas capacity is significantly higher, primarily due to the regasification process facilitated by the waste heat generated by the entire plant. This indicates that LNG cold energy recovery utilizes waste heat to convert natural gas from a liquefied state (regasification) and then utilize it as a fuel source. However, to increase the biomethanol capacity, certain measures can be taken. One possible approach is to increase the number of SOEC cells within the plant as with an increase in the number of cells, the overall capacity for biomethanol production can be increased. Furthermore, another way of enhancing biomethanol capacity involves increasing biomass input into the gasification process. By introducing a larger amount of biomass, more raw material is available for conversion into syngas entering the biomethanol synthesis unit (MSU), leading to an overall increase in the production capacity of this fuel.

Table 6.1 also summarizes the key balances and performance of the biomass-to-methanol configuration based on wood gasification and high-temperature electrolysis. The solid-oxide stack (three modules of eighty cells) is supplied with 260 kg/h of steam, while the gasifier processes 0.093 m³/h of woody biomass. Process integration with LNG regasification is evident: 2000 kg/h of LNG feeds the LNG–GT block, which returns 358 kW of electrical power to the site and supports a co-product natural-gas stream of about 1900 kg/h. The methanol loop is charged with 401 kg/h of liquid CO_2 and produces 162 kg/h of biomethanol, yielding an overall energy efficiency near 82%. These figures confirm the thesis goal that tight coupling of gasification, SOEC, and LNG-GT enables efficient hydrogen utilization, electrolytic hydrogen is directed to synthesize liquid fuel while regasification heat and gas turbines power offset utility demand.

Table 6.1. Overall results of the proposed system for biofuels generation

Parameter	Value	Unit
Input water of SOEC	260	kg/h
Input biomass	0.0928	m^3/h
Input LNG	2000	kg/h
Input liquid CO_2	401	kg/h
Number of SOEC cells	3 × 80	-
Power generation of LNG-GT subsystem	357.77	kW
Natural gas capacity	1900	kg/h
Biomethanol capacity	162.23	kg/h
Overall energy efficiency	81.96	%
Waste HCl from gasifier	2.69	kg/h
Waste heat from gasifier	160.7	kW
Wastewater from gasifier	6.135	L/h
Wood ash from gasifier	20.4	kg/h
Fossil CO_2 / CO emissions from methanol synthesis	6.02 / 1.91	kg/h
Biogenic CO_2 / CO emissions from methanol synthesis	1.13 / 0.819	kg/h
H_2O / H_2 / CH_3OH / N_2 emissions from methanol synthesis	0.036 / 0.827 / 0.221 / 0.0125	kg/h

Guided by the preceding results, this thesis probes a high-leverage variables such as H_2O conversion of WGSR. Its marginal effects are quantified on the energy efficiency and fuel capacity to map operating windows and trade-offs, directly serving the thesis goal of optimizing hydrogen utilization in a BtM system. Fig. 6.3 illustrates the effect of H_2O conversion in the water-gas shift reaction process on the production capacities of natural gas and biomethanol. As shown, the natural gas capacity remains constant at 16644 tonne/yr by enhancing H_2O conversion in the WGSR because LNG cold energy recovery occurs before the WGSR process, and thw two processes are not directly connected. In contrast, biomethanol generation rises significantky 0 by 58% - as H_2O conversion increases from 0.2 to 0.9. This occurs because higher H_2O conversion maximizes the H_2 and CO_2 content in the flue gas, which are subsequently added to the methanol synthesis unit. In Fig. 6.3, the influence of H_2O conversion in WGRS on energy efficiency is shown. An increase in H_2O conversion improves the energy efficiency. A 3% improvement in energy efficiency is due to a large amount of enhancement in biomethanol production shown in Fig. 6.3 and described before.

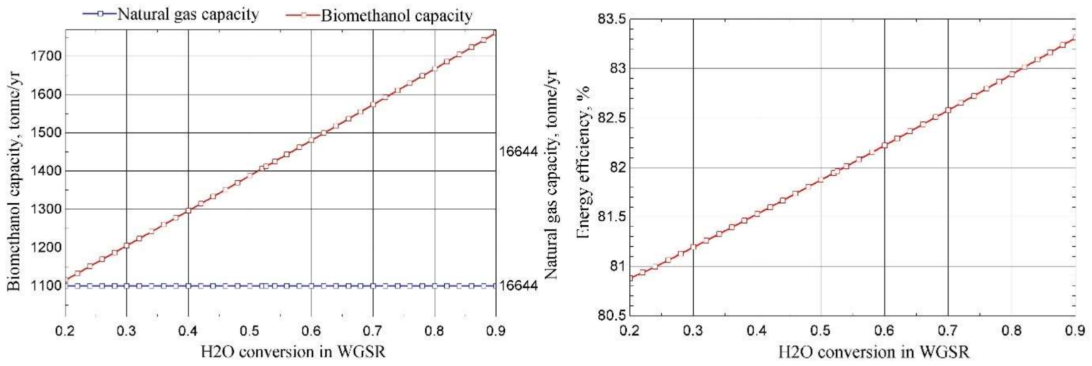

Fig. 6.3. Impact of H_2O conversion in WGSR on the fuel capacity and energy efficiency.

6.3. Techno-economic results of the biomass-to-methanol system

This section presents the techno-economic part of the thesis hypotheses and to pinpoint the cost drivers that govern optimal hydrogen utilization in BtM systems. By decomposing CAPEX, it shows where design and policy levers matter most so optimization can find key variables. In short, it translates the process design into a clear cost-reduction roadmap, and it enables gasification comparison with the digestion-based route. Fig. 6.4 breaks down the plant's fixed capital investment, highlighting the concentration of costs in the biomass-to-methanol system. Electrolyzer represent the largest share, accounting for 44% of total capital expenditure (CAPEX). Fuel-synthesis equipment contributes 29%, reflecting the high-pressure reactors, heat-exchange network, and downstream compression typically required. The gasification unit accounts for 13%, while gas and power generation represent 14%. Together, these conversion and utility systems comprise just over a quarter of total CAPEX. Overall, nearly three-quarters of capital is tied up in the electrolyzer and fuel synthesis sections (73%), meaning that design optimization, module sizing, and cost reductions efforts in these areas will dominate overall project economics and CAPEX risk.

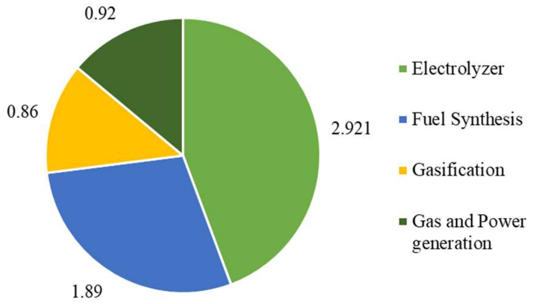

Fig. 6.4 Fixed capital investment of subsystems of the biomass-to-methanol system in M$.

Fig. 6.5 presents a bar chart of component's CAPEX, with the total investment estimated at approximately 6585 k$. Costs are dominated by the electrolyzer and gas compressors, which together account for about two-thirds of the budget. The next tier of costs is an order of magnitude lower: syngas cleaning and gas turbines, followed by the distillation tower, methanol reactor, and gasification unit. The remaining components, such as WGS reactors and heaters/combustor are relatively minor. Practically, cost-reduction efforts should prioritize electrolyzer procurement and high-pressure compression, with secondary attention to gas cleanup and turbines.

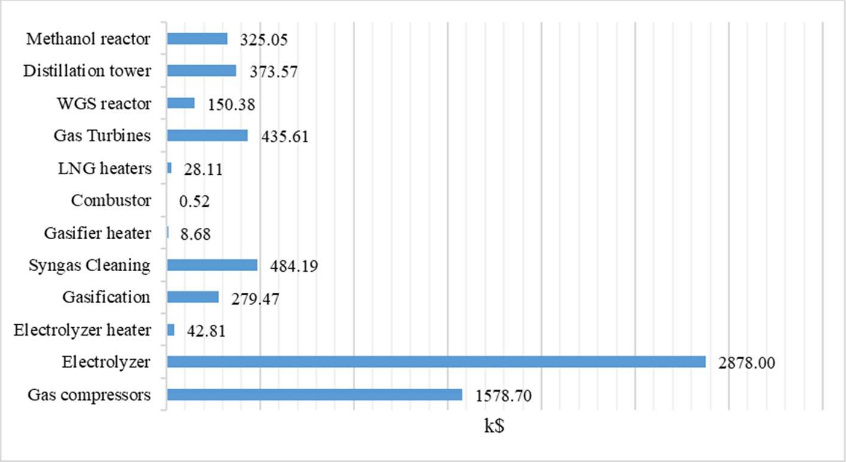

Fig. 6.5 Detailed CAPEX of different components of the biomass-to-methanol system

The NPV profile presented in Fig. 6.6 validates the economic feasibility of the gasification-based BtM route, an essential test of the hypothesis that hydrogen-enabled BtM system can be both efficient and cost-effective. It informs optimal sizing/integration, supports comparison to the biogas-based pathway, and guides financing and economic decisions based on payback time. As shown in Fig. 6.6, the net present value profile of the biomass-to-methanol system rises from an initial deficit of −25 M$ to +35 M$ by year 25, with the breakeven point (payback time) at 10.93 years. After payback, value accrues at roughly 2.5 M$/year, reaching +2.7 M$ (year 12). Overall, the terminal surplus is 1.4 times larger than the magnitude of the initial outlay, indicating predictable cash flows, resilient margins, and a persuasive long-run value proposition under the stated assumptions.

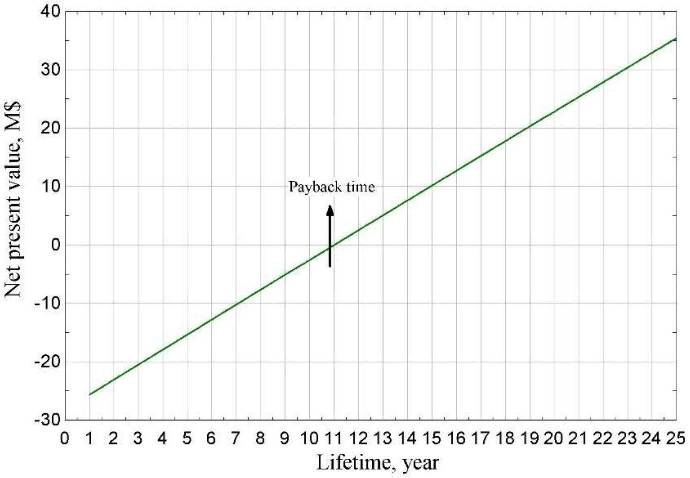

Fig. 6.6 Net present value of the biomass-to-methanol system.

Because wood price volatility is a primary OPEX risk for BtM system based on gasification, the following sensitivity checks the economic robustness of this system, directly tied to the thesis goal of cost-optimal hydrogen utilization. It also informs if the polygeneration design remains viable under biomass price ranges. In Fig. 6.7, across the analyzed range (0–0.20 $/kg), biomass price exhibits a linear effect on both LCOF and payback time. The LCOF rises from 956 $/tonne at 0 $/kg to 973 $/tonne at 0.20 $/kg, an increment by 1.8%. The payback time increases from 10.7 to 11.7 years over the same interval, indicating low effect of biomass price to both metrics while payback time is the more biomass-price-sensitive objective in relative terms.

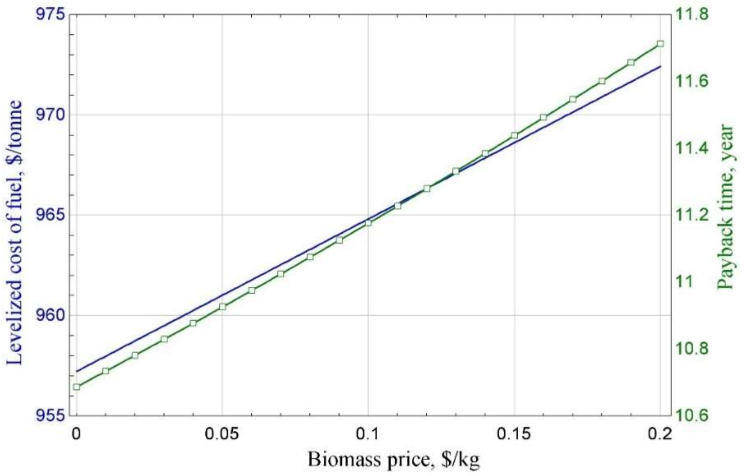

Fig. 6.7 The effect of biomass price on the levelized cost of fuel and payback time in the biomass-to-methanol system.

6.4. Attributional environmental results of the biomass-to-methanol system

This attributional LCA section is essential to the thesis goal of optimizing hydrogen-enabled polygeneration systems because it pinpoints the environmental hotspots under. By quantifying these burdens, it directs the optimization levers, ensuring the BtM design meets environmental targets. In Table 6.2, almost every environmental impact in the biomass-to-methanol setup is driven by the SOEC process and its electricity demand. Total climate change is about 0.17 kgCO$_2$eq, of which SOEC accounts for 45%, methanol synthesis for 22%, and the wind-power supply chain 16%. Gasification and the LNG-GT units contribute only marginally. A similar pattern is observed for ozone formation affecting human health (0.00042 kgNOxeq), and for acidification (0.00050 kgSAF$_2$-eq). Terrestrial ecotoxicity is found to be 1.61 kg1.4DCBeq, with 64% of SOEC. Land use, however, is an outlier, being almost entirely dominated by biomass gasification, which contributes 97% (0.250 m^2·a crop-eq) . In summary, reducing the electricity demand of the SOEC and carefully managing biomass sourcing are critical to lowering the overall environmental footprint, particularly the land-use impact.

Table. 6.2 Detailed LCA results of the biomass-to-methanol system.

Impact category	Unit	Total	Methanol synthesis	Gasification	LNG-GT	SOEC	Wind energy
Global warming	kg CO2 eq	0.166595	0.037127	0.009192	0.019588	0.0745	0.026188
Stratospheric ozone depletion	kg CFC11 eq	4.63E-08	0	4.97E-09	3.87E-09	2.74E-08	1.01E-08
Ionizing radiation	kBq Co-60 eq	0.000776	0	6.18E-05	0.000161	0.000414	0.000139
Ozone formation, Human health	kg NOx eq	0.00042	6.42E-05	5.24E-05	1.92E-05	0.000207	7.72E-05
Fine particulate matter formation	kg PM2.5 eq	0.000249	0	2.64E-05	1.43E-05	0.000152	5.66E-05
Ozone formation, Terrestrial ecosystems	kg NOx eq	0.000477	0.000104	5.48E-05	1.97E-05	0.000217	8.12E-05
Terrestrial acidification	kg SO2 eq	0.000501	0	5.86E-05	3.77E-05	0.000295	0.000109
Freshwater eutrophication	kg P eq	1.35E-05	0	4.07E-06	7.38E-07	6.33E-06	2.34E-06
Marine eutrophication	kg N eq	5.05E-06	0	2.53E-07	8.83E-07	2.91E-06	1.01E-06
Terrestrial ecotoxicity	kg 1.4-DCB	1.606989	0.000166	0.041327	0.163997	1.026842	0.374658
Freshwater ecotoxicity	kg 1.4-DCB	0.000418	1.8E-07	4.76E-05	2.83E-05	0.000249	9.24E-05
Marine ecotoxicity	kg 1.4-DCB	0.001293	6.15E-07	8.99E-05	6.45E-05	0.000827	0.000311

Human carcinogenic toxicity	kg 1.4-DCB	0.018226	0	0.000395	0.000223	0.012729	0.004878
Human non-carcinogenic toxicity	kg 1.4-DCB	0.086085	0.000213	0.003628	0.005102	0.056153	0.020988
Land use	m2a crop eq	0.25812	0	0.250354	0.000341	0.005391	0.002034
Mineral resource scarcity	kg Cu eq	0.003147	0	5.71E-05	7.05E-05	0.002186	0.000834
Fossil resource scarcity	kg oil eq	0.03453	0	0.002804	0.004478	0.020085	0.007164
Water consumption	m3	0.002845	0	-2.4E-06	0.000143	0.002411	0.000293

6.5. Summary of biomass-to-methanol system using gasification

This section summarizes the gasification-route findings into the exact design levers that govern hydrogen use, efficiency, costs, and CO_2 emissions in a polygeneration context. By quantifying the trade-offs, it directly tests the hypotheses and yields decision rules for optimizing hydrogen-enabled polygeneration, while setting up a comparison against the digestion-based route.

- The proposed cycle uses 255 tonne/yr of hydrogen from the SOEC in the methanol plant, consumes 1075 tonne/yr of biomass, produces 16644 tonne/yr of natural gas and 1412 tonne/yr of biomethanol.
- To enhance efficiency, it is necessary to increase the water conversion of the WGSR.
- The biomethanol capacity increases by 58% when the H_2O conversion increases from 0.2 to 0.9 in the WGRS, thus, a 3% improvement can be achieved in the energy efficiency.
- Economically, SOEC and fuel synthesis have the highest CAPEX. This system's payback time and LCOF are found to be 10.93 years and 961 $/tonne, respectively. Biomass price does not have significant effect on cost indicators.
- Environmentally, biomethanol system integrated with LNG and biomass gasification achives a GWP of 0.1666 kgCO2eq/kgFuel and a FDP of 0.03453 kgoileq/kgFuel.

7. Biomass-to-methanol with energy storage

This chapter introduces a novel biomethanol production system with gasification, compressed air, and thermal energy storage (CAES/TES) systems. This system is based on heat recovery to probe a stronger form of process integration than in Chapter 6. It harvests experimentally validated waste heat from the CAES installation of the group for energy storage (GEST) led by Prof. Bartela at the Silesian University of Technology. This dynamic waste heat relates to a TES so it can be a steady thermal supply and cover the reboiler of biomethanol distillation and LNG regasification duties, cut purchased heat and electricity, unlock larger fuel capacity, and improve efficiency, techno-economics, and LCA. Using lab-grade data ensures realism for a dynamic source matched to steady demands, while comparison with the previous biomethanol plants isolates the incremental value of storage-enabled heat integration for optimal hydrogen utilization, supporting selection of the best performer among the four proposed biomethanol systems.

7.1. Description of biomass-to-methanol system with energy storage

The system proposed encompasses several interconnected subsystems: biomass gasification, SOEC, methanol synthesis, compressed air energy storage, power generation and natural gas production. These subsystems are seamlessly integrated with an LNG cold energy recovery system to achieve multiple objectives.

- Recovering waste heat from the methanol synthesis unit
- Making use of the excess oxygen from the electrolyzer in the gas turbine cycle
- compensating for electrical requirements
- generating a substantial amount of natural gas
- Enabling the production of additional biomethanol

The production of biofuels is based on the utilization of biomass, input heat from the CAES heat exchanger, and electricity as the primary drivers. In this context, the gasification agents, namely oxygen from the electrolyzer and steam, are critical for generating syngas. This syngas, along with the hydrogen produced in the solid oxide electrolyzer, are then introduced into the methanol synthesis unit to facilitate the production of biomethanol.

Figure 7.1 illustrates the use of heat recovered from the cooling process, which is directed at SOEC. It is important to note that, in this study, the elevated temperature electrolyzer operates as an endothermic process, requiring additional heat. Furthermore, the thermal energy from hydrogen and oxygen is utilized for the heat recovery steam generator (HRSG 2). The proposed system requires the use of LNG and CO_2 to generate natural gas and produce additional biomethanol. The liquefied natural gas regasification unit plays a crucial role in recovering waste heat from the methanol synthesis unit to generate both electricity and natural gas. A portion of the natural gas is then directed to a gas turbine, making use of the surplus oxygen from the electrolyzer and CO_2. Additionally, a water gas shift reactor is introduced to enhance the hydrogen content and reduce CO levels in the flue gas. This enriched flue gas is combined with the syngas and hydrogen to enable extra generation of methanol.

Another solution for large-scale energy storage processes is compressed air energy storage installations which convert electrical energy by the compressor into the potential energy of the compressed gas. The compressed gas is stored until the period of the highest electricity demand, when the discharge phase of the CAES installation takes place, gas goes to the expander which powers the electric generator [184]. Usually, if heat is not stored within the installation, the gas parameters are increased before the expander through a combustion chamber, usually powered by natural gas [185]. Such systems that use fuel in the combustion chamber to increase the parameters of the air directed to the expander are called diabatic CAES. However, there is also a solution that allows to store heat and use it before the air expansion process.

As depicted in Fig. 7.1, a thermal energy storage system has been implemented to ensure a consistent supply of heat to the biofuels plant. This is achieved through the CAES heat exchanger situated between two compressors, significantly elevating energy efficiency to its maximum potential. Heat from the compressor inter-stage cooling section is directed to the modeled thermal energy storage (TES), then it can be used to thermal integration with reboiler of the distillation column for biomethanol production and LNG heat exchangers for enhanced natural gas generation.

Because CAES operates transiently, the recovered heat is stored in a liquid thermal energy storage (TES) unit to deliver a steady heat supply to the biofuels plant. The following CAES system operation was adopted for the following assumptions: 8 hours of charging process. 12 hours of storage process. 4 hours of discharging process. However, other installations within the designed system operated continuously. In the case of the adopted solution, heat from the CAES installation could be recovered for 8 hours a day, because it was assumed that the process of charging the installation would take place during the night valley, when the purchase price of electricity is the lowest. The temperature of the hot air stream from CAES installation ranges from 215°C to 260°C, which results from the variable operating parameters of air compressors. At the calculation stage, the decrease in heat energy potential resulting from stratification for energy storage was modeled. Since the CAES works only 8 hours a day, thermal energy storage (TES) is modelled to provide steady-state heat to the biomethanol plant. In summary, the proposed system optimizes the utilization of biomass resources, incorporates efficient waste heat recovery, maximizes the integration of various subsystems, and improves biofuel production through the utilization of LNG, CO_2, and surplus oxygen from the electrolyzer.

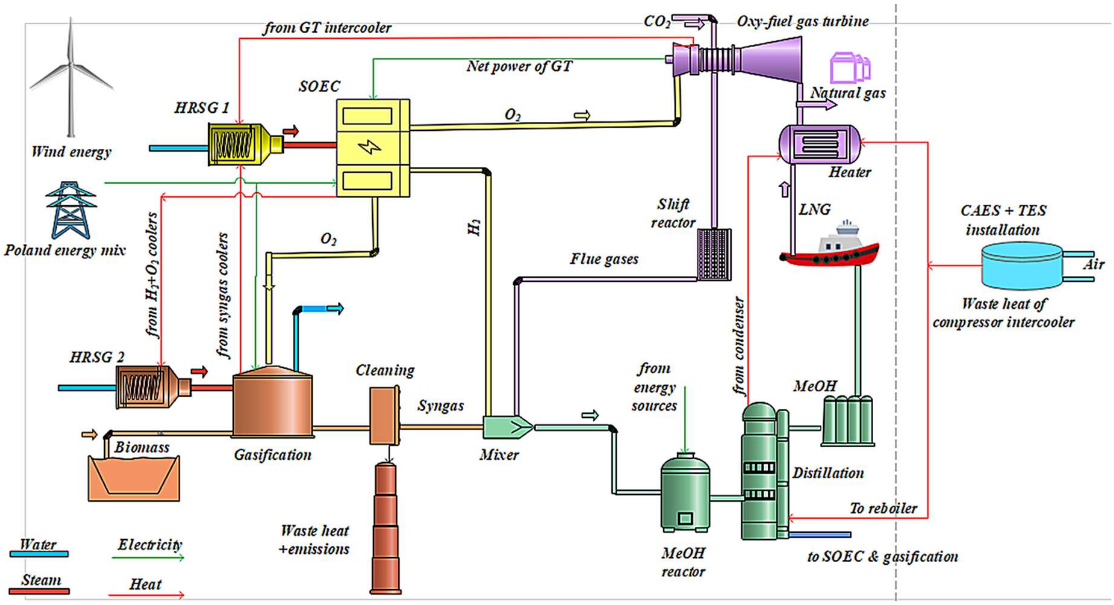

Fig. 7.1. Schematic diagram of the proposed cycle to produce natural gas and biomethanol.

7.2. Thermodynamic results of biomass-to-methanol system with energy storage

This section establishes the thermodynamic baseline for the storage-integrated BtM design to show exactly where power is consumed and recovered. By quantifying subsystem loads, it pinpoints the optimization levers that directly test the hypothesis on efficient hydrogen utilization in polygeneration units. This section presents the primary findings of the proposed system modeled using Aspen Plus software, which are detailed in Fig. 7.2 and Fig. 7.3. Figure 7.2 illustrates that the electrolyzer exhibits the highest power consumption at 1035 kW, underscoring the need for improvements in the electrolysis cell. In industry, the specific energy consumption of SOEC is 33 kWh/kg of hydrogen [186], which is like that of the present study as hydrogen flow and power consumption are found to be 29.09 kg/h and 1035 kW, respectively. The SOEC consumes 1035 kW of electricity because of high mass flow rate of inlet steam (260 kg/h) and containing 238 cells. Certain components, such as the gasification and heat storage, contribute minimally to the overall power consumption, each at around 1%, since they include only a compressor and a pump. In addition, the methanol synthesis unit needs 261 kW of power due to high number of compressors to increase the pressure of input gases to 51 bar.

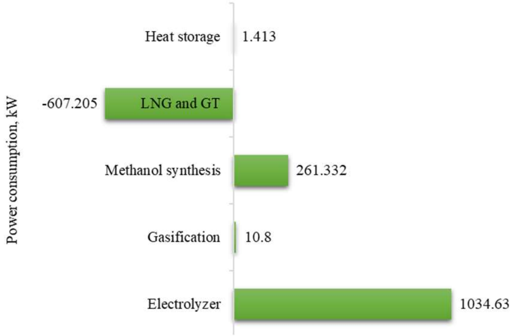

Fig. 7.2 Power consumption of different subsystems of the proposed plant.

In addition to power consumption values provided in Fig. 7.2, Table 7.1 documents the main mass flows and the achieved conversion performance for the biomethanol production based on biomass-gasification, solid-oxide electrolysis, and LNG/GT system with energy storage. The solid-oxide electrolysis cell is fed with 260 kg/h of steam; the gasifier processes roughly 0.092 m^3/h of woody biomass; 18.92 m^3/h of liquefied natural gas is regasified; and 401 kg/h of liquid CO_2 is supplied to the LNG-GT subsystem. Under these conditions the plant produces 162.41 kg/h of biomethanol and reaches an overall energy efficiency of 95.27%, which supports the thesis hypothesis that strong heat integration especially between LNG regasification, methanol synthesis, and CAES/TES energy storage, enables highly efficient use of electrolytic hydrogen.

The table also shows that residue and by-product streams are modest. Gasification lost about 20.4 kg/h of ash and 6.135 L/h of wastewater, while acid gases and ammonia appear only at trace levels. In the synthesis section, vented fossil and biogenic carbon oxides are limited to a few flow rates, and only minor traces of water, hydrogen, methanol, and nitrogen leave with the off-gas of methanol synthesis.

Together, these balances demonstrate that most of the incoming carbon is directed to produce or captured, waste streams are small, and the thermal coupling of the subsystems delivers the intended outcome of this thesis: efficient hydrogen utilization with low environmental burden in bio-based methanol production.

Table 7.1. Main thermodynamic results of biomethanol production using energy storage.

Parameter	Value	Unit
Input water of SOEC	260	kg/h
Input woody biomass	0.092	m^3/h
Input LNG	18.9155	m^3/h
Input liquid CO_2	401	Kg/h

Biomethanol production	162.41	Kg/h
Waste H_2S, COS, NH_3, HCl, and H_2O of gasifier	0.3934 / 0.0098 / 0.0034 / 2.6915 / 5.88	Kg/h
Wastewater from gasifier	6.135	L/h
Wood ash of gasifier	20.4	Kg/h
Waste heat of gasifier	110.079	kW
Water consumption of LNG-GT unit	50	Kg/h
Fossil CO_2 / CO emissions from methanol synthesis	6.07 / 1.91	Kg/h
Biogenic CO_2 / CO emissions from methanol synthesis	1.07 / 0.819	Kg/h
H_2O / H_2 / CH_3OH / N_2 emissions from methanol synthesis	0.036 / 0.827 / 0.221 / 0.0125	Kg/h
Energy efficiency	95.27	%

In addition, the following analysis identifies the TES working fluid as a high-leverage design variable for the storage-integrated BtM plant. Selecting a working fluid with lower required volume supports optimal hydrogen utilization by reducing auxiliary energy demand. Fig. 7.3 illustrates the influence of different working fluids for the thermal energy storage (TES) tank, which is modeled under both steady and dynamic conditions. As shown in the figure, the highest tank volumes are calculated when Syltherm 800 is used as the working fluid: 378.2 m³ for steady conditions and 326 m³ for dynamic conditions. The present study focuses on decreasing the tank volume, so Therminol 59 is identified as the optimal working fluid for TES. This conclusion is based on its significantly lower tank volumes: 267.7 m³ under steady conditions and 304.8 m³ under dynamic conditions.

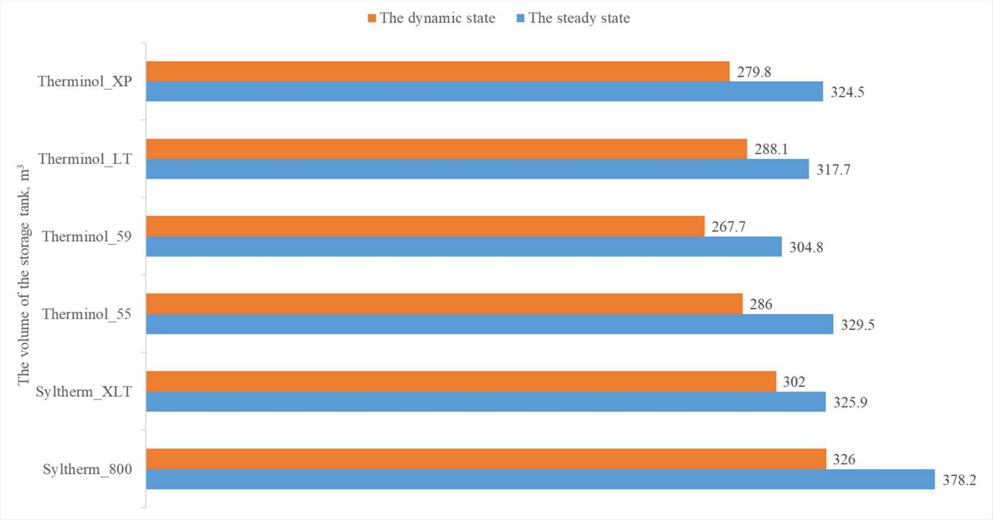

Fig. 7.3. Volume of thermal energy storage (TES) working with different fluids.

The following sensitivity analysis illustrates the effect of methanol reactor temperature on fuel capacity, power consumption, and energy efficiency. By exposing the capacity and efficiency trade-off, it yields an optimal temperature for optimization of the biomethanol plant. Fig. 7.4 illustrates how the temperature of the methanol reactor impacts biomethanol capacity and net input electricity. Increasing the methanol reactor temperature from 210 °C to 400 °C results in a substantial increase in biomethanol capacity from 900 tonne/yr to 2300 tonne/yr. This enhancement stems from improved conversion of input gases to liquid water and biomethanol within the reactor, leading to an increased methanol mole fraction in the reactor outlet. On the other hand, when the temperature of methanol reactors increases from 210 °C to 400 °C, the size of methanol production unit enhances leading to having a large amount of waste heat. In turn, this waste heat is used to produce power in natural gas and gas turbines. Therefore, when the temperature of methanol reactor increases from 210 °C to 400 °C, 5.55% less electricity is needed for the whole plant. Figure 7.4 showcases the effect of the methanol reactor temperature on energy efficiency, displaying an upward trend. The 1.58 percentage increase in energy efficiency correlates with a 155% rise in biomethanol capacity and 5.55% reduction in input power. Therefore, maximizing the methanol reactor temperature is beneficial as increase in biomethanol capacity and energy efficiency proves advantageous.

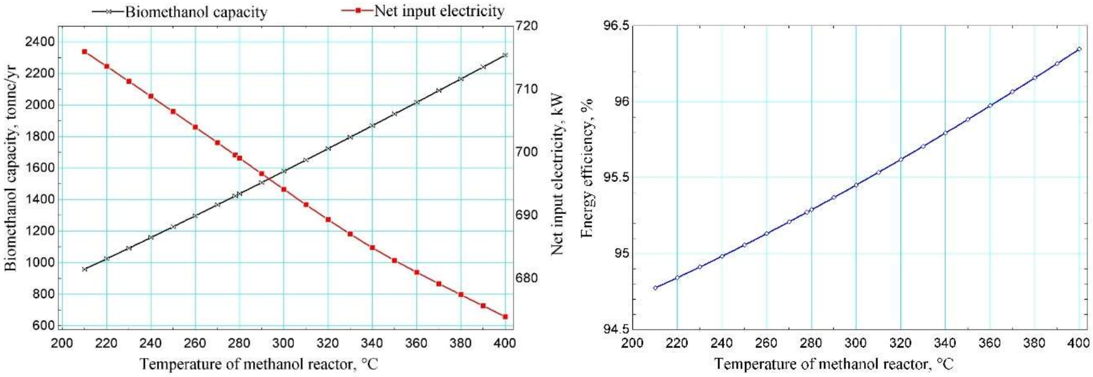

Fig. 7.4 Impact of temperature of methanol reactor on input power, fuel capacity, and energy efficiency.

7.3. Techno-economic results of the biomethanol system with energy storage

This subsection shows which components dominate CAPEX to focus on optimizing those subsystems in the BtM configuration with energy storage. It verifies the hypothesis that deeper integration of energy storage and biomethanol installations can deliver better techno-economics. In Fig. 7.5, the fixed-capital profile is dominated by power and natural-gas production (36%) and the electrolyzer (29%), which together account for 65% of CAPEX. Methanol synthesis accounts for 23%, while gasification contributes 10%. Thermal energy storage is minor at 2%. Overall, the core conversion technologies (electrolyzer and methanol synthesis) represent 52% of CAPEX, and including gasification brings the process section to 62%. This highlights that cost optimization should prioritize the energy recovery and electrolyzer blocks, with secondary attention to fuel synthesis and gasification.

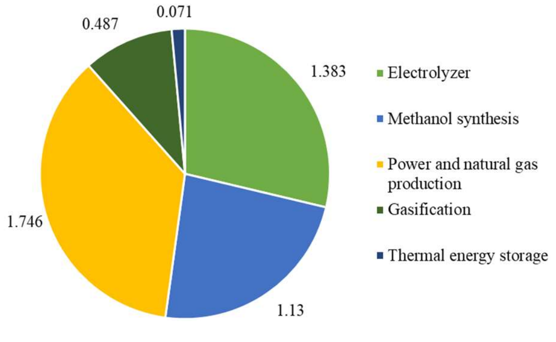

Fig. 7.5 Fixed capital investments of the BtM system with CAES in M$.

As shown in Fig. 7.6, fixed capital is dominated by three components: gas compressors (1505 k$) and the electrolyzer (1298 k$), which together account for 57% of the total expenses, and gas turbines (904 k$), which raise the top-three share to 76%. The distillation tower (376 k$) and methanol synthesis (326 k$) together add 14%, while the WGS reactor (151 k$) contributes a further 3%. The balance-of-plant - LNG heat recovery, HRSG, gasifier, and thermal energy storage - each account for less than 100 k$. In summary, cost optimization should prioritize compression, the electrolyzer, and turbines, as the small utilities have limited influence on total cost.

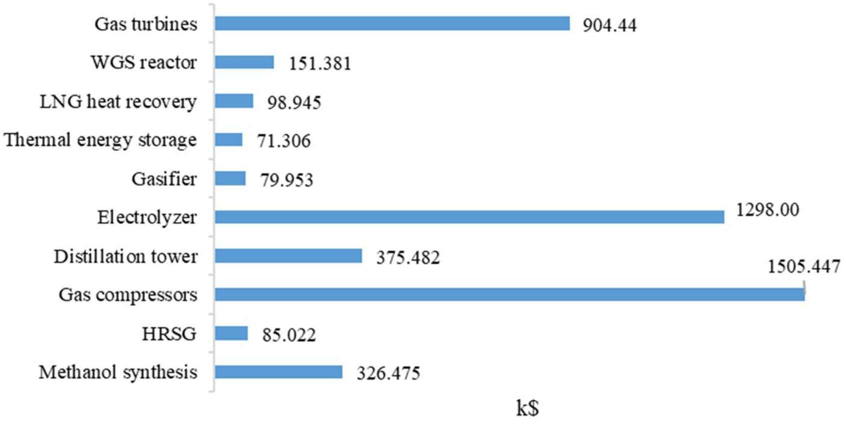

Fig. 7.6 Fixed capital investment of different components in the BtM with CAES system

Figure 7.7 demonstrates cost viability of the CAES integrated BtM configuration quantifying payback and long-run NPV as core techno-economic objectives. It tests the hypothesis that hydrogen-enabled integration with energy storage can improve the cost-optimal pathway for polygeneration scale-up. As shown in Fig. 7.7, the cash-flow profile increases linearly over the horizon, indicating stable, predictable operating margins. The curve crosses the zero line at year 2, a remarkably short payback that minimizes capital exposer and enables early flexibility for debt service or reinvestment. Beyond breakeven, value grows steadily without reversals, indicating resilience to routine volatility in prices and costs. By year 25, the project will achieve an NPV of 300 M$, providing a substantial contingency buffer and a strong basis for long-term returns.

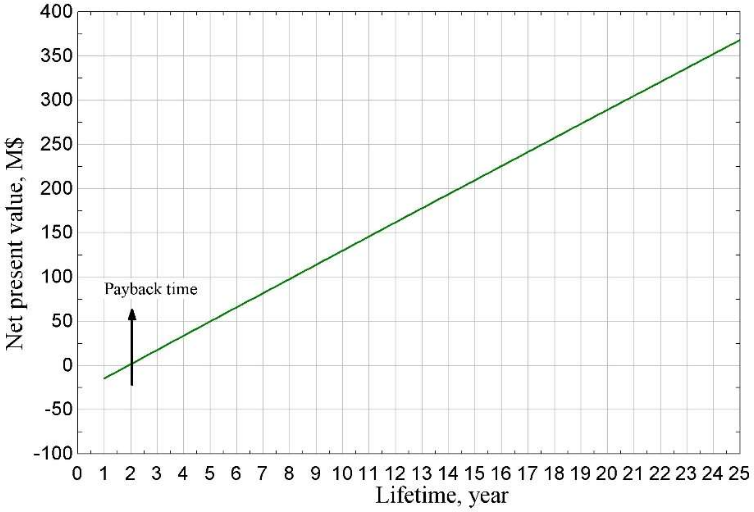

Fig. 7.7. Net present value of the BtM system with CAES.

The following sensitivity analysis is presented because LNG is a first-order OPEX driver and integration lever in the BtM-CAES design. Mapping how LCOF and payback period with LNG price tests the hypothesis that hydrogen-based, storage-integrated biomethanol plant can stay cost-optimal under market volatility, identifies a practical price threshold, and informs operation choices while supporting the thesis goal of minimizing cost for optimal H_2 utilization. In Fig. 7.8, the LNG price is a first-order driver of both unit cost and capital recovery for the BtM-CAES system. From 1 to 11 \$/GJ, the LCOF rises almost linearly from 170 to 760 \$/tonne, an increase of roughly 4.5-fold, even modest fuel-price movements propagate directly into product cost. Payback time responds nonlinearly. It is flat at low prices, then increases gradually. A practical threshold appears around 8 \$/GJ (base market price), where payback crosses 2 years. Above this point the curve steepens markedly, reaching nearly 11 \$/GJ in the 5th year. Therefore, it is better to keep LNG prices less than 8 \$/GJ preserving a 2-year payback and containing LCOF below 500 \$/t.

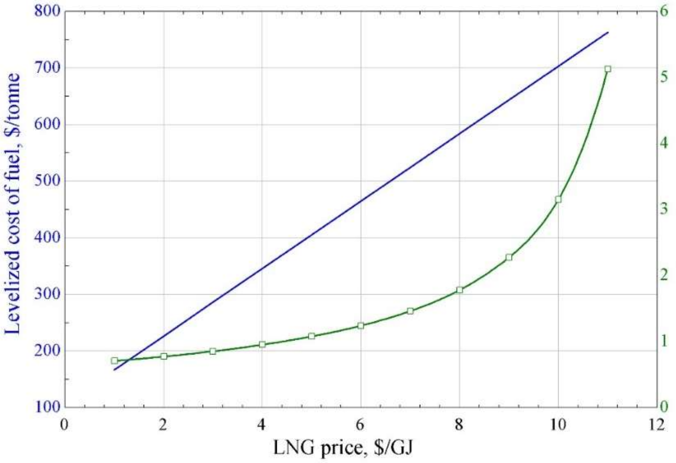

Fig. 7.8 The effect of LNG price on cost objectives of the BtM system with CAES.

7.4. Attributional environmental results of the biomethanol system with energy storage

Attributional LCA results quantify the actual, present-day environmental footprint of the BtM-CAES configuration and pinpoint the dominant hotspots. This directly tests the hypothesis that hydrogen-enabled, storage-integrated polygeneration can cut LCA impacts. Reporting ALCA also gives a transparent baseline for comparison and strengthens the optimization targets. Table 7.2 shows the LCA results of the BtM system with CAES in which climate change impacts are modest but clearly driven by the electro-intensive units: the total GWP is 0.135 $kgCO_2eq/kgFuel$, with SOEC contributing 0.042, methanol synthesis to 0.037, and the embodied burdens of wind power to 0.026 $kgCO_2eq/kgFuel$. The LNG-GT units add 0.020, while biomass gasification is minor, equal to 0.009. This pattern underscores that, even with CAES waste-heat integration, electricity demand and materials requirement for the electrolyzer and renewable supply dominate the environmental footprint. Beyond climate change, a notable outlier is terrestrial ecotoxicity (1.10 kg1.4-DCBeq), largely linked to metals and manufacturing in SOEC and wind infrastructure. Biomass contributes mainly through land use (0.26 $m^2{\cdot}a$ crop-eq), almost entirely from feedstock provision. In conclusion, the system's environmental profile is shaped by the electricity-intensive conversion chain and capital-intensive renewables, with biomass affecting mainly land occupation.

Table 7.2. Detailed LCA results for the biomass-to-methanol system with CAES.

Impact category	Unit	Total	Methanol synthesis	Gasification	LNG-GT	SOEC	Wind energy
Global warming	kg CO2 eq	0.134625	0.037365	0.009368	0.019567	0.042126	0.026199
Stratospheric ozone depletion	kg CFC11 eq	0	0	0	0	0	0
Ionizing radiation	kBq Co-60 eq	0.000626	0	6.3E-05	0.000161	0.000264	0.000139

Ozone formation, Human health	kg NOx eq	0.000311	6.42E-05	5.34E-05	0	0	0
Fine particulate matter formation	kg PM2.5 eq	0.000169	0	2.69E-05	0	0	0
Ozone formation, Terrestrial ecosystems	kg NOx eq	0.000362	0.000104	0	0	0.000102	0
Terrestrial acidification	kg SO2 eq	0.000351	0	0	0	0.000144	0.000109
Freshwater eutrophication	kg P eq	0	0	0	0	0	0
Marine eutrophication	kg N eq	0	0	0	0	0	0
Terrestrial ecotoxicity	kg 1.4-DCB	1.101706	0.000166	0.042118	0.163815	0.520786	0.37482
Freshwater ecotoxicity	kg 1.4-DCB	0.000289	1.8E-07	4.85E-05	2.83E-05	0.00012	9.25E-05
Marine ecotoxicity	kg 1.4-DCB	0.000849	6.14E-07	9.16E-05	6.45E-05	0.000381	0.000311
Human carcinogenic toxicity	kg 1.4-DCB	0.01094	0	0.000403	0.000223	0.005434	0.004881
Human non-carcinogenic toxicity	kg 1,4-DCB	0.056301	0.000213	0.003697	0.005096	0.026297	0.020998
Land use	m2a crop eq	0.259963	0	0.255146	0.000341	0.002441	0.002035
Mineral resource scarcity	kg Cu eq	0.001914	0	5.82E-05	7.04E-05	0.000951	0.000834
Fossil resource scarcity	kg oil eq	0.025401	0	0.002858	0.004473	0.010903	0.007167
Water consumption	m3	0.002452	0	-2.5E-06	0.000143	0.002019	0.000293

7.5. Summary of biomethanol production with energy storage

This subsection confirms the core hypothesis that tightly integrating SOEC-driven hydrogen with methanol synthesis and recovering waste heat via CAES/TES improves plant efficiency, fuel output, and environmental performance. By grounding the heat-recovery block in experimental CAES data, the work links modeling to practice and outlines a credible path to pilot validation. Taken together, the results provide comparable metrics across four biomethanol configurations, enabling selection of the most effective hydrogen-utilization design.

- The proposed system produces 69251 tonne/yr of natural gas, 1424 tonne/yr of biomethanol.
- The electrolyzer exhibits the highest power consumption at 1035 kW. Additionally, the methanol synthesis unit requires 261 kW of power. The gas and natural gas turbines generate 607 kW of output electricity.
- The improved BtM with CAES/TES achieves high efficiency (95%), competitive cost (602 \$/tonne), and a low GWP (0.135 kgCO$_2$eq/kgFuel), validating the importance of high-temperature, deeply integrated heat recovery in energy storage systems.

The practical outcome of the proposed plant is the improvement of energy and environmental objectives by waste heat recovery from compressed air energy storage (CAES).

8. Ammonia production plants

This chapter extends the thesis beyond biomethanol to a second flagship product, ammonia, to test the hydrogen use hypotheses on a carbon-free fuel with strong storage, trade, and end-use potential. This thesis benchmarks three routes, power-to-ammonia (PtA), biomass-to-ammonia (BtA) with co-current water gas shift (CO-WGS), and biomass-to-ammonia (BtA) with counter-current WGS (CC-WGS), under consistent assumptions. This chapter also tests solar photovoltaic (PV) panels as another renewable energy source (RES). Comparing these plants quantifies how power based, or biomass-based ammonia production affects energy efficiency, techno-economics, and environmental results. The outcome is a clear design rules for optimal hydrogen utilization in polygeneration systems.

8.1. Description of power-to-ammonia plant

This subsection presents the power-to-ammonia (PtA) plant. An alkaline electrolyzer is used for H_2 production because, unlike the SOEC used in earlier biomethanol cases (the largest power consumer and a major CAPEX driver), alkaline electrolysis offers a more mature, lower-cost baseline for PtA benchmarking. An air separation unit (ASU) is included to supply the required high-purity N_2 for the Haber–Bosch loop, while co-produced O_2 is sold. All subsystems are powered by solar PV, aligning with the thesis goals of maximizing renewable (RES) integration and optimal hydrogen utilization. This configuration verifies the hypotheses on energy integration, techno-economics, and LCA under a carbon-free ammonia route. Fig. 8.1 shows the block flow diagram of the proposed two green ammonia configurations, PtA and BtA. The green hydrogen production stage recognizes the main difference between the two configurations. In Fig. 8.1(a), the PtA case, hydrogen is produced by an alkaline water electrolysis unit. in the BtA case, green hydrogen is obtained by integrating biomass gasification with the multi-tube WGS membrane reactors unit, as shown in Fig. 8.2(a). Another difference in designing these two configurations is that the BtA case is equipped with a CO_2 separation unit, where CO_2 is separated through compression and condensation stages. In both configurations, the N_2 required by the Haber-Bosch process is produced in the air separation unit (ASU). The solar photovoltaic panel unit provides the electrical power needed by the two green plants. Also, O_2 generated in the PtA case is sold as a by-product, while in the BtA case, captured CO_2 and excess N_2 generated by ASU are sold as by-products.

The process flow diagram (PFD) of the PtA case is illustrated in Fig. 8.1(b). According to the figure, water enters the process at ambient conditions and is mixed with anode and cathode recycled streams. Then, it is pressurized up to 20 bar by a pump and fed into the electrolysis stack. During electrolysis, hydrogen is generated in the cathode, while oxygen is produced in the anode. The outlet streams of the electrolyzer are introduced into the gas-liquid separators to remove water content. Pure oxygen exits at 20 bar, and pure hydrogen is fed to the ammonia synthesis loop. The N_2 required by the Haber-Bosch process is produced at air separation unit (ASU) from which pure nitrogen product is sent to the ammonia synthesis loop. Also, a portion of oxygen produced is fed to the biomass gasification unit as a gasification agent, and the rest is sold as a by-product. The pure N_2 stream is mixed with the pure H_2 stream and passes through a multi-stage compressor with intercooling stages. Finally, the mixture of H_2 and N_2 with an H_2/N_2 ratio of 3 is sent to the ammonia synthesis loop at 200 °C and 200 bar. The fresh mixture gas is mixed with the recycle stream of the ammonia separator, passes through a preheater, and then is fed to the first ammonia synthesis catalytic reactor. Three adiabatic synthesis reactors are placed in series so that the inlet temperature of each reactor is set at 400 °C. The outlet product of the third catalytic reactor, the raw ammonia, is sent to the condensation stage. The stream is chilled in the refrigeration stage and then purified in a high-pressure separator to obtain pure liquid ammonia.

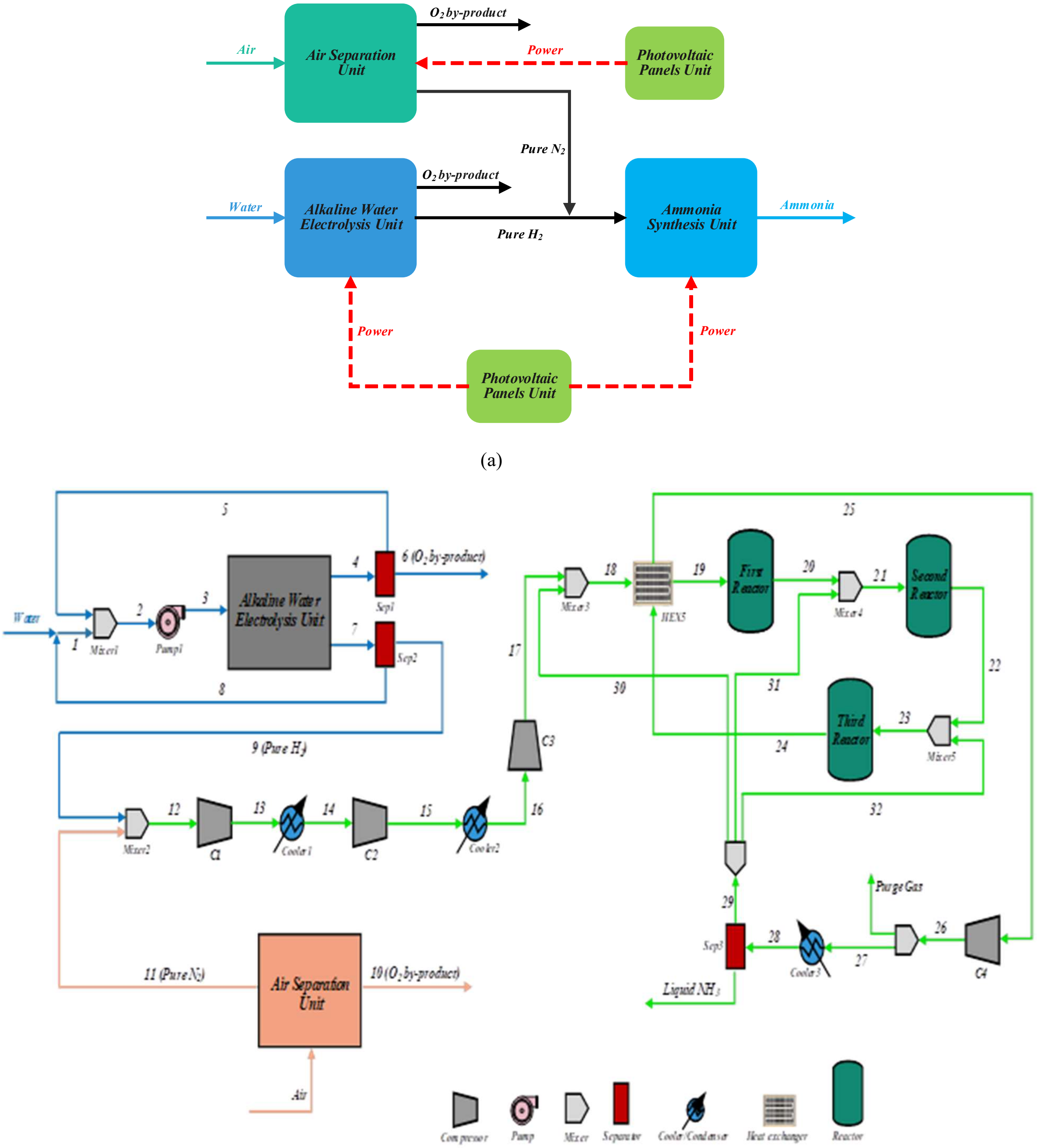

(a)

(b)

Fig. 8.1. Process flow diagram of the PtA plant.

8.2. Description of biomass-to-ammonia plants

This subsection presents the biomass-to-ammonia (BtA) plants where wood gasification supplies syngas and a membrane-assisted WGS reactor produces high-purity H_2. This work compares co-current (CO-WGS) vs counter-current (CC-WGS) operation to test the hypotheses on optimal H_2 recovery and purity, and how WGS integration choices affect energy, cost, and LCA outcomes. ASU provides N_2 for Haber–Bosch and O_2 that is utilized in gasification, an explicit thesis goal on oxygen management. A CO_2 capture and storage (CCS) block handles WGS off-gas to improve environmental performance and generate liquid CO_2. As with PtA, PV panels drive the plant, keeping the route fully renewable.

Together, these BtA configurations test which hydrogen production methods is preferred, thermochemical H_2 (via gasification-WGS) or electrolysis-only PtA. Fig. 8.2(b) illustrates the PFD of the BtA configuration. The main difference between BtA systems is the modeling of the WGS membrane reactor. As mentioned earlier, in BtA system with CO-WGS, the membrane reactor unit operates in co-current mode, while in CC-WGS system, a counter-current mode is developed. In co-current mode, feed gas and sweep stream are fed to the catalytic membrane reactor in the same direction, but feed and sweep streams move in the opposite direction in counter-current mode. In the figure, dashed lines are related to the counter-current mode. The biomass feedstock is introduced into the gasification unit and is converted to raw syngas using steam and pure oxygen, supplied by the ASU, as gasification agents. In the next step, the raw syngas passes through the WGS membrane reactor unit to produce pure H_2. Steam is used to sweep the H_2 molecules extracted by membrane tubes. Based on the co-current mode, a stream rich in hydrogen exits at the outlet of the permeation side, while the outlet stream of the reaction side, rich in CO_2, is sent to the CO_2 separation unit. The stream, a mixture of H_2 and steam, first passes through compression and condensation stages to separate the water content, and then a highly pure H_2 stream is sent to the ammonia synthesis loop. Also, the stream is first introduced into the catalytic burner, where unutilized syngas is converted to CO_2 and H_2O in the presence of pure O_2. Finally, the stream rich in CO_2 passes through compression and condensation stages, and finally, liquid CO_2, with a purity of 99.7% at ambient temperature and 65 bar, is separated. Like the PtA case, the N_2 required by the Haber-Bosch process is produced in the ASU. The mixture of H_2 and N_2 with an H_2/N_2 ratio of 3 is sent to the same ammonia synthesis loop at 200 °C and 200 bar as the PtA case. The process description for the counter-current mode is the same as for the co-current mode.

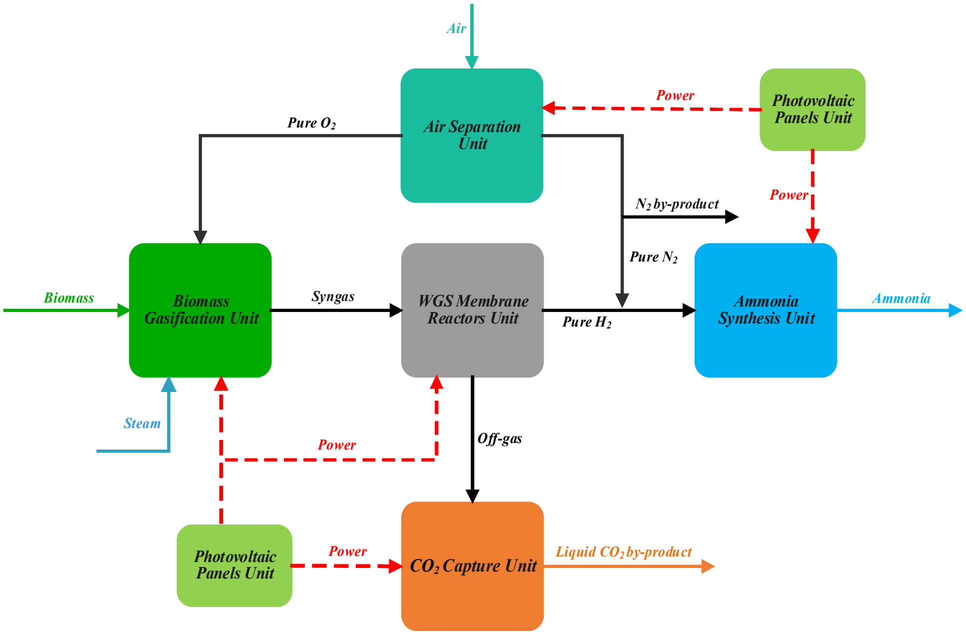

(a)

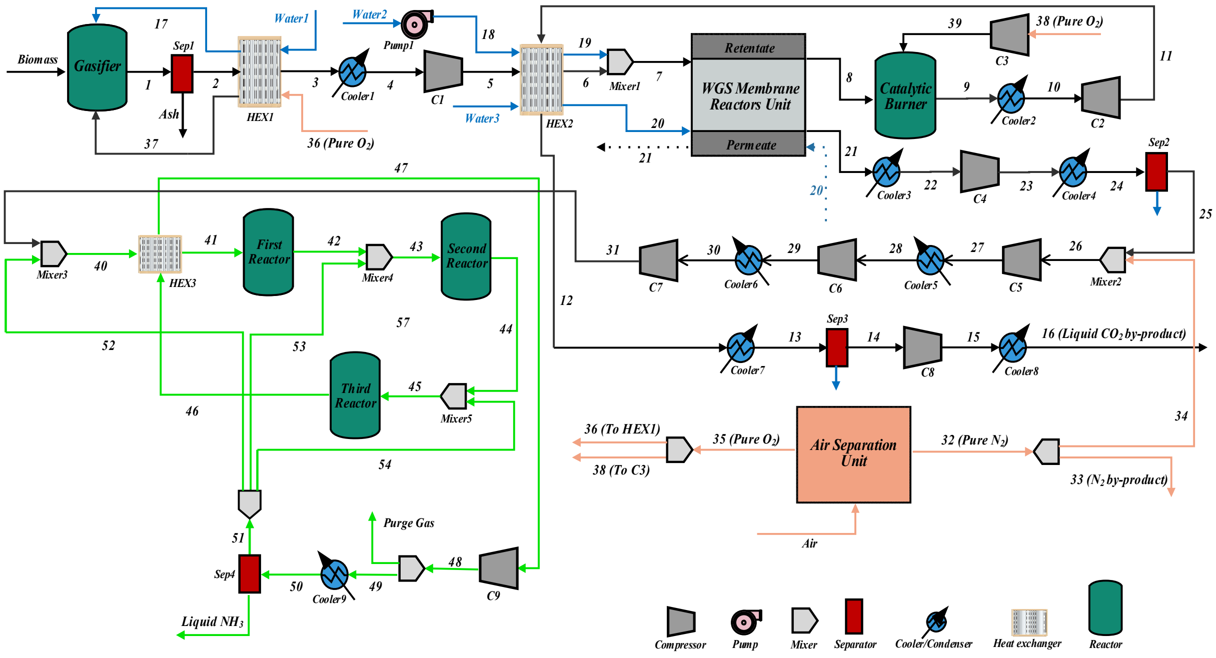

(b)

Fig. 8.2. Process flow diagram of the biomass-to-ammonia plants/

8.3. Thermodynamic results of ammonia production systems

Table 8.1 summarizes the key inventories for the power-to-ammonia (PtA) concept using an alkaline water electrolyzer (ALE) and the biomass-to-ammonia (BtA) concept based on wood gasification with a counter-current WGS membrane reactor (CC-WGS). The two cases are normalized to the same ammonia output (83472 kg/h) to enable a like-for-like comparison of hydrogen-supply strategies.

PtA plant is dominated by the electrolysis cell. The ALE draws 832 MW and requires 159.76 m³/h of process water and 895 kg/h of KOH electrolyte. The ASU electrical load is modest. The ammonia loop consumes 48.5 MW. No CCS, gasifier, or WGS units are present. Consequently, the photovoltaic (PV) field must deliver 885.76 MW in total to operate the plant at steady state. PtA achieves an energy efficiency of 50.19%.

Improved BtA with CC WGS replaces electrolysis with thermochemical H_2 production. The gasifier processes 141.92 kg/h of woody biomass and 17.98 m³/h of water and discharges 1037 kg/h of ash. To supply both O_2 for gasification and N_2 for ammonia synthesis, the ASU intake rises to 414663 kg/h. Downstream, the CC-WGS and CCS store 275182 kg/h of CO_2 as a compressed liquid stream. Electrical demand is distributed among the ASU, ammonia loop, CCS, gasifier auxiliaries, and WGS membrane reactor. In BtA case, the total power consumption provided by PV is roughly one-third of the PtA case because the power-intensive electrolyzer is absent. Energy efficiency of BtA with CC WGS is found to be 54.64%, which is highly efficient compared to PtA case.

At identical NH_3 capacity, PtA is electricity- and reagent-intensive but without feedstock. BtA is biomass-, and CCS-intensive yet far less electricity-consumer and inherently couples H_2 generation with CO_2 capture. These contrasting mass–energy footprints quantify the trade-offs central to optimizing hydrogen utilization across thermochemical and electrochemical pathways.

Table 8.1. Mass and energy results of two selected green ammonia plants.

Parameter	PtA	Improved BtA with CC WGS	Unit
Water consumption of ALE	159.76	0	m^3/h
Water consumption of gasifier	0	17.98	m^3/h
Input woody biomass of gasifier	0	141.92	Kg/h
Consumption of KOH electrolyte	895	0	Kg/h
Input air of ASU	90302	414663	Kg/h
CO_2 separated in CCS	0	275182	Kg/h
Output ash of gasifier	0	1037	Kg/h
Ammonia capacity	83472	83472	kg/h
Power consumption of ALE	832	0	MW
Power consumption of ASU	5.26	24.173	MW
Power consumption of ammonia synthesis	48.5	54.32	MW
Power consumption of CCS	0	57.955	MW
Power consumption of gasifier	0	69.168	MW
Power consumption of WGS	0	46.093	MW
Total power generated by PV cells	885.76	251.709	MW
Energy efficiency	50.19	54.64	%

Current density and temperature are the two primary parameters that set electrolyzer and thus whole PtA plant performance. They determine cell voltage and power draw, H_2/O_2 production rates, and thermal coupling opportunities across the plant. By mapping overall efficiency versus current density at several temperatures, it is possible to test the effect of hydrogen production unit. Three configurations of the green ammonia plant described in the system description section were investigated through techno-economic analysis with a capacity production of 2000 tonne/day. Figure 8.3 illustrates how the overall energy efficiency of the PtA system changes with current density at different operating temperatures. The graph shows that higher operating temperatures lead to higher overall energy efficiency, as the electrolysis cell performs more efficiently at higher temperatures. At a given temperature, the graph shows an optimal point for overall energy efficiency, which varies with current density. The overall energy efficiency initially increases at lower current densities, reaches a peak, and then decreases with current density. At operating temperatures of 50, 60, 70, and 80 °C, the overall energy efficiency values are 0.472, 0.481, 0.492, and 0.502, respectively, with current densities of 0.25, 0.2, and 0.175 A/cm2.

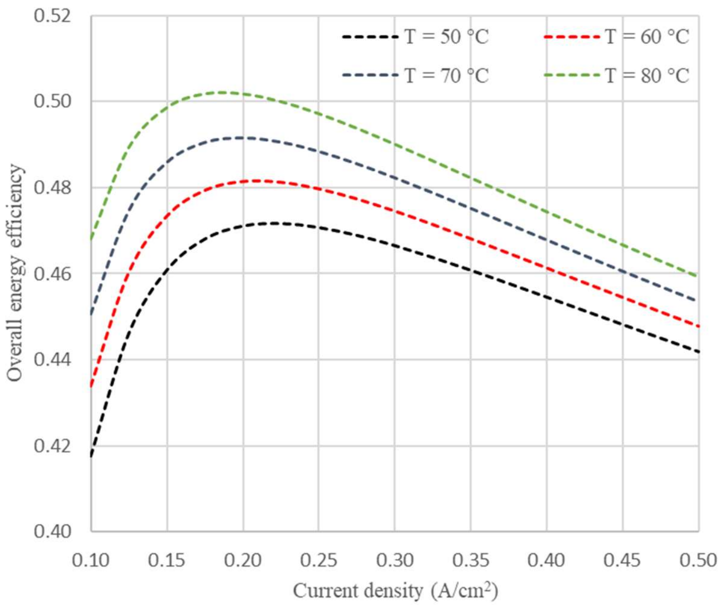

Fig. 8.3 Variations in the overall energy efficiency of the PtA system with current density at different operating temperatures.

Equivalence ratio of oxygen (ER_{O2}) and steam biomass ratio (SBR) are the key gasification levers that affect H_2 in syngas and whole-plant efficiency. Counter-current WGS membrane reactors are compared with co-current because they affect H_2 production. Together, these results validate the hypotheses on oxygen management and integrated H_2 use and directly inform efficiency enhancement. Figure 8.4 shows the variations in the overall energy efficiency of the BtA systems with O_2-equivalence and steam-to-biomass ratios. It is noted that, in Figs. 8.4, the CO, CC, and SBR represent the co-current, counter-current, and steam-to-biomass ratio, respectively. As can be seen, the lower the O_2-equivalence ratio, the higher the overall energy efficiency. Also, an increase in the steam-to-biomass ratio slightly leads to a rise in overall energy efficiency. Generally, at a lower O_2-equivalence ratio and a higher steam-to-biomass ratio, more hydrogen is generated in the gasification unit, which is favorable. The results reveal that the performance of the CC-WGS is better than CO-WGS due to the membrane reactor's more efficient performance in counter-current mode. In the counter-current mode, a more uniform driving force along the reactor is obtained, which leads to a higher hydrogen recovery rate than in the co-current mode. It should be noted that, since hydrogen is recovered by the membrane tubes, the reaction shifts to produce more product (hydrogen) based on Le Chatelier's Principle. So, it can be concluded that in the counter-current mode, a higher CO conversion is obtained due to a higher hydrogen recovery rate than in the co-current mode. The highest overall energy efficiency for BtA systems is 0.516 and 0.546, obtained with an O_2-equivalence ratio of 0.1 and a steam-to-biomass ratio of 0.8.

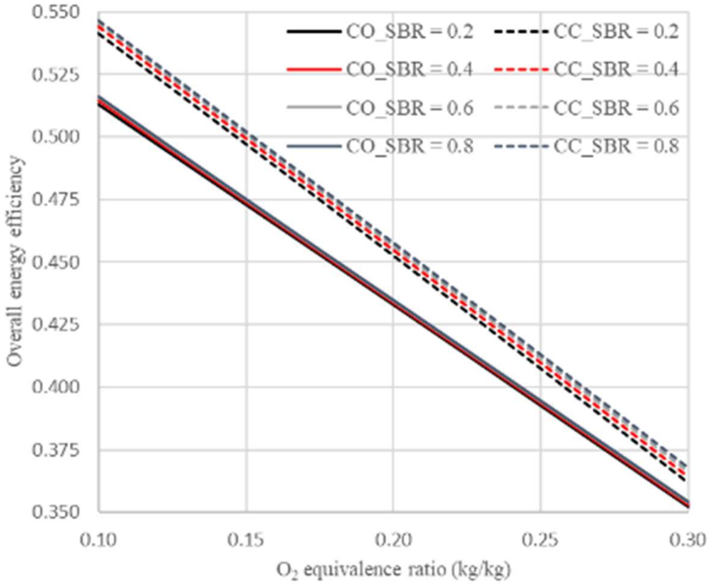

Fig. 8.4. Variations in the overall energy efficiency of the BtA systems with O_2-equivalence/steam-to-biomass ratios.

8.4. Techno-economic results of the ammonia production systems

To economically optimize the hydrogen production system, alkaline electrolysis in this case, the effect of different electrolysis temperatures and current densities on the LCOA are illustrated in Fig. 8.5. It can be observed that an increase in temperature and current density results in a decrease in LCOA. This is due to a reduction in overpotentials within the cell as the operating temperature increases, leading to a lower operating voltage and less electrical power required by the cell. Additionally, an increase in current density at a constant hydrogen production capacity reduces the active area needed by the electrolysis cell. Therefore, a lower LCOA is achieved at higher temperatures and current densities. Specifically, at an operating temperature of 80°C, the LCOA decreases by 54.83% from 872.3 to 394.01 $/tonne as the current density increases from 0.1 to 0.5 A/cm².

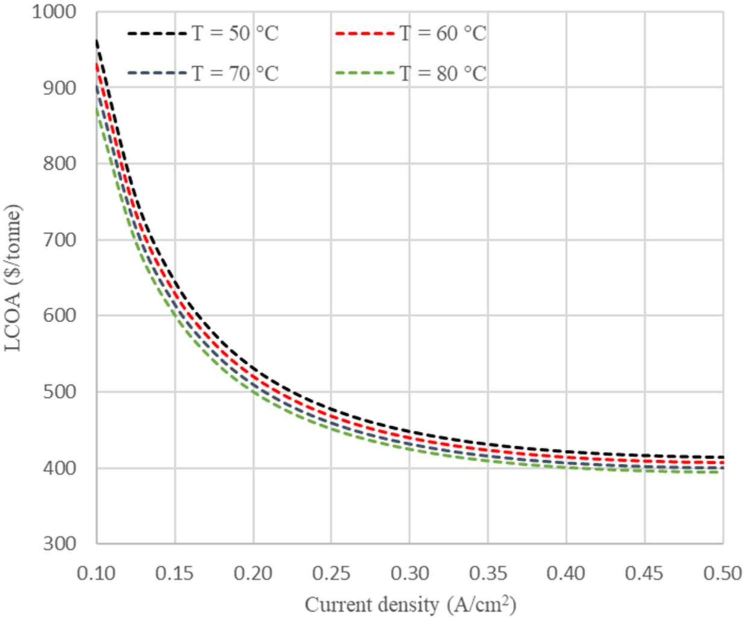

Fig. 8.5. The LCOA for PtA system at different operating temperatures and current densities.

Figure 8.6 is provided to economically compare two biomass-to-ammonia routes and to expose how gasifier/WGS operating points drive costs. This aligns with the thesis objective of optimizing hydrogen utilization through integrated design by locating the operating region that minimizes LCOA. The LCOA for BtA systems at different O_2-equivalence/steam-to-biomass ratios are compared in Fig. 8.6. As shown, LCOA decreases with an increase in O_2-equivalence ratio because, at higher O_2-equivalence ratios, systems' by-product sale revenue increases. As the O_2-equivalence ratio increases, a considerable amount of syngas generated inside the gasifier is converted into CO_2 and water through combustion reactions. Furthermore, as the O_2-equivalence ratio increases, so does the N_2 by-product in the air separation unit. With increases in CO_2 and N_2 production rates, by-product sale revenue increases, leading to a lower LCOA. Also, LCOA slightly decreases with the steam-to-biomass ratio. As expected, system based on CC-WGS is more cost-effective than the CO-WGS since the membrane reactor is more efficient in hydrogen recovery in counter-current (CC) mode in comparison with the co-current (CO) mode, as explained in Fig. 8.6. At the steam-to-biomass ratio (SBR) of 0.2, as the O_2-equivalence ratio increases from 0.1 to 0.3, the LCOA decreases by 15.18% from 551.88 to 468.13 \$/tonne for the CO-WGS system and 16.12% from 507.71 to 425.85 \$/tonne for CC-WGS system.

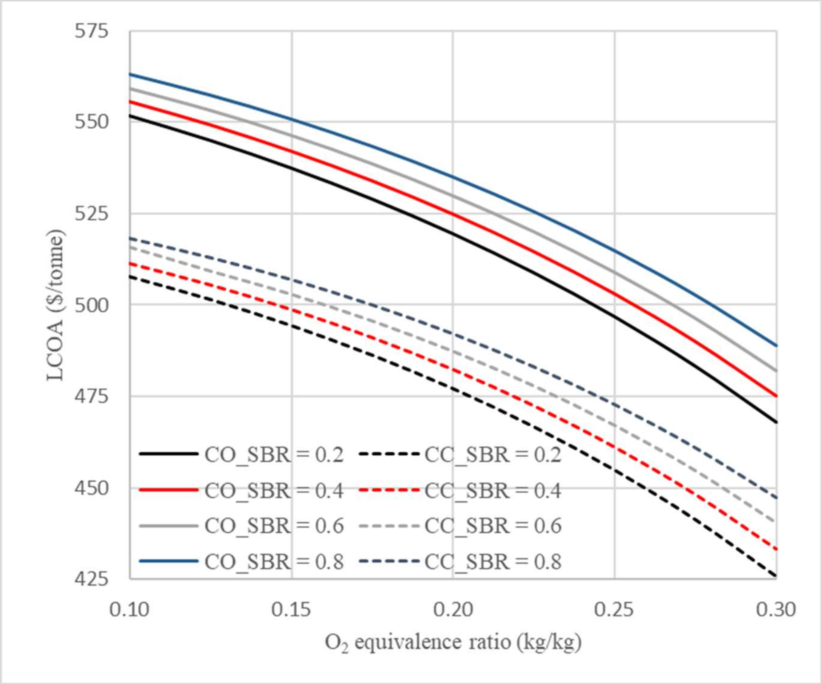

Fig. 8.6. The LCOA for BtA systems at different O_2-equivalence/steam-to-biomass ratios.

8.5. Attributional environmental results of the ammonia plants

Ammonia is treated as a strategic hydrogen-utilization route, a dense, carbon-free chemical hydrogen energy carrier that can be synthesized, transported, and reconverted using mature infrastructure. Therefore, after completing rigorous energy and techno-economic assessments for three alternative ammonia plants, the environmental analysis is done to two configurations: PtA and BtA with a CC-WGS membrane reactor. Conducting an attributional LCA (ReCiPe 2016, midpoint H) on this systems therefore provides:

- A clear test of whether their thermodynamic and techno-economic advantages translate into lower cradle-to-gate impacts per 1 kg of NH_3.
- A robust lower-bound benchmark for the pathway's environmental performance.

- A subsystem-resolved hotspot analysis to guide targeted improvements and co-product handling (N_2, captured CO_2).

According to Table 8.2, key LCA findings for the PtA plant (per 1 kg NH_3) are written below.

- Climate change: 0.772 kg CO_2-eq, dominated by the alkaline electrolyzer (93.5%) powered by solar PV cells.
- Toxicity indicators are material-intensive where terrestrial ecotoxicity equals 14.388 kg1.4-DCBeq, human non-carcinogenic toxicity is found to be 0.4346 kg 1.4DCBeq. in both, the electrolyzer provides ≈ 93% of burdens, reflecting upstream supply chains for electrodes, stacks, and PV components.
- Fossil resource scarcity is calculated 0.201 kgoileq and land use of 0.3113 m^2acrop-eq. In each case the electrolyzer accounts for 93% due to high power consumption coming from renewable energy.

Therefore, the PtA pathway achieves a low operational-emissions profile. Residual burdens concentrate on materials and electricity embodied in the electrolyzer and, secondarily, PV manufacturing. Priority levers therefore include increasing electrolyzer efficiency and lifetime, reducing stack material intensity (and enhancing recycling), and sourcing lower-impact PV supply.

Table 8.2. Detailed LCA results of the PtA plant.

Impact category	Unit	Total	Alkaline electrolyzer	Air separation unit	Solar PV cells
Global warming	kg CO2 eq	0.772372	0.721817	0.00309	0.047464
Stratospheric ozone depletion	kg CFC11 eq	3.05E-07	2.85E-07	1.22E-09	1.88E-08
Ionizing radiation	kBq Co-60 eq	0.004066	0.003802	1.61E-05	0.000248
Ozone formation, Human health	kg NOx eq	0.002068	0.001933	8.25E-06	0.000127
Fine particulate matter formation	kg PM2.5 eq	0.001596	0.001492	6.38E-06	9.8E-05
Ozone formation, Terrestrial ecosystems	kg NOx eq	0.002178	0.002036	8.7E-06	0.000134
Terrestrial acidification	kg SO2 eq	0.003317	0.0031	1.33E-05	0.000204
Freshwater eutrophication	kg P eq	5.79E-05	5.44E-05	2.18E-07	3.34E-06
Marine eutrophication	kg N eq	1.83E-05	1.74E-05	5.44E-08	8.35E-07
Terrestrial ecotoxicity	kg 1.4-DCB	14.3882	13.4151	0.059485	0.913612
Freshwater ecotoxicity	kg 1.4-DCB	0.000874	0.000816	3.56E-06	5.47E-05
Marine ecotoxicity	kg 1.4-DCB	0.011634	0.010848	4.81E-05	0.000738
Human carcinogenic toxicity	kg 1.4-DCB	0.007005	0.006547	2.8E-05	0.00043
Human non-carcinogenic toxicity	kg 1.4-DCB	0.434574	0.405479	0.001779	0.027316
Land use	m2a crop eq	0.311268	0.290159	0.00129	0.019819
Mineral resource scarcity	kg Cu eq	0.010336	0.009669	4.08E-05	0.000627
Fossil resource scarcity	kg oil eq	0.201003	0.187843	0.000804	0.012356
Water consumption	m3	0.027184	0.025468	0.000105	0.001612

Table 8.3 shows the detailed LCA results of this configuration for ammonia production. The biomass-to-ammonia system integrates oxygen-blown biomass gasification with a counter-current WGS membrane reactor that upgrades pure H_2 for Haber–Bosch, while an air separation supplies O_2 to the gasifier and N_2 to synthesis, on-site solar PV cells provide the needed electricity, and a unit to separates CO_2 from the WGS off-gas. Operating scale from the life cycle inventory shows a total electric load of 251.7 MW (gasifier 69.2, WGS 46.1, ammonia synthesis 54.3, CCS 58.0, ASU 24.2 MW) with major

mass flows of biomass 176535 kg/h, input air of 414663 kg/h, water to WGS 150811 kg/h, captured CO_2 275182 kg/h at 99.8 % and 65 bar, N_2 by-product 249485 kg/h at 99.99% and 5.5 bar, and NH_3 product 83472 kg/h at 99.93 % and 200 bar. The ReCiPe-2016 midpoint (H) results per 1 kg of NH_3 indicate:

- A low global warming potential (GWP) of 0.1749 $kgCO_2eq$, with the WGS membrane section contributing 0.1188 (68 %).
- Toxicity indicators follow the same hotspot pattern in which WGS reactor and PV cells contribute the most: terrestrial ecotoxicity 3.1002 kg1.4DCBeq, and human non-carcinogenic toxicity 0.0922 kg1.4DCBeq.
- Land use is 0.7112 m^2acropeq, driven by biomass supply and burdens accruing in the biomass gasifier.
- Mineral resource scarcity is 0.002145 kgCueq, reflecting used metals in processing equipment.
- Low fossil resource scarcity of 0.04605 kgoileq, consistent with biogenic feedstock use and captured biogenic CO_2.

Table 8.3. Detailed LCA results of the biomass-to-ammonia plant using CC-WGS.

Impact category	Unit	Total	Counter-current WGS membrane reactor	Air separation unit	Solar PV cells
Global warming	kg CO2 eq	0.174961	0.118803	0.003058	0.0531
Stratospheric ozone depletion	kg CFC11 eq	6.98E-08	4.75E-08	1.21E-09	2.1E-08
Ionizing radiation	kobo Co-60 eq	0.000843	0.00055	1.6E-05	0.000277
Ozone formation, Human health	kg NOx eq	0.000523	0.000373	8.17E-06	0.000142
Fine particulate matter formation	kg PM2.5 eq	0.000349	0.000233	6.31E-06	0.00011
Ozone formation, Terrestrial ecosystems	kg NOx eq	0.000553	0.000395	8.61E-06	0.00015
Terrestrial acidification	kg SO2 eq	0.00073	0.000489	1.32E-05	0.000228
Freshwater eutrophication	kg P eq	1.14E-05	7.46E-06	2.15E-07	3.74E-06
Marine eutrophication	kg N eq	3.38E-06	2.39E-06	5.38E-08	9.35E-07
Terrestrial ecotoxicity	kg 1,4-DCB	3.100189	2.019239	0.058865	1.022086
Freshwater ecotoxicity	kg 1,4-DCB	0.000193	0.000129	3.52E-06	6.12E-05
Marine ecotoxicity	kg 1,4-DCB	0.002505	0.001631	4.76E-05	0.000826
Human carcinogenic toxicity	kg 1,4-DCB	0.001499	0.00099	2.77E-05	0.000481
Human non-carcinogenic toxicity	kg 1,4-DCB	0.092288	0.059969	0.00176	0.030559
Land use	m2a crop eq	0.711229	0.687781	0.001277	0.022172
Mineral resource scarcity	kg Cu eq	0.002145	0.001403	4.04E-05	0.000701
Fossil resource scarcity	kg oil eq	0.046047	0.031428	0.000796	0.013823
Water consumption	m3	0.005606	0.003699	0.000104	0.001803

8.6. Summary of ammonia production plants

This subsection compares three green-ammonia configurations in terms of efficiency, cost, and environmental outcomes, where targeted integration of H_2, O_2, heat, and power delivers system-level advantages unattainable by isolated units.

- In PtA system, the investigation of electrolysis's operating temperature effect reveals that at a given current density, the overall energy efficiency increases with operating temperature. Also, at a given operating temperature, the overall energy efficiency initially increases at lower current densities, reaching a peak and then decreases. Moreover, the levelized cost of ammonia production is reduced with the electrolysis' operating temperature and current density.
- In BtA systems, the overall energy efficiency and levelized cost of ammonia increase with the steam-to-biomass ratio, while the increasing O_2-equivalence ratio reduces the overall energy efficiency and LCOF.
- From energy and techno-economic viewpoints, CC-WGS system is preferable to the CO-WGS system due to the more efficient performance of membrane reactors in hydrogen applications.
- The highest overall energy efficiency (54.64%) is obtained in the biomass-to-ammonia concept followed by counter-current membrane reactor.
- In biomass-to-ammonia case, the co-current and counter-current modes achieve levelized cost of 562.98 $/tonne and 513.28 $/tonne, respectively.
- The biomass-to-ammonia concept followed by counter-current membrane reactor is preferable to the co-current mode.
- The BtA route with counter-current membrane WGS is preferred, acceptable efficiency (54.6%), the lowest cost among all plants (513 $/tonne), and near-zero GHG intensity (0.175 $kgCO_2eq/kgFuel$) due to superior H_2/O_2 and N_2 management.

9. Biojet fuel production system

This chapter introduces a hydrogen-enabled biomass-to-jet-fuel pathway to generalize the thesis beyond methanol and ammonia and to test the hypotheses in a hard-to-abate sector, i.e. aviation. Its purpose is to evaluate whether the best-performing subsystems identified earlier (oxygen-blown gasification, high-temperature SOEC, and LNG–GT energy recovery) can be co-integrated with Fischer–Tropsch synthesis to unlock system-level gains. The chapter probes key integration synergies (high-temperature coupling of SOEC–gasification and cold/low-temperature pairing of FT–LNG) and compares renewable wind power with the Poland electricity mix to quantify power-source sensitivity. In doing so, it identifies design levers and trade-offs that indicate whether coordinated use of H_2, O_2, heat, and power can deliver economical, efficient, and lower-impact sustainable aviation fuel (SAF) production.

9.1. Description of biojet fuel production system

Fig. 9.1 shows a process for producing biojet fuel and natural gas. The primary energy sources of this system are woody biomass, wind energy and the Polish electricity mix, respectively. First, the woody biomass is sent to a gasification unit, where steam and oxygen serve as gasification agents. Steam needed for gasification is generated using the thermal energy of hydrogen-oxygen coolers, and oxygen is directed from the SOEC to the gasifier. Surplus water is generated in the gasification unit, and syngas is purified from emissions and waste heat using a cleaning system. Then, pure syngas is directed to the bio-jet fuel production system.

One of the most important units in this system is the solid oxide electrolyzer. Steam needed in this electrolyzer is generated from a heat integration with syngas coolers and an intercooler of a gas turbine. Part of the input electricity of the SOEC is provided by the electricity sources (wind or Polish mix), a small portion of which is directed from the net power generation in the gas turbine. As a result, the hydrogen produced from this electrochemical reaction is directed to the bio-jet fuel production unit, while the oxygen is utilized in the oxyfuel gas turbine and gasification subsystems.

In the proposed cycle, an LNG regasification unit is incorporated to capture waste heat from the Fischer–Tropsch process while converting LNG into its gaseous state. Of the regasified output, 90% is delivered to end users, whereas the remaining 10% is directed toward an oxy-fuel gas turbine. Oxygen produced from the solid oxide electrolysis cell is compressed to 35 bar and supplied to a fuel-rich combustor, where it also interacts with CO_2 while providing additional heating. Before entering the gas turbine for power generation, the combustion gases are cooled to 1200 °C through an intercooler. Finally, the turbine exhaust is discharged into the atmosphere, leading to both energy losses and greenhouse gas emissions. However, flue gases are mixed with hydrogen from SOEC and syngas from the gasification in the present work. In this way, exhaust gas recycling contributes to the further production of biojet fuel. Finally, the waste heat from the FT synthesis is utilized in conjunction with the LNG regasification system, the bio-jet fuel is transported to the users, and water is recycled to the SOEC and the gasifier.

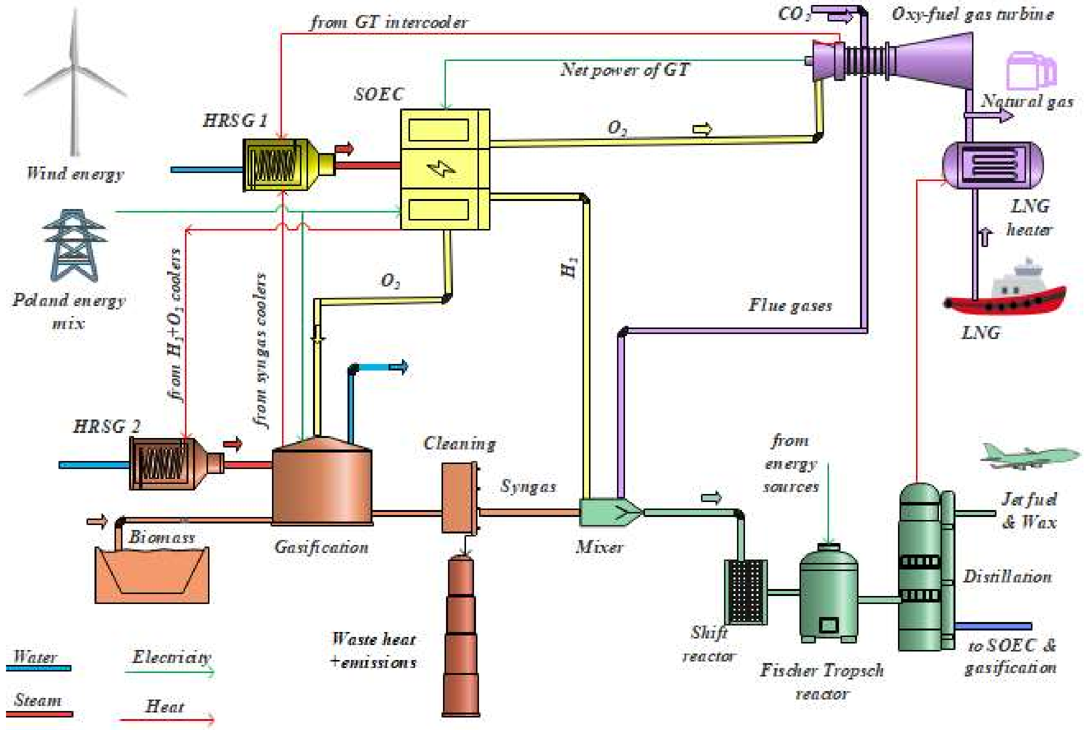

Fig. 9.1. Schematic diagram of the proposed plant for biojet fuel and natural gas production.

9.2. Thermodynamic results of biojet fuel production system

Fig. 9.2 depicts the mass/energy results provided by the thermodynamic analysis using Aspen Plus software. The integrated bio-jet fuel and natural gas production system combines renewable energy, biomass gasification, electrolysis, Fischer-Tropsch synthesis, and oxyfuel combustion to produce synthetic fuels, including jet fuel, wax, and light hydrocarbons. The process begins with gasification of 1500 kg/h of woody biomass with a lower heating value (LHV) of 18010 kJ/kg using 1080 kg/h of steam at 20 bar produced from a heat integration with hydrogen and oxygen coolers, generating syngas (1889 kg/h) containing gases emissions into the air, along with waste heat of the combustor (1.55 MW), ash mixed with water (325 kg/h) and minor pollutants such as HCl, H_2S, COS, NH_3, and HCN, as reported in Fig. 9.2. Syngas undergoes a cleaning process to remove impurities before being mixed with 280 kg/h of hydrogen produced by a SOEC powered by wind energy or the mix of Poland's electricity, respectively. The total power demand of the proposed system is 10.583 MW. The mixed gases then pass through a reversed shift reactor, where the hydrogen-to-carbon monoxide ratio is selected as 2 for the Fischer-Tropsch synthesis. In the Fischer-Tropsch reactor, syngas is converted into hydrocarbons, producing 966 kg/h of jet fuel, 189 kg/h of wax, and 244 kg/h of light hydrocarbons, which are subsequently separated by distillation. Meanwhile, an oxyfuel gas turbine operates using 450 kg/h of natural gas and 1365 kg/h of oxygen from the electrolyzer, producing a net power output of 0.86 MW, along with 2615 kg/h of flue gases, including 41% of CO_2, 35% of H_2O and 24% of CO on a mass basis. The electrolyzer, which consumes 2500 kg/h of steam, generates 280 kg/h of hydrogen and 2220 kg/h of oxygen, supplied to the gasifier and the oxy-gas turbine. Additionally, a liquefied natural gas (LNG) heater processes 3000 kg/h of LNG, utilizing 3.42 MW of waste heat from the FT synthesis system. Water is efficiently recycled into the electrolyzer and gasifier.

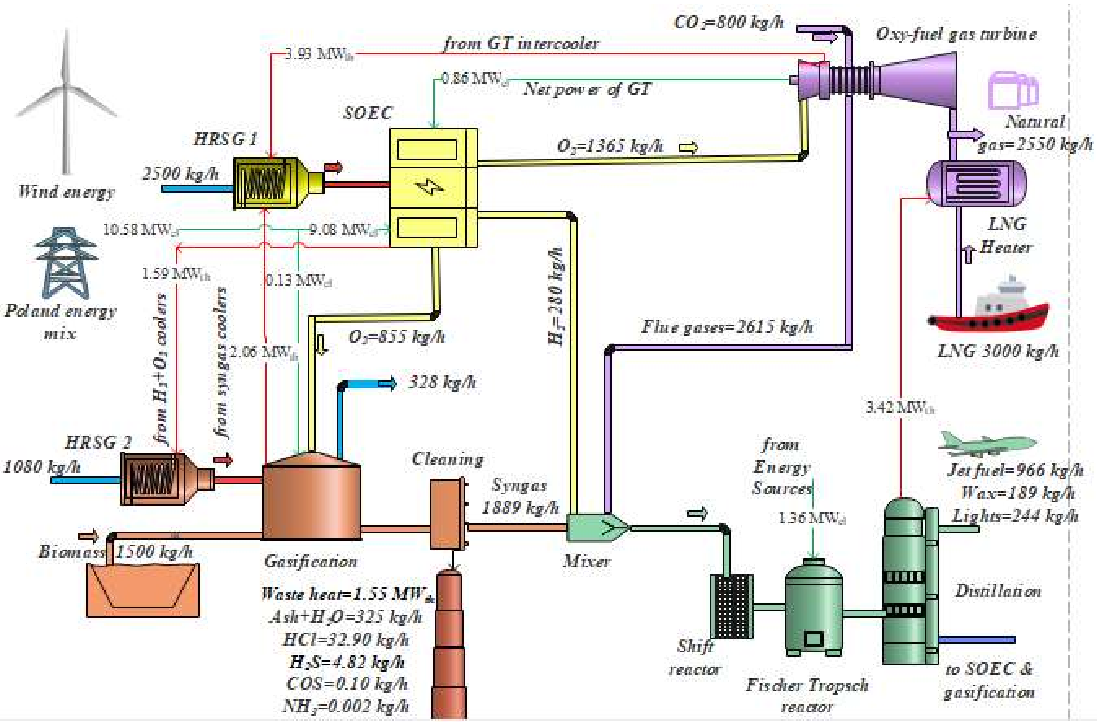

Fig. 9.2. The life cycle inventory (LCI) of the proposed system derived from process modeling.

The following sensitivity isolates a primary design lever for the thesis called SOEC operating temperature. Because the SOEC is the dominant electricity consumer and hydrogen generator, its temperature directly governs the outcomes. SOEC temperature affects thermal duty as well, creating a purposeful trade-off that motivates the core hypothesis of this work: high-temperature electrolysis performs best when thermally integrated with gasification. Figure 9.3 examines the influence of SOEC temperature on electrical efficiency and specific power demand. The results show that as the temperature increases from 600 °C to 1000 °C, electrical efficiency improves significantly, increasing from approximately 37.5% to approximately 72.0%, indicating better energy utilization at higher temperatures. On the contrary, the specific power demand decreases over the same temperature range, dropping from around 9.0 kWh/L to 4.5 kWh/L, reflecting reduced energy requirements for operation. This inverse relationship demonstrates that higher temperatures enhance system performance by simultaneously increasing efficiency and reducing energy demand. These findings underscore the crucial role of temperature enhancement in enhancing the overall performance of SOEC systems. However, temperature enhancement would increase the rate of input thermal energy.

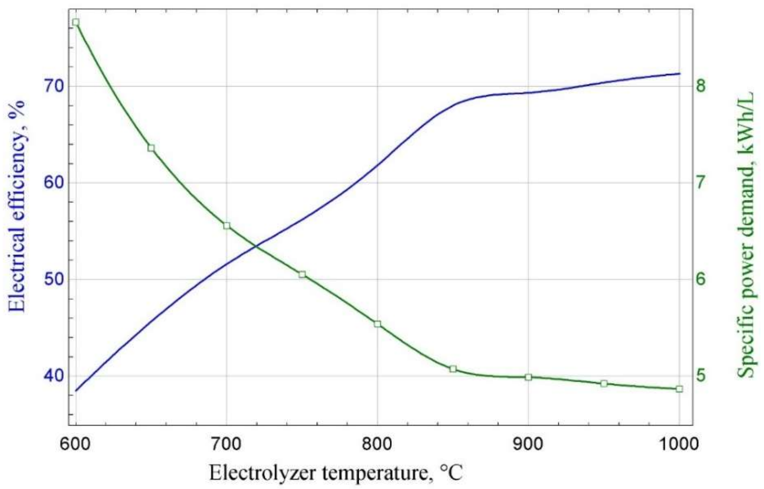

Fig. 9.3. The effect of SOEC temperature on efficiency and power demand.

Figure 9.4 targets a central integration lever: CO_2 injection to the oxy-fuel gas turbine. In the SAF polygeneration layout, CO_2 injection simultaneously tunes Brayton-cycle efficiency and specific power demand and allocates carbon between power generation and the downstream SAF synthesis. This directly tests the hypotheses on oxy-fuel GT integration, coordinated oxygen/CO_2 management, and system-level optimization of hydrogen-enabled polygeneration for improved efficiency, cost, and LCA performance. Figure 9.4 illustrates the relationship between the amount of CO_2 in the gas turbine, measured in tonne/h, and two key performance metrics: electrical efficiency and specific power demand. As the inlet CO_2 increases from 0.46 to 0.88 t/h, the electrical efficiency exhibits a clear upward trend, starting at approximately 52% and steadily rising to around 56.5%. On the contrary, the specific power demand decreases over the same range, starting at 6.65 kWh/L and decreasing linearly to around 6.0 kWh/L. This inverse relationship highlights a trade-off in operational performance, where higher CO_2 emissions lead to higher electrical efficiency and reduced specific power demand. The linearity and consistency of the trends emphasize predictable improvements in performance with increased CO_2 rate.

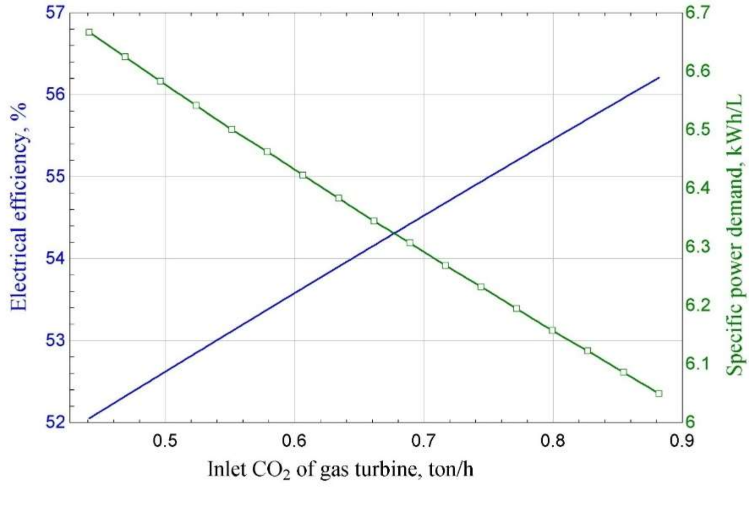

Fig. 9.4. The effect of the CO_2 injection into the gas turbine on efficiency and power demand.

9.3. Techno-economic results of biojet fuel production system

This subsection is presented to pinpoint where capital investment is locked up in the SAF polygeneration system. It identifies the dominant CAPEX drivers, thereby guiding optimization. It also reveals which components improve performance without major capital, and where process intensification could reduce costs for optimal hydrogen utilization in biojet fuel production. Fig. 9.5 illustrates the distribution of fixed capital investment across four key components. The electrolyzer accounts for the largest share at 41% of total investment, f, followed by fuel synthesis at 38%. Together, these two categories dominate capital structure, representing 79% of the total expenditure, which highlights their critical importance or higher cost requirements. On the contrary, gas and power generation account for significantly smaller shares, at 12% and 9%, respectively. This distribution indicates that capital is concentrated primarily on the electrolyzer and fuel synthesis due to their pivotal roles and high energy demands, whereas gasification and gas and power generation are less capital-intensive.

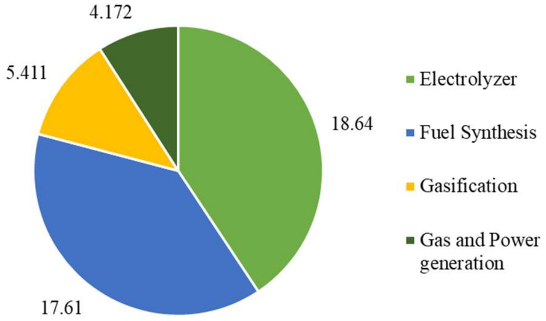

Fig. 9.5. The distribution of fixed capital investment of biojet fuel production in M$.

To be more specific, Fig. 9.6 illustrates the equipment costs for various components involved in the power and biomass-to-fuel process. The most notable observation is the exceptionally high cost of the electrolyzer, exceeding 18 M$, making it by far the most expensive unit. In the gasification subsystem, syngas cleaning represents the highest equipment cost at 2 M$. In the fuel synthesis section, the distillation towers and the hydrocracking reactor have the highest costs, ranging from approximately 6 M$ to 8 M$, respectively. Equipment such as the combustor, LNG heater, and NG compressor typically have low costs, typically below 1 M$.

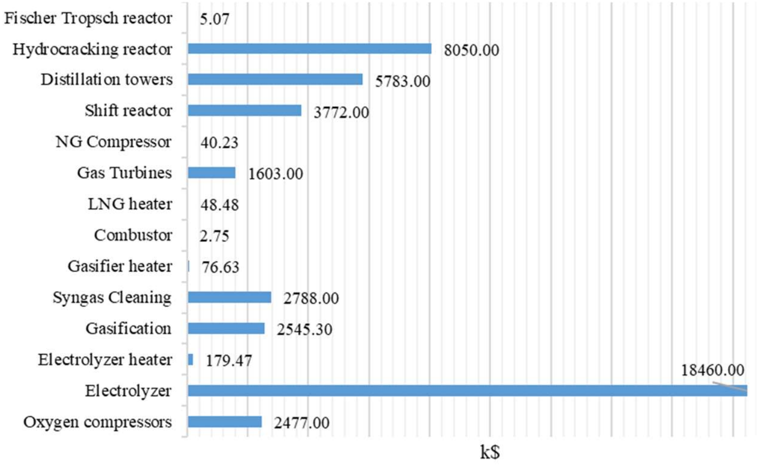

Fig. 9.6. The distribution of fixed capital investment for various subsystems.

Figure 9.7 presents long-term economic viability of the SAF polygeneration concept and to test the thesis hypothesis that hydrogen use can deliver competitive economics. The 25-year net present value (NPV) trajectory makes payback and capital recovery explicit for this capital-intensive configuration. In short, the NPV profile connects process integration choices to investment performance, directly supporting the thesis goals of minimizing cost. It displays the net present value of the system over 25 years. The NPVs range from approximately -200 M$ to around 50 M$. Most NPVs are negative, indicating that the net savings are less than investments. Negative NPVs dominate the chart, with a steep rise from -200 M$ towards zero, which is reached only after 20 years. Therefore, in the base case, the payback time of the proposed bio-jet fuel plant is 20 years. This figure clearly illustrates the variations in economic performance across the project lifetime.

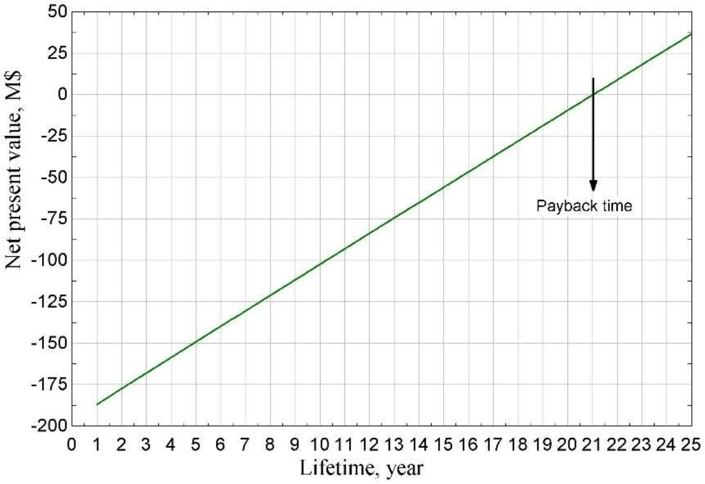

Fig. 9.7. Net present values (NPV) of the proposed system for 25 years.

Figure 9.8 presents electricity price as a first-order driver of hydrogen-enabled SAF plants which dominates both the levelized cost of fuel and capital recovery. Mapping LCOF directly tests the hypotheses on optimal hydrogen utilization under different power costs and the influence of renewable supply choice on techno-economics. It illustrates the relationship between the price of electricity in $/kWh and two critical parameters, namely the LCOF in $/L and the payback time in years. As the price of input electricity increases from 0 to 0.12 $/kWh, both the levelized cost of fuel and the payback time show an upward trend. The LCOF, represented by the blue line, starts at approximately 0.87 $/L when electricity is free and increases linearly to around 1.7 $/L at an electricity price of 0.12 $/kWh. This linear increase suggests a direct correlation between electricity costs and fuel production costs, as electricity constitutes a significant portion of operating expenses in bio-jet fuel production.

However, the payback time, shown by the green curve, follows an exponential growth pattern. It begins at around ten years when the electricity price is minimal and increases to approximately 70 years as the electricity price reaches 0.12 $/kWh. This sharp increase is due to the compounding effect of higher operational costs, which decreases profitability and extends the time required to recover the initial investment.

In the base case of 0.05 $/kWh, the levelized cost of fuel results at 1.25 $/L, while the selling price of jet fuel is assumed to be 1.25 $/L. In summary, the proposed system is economically feasible. For comparison, the cost of electricity from the Polish energy mix and wind turbines is assumed to be 0.65 $/kWh and 0.88 $/kWh, respectively [147], [148]. Using the Polish energy mix results in a payback period of 24 years and a levelized cost of 1.35 $/L. In contrast, when wind turbines are used, the payback period extends to 33 years with a levelized cost of 1.55 $/L. Therefore, the Polish energy mix is the more economically viable option.

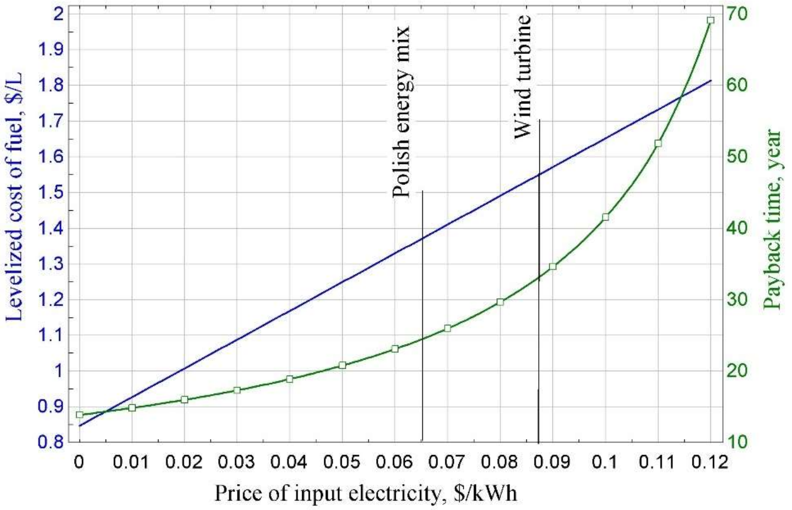

Fig. 9.8 Analysis of the influence of the electricity price for the levelized cost of fuel and the payback time.

9.4. Attributional environmental results of biojet fuel production

This section presents the life cycle assessment (LCA) of the proposed system for producing biojet fuel and natural gas from woody biomass and power. The LCA aims to evaluate the environmental performance of the system, with particular emphasis on greenhouse gas emissions as well as other key impact categories relevant to sustainability. By providing a systematic comparison of the Polish energy mix and wind energy pathways, the assessment offers insights into the potential advantages and trade-offs of this biomass- and power-integrated approach.

Table 9.1 presents a detailed quantitative comparison of environmental impact metrics between biofuel processes utilizing wind energy and Poland's electricity mix, categorized by technologies such as SOEC, gasification, and LNG-GT. Impacts are measured in several key environmental indicators, such as global warming potential, ozone depletion, and resource scarcity.

In terms of global warming potential, total emissions for wind energy are significantly lower, at 0.4647 kgCO_2eq/kgSAF, compared to 8.8739 kgCO_2eq/kgSAF for Poland's electricity mix. Breaking it down further, SOEC shows 0.3117 kgCO_2eq/kgSAF for wind versus 7.5347 kgCO_2eq/kgSAF for Poland's mix, while gasification reduces GWP to 0.02 kgCO_2eq/kgSAF under wind energy but increases to 0.13 kgCO_2eq/kgSAF in Poland's mix. Impact of energy source itself experiences a significant reduction, from 1.11 kgCO_2eq/kgSAF in the Polish mix to 0.028 kgCO_2eq/kgSAF in wind energy.

Ionizing radiation has a value of 0.0158 kBqCo-60eq/kgSAF for wind energy, compared to 0.0569 kBqCo-60eq/kgSAF for Poland's energy mix due to the electricity generation by nuclear power plants in Poland.

In ozone formation (human health), wind energy consistently shows lower emissions, with 0.0013 kgNO_xeq/kgSAF under wind turbines compared to 0.0179 kgNO_xeq/kgSAF for Poland's electricity mix. Similar trends are observed in fine particulate matter, where wind energy records 0.00107 kgPM2.5eq under total impacts, compared to 0.0156 kgPM2.5eq for Poland's electricity mix. Terrestrial acidification and freshwater eutrophication also show stark differences: wind energy has an impact of 0.0026 kgSO_2eq, compared to 0.0458 kgSO_2eq for the total energy mix. For freshwater eutrophication, the total impact under wind energy is 0.0003 kg Peq, while the mix is 0.0108 kg Peq. In summary, wind energy's low environmental impacts stem from its non-combustive, zero-emission generation process, unlike coal-based energy mixes, such as those in Poland, which produce substantial air and water pollutants.

Land use is another significant category where wind energy has a total impact of 1.17 m^2/a, less than Poland's 1.29 m^2/a. In the scarcity of mineral resources, the total impact is 0.0104 kgCueq, compared to Poland's 0.0031 kgCueq. Wind energy looks worse than the Polish energy mix in the mineral resource scarcity category as building wind turbines requires a lot of metals and minerals. Large amounts of steel, copper, and sometimes rare earth elements are needed for the towers, blades, and generators. In contrast, Poland's fossil-based electricity relies mainly on burning fuel and does not consume as many minerals per unit of energy, so its score in this specific category is lower.

Lastly, in the scarcity of fossil resources, wind energy shows a total impact of 0.32 kgoileq, a sharp decrease from 2.41 kgoileq for Poland's energy mix since wind turbines do not burn fossil fuels during operation, so their fossil resource use is limited to the materials needed for construction, whereas Poland's fossil-based mix relies heavily on extracting and consuming fossil fuels, which drives the much higher impact.

Table 9.1. Detailed LCA results using two energy sources for biojet fuel production.

Impact category	Unit	Total		SOEC		Gasification		LNG-GT		Energy source	
		Wind	Poland	Wind	Poland	Wind	Poland	Wind	Poland	Wind	Poland
Global Warming	kg CO2 eq	0.4647	8.8739	0.3117	7.5347	0.0292	0.1326	0.0947	0.0947	0.0280	1.1110
Ionizing radiation	kBq Co-60 eq	0.0158	0.0568	0.0115	0.0467	0.0006	0.0011	0.0024	0.0024	0.0010	0.0060
Ozone formation, Human health	kg NOx eq	0.0013	0.0179	0.0008	0.0151	0.0001	0.0003	0.0001	0.0001	0.0000	0.0020
Fine particulate matter formation	kg PM2.5 eq	0.0010	0.0156	0.0008	0.0133	0.0000	0.0002	0.0001	0.0001	0.0001	0.0010
Ozone formation, Terrestrial ecosystems	kg NOx eq	0.0014	0.0180	0.0009	0.0152	0.0001	0.0004	0.0001	0.0001	0.0001	0.002
Terrestrial acidification	kg SO2 eq	0.0026	0.0457	0.0020	0.0390	0.0001	0.0006	0.0002	0.0002	0.0002	0.0050
Freshwater eutrophication	kg P eq	0.0003	0.0108	0.0002	0.0092	0.0000	0.0001	0.0000	0.0000	0.0000	0.0010
Marine eutrophication	kg N eq	0.0000	0.0006	0.0000	0.0005	0.0000	0.0000	0.0000	0.0000	0.0000	0.0000
Terrestrial ecotoxicity	kg 1.4-DCB	12.4064	6.9279	10.3950	5.6892	0.2426	0.1752	0.2589	0.2589	0.0000	0.8043
Freshwater ecotoxicity	kg 1.4-DCB	0.4882	0.3035	0.4176	0.2589	0.0063	0.0040	0.0020	0.0020	0.0620	0.0380
Marine ecotoxicity	kg 1.4-DCB	0.5958	0.4190	0.5094	0.3576	0.0077	0.0056	0.0027	0.0027	0.0750	0.0530
Human carcinogenic toxicity	kg 1.4-DCB	0.1319	0.6678	0.1084	0.5687	0.0035	0.0101	0.0044	0.0044	0.0150	0.0840
Human non-carcinogenic toxicity	kg 1.4-DCB	2.1399	13.3222	1.8015	11.4064	0.0338	0.1712	0.0424	0.0424	0.2620	1.7020
Land use	m2a crop eq	1.1756	1.2975	0.0136	0.1183	1.1583	1.1598	0.0019	0.001	0.0010	0.0170
Mineral resource scarcity	kg Cu eq	0.0104	0.0031	0.0087	0.0024	0.0002	0.0001	0.0002	0.0002	0.0012	0.0003
Fossil resource scarcity	kg oil eq	0.3233	2.4149	0.1917	1.9883	0.0089	0.0346	0.1155	0.1155	0.0070	0.2764

Water consumption	m3	0.0034	0.2696	0.0027	0.2313	0.0000	0.0033	0.0002	0.0002	0.0003	0.0346

Fig. 9.9 explains how the electricity supply governs the life cycle GHG footprint of the SAF pathway. Contrasting Poland electricity mix with wind energy directly tests the hypothesis that renewable sourcing lowers impacts in hydrogen-based and electrified plants. Practically, these results prioritize decarbonization levers and establish environmentally-friendly subsystems. It compares the shares for the global warming potential (GWP) associated with producing sustainable aviation fuel (SAF) using two different energy sources: Poland's electricity mix and wind turbines. In Fig. 9.9(a), using Poland's electricity mix, 97.3% of the total GWP comes from the Polish energy mix itself, highlighting the heavy dependence on fossil fuels like coal and natural gas. Minor contributions come from LNG at 1.6%, CO_2 at 0.8%, and biomass at just 0.3%. In contrast, Fig. 9.9(b) shows that when wind turbines are used, the environmental burden is more balanced. Wind energy accounts for 48.4% of the greenhouse gas (GWP), with LNG contributing 30.8%, CO_2 at 15.1%, and biomass at 5.7%.

Although wind energy still represents the largest share in this setup, it is worth noting that this includes its full life cycle impact, from manufacturing to operation. Overall, the comparison clearly shows that producing SAF with wind energy results in a substantially lower environmental footprint compared to using Poland's conventional energy mix. This highlights the crucial role of renewable energy sources in reducing the climate impact of alternative fuels and underscores the need to decarbonize national energy grids for a more sustainable future.

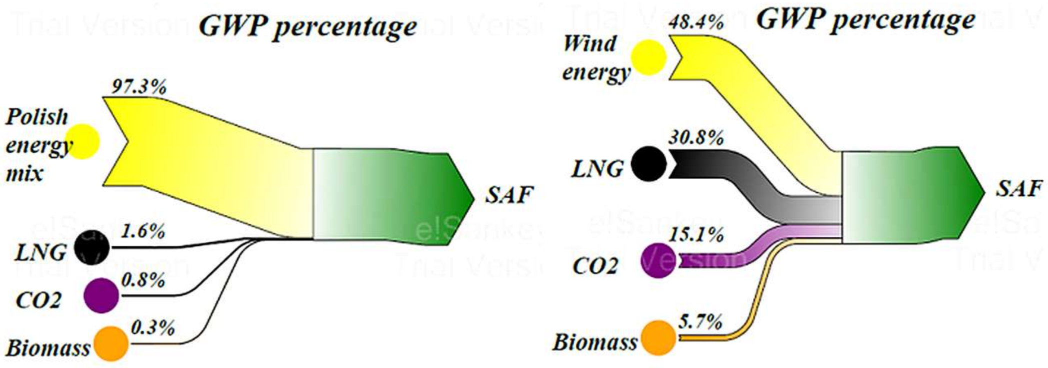

(a) (b)

Fig. 9.9. Overall GWP percentage of the proposed system. a) Poland's electricity mix. b) Wind turbines.

Figure 9.10 provides a detailed comparison of the environmental impact assessment. The analysis focuses on environmental metrics across the most important categories, using Poland's electricity mix versus wind energy. As shown, the environmental impacts are segmented into several key indicators, including global warming, terrestrial ecotoxicity, human carcinogenic toxicity, human non-carcinogenic toxicity, land use, and fossil resource scarcity.

In Fig. 9.10, in most categories, such as global warming, terrestrial ecotoxicity, and both human carcinogenic and non-carcinogenic toxicity, the SOEC subsystem dominates, contributing approximately 65–75% for wind energy and rising to 80–85% for the Polish energy mix. This indicates that electricity demand for electrolysis poses a significant environmental burden, particularly when the electricity is sourced from fossil-fuel-intensive grids. The higher share of SOEC in the Polish energy mix results from the carbon- and pollutant-intensive nature of coal-based electricity generation.

LNG-GT shows a noticeable contribution to fossil resource scarcity, particularly in the wind scenario (around 30%), reflecting its reliance on natural gas production, which contributes to greenhouse gas emissions.

Gasification emerges as the primary driver of land use impact, accounting for approximately 90% and 85% of wind and Polish energy sources, respectively. This is likely due to the cultivation, extraction, or handling of biomass feedstocks, which require a substantial amount of land.

The energy source subsystem itself contributes relatively little (generally under 10%) across all categories because once the electricity is delivered, the upstream processes (e.g., electrolysis and fuel synthesis units) carry most of the environmental load.

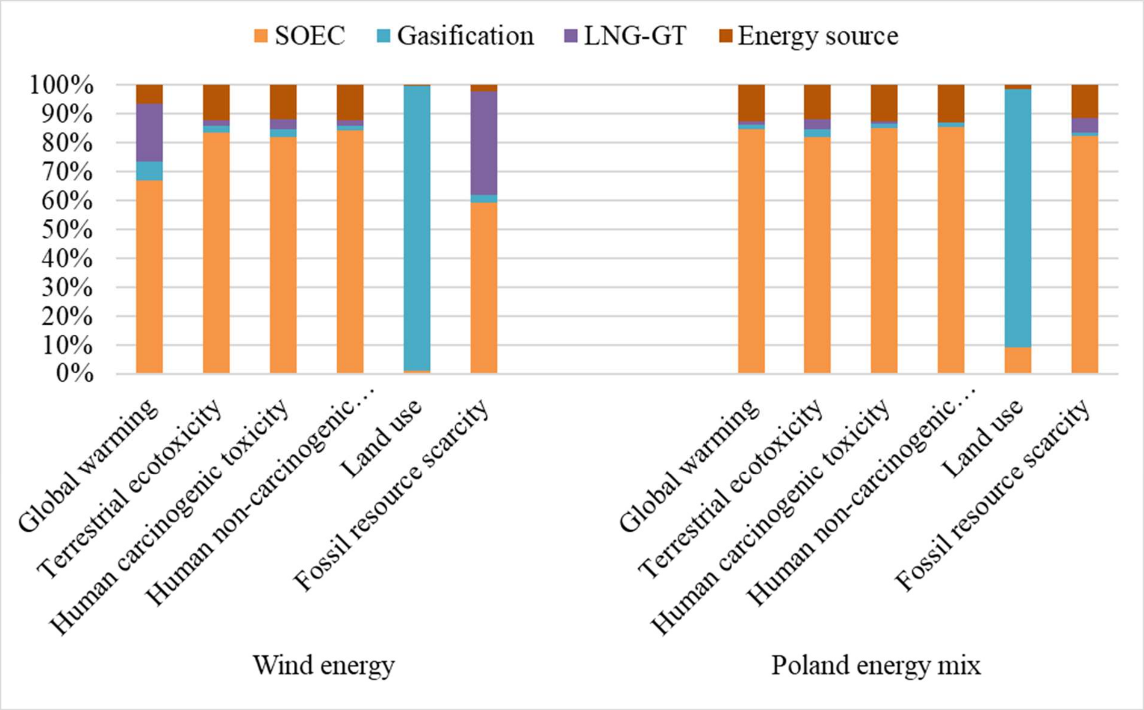

Fig. 9.10. The effect of energy sources on environmental impact categories.

9.5. Summary of biojet fuel production system

This subsection is included to synthesize the SAF case into decision-ready insights. It identifies the dominant levers for hydrogen-enabled, highly electrified SAF. Framing these elements together tests the core hypothesis that coordinated use of H_2, O_2, heat, and power can improve the energy, economics, environmental performance. The summary therefore guides optimization priorities and provides a clear basis for comparing SAF against the methanol and ammonia pathways to select an overall optimal configuration. Main conclusions can be summarized as follows:

- Increasing the SOEC temperature and the inlet CO_2 flow rate increases energy efficiency while reducing specific power demand.
- Most investments are concentrated in electrolyzer (41%) and fuel synthesis (38%), collectively accounting for 79% of the total investment. On the contrary, gasification and gas and power generation require significantly less capital, indicating their lower cost intensity and demands.
- Electricity priced at 0.05 $/kWh shows a break-even scenario, with the levelized cost of fuel matching the selling price at 1.25 $/L, resulting in a payback time of 20 years.
- Using the Polish energy mix results in a payback period of 24 years and a levelized cost of 1.35 $/L. In contrast, when wind turbines are used, the payback period extends to 33 years

with a levelized cost of 1.55 $/L. Therefore, the Polish energy mix is the more economically viable option.

- Wind energy outperforms Poland's electricity mix in most of the environmental indicators. The reductions are substantial, particularly concerning climate change (a 94% reduction) and fossil resource scarcity (an 87% reduction), demonstrating the critical role of renewable energy in achieving carbon neutrality and mitigating environmental degradation.
- The biojet pathway remains strategically important for hard-to-electrify aviation with LCOF of 1893 $/tonne, a GWP of 0.464 kgCO2eq/kgFuel.

10.Comparison of results

This chapter consolidates the results from eight proposed pathways based on renewable energy, biogas-to-methanol (base and improved), biomass-to-methanol (with and without LNG/energy storage systems), power-to-ammonia, biomass-to-ammonia (CO/CC WGS), and biojet fuel via FT synthesis, into a single comparative assessment to identify the best hydrogen-enabled configuration. It benchmarks common KPIs (energy efficiency, levelized costs, and cradle-to-gate LCA indicators). This comparison directly tests the hypotheses that coordinated use of H_2, O_2, heat, and power, together with storage and waste-heat recovery, can deliver superior outcomes. The outcome is a defensible selection of the best system for hydrogen utilization and bio-based fuel/chemical production, plus generalizable design rules to guide optimization.

As presented in Table 10.1, across the biomethanol options, the improved BtM with energy storage (System 4 shown in the Table) is the strongest all-round choice for hydrogen utilization due to heat recovery from CAES/TES energy storage and high fuel production. It achieves the highest energy efficiency at 95.27% and the largest fuel capacity at 8062 kg/h, while also posting the lowest environmental burdens among the BtM routes (GWP = 0.1346 kgCO$_2$-eq/kgFuel, FDP = 0.0254 kgoileq/kgFuel). Its cost, 602.2 \$/tonne, is narrowly above the cheapest case. If minimizing unit cost is the sole criterion, the Improved biogas-based methanol production base integrated with LNG regasification (System 2) is lowest-cost at 574.4 \$/tonne because biogas plants are cheaper than gasification. It has solid efficiency (84%) and mid-range impacts (GWP 0.2059, FDP 0.0415). The gasification variant (System 3) trails on cost (961 \$/tonne) and efficiency (81.96%). Relative to fossil market methanol (1100 \$/tonne, $\eta = 71\%$, GWP 0.908, FDP 0.907), both System 2 and System 4 are decisively superior: System 4 cuts GWP by 85% and FDP by 97% while lifting efficiency by 24.3%, and System 2 remains 48% cheaper than fossil with markedly lower impacts. In the context of the thesis objective, optimizing hydrogen utilization through deep thermal and process integration, System 4 is the preferred design, translating high-temperature SOEC integration and CAES/TES heat recovery into the highest conversion of input H_2 into saleable biomethanol at the lowest environmental cost.

For ammonia production, the improved BtA (system 7) configuration using biomass gasification and counter-current WGS membrane is the best-balanced option. At essentially the same plant capacity (83472 kg/h), it delivers the highest energy efficiency among the green ammonia options (54.64%), the lowest LCOF (513.28 \$/tonne), and the lowest environmental burdens (GWP = 0.175 kgCO$_2$-eq/kgFuel, FDP = 0.046 kgoileq/kgFuel). The PtA route using alkaline electrolysis is weaker on all KPIs, and the Basic BtA (with co-current WGS) lags on both efficiency (51.60%) and cost (562.98 \$/tonne). Against fossil market ammonia, the Improved BtA cuts GWP by 93% and FDP by 95% while also being 46% cheaper on LCOF. In the context of optimizing hydrogen utilization, the counter-current membrane WGS in the improved BtA maximizes H_2 recovery from syngas, translating into the best energy–cost–emission performance among the ammonia options.

For biojet fuel production, the proposed gasifier, SOEC, LNG route is the clear winner across all KPIs and outperforms fossil jet fuel on every axis. It delivers a fuel capacity of 3949 kg/h, the highest energy efficiency (56.21%), the lowest LCOF (1893 \$/tonne) and markedly better environmental metrics, GWP = 0.464 kgCO$_2$eq/kgFuel (50% lower than that of fossil jet fuel) and FDP = 0.3233 kgoileq/kgFuel (73% lower than 1.2 for fossil based). These improvements align directly with the thesis aim of optimizing hydrogen utilization: high-temperature SOEC hydrogen is used to upgrade biogenic syngas in FT synthesis while LNG/GT energy recovery tightens integration, raising conversion efficiency and cutting both cost and life-cycle burdens.

Table. 10.1. Results comparison of all proposed systems for hydrogen utilization.

System	Subsystems	$\dot{m}_F$, kg/h	η, %	LCOF, $/tonne	GWP, kgCO2eq/kgFuel	FDP, kgoileq/kgFuel
-	Biomethanol production					
1-Basic BtM	Anaerobic digestion, biogas upgrading, SOEC, methanol synthesis	366	64.55	633.7	-	-
2- Improved BtM	Anaerobic digestion, biogas upgrading, SOEC, methanol synthesis, LNG-GT	2893	84	574.4	0.2059	0.0415
3- Improved BtM using gasification	Gasifier, SOEC, MeOH, LNG-GT	2061	81.96	961	0.1666	0.0345
4- Improved BtM using energy storage	Gasifier, SOEC, MeOH, LNG-GT, CAES/TES	8062	95.27	602.2	0.1346	0.0254
-	Market MeOH [152], [187], [188]	-	71.00	1100	0.908	0.907
-	Ammonia production					
5- PtA	Air separation, Alkaline electrolyzer, Ammonia synthesis	83399	50.19	540.77	0.772	0.201
6- Basic BtA	Air separation, Biomass gasification, CO-WGS, Ammonia synthesis, CCS	83472	51.60	562.98	-	-
7- Improved BtA	Air separation, Biomass gasification, CC-WGS, Ammonia synthesis, CCS	83472	54.64	513.28	0.175	0.046
-	Market Ammonia [155], [187]	-	66.36 (Exergy based)	950	2.66	0.945
-	Biojet fuel production					
8- Biojet fuel production	Biomass gasification, SOEC, FT synthesis, LNG-GT	3949	56.21	1893	0.464	0.3233
-	Market jet fuel [20], [77], [187]	-	49.9 (for SAF)	2694	0.923	1.2

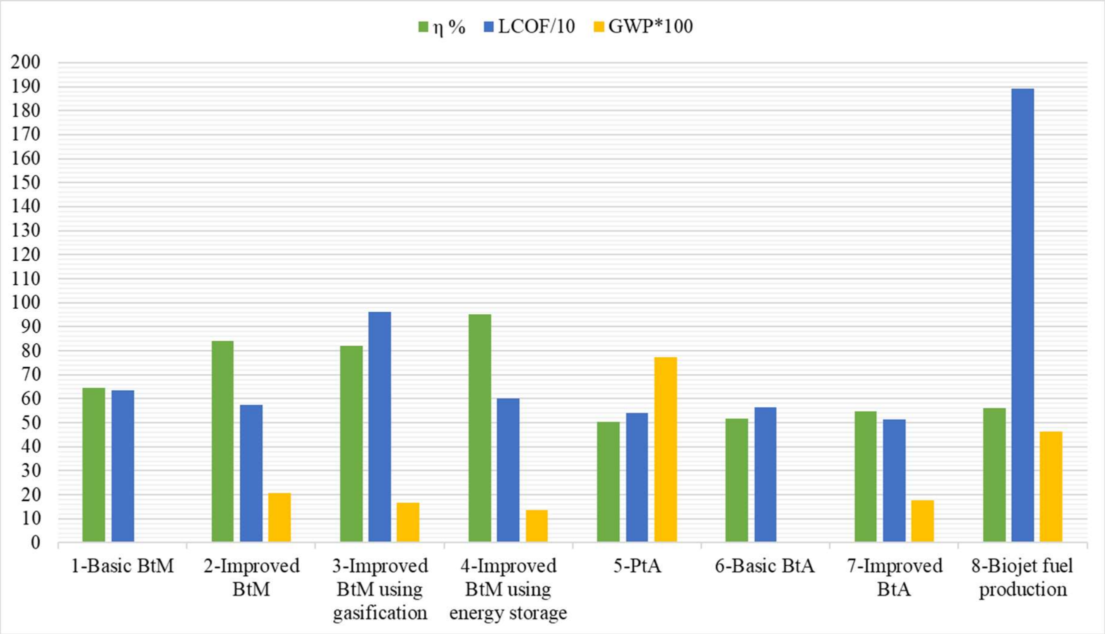

Fig. 10.1. Results comparison of all proposed systems for hydrogen utilization.

The bar chart presented in Fig. 10.1 compacts the same data as Table 10.1 but plots only the three decision KPIs, overall energy efficiency (η), levelized cost of fuel (LCOF divided by 10), and climate impact (GWP, scaled ×100). Three plants stand out as the most optimal configurations for hydrogen utilization. Overall, the comparison recommends leveraging the following subsystems to optimize hydrogen utilization across energy, techno-economic, and life-cycle assessment (LCA) performance:

- Biomass gasification with combined O_2/steam agents
- High-temperature SOEC for maximum efficiency, and low-temperature ALE for cost-effectiveness
- Counter-current water–gas shift (WGS) membrane reactor
- Integrated heat recovery among the LNG–gas turbine (LNG-GT), CAES/TES storage, and fuel-synthesis loops
- Coordinated O_2/CO_2 management across subsystems

11.Conclusions

Hydrogen, treated as a unifying energy carrier and design variable, enables rigorous optimization of polygeneration systems that co-produce liquid and gaseous fuels while balancing efficiency, cost, and environmental performance. This thesis integrates thermodynamic modeling with techno-economic assessment and life-cycle analysis across eight novel routes (biogas-to-methanol, two biomass-to-methanol configurations including LNG heat recovery and energy storage systems, three ammonia scenarios, and biojet fuel production). The result is a coherent framework and a set of generalizable design rules showing how electrolyzer-centric heat, O_2, and H_2 utilization, targeted separations, and strategic co-production reshape plant-level trade-offs and push bio-based fuels toward lower emissions and economic feasibility. Main conclusions of the thesis can be summarized as follows:

- Chemical storage of liquid biofuels is easier and safer than compressed/cryogenic H_2 gas storage.
- High-temperature electrolysis cell (SOEC) enables energy-synergistic heat and power integration, delivers O_2 to displace air separation, and supplies H_2 to produce biomethanol, ammonia, and biojet fuel, collectively lifting system efficiency.
- The ammonia cases highlight that the least-cost PtA with alkaline electrolyzer is not the most energy-efficient, while biomass-to-ammonia with membrane WGS maximizes efficiency.
- Counter-current WGS membrane reactors consistently outperform co-current designs on H_2 recovery and overall efficiency. LNG cold-energy recovery and oxy-fuel gas turbines lower net power demand.
- Cogeneration of biomethanol and natural gas with O_2/CO_2 management shortens payback time and increases robustness to electricity-price volatility compared with single-product plants.
- Electrolyzer and fuel-synthesis units dominate CAPEX. Therefore, electricity price, sourcing, and electrolyzer temperature/current density are first-order determinants of levelized cost across all pathways.
- Raising WGSR conversion, methanol reactor temperature, or SOEC size increases conversion efficiency but can lift power demand or CO2 emissions.
- Wind energy significantly reduces cradle-to-gate GHG emissions and fossil resource depletion relative to the Poland electricity mix. process intensification (oxy-gas turbine with CO_2 injection, LNG cold-energy recovery) further improves footprints and can reduce site water use.
- SOEC is preferred when high-temperature integration is feasible.
- A counter-current WGS membrane reactor is selected for ammonia production.
- LNG cold-energy recovery and oxy-combustion are included when grid relief and flue-gas recycling are priorities.
- Cogeneration of natural gas and biofuels is advantageous under high or volatile electricity prices.
- Renewable energy is chosen when environmental sustainability is prioritized.

- Compressed air and thermal energy storage modules convert transient waste heat into steady biomethanol product, reducing grid variability and efficiency enhancement.
- Design optimization workflow yields decision-ready trade-off maps for efficiency, cost, and emissions based on heat-power integration, electrolyzer placement/sizing, and subsystems coupling with TEA-LCA feedback.
- The improved BtM with CAES/TES is the overall optimum for hydrogen utilization, highest efficiency (95%), competitive cost (602 \$/tonne), and the lowest GWP (0.135 kgCO_2eq/kgFuel), validating the thesis on high-temperature, deeply integrated heat recovery around SOEC, gasification, and LNG.
- For ammonia, the BtA route with counter-current membrane WGS is preferred, acceptable efficiency (54.6%), the lowest cost among all plants (513 \$/tonne), and near-zero GHG intensity (0.175 kgCO_2eq/kgFuel) due to superior H_2/O_2 and N_2 management.
- The biojet pathway remains strategically important for hard-to-electrify aviation (efficiency 56%, cost 1893 \$/tonne, GWP 0.464 kgCO2eq/kgFuel).
- Optimal hydrogen utilization emphasizes O_2/steam gasification, high-temperature SOEC (with ALE as a cost lever), counter-current WGS membranes, integrated heat recovery between LNG–GT and CAES/TES and coordinated O_2/CO_2 utilization across subsystems.
- The Polish energy mix is the more economically viable option than wind turbines. However, wind energy outperforms Poland's electricity mix in most of the environmental indicators. The reductions are substantial, particularly concerning climate change and fossil resource scarcity, demonstrating the critical role of renewable energy in achieving carbon neutrality and mitigating environmental degradation.

Appendix: Main assumptions for all subsystems

Table A.1. Input data for modeling alkaline electrolysis cells [84].

Parameter	Value	Unit
Operating pressure	1	bar
Operating temperature	50-80	℃
Current density	0.1-0.5	A/cm2
Heat loss	10	%

Table A.2. Assumptions of the SOEC subsystem

Parameter	Value	Ref.
Water consumption for (biomethanol production)	260 kg/h	[189]
Water consumption for (biojet fuel production)	2500 kg/h	
Split fractions of stream 45 and 50	10% and 90%	[29]
Stack temperature	750 ℃	[87]
Outlet temperature of H_2, FG, and syngas coolers	80 ℃	[87]
Faraday's constant, F	96487 ℃/mol	[190]
Anode effective diffusion, $D_{\mathrm{a}}^{\mathrm{eff}}$	$2\cdot10^{-5}$ m^2/s	[88]
Cathode effective diffusion, $D_{\mathrm{c}}^{\mathrm{eff}}$	$5.11\cdot10^{-5}$ m^2/s	[88]
Anode activation energy, $E_{\mathrm{a}}^{\mathrm{act}}$	120 000 J/mol	[88]
Cathode activation energy, $E_{\mathrm{c}}^{\mathrm{act}}$	100 000 J/mol	[88]
Anode pre-exponential factor, γ_{a}	2.05 A/m^2	[91]
Cathode pre-exponential factor, γ_{c}	1.34 A/m^2	[91]
Anode thickness, δ_{a}	$1.75\cdot10^{-5}$ m	[88]
Cathode thickness, δ_{c}	$3.13\cdot10^{-4}$ m	[88]
Electrolyte thickness, δ_{e}	$1.25\cdot10^{-5}$ m	[88]
The ideal gases constant, R	8.314 J/mol/K	[191]
Current density, J	10 000 A/m^2	[192]
Cell active area, A_{cell}	0.324 m^2	[87]

Table A.3. Elemental analysis of the organic component in sewage sludge [92].

Component	Value
H	4.89%
C	35.65%
N	5.16%
O	21.72%
S	2.97%
LHV	5000 kJ/kg

Table A.4. Input data used to model the anaerobic digestion unit.

Parameter	Value	Ref.

Type of digestion	Thermophilic	[92]
The thermal pretreatment tank's outlet temperature	90 °C, 30 minutes	[92]
Digester's output temperature	55 °C	[92]
Temperature of sewage sludge	18 °C	[92]
Methane content	63.35%	[92]
Number of digesters	4	[92]
Digester volume	3000 m^3	[92]
Percentage of volatile solid and ash	70.39% and 29.61%	[92]
Mass flow rate of biomass	8.6 kg/s	[92]
Anaerobic biodegradability	0.48309	[92]
Biogas potential	0.3648	[92]

Table A.5. Assumptions of the biogas upgrading unit.

Parameter	Value	Ref.
Discharge pressure of biogas compressor 1 and 2	3.16 and 10 bar	[193]
Outlet temperature of biogas cooler 1 and 2	50 and 20 °C	[193]
The absorber and stripper's number	8 and 10	[193]
Dimensions of absorber and stripper packing	38 and 50 mm	[193]
Absorber and stripper height	5.8 and 4.8 m	[193]
The absorber and stripper's diameter	0.77 and 1 m	[193]
Air flow rate	1287 kg/h	[193]
Air compressor discharge pressure of air compressor	1.16 bar	[193]
Water pump discharge pressure	10 bars	[193]
Calculation	Rate based, NRTL	[193]

Table A.6. Ultimate analysis of biomass utilized in the proposed systems [101]

Component	Input biomass (%)	Decomposition yield Mass basis (%)
C	49.02	10
O_2	22.28	30
Ash	18.5	0
H_2	6.38	20
Cl_2	2.37	10
N_2	1.11	20
S	0.34	10
LHV	18010 (kJ/kg)	-

Table A.7. Input data used to model biomass gasification subsystem.

Parameter	Value	Ref.
Biomass gasification unit		

Biomass flow rate for (biomethanol production)	122.7 kg/h	[101]
Biomass flow rate for (biojet fuel production)	1500 kg/h	[194]
Input steam for (biomethanol production)	88.57 kg/h	[101]
Input steam for (biomethanol production with CAES)	130 kg/h	[101]
Discharge pressure of the water pump	20 bars	[101]
O_2 entering the gasification unit	70.86 kg/h	[101]
Split fraction of streams 7 and 21	50%	[101]
Temperature of O_2 leaving the cooler 1 and 2	250 °C	[101]
Discharge pressure of O_2 compressor	10 bars	[101]
Temperature of water leaving the cooler	40 °C	[101]
Split fraction of O_2 entering the combustor, water separator, and gasifier	86.8%, 7.11%, and 6.09%	[101]
The split fraction of carbon entering the combustor, gasifier, and pyrolysis	79.91%, 0.11%, and 19.98%	[101]
Split fraction of stream 26, 27, and 28	42.43%, 10%, and 47.57%	[101]
Split fractions of stream 29, 32, and 33	25.22%, 18.26%, and 56.52%	[101]
Split fractions of stream 30 and 31	21.82% and 78.18%	[101]
Temperature of gases leaving the cooler 1 and 2	400 °C and 180 °C	[101]
O_2 equivalence ratio	0.1-0.3	[97]
Steam to biomass ratio	0.2-0.8	[195]
Oxygen to biomass ratio	0.57	

Table A.8. Assumptions of the ammonia synthesis unit [84].

Parameter	Value	Unit
Reactor inlet temperature	400	℃
Reactor pressure	200	bar
Ammonia purity	0.999	mol/mol

Table A.9. Assumptions of the methanol synthesis unit.

Parameter	Value	Ref.
Pressure of gases entering the MSU	51 bars	[196]
The outlet temperature of the coolers between 4SCP of H_2 and FG	157 °C	[102]
The outlet temperature of the coolers between 4SCP of syngas	125.6 °C	[102]
Pressure Drop in heat exchangers in the MSU	1 bar	[102]
Inlet and outlet temperature of methanol reactor	210 and 278 °C	[196]
Inlet temperature of the distillation column	80 °C	[102]
Inlet temperature of drum	35 °C	[102]
Outlet temperature and pressure of the valve	32 °C and 1.2 bar	[102]
Number of stages in the distillation column	20	[196]

Pressure of the partial condenser and reboiler	1 bar	[197]
Temperature of Methanol and water leaving their coolers	40 ℃	[102]
Outlet pressure of methanol compressor	1.2 bar	[102]
Isentropic Efficiency of the methanol and gas compressors	0.85	[198]
Split fraction of exhaust gases from stream 79	1.01%	[102]

Table A.10. Input data to model LNG and gas turbine systems.

Parameter	Value	Ref.
Temperature and pressure of input LNG	-162 ℃ and 1.2 bar	[199]
Mass flow of input LNG (biomass-to-methanol)	2000 kg/h	[200]
Mass flow of input LNG (biomass-to-methanol with CAES)	8000 kg/h	Assumed
Mass flow of input LNG (biogas-to-methanol)	2600 kg/h	[200]
Mass flow of input LNG (biojet fuel production)	3000 kg/h	[194]
Isentropic efficiency of the LNG pump	0.7	[201]
Outlet pressure of the LNG pump	103 bars	[200]
Outlet pressure of the NG turbine	20 bars	[200]
Isentropic efficiency of the NG turbine	0.87	[202]
Open Brayton cycle		
Split fraction of produced natural gas	0.85	[183]
Outlet temperature and pressure of the combustor	1160 ℃ and 35 bar	[183]
Isentropic efficiency of the NG compressor	0.88	[99]
Temperature and pressure of utilized CO_2	-55 ℃ and 7 bar	[183]
Mass flow of input CO_2 (biomethanol production)	401 kg/h	[183]
Mass flow of input CO_2 (biojet fuel production)	800 kg/h	[194]
Isentropic efficiency of the CO_2 pump	0.8	[203]
The outlet temperature of the coolers between 4SCP of O_2	750 ℃	[189]
Outlet pressure of the gas turbine	1.7 bar	[183]

Table A.11. Assumptions of the WGSR.

Parameter	Value	Ref.
Mass flow rate and temperature of the input water	50 kg/h and 25 ℃	[204]
H_2O conversion in the WGSR	52.5%	[204]
Operating temperature (feed/sweep)	450 and 150 ℃	[104]
Operating pressure (feed/sweep)	20 and 1 bar	[205]
Steam to carbon ratio	2.5	[205]
Sweep-to-feed ratio	0.15	Assumed
Number of membrane tubes per reactor	110	Assumed
Number of reactors	1800-2000	Assumed

Table A.12 Operating conditions of the air separation unit.

Parameter	Value	Unit	Ref.
Operating pressure	1	atm	[67]
Oxygen purity	0.995	mol/mol	
Energy consumption	160	kWh/tonne O_2	

Table A.13. Assumptions of the energy storage subsystems.

Parameter	Value	Ref.
Compressed air energy storage (CAES)		
Temperature after 2nd stage of compressor	400 °C	[108]
Charging/Storage/Discharging stage	8/12/4 hours	[108]
Working fluid	Air	[108]
Nominal isentropic efficiency of compressor sections	88%	[108]
Electromechanical efficiency of compressor	98%	[108]
Nominal isentropic efficiency of expander	90%	[108]
Electromechanical efficiency of expander	98%	[108]
Minimum reservoir pressure	5.6 MPa	[108]
Maximum reservoir pressure	8.0 MPa	[108]
Air reservoir volume	63 000 m^3	[108]
Air temperature in reservoir	30 °C	[108]
Packed bed particle diameter	16 mm	[108]
Thermal energy storage (TES)		
Working fluid	Therminol 59	[206]
Inlet temperature of the cold storage tank	-46°C	[206]
Pressure ratio of pump	4	[206]

Table A.14. Specifications of distillation columns [118].

Distillation column	Reflux ratio	Light key component	Light recovery	Heavy key component	Heavy recovery
DSTWU 1	-1.4	C_4H_{10}	0.95	C_6H_{14}	0.04
DSTWU 2	-1.4	$C_{16}H_{34}$	0.90	$C_{17}H_{36}$	0.10
DSTWU 3	-1.4	C_4H_{10}	0.95	C_6H_{14}	0.04
DSTWU 4	-1.4	$C_{16}H_{34}$	0.90	$C_{17}H_{36}$	0.10

Table A.15 Data set applied in system modeling of biojet fuel production [118], [129]

Parameter	Value
Split fraction of hydrogen entering the hydrocracking reactor	0.1
The pressure of inlet gases	1 bar
The temperature of the shift reactor	800 °C
Pressure and temperature of the Fischer-Tropsch reactor	185 °C and 20 bar
Temperature of 3-phase separator	35 °C

Temperature of distillation columns	90 °C
Temperature and pressure of the hydrocracking reactor	319 °C and 3.5 bar
Flash temperature	20 °C
Temperature and pressure of the products	20 °C and 1 bar
Catalyst	Cobalt
Conversion of CO	0.9
The molar ratio of H_2 to CO	2
Equation of state	PRMHV2

References

[1] "Shedding light on energy in Europe – 2025 edition - Interactive publications - Eurostat." Accessed: Aug. 28, 2025. [Online]. Available: https://ec.europa.eu/eurostat/web/interactive-publications/energy-2025?utm_source=chatgpt.com#energy-sources

[2] "About the EU ETS - European Commission." Accessed: Aug. 28, 2025. [Online]. Available: https://climate.ec.europa.eu/eu-action/carbon-markets/eu-emissions-trading-system-eu-ets/about-eu-ets_en?utm_source=chatgpt.com

[3] "How Does Anaerobic Digestion Work? | US EPA." Accessed: Aug. 29, 2025. [Online]. Available: https://www.epa.gov/agstar/how-does-anaerobic-digestion-work

[4] A. AlNouss, G. McKay, and T. Al-Ansari, "Enhancing waste to hydrogen production through biomass feedstock blending: A techno-economic-environmental evaluation," *Appl Energy*, vol. 266, p. 114885, May 2020, doi: 10.1016/J.APENERGY.2020.114885.

[5] "Gasification Solutions." Accessed: Sep. 14, 2025. [Online]. Available: https://gasification.tumblr.com/

[6] N. Johnson, M. Liebreich, D. M. Kammen, P. Ekins, R. McKenna, and I. Staffell, "Realistic roles for hydrogen in the future energy transition," *Nature Reviews Clean Technology 2025 1:5*, vol. 1, no. 5, pp. 351–371, Apr. 2025, doi: 10.1038/s44359-025-00050-4.

[7] T. International Renewable Energy Agency, "GREEN HYDROGEN COST REDUCTION SCALING UP ELECTROLYSERS TO MEET THE 1.5°C CLIMATE GOAL H 2 O 2," 2020.

[8] A. Buttler and H. Spliethoff, "Current status of water electrolysis for energy storage, grid balancing and sector coupling via power-to-gas and power-to-liquids: A review," *Renewable and Sustainable Energy Reviews*, vol. 82, pp. 2440–2454, Feb. 2018, doi: 10.1016/J.RSER.2017.09.003.

[9] J. Milewski, M. Wołowicz, and J. Lewandowski, "Comparison of SOE/SOFC system configurations for a peak hydrogen power plant," *Int J Hydrogen Energy*, vol. 42, no. 5, pp. 3498–3509, 2017, doi: https://doi.org/10.1016/j.ijhydene.2016.08.067.

[10] M. Ni, M. K. H. Leung, and D. Y. C. Leung, "Technological development of hydrogen production by solid oxide electrolyzer cell (SOEC)," *Int J Hydrogen Energy*, vol. 33, no. 9, pp. 2337–2354, 2008, doi: https://doi.org/10.1016/j.ijhydene.2008.02.048.

[11] J. Milewski, J. Kupecki, A. Szczęśniak, and N. Uzunow, "Hydrogen production in solid oxide electrolyzers coupled with nuclear reactors," *Int J Hydrogen Energy*, vol. 46, no. 72, pp. 35765–35776, 2021, doi: https://doi.org/10.1016/j.ijhydene.2020.11.217.

[12] G. Schiller *et al.*, "Solar heat integrated solid oxide steam electrolysis for highly efficient hydrogen production," *J Power Sources*, vol. 416, pp. 72–78, 2019, doi: https://doi.org/10.1016/j.jpowsour.2019.01.059.

[13] L. A. Jolaoso, J. Asadi, C. Duan, and P. Kazempoor, "A novel green hydrogen production using water-energy nexus framework," *Energy Convers Manag*, vol. 276, Jan. 2023, doi: 10.1016/j.enconman.2022.116344.

[14] "Guide to Safety of Hydrogen and Hydrogen Systems (ANSI/AIAA G-095A-2017)," *Guide to Safety of Hydrogen and Hydrogen Systems (ANSI/AIAA G-095A-2017)*, Jan. 2017, doi: 10.2514/4.105197.

[15] "Safety, Codes and Standards | Department of Energy." Accessed: Aug. 29, 2025. [Online]. Available: https://www.energy.gov/eere/fuelcells/safety-codes-and-standards

[16] I. - International Energy Agency, "Global Hydrogen Review 2023," 2023, Accessed: Aug. 29, 2025. [Online]. Available: www.iea.org

[17] D. Katla-Milewska, S. M. Nazir, and A. Skorek-Osikowska, "Synthetic natural gas (SNG) production with higher carbon recovery from biomass: Techno-economic assessment," *Energy Convers Manag*, vol. 300, p. 117895, Jan. 2024, doi: 10.1016/J.ENCONMAN.2023.117895.

[18] T. N. Do and J. Kim, "Process development and techno-economic evaluation of methanol production by direct CO2 hydrogenation using solar-thermal energy," *Journal of CO2 Utilization*, vol. 33, pp. 461–472, Oct. 2019, doi: 10.1016/j.jcou.2019.07.003.

[19] H. Ishaq and I. Dincer, "Investigation and optimization of a new hybrid natural gas reforming system for cascaded hydrogen, ammonia and methanol synthesis," *Comput Chem Eng*, vol. 148, p. 107234, May 2021, doi: 10.1016/J.COMPCHEMENG.2021.107234.

[20] M. Dossow, V. Dieterich, A. Hanel, H. Spliethoff, and S. Fendt, "Improving carbon efficiency for an advanced Biomass-to-Liquid process using hydrogen and oxygen from electrolysis," *Renewable and Sustainable Energy Reviews*, vol. 152, Dec. 2021, doi: 10.1016/j.rser.2021.111670.

[21] C. Su, H. Wei, Z. Wang, H. Ayed, A. Mouldi, and A. A. Shayesteh, "Economic accounting and high-tech strategy for sustainable production: A case study of methanol production from CO2 hydrogenation," *Int J Hydrogen Energy*, vol. 47, no. 62, pp. 25929–25944, Jul. 2022, doi: 10.1016/j.ijhydene.2022.01.124.

[22] E. Moioli, A. Wötzel, and T. Schildhauer, "Feasibility assessment of small-scale methanol production via power-to-X," *J Clean Prod*, vol. 359, Jul. 2022, doi: 10.1016/j.jclepro.2022.132071.

[23] "How can biogenic CO2 be used to address the climate crisis? | World Economic Forum." Accessed: Dec. 18, 2024. [Online]. Available: https://www.weforum.org/stories/2023/10/biogenic-co2-climate-green-hydrogen/?utm_source=chatgpt.com

[24] B. Hernández, E. León, and M. Martín, "Bio-waste selection and blending for the optimal production of power and fuels via anaerobic digestion," *Chemical Engineering Research and Design*, vol. 121, pp. 163–172, 2017, doi: 10.1016/j.cherd.2017.03.009.

[25] Y. K. Nugroho, L. Zhu, and C. Heavey, "Building an agent-based techno-economic assessment coupled with life cycle assessment of biomass to methanol supply chains," *Appl Energy*, vol. 309, Mar. 2022, doi: 10.1016/j.apenergy.2021.118449.

[26] R. Rinaldi, G. Lombardelli, M. Gatti, C. G. Visconti, and M. C. Romano, "Techno-economic analysis of a biogas-to-methanol process: Study of different process configurations and conditions," *J Clean Prod*, vol. 393, Mar. 2023, doi: 10.1016/j.jclepro.2023.136259.

[27] M. Fedeli and F. Manenti, “Assessing process effectiveness with specific environmental and economic impact of heat, power & chemicals (HPC) option as future perspective in biogas,” *Cleaner Chemical Engineering*, vol. 2, p. 100016, Jun. 2022, doi: 10.1016/j.clce.2022.100016.

[28] R. Rivera-Tinoco *et al.*, “Investigation of power-to-methanol processes coupling electrolytic hydrogen production and catalytic CO2 reduction,” *Int J Hydrogen Energy*, vol. 41, no. 8, pp. 4546–4559, Mar. 2016, doi: 10.1016/j.ijhydene.2016.01.059.

[29] F. Lonis, V. Tola, and G. Cau, “Renewable methanol production and use through reversible solid oxide cells and recycled CO2 hydrogenation,” *Fuel*, vol. 246, pp. 500–515, Jun. 2019, doi: 10.1016/j.fuel.2019.02.108.

[30] Q. Chen, Y. Gu, Z. Tang, and Y. Sun, “Comparative environmental and economic performance of solar energy integrated methanol production systems in China,” *Energy Convers Manag*, vol. 187, pp. 63–75, May 2019, doi: 10.1016/j.enconman.2019.03.013.

[31] L. Wang *et al.*, “Power-to-fuels via solid-oxide electrolyzer: Operating window and techno-economics,” *Renewable and Sustainable Energy Reviews*, vol. 110, pp. 174–187, Aug. 2019, doi: 10.1016/j.rser.2019.04.071.

[32] S. Ali, K. Sørensen, and M. P. Nielsen, “Modeling a novel combined solid oxide electrolysis cell (SOEC) - Biomass gasification renewable methanol production system,” *Renew Energy*, vol. 154, pp. 1025–1034, Jul. 2020, doi: 10.1016/j.renene.2019.12.108.

[33] H. Zhang and U. Desideri, “Techno-economic optimization of power-to-methanol with co-electrolysis of CO2 and H2O in solid-oxide electrolyzers,” *Energy*, vol. 199, p. 117498, 2020, doi: https://doi.org/10.1016/j.energy.2020.117498.

[34] M. J. Bos, S. R. A. Kersten, and D. W. F. Brilman, “Wind power to methanol: Renewable methanol production using electricity, electrolysis of water and CO2 air capture,” *Appl Energy*, vol. 264, Apr. 2020, doi: 10.1016/j.apenergy.2020.114672.

[35] K. Im-orb, A. N. Phan, and A. Arpornwichanop, “Bio-methanol production from oil palm residues: A thermodynamic analysis,” *Energy Convers Manag*, vol. 226, Dec. 2020, doi: 10.1016/j.enconman.2020.113493.

[36] H. Ishaq and I. Dincer, “Evaluation of a wind energy based system for co-generation of hydrogen and methanol production,” *Int J Hydrogen Energy*, vol. 45, no. 32, pp. 15869–15877, Jun. 2020, doi: 10.1016/j.ijhydene.2020.01.037.

[37] N. Monnerie, P. G. Gan, M. Roeb, and C. Sattler, “Methanol production using hydrogen from concentrated solar energy,” *Int J Hydrogen Energy*, vol. 45, no. 49, pp. 26117–26125, Oct. 2020, doi: 10.1016/j.ijhydene.2019.12.200.

[38] Z. Qin, Y. Tang, Z. Zhang, and X. Ma, “Techno-economic-environmental analysis of coal-based methanol and power poly-generation system integrated with biomass co-gasification and solar based hydrogen addition,” *Energy Convers Manag*, vol. 228, Jan. 2021, doi: 10.1016/j.enconman.2020.113646.

[39] M. Ostadi, L. Bromberg, D. R. Cohn, and E. Gençer, “Flexible methanol production process using biomass/municipal solid waste and hydrogen produced by electrolysis and natural gas pyrolysis,” *Fuel*, vol. 334, p. 126697, 2023, doi: https://doi.org/10.1016/j.fuel.2022.126697.

[40] G. Cinti, A. Baldinelli, A. Di Michele, and U. Desideri, “Integration of Solid Oxide Electrolyzer and Fischer-Tropsch: A sustainable pathway for synthetic fuel,” *Appl Energy*, vol. 162, pp. 308–320, 2016, doi: https://doi.org/10.1016/j.apenergy.2015.10.053.

[41] J. Kotowicz, M. Jurczyk, and D. Węcel, “The possibilities of cooperation between a hydrogen generator and a wind farm,” *Int J Hydrogen Energy*, vol. 46, no. 10, pp. 7047–7059, 2021, doi: https://doi.org/10.1016/j.ijhydene.2020.11.246.

[42] D. Węcel, M. Jurczyk, W. Uchman, and A. Skorek-Osikowska, “Investigation on System for Renewable Electricity Storage in Small Scale Integrating Photovoltaics, Batteries, and Hydrogen Generator,” *Energies (Basel)*, vol. 13, no. 22, 2020, doi: 10.3390/en13226039.

[43] J. Kupecki *et al.*, “Energy analysis of a 10 kW-class power-to-gas system based on a solid oxide electrolyzer (SOE),” *Energy Convers Manag*, vol. 199, p. 111934, 2019, doi: https://doi.org/10.1016/j.enconman.2019.111934.

[44] P. Ran, Y. Wang, Y. Wang, Z. Li, and P. Zhang, “Thermodynamic, economic and environmental investigations of a novel solar heat enhancing compressed air energy storage hybrid system and its energy release strategies,” *J Energy Storage*, vol. 55, p. 105423, 2022, doi: https://doi.org/10.1016/j.est.2022.105423.

[45] T. Kowalczyk, “Comparative analysis of hybrid energy storage based on a gas–gas system and a conventional compressed air energy storage based on a recuperated gas turbine round trip efficiency, exergy losses, and heat exchanges start-up losses,” *Energy Convers Manag*, vol. 258, p. 115467, 2022, doi: https://doi.org/10.1016/j.enconman.2022.115467.

[46] A. Zheng, Z. Cao, Y. Xu, H. Chen, and J. Deng, “Analysis of hybrid Adiabatic Compressed Air Energy Storage - Reverse Osmosis desalination system with different topological structures,” *Desalination*, vol. 530, p. 115667, 2022, doi: https://doi.org/10.1016/j.desal.2022.115667.

[47] S. Wu, C. Zhou, E. Doroodchi, and B. Moghtaderi, “Thermodynamic analysis of a novel hybrid thermochemical-compressed air energy storage system powered by wind, solar and/or off-peak electricity,” *Energy Convers Manag*, vol. 180, pp. 1268–1280, 2019, doi: https://doi.org/10.1016/j.enconman.2018.11.063.

[48] S. Houssainy, M. Janbozorgi, P. Ip, and P. Kavehpour, “Thermodynamic analysis of a high temperature hybrid compressed air energy storage (HTH-CAES) system,” *Renew Energy*, vol. 115, pp. 1043–1054, 2018, doi: https://doi.org/10.1016/j.renene.2017.09.038.

[49] Ł. Bartela, “A hybrid energy storage system using compressed air and hydrogen as the energy carrier,” *Energy*, vol. 196, p. 117088, 2020, doi: https://doi.org/10.1016/j.energy.2020.117088.

[50] X. Liu, A. Elgowainy, and M. Wang, “Life cycle energy use and greenhouse gas emissions of ammonia production from renewable resources and industrial by-products,” *Green Chemistry*, vol. 22, no. 17, pp. 5751–5761, Aug. 2020, doi: 10.1039/D0GC02301A.

[51] “Argus Ammonia Daily,” 2025, Accessed: Aug. 31, 2025. [Online]. Available: https://www.argusmedia.com/en/privacy-policy

[52] R. M. Nayak-Luke and R. Bañares-Alcántara, “Long-Term Energy Storage: What is the Need and is Ammonia a Solution?,” in *13th International Symposium on Process Systems Engineering (PSE 2018)*, vol. 44, M. R. Eden, M. G. Ierapetritou, and G. P. Towler, Eds., in Computer Aided

Chemical Engineering, vol. 44. , Elsevier, 2018, pp. 1843–1848. doi: https://doi.org/10.1016/B978-0-444-64241-7.50302-5.

[53] A. Shokri Kalan, S. Heidarabadi, M. Khaleghi, H. Ghiasirad, and A. Skorek-Osikowska, “Biomass-to-energy integrated trigeneration system using supercritical CO2 and modified Kalina cycles: Energy and exergy analysis,” *Energy*, vol. 270, p. 126845, May 2023, doi: 10.1016/J.ENERGY.2023.126845.

[54] B. Aljafari, S. Alqaed, J. Mustafa, F. A. Almehmadi, and M. Sharifpur, “Energy-Economic-Environmental (3E) modeling of a near-zero energy community using the solar-power system: A case study of Najran city,” *J Taiwan Inst Chem Eng*, vol. 148, p. 104685, 2023, doi: https://doi.org/10.1016/j.jtice.2023.104685.

[55] G. Puig-Samper, E. Bargiacchi, D. Iribarren, and J. Dufour, “Life-cycle assessment of hydrogen systems: A systematic review and meta-regression analysis,” *J Clean Prod*, vol. 470, p. 143330, Sep. 2024, doi: 10.1016/J.JCLEPRO.2024.143330.

[56] J. R. Gomez, J. Baca, and F. Garzon, “Techno-economic analysis and life cycle assessment for electrochemical ammonia production using proton conducting membrane,” *Int J Hydrogen Energy*, vol. 45, no. 1, pp. 721–737, 2020, doi: https://doi.org/10.1016/j.ijhydene.2019.10.174.

[57] L. Lin, Y. Tian, W. Su, Y. Luo, C. Chen, and L. Jiang, “Techno-economic analysis and comprehensive optimization of an on-site hydrogen refuelling station system using ammonia: hybrid hydrogen purification with both high H2 purity and high recovery,” *Sustainable Energy Fuels*, vol. 4, no. 6, pp. 3006–3017, 2020, doi: 10.1039/C9SE01111K.

[58] M. J. Palys and P. Daoutidis, “Using hydrogen and ammonia for renewable energy storage: A geographically comprehensive techno-economic study,” *Comput Chem Eng*, vol. 136, p. 106785, 2020, doi: https://doi.org/10.1016/j.compchemeng.2020.106785.

[59] R. M. Nayak-Luke and R. Bañares-Alcántara, “Techno-economic viability of islanded green ammonia as a carbon-free energy vector and as a substitute for conventional production,” *Energy Environ. Sci.*, vol. 13, no. 9, pp. 2957–2966, 2020, doi: 10.1039/D0EE01707H.

[60] Z. Cesaro, M. Ives, R. Nayak-Luke, M. Mason, and R. Bañares-Alcántara, “Ammonia to power: Forecasting the levelized cost of electricity from green ammonia in large-scale power plants,” *Appl Energy*, vol. 282, p. 116009, 2021, doi: https://doi.org/10.1016/j.apenergy.2020.116009.

[61] B. Lee, D. Lim, H. Lee, and H. Lim, “Which water electrolysis technology is appropriate?: Critical insights of potential water electrolysis for green ammonia production,” *Renewable and Sustainable Energy Reviews*, vol. 143, p. 110963, 2021, doi: https://doi.org/10.1016/j.rser.2021.110963.

[62] M. Qi *et al.*, “Proposal and surrogate-based cost-optimal design of an innovative green ammonia and electricity co-production system via liquid air energy storage,” *Appl Energy*, vol. 314, p. 118965, 2022, doi: https://doi.org/10.1016/j.apenergy.2022.118965.

[63] H. Zhao, L. M. Kamp, and Z. Lukszo, “The potential of green ammonia production to reduce renewable power curtailment and encourage the energy transition in China,” *Int J Hydrogen Energy*, vol. 47, no. 44, pp. 18935–18954, 2022, doi: https://doi.org/10.1016/j.ijhydene.2022.04.088.

[64] M. Fasihi, R. Weiss, J. Savolainen, and C. Breyer, “Global potential of green ammonia based on hybrid PV-wind power plants,” *Appl Energy*, vol. 294, p. 116170, 2021, doi: https://doi.org/10.1016/j.apenergy.2020.116170.

[65] N. Campion, H. Nami, P. R. Swisher, P. Vang Hendriksen, and M. Münster, “Techno-economic assessment of green ammonia production with different wind and solar potentials,” *Renewable and Sustainable Energy Reviews*, vol. 173, p. 113057, 2023, doi: https://doi.org/10.1016/j.rser.2022.113057.

[66] C. Wang, S. D. C. Walsh, T. Longden, G. Palmer, I. Lutalo, and R. Dargaville, “Optimising renewable generation configurations of off-grid green ammonia production systems considering Haber-Bosch flexibility,” *Energy Convers Manag*, vol. 280, p. 116790, 2023, doi: https://doi.org/10.1016/j.enconman.2023.116790.

[67] H. Zhang, L. Wang, J. Van herle, F. Maréchal, and U. Desideri, “Techno-economic comparison of green ammonia production processes,” *Appl Energy*, vol. 259, p. 114135, 2020, doi: https://doi.org/10.1016/j.apenergy.2019.114135.

[68] J. Andersson and J. Lundgren, “Techno-economic analysis of ammonia production via integrated biomass gasification,” *Appl Energy*, vol. 130, pp. 484–490, 2014, doi: https://doi.org/10.1016/j.apenergy.2014.02.029.

[69] M. Akbari, A. O. Oyedun, and A. Kumar, “Ammonia production from black liquor gasification and co-gasification with pulp and waste sludges: A techno-economic assessment,” *Energy*, vol. 151, pp. 133–143, 2018, doi: https://doi.org/10.1016/j.energy.2018.03.056.

[70] J. S. Cardoso, V. Silva, J. A. M. Chavando, D. Eusébio, M. J. Hall, and M. Costa, “Small-Scale Biomass Gasification for Green Ammonia Production in Portugal: A Techno-Economic Study,” *Energy & Fuels*, vol. 35, no. 17, pp. 13847–13862, 2021, doi: 10.1021/acs.energyfuels.1c01928.

[71] D. Wen and M. Aziz, “Design and analysis of biomass-to-ammonia-to-power as an energy storage method in a renewable multi-generation system,” *Energy Convers Manag*, vol. 261, p. 115611, 2022, doi: https://doi.org/10.1016/j.enconman.2022.115611.

[72] D. Wen and M. Aziz, “Techno-economic analyses of power-to-ammonia-to-power and biomass-to-ammonia-to-power pathways for carbon neutrality scenario,” *Appl Energy*, vol. 319, p. 119272, 2022, doi: https://doi.org/10.1016/j.apenergy.2022.119272.

[73] T. J. Skone *et al.*, “Comprehensive Analysis of Coal and Biomass Conversion to Jet Fuel: Oxygen Blown, Transport Reactor Integrated Gasifier (TRIG) and Fischer-Tropsch (F-T) Catalyst Configurations,” Feb. 2014, doi: 10.2172/1515253.

[74] M. Rafati, L. Wang, D. C. Dayton, K. Schimmel, V. Kabadi, and A. Shahbazi, “Techno-economic analysis of production of Fischer-Tropsch liquids via biomass gasification: The effects of Fischer-Tropsch catalysts and natural gas co-feeding,” *Energy Convers Manag*, vol. 133, pp. 153–166, Feb. 2017, doi: 10.1016/j.enconman.2016.11.051.

[75] L. J. F. Comidy, M. D. Staples, and S. R. H. Barrett, “Technical, economic, and environmental assessment of liquid fuel production on aircraft carriers,” *Appl Energy*, vol. 256, Dec. 2019, doi: 10.1016/j.apenergy.2019.113810.

[76] H. Real Guimarães *et al.*, “Bottlenecks and potentials for the gasification of lignocellulosic biomasses and Fischer-Tropsch synthesis: A case study on the production of advanced liquid biofuels in Brazil,” *Energy Convers Manag*, vol. 245, Oct. 2021, doi: 10.1016/j.enconman.2021.114629.

[77] M. Hillestad *et al.*, “Improving carbon efficiency and profitability of the biomass to liquid process with hydrogen from renewable power,” *Fuel*, vol. 234, pp. 1431–1451, Dec. 2018, doi: 10.1016/j.fuel.2018.08.004.

[78] G. Cinti, A. Baldinelli, A. Di Michele, and U. Desideri, “Integration of Solid Oxide Electrolyzer and Fischer-Tropsch: A sustainable pathway for synthetic fuel,” *Appl Energy*, vol. 162, pp. 308–320, Jan. 2016, doi: 10.1016/j.apenergy.2015.10.053.

[79] U. Lee, H. Cai, L. Ou, P. T. Benavides, Y. Wang, and M. Wang, “Life cycle analysis of gasification and Fischer-Tropsch conversion of municipal solid waste for transportation fuel production,” *J Clean Prod*, vol. 382, Jan. 2023, doi: 10.1016/j.jclepro.2022.135114.

[80] A. Almena, R. Siu, K. Chong, P. Thornley, and M. Röder, “Reducing the environmental impact of international aviation through sustainable aviation fuel with integrated carbon capture and storage,” *Energy Convers Manag*, vol. 303, Mar. 2024, doi: 10.1016/j.enconman.2024.118186.

[81] M. Fernanda Rojas Michaga *et al.*, “Bioenergy with carbon capture and storage (BECCS) potential in jet fuel production from forestry residues: A combined Techno-Economic and Life Cycle Assessment approach,” *Energy Convers Manag*, vol. 255, Mar. 2022, doi: 10.1016/j.enconman.2022.115346.

[82] N. Vela-García, D. Bolonio, M. J. García-Martínez, M. F. Ortega, D. Almeida Streitwieser, and L. Canoira, “Biojet fuel production from oleaginous crop residues: thermoeconomic, life cycle and flight performance analysis,” *Energy Convers Manag*, vol. 244, Sep. 2021, doi: 10.1016/j.enconman.2021.114534.

[83] Z. Zakaria and S. K. Kamarudin, “A review of alkaline solid polymer membrane in the application of AEM electrolyzer: Materials and characterization,” *Int J Energy Res*, vol. 45, no. 13, pp. 18337–18354, 2021, doi: https://doi.org/10.1002/er.6983.

[84] F. K. Bahnamiri, M. Khalili, P. Pakzad, and M. Mehrpooya, “Techno-economic assessment of a novel power-to-liquid system for synthesis of formic acid and ammonia, based on CO2 electroreduction and alkaline water electrolysis cells,” *Renew Energy*, vol. 187, pp. 1224–1240, 2022, doi: https://doi.org/10.1016/j.renene.2022.01.085.

[85] M. Sánchez, E. Amores, D. Abad, L. Rodríguez, and C. Clemente-Jul, “Aspen Plus model of an alkaline electrolysis system for hydrogen production,” *Int J Hydrogen Energy*, vol. 45, no. 7, pp. 3916–3929, 2020, doi: https://doi.org/10.1016/j.ijhydene.2019.12.027.

[86] M. Ni, M. K. H. Leung, and D. Y. C. Leung, “Parametric study of solid oxide steam electrolyzer for hydrogen production,” *Int J Hydrogen Energy*, vol. 32, no. 13, pp. 2305–2313, 2007, doi: https://doi.org/10.1016/j.ijhydene.2007.03.001.

[87] R. Daneshpour and M. Mehrpooya, “Design and optimization of a combined solar thermophotovoltaic power generation and solid oxide electrolyser for hydrogen production,” *Energy Convers Manag*, vol. 176, pp. 274–286, Nov. 2018, doi: 10.1016/j.enconman.2018.09.033.

[88] A. A. AlZahrani and I. Dincer, “Thermodynamic and electrochemical analyses of a solid oxide electrolyzer for hydrogen production,” *Int J Hydrogen Energy*, vol. 42, no. 33, pp. 21404–21413, 2017, doi: https://doi.org/10.1016/j.ijhydene.2017.03.186.

[89] M. Ni, M. K. H. Leung, and D. Y. C. Leung, “A modeling study on concentration overpotentials of a reversible solid oxide fuel cell,” *J Power Sources*, vol. 163, no. 1, pp. 460–466, 2006, doi: https://doi.org/10.1016/j.jpowsour.2006.09.024.

[90] E. Gholamian, V. Zare, and S. M. Mousavi, “Integration of biomass gasification with a solid oxide fuel cell in a combined cooling, heating and power system: A thermodynamic and environmental analysis,” *Int J Hydrogen Energy*, vol. 41, no. 44, pp. 20396–20406, 2016, doi: https://doi.org/10.1016/j.ijhydene.2016.07.217.

[91] A. Habibollahzade, E. Gholamian, and A. Behzadi, “Multi-objective optimization and comparative performance analysis of hybrid biomass-based solid oxide fuel cell/solid oxide electrolyzer cell/gas turbine using different gasification agents,” *Appl Energy*, vol. 233–234, pp. 985–1002, Jan. 2019, doi: 10.1016/j.apenergy.2018.10.075.

[92] S. Mirmasoumi, R. K. Saray, and S. Ebrahimi, “Evaluation of thermal pretreatment and digestion temperature rise in a biogas fueled combined cooling, heat, and power system using exergo-economic analysis,” *Energy Convers Manag*, vol. 163, pp. 219–238, 2018, doi: https://doi.org/10.1016/j.enconman.2018.02.069.

[93] I. Angelidaki *et al.*, “Biogas upgrading and utilization: Current status and perspectives,” *Biotechnol Adv*, vol. 36, no. 2, pp. 452–466, 2018, doi: https://doi.org/10.1016/j.biotechadv.2018.01.011.

[94] A. Skorek-Osikowska, M. Martín-Gamboa, and J. Dufour, “Thermodynamic, economic and environmental assessment of renewable natural gas production systems,” *Energy Conversion and Management: X*, vol. 7, Sep. 2020, doi: 10.1016/j.ecmx.2020.100046.

[95] Y. Liu, C. Liao, Y. Tang, J. Tang, Y. Sun, and X. Ma, “Techno-environmental-economic evaluation of the small-scale municipal solid waste (MSW) gasification-based and incineration-based power generation plants,” *J Taiwan Inst Chem Eng*, vol. 141, p. 104594, 2022, doi: https://doi.org/10.1016/j.jtice.2022.104594.

[96] H. Ghiasirad, T. Gholizadeh Baris, S. Rostami, B. Stanek, A. Skorek-Osikowska, and L. Bartela, “A Triple Solar Desalination System Integrated with a Biomass Fuelled SCO2 Power Cycle: Thermodynamic Modelling,” *36th International Conference on Efficiency, Cost, Optimization, Simulation and Environmental Impact of Energy Systems (ECOS 2023)*, pp. 1854–1865, 2023, doi: 10.52202/069564-0168.

[97] Q. Eri, W. Wu, and X. Zhao, “Numerical Investigation of the Air-Steam Biomass Gasification Process Based on Thermodynamic Equilibrium Model,” *Energies (Basel)*, vol. 10, no. 12, 2017, doi: 10.3390/en10122163.

[98] A. Bauen, “Biomass Gasification,” in *Encyclopedia of Energy*, C. J. Cleveland, Ed., New York: Elsevier, 2004, pp. 213–221. doi: https://doi.org/10.1016/B0-12-176480-X/00356-9.

[99] A. Skorek-Osikowska, “Thermodynamic and environmental study on synthetic natural gas production in power to gas approaches involving biomass gasification and anaerobic digestion,” *Int J Hydrogen Energy*, vol. 47, no. 5, pp. 3284–3293, 2022, doi: https://doi.org/10.1016/j.ijhydene.2021.01.002.

[100] N. Cerone and F. Zimbardi, “Effects of Oxygen and Steam Equivalence Ratios on Updraft Gasification of Biomass,” *Energies (Basel)*, vol. 14, no. 9, 2021, doi: 10.3390/en14092675.

[101] A. Skorek-Osikowska, M. Martín-Gamboa, and J. Dufour, “Thermodynamic, economic and environmental assessment of renewable natural gas production systems,” *Energy Conversion and Management: X*, vol. 7, Sep. 2020, doi: 10.1016/j.ecmx.2020.100046.

[102] B. Eisavi, F. Ranjbar, H. Nami, and A. Chitsaz, “Low-carbon biomass-fueled integrated system for power, methane and methanol production,” *Energy Convers Manag*, vol. 253, Feb. 2022, doi: 10.1016/j.enconman.2021.115163.

[103] L. Meng and T. Tsuru, “Chapter 6 - Microporous Silica Membrane Reactors,” in *Current Trends and Future Developments on (Bio-) Membranes*, A. Basile and K. Ghasemzadeh, Eds., Elsevier, 2019, pp. 127–156. doi: https://doi.org/10.1016/B978-0-12-816350-4.00006-4.

[104] S. S. Hla *et al.*, “Kinetics of high-temperature water-gas shift reaction over two iron-based commercial catalysts using simulated coal-derived syngases,” *Chemical Engineering Journal*, vol. 146, no. 1, pp. 148–154, 2009, doi: https://doi.org/10.1016/j.cej.2008.09.023.

[105] M. E. Adrover, D. Borio, and M. Pedernera, “Comparison between WGS membrane reactors operating with and without sweep gas: Limiting conditions for co-current flow,” *Int J Hydrogen Energy*, vol. 42, no. 8, pp. 5139–5149, 2017, doi: https://doi.org/10.1016/j.ijhydene.2016.11.075.

[106] A. S. Augustine, Y. H. Ma, and N. K. Kazantzis, “High pressure palladium membrane reactor for the high temperature water–gas shift reaction,” *Int J Hydrogen Energy*, vol. 36, no. 9, pp. 5350–5360, 2011, doi: https://doi.org/10.1016/j.ijhydene.2011.01.172.

[107] M. Aneke and M. Wang, “Improving the Energy Efficiency of Cryogenic Air Separation Units (ASU) through Compressor Waste Heat Recovery using Direct Binary Heat Engine Cycle,” in *12th International Symposium on Process Systems Engineering and 25th European Symposium on Computer Aided Process Engineering*, vol. 37, K. V Gernaey, J. K. Huusom, and R. Gani, Eds., in Computer Aided Chemical Engineering, vol. 37. , Elsevier, 2015, pp. 2375–2380. doi: https://doi.org/10.1016/B978-0-444-63576-1.50090-X.

[108] Ł. Bartela, J. Ochmann, S. Waniczek, M. Lutyński, G. Smolnik, and S. Rulik, “Evaluation of the energy potential of an adiabatic compressed air energy storage system based on a novel thermal energy storage system in a post mining shaft,” *J Energy Storage*, vol. 54, p. 105282, 2022, doi: https://doi.org/10.1016/j.est.2022.105282.

[109] J. Ochmann, K. Rusin, S. Rulik, S. Waniczek, and Ł. Bartela, “Experimental and computational analysis of packed-bed thermal energy storage tank designed for adiabatic compressed air energy storage system,” *Appl Therm Eng*, vol. 213, p. 118750, 2022, doi: https://doi.org/10.1016/j.applthermaleng.2022.118750.

[110] Y. Yao, X. Liu, D. Hildebrandt, and D. Glasser, “The effect of CO2 on a cobalt-based catalyst for low temperature Fischer–Tropsch synthesis,” *Chemical Engineering Journal*, vol. 193–194, pp. 318–327, Jun. 2012, doi: 10.1016/J.CEJ.2012.04.045.

[111] D. Selvatico, A. Lanzini, and M. Santarelli, “Low Temperature Fischer-Tropsch fuels from syngas: Kinetic modeling and process simulation of different plant configurations,” *Fuel*, vol. 186, pp. 544–560, Dec. 2016, doi: 10.1016/J.FUEL.2016.08.093.

[112] H. S. Song, D. Ramkrishn, S. Trinh, and H. Wright, “Operating strategies for Fischer-Tropsch reactors: A model-directed study,” *Korean Journal of Chemical Engineering*, vol. 21, no. 2, pp. 308–317, 2004, doi: 10.1007/BF02705414/METRICS.

[113] B. Todic *et al.*, “Kinetic model of Fischer-Tropsch synthesis in a slurry reactor on Co-Re/Al2O3 catalyst,” *Ind Eng Chem Res*, vol. 52, no. 2, pp. 669–679, Jan. 2013, doi: 10.1021/IE3028312/SUPPL_FILE/IE3028312_SI_001.PDF.

[114] C. D. Collins, “Implementing Phytoremediation of Petroleum Hydrocarbons,” pp. 99–108, 2007, doi: 10.1007/978-1-59745-098-0_8.

[115] V. Calemma, C. Gambaro, W. O. Parker, R. Carbone, R. Giardino, and P. Scorletti, “Middle distillates from hydrocracking of FT waxes: Composition, characteristics and emission properties,” *Catal Today*, vol. 149, no. 1–2, pp. 40–46, Jan. 2010, doi: 10.1016/J.CATTOD.2009.03.018.

[116] H. S. Song, D. Ramkrishn, S. Trinh, and H. Wright, “Operating strategies for Fischer-Tropsch reactors: A model-directed study,” *Korean Journal of Chemical Engineering*, vol. 21, no. 2, pp. 308–317, 2004, doi: 10.1007/BF02705414/METRICS.

[117] F. J. Campanario and F. J. Gutiérrez Ortiz, “Techno-economic assessment of bio-oil aqueous phase-to-liquids via Fischer-Tropsch synthesis and based on supercritical water reforming,” *Energy Convers Manag*, vol. 154, pp. 591–602, Dec. 2017, doi: 10.1016/J.ENCONMAN.2017.10.096.

[118] M. M. Paulsen, S. B. Petersen, E. M. Lozano, and T. H. Pedersen, “Techno-economic study of integrated high-temperature direct air capture with hydrogen-based calcination and Fischer–Tropsch synthesis for jet fuel production,” *Appl Energy*, vol. 369, Sep. 2024, doi: 10.1016/j.apenergy.2024.123524.

[119] F. J. Campanario and F. J. Gutiérrez Ortiz, “Fischer-Tropsch biofuels production from syngas obtained by supercritical water reforming of the bio-oil aqueous phase,” *Energy Convers Manag*, vol. 150, pp. 599–613, Oct. 2017, doi: 10.1016/J.ENCONMAN.2017.08.053.

[120] “A guide to the guidelines: The UNIDO method of economic project evaluation (World Bank staff working paper): Amazon.co.uk: Hansen, John R: Books.” Accessed: Apr. 08, 2025. [Online]. Available: https://www.amazon.co.uk/guide-guidelines-economic-project-evaluation/dp/B000739J2U

[121] F. Cheng, A. A. Small, and L. M. Colosi, “The levelized cost of negative CO2 emissions from thermochemical conversion of biomass coupled with carbon capture and storage,” *Energy Convers Manag*, vol. 237, p. 114115, Jun. 2021, doi: 10.1016/J.ENCONMAN.2021.114115.

[122] M. Peters, K. Timmerhaus, and R. West, “Heat-Transfer Equipment—Design and Costs,” *Plant Design and Economics for Chemical Engineers*, pp. 716–724, 2002.

[123] H. Ghiasirad, M. Khalili, F. K. Bahnamiri, P. Pakzad, and A. Skorek-Osikowska, “Techno-economic comparison of power-to-ammonia and biomass-to-Ammonia plants using electrolyzer, CO2 capture and water-gas-shift membrane reactor,” *J Taiwan Inst Chem Eng*, vol. 151, Oct. 2023, doi: 10.1016/j.jtice.2023.105097.

[124] N. Asgari, R. Khoshbakhti Saray, and S. Mirmasoumi, “Seasonal exergoeconomic assessment and optimization of a dual-fuel trigeneration system of power, cooling, heating, and domestic

hot water, proposed for Tabriz, Iran," *Renew Energy*, vol. 206, pp. 192–213, Apr. 2023, doi: 10.1016/j.renene.2023.02.028.

[125] M. Ostadi, L. Bromberg, D. R. Cohn, and E. Gençer, "Flexible methanol production process using biomass/municipal solid waste and hydrogen produced by electrolysis and natural gas pyrolysis," *Fuel*, vol. 334, Feb. 2023, doi: 10.1016/j.fuel.2022.126697.

[126] A. Ebrahimi-Moghadam, A. J. Moghadam, M. Farzaneh-Gord, and K. Aliakbari, "Proposal and assessment of a novel combined heat and power system: Energy, exergy, environmental and economic analysis," *Energy Convers Manag*, vol. 204, Jan. 2020, doi: 10.1016/j.enconman.2019.112307.

[127] H. Ghiasirad *et al.*, "LCA and exergy-economic evaluation of a biogas-to-fuels system using CO2 hydrogenation and exhaust gas recycling," *Energy Conversion and Management: X*, vol. 26, p. 100897, 2025, doi: https://doi.org/10.1016/j.ecmx.2025.100897.

[128] J. Andersson, J. Lundgren, and M. Marklund, "Methanol production via pressurized entrained flow biomass gasification - Techno-economic comparison of integrated vs. stand-alone production," *Biomass Bioenergy*, vol. 64, pp. 256–268, 2014, doi: 10.1016/j.biombioe.2014.03.063.

[129] A. Skorek-Osikowska, M. Martín-Gamboa, and J. Dufour, "Thermodynamic, economic and environmental assessment of renewable natural gas production systems," *Energy Conversion and Management: X*, vol. 7, Sep. 2020, doi: 10.1016/j.ecmx.2020.100046.

[130] C. N. Hamelinck and A. P. C. Faaij, "Future prospects for production of methanol and hydrogen from biomass."

[131] L. R. Clausen, B. Elmegaard, and N. Houbak, "Technoeconomic analysis of a low CO2 emission dimethyl ether (DME) plant based on gasification of torrefied biomass," *Energy*, vol. 35, no. 12, pp. 4831–4842, 2010, doi: https://doi.org/10.1016/j.energy.2010.09.004.

[132] M. Haghanimanesh, E. Baniasadi, J. Karimi Kerdabadi, and X. Yu, "Exergoeconomic analysis of a novel trigeneration cycle based on steel slag heat recovery and biogas production in steelmaking plants," *Energy Convers Manag*, vol. 263, Jul. 2022, doi: 10.1016/j.enconman.2022.115688.

[133] P. Rotunno, A. Lanzini, and P. Leone, "Energy and economic analysis of a water scrubbing based biogas upgrading process for biomethane injection into the gas grid or use as transportation fuel," *Renew Energy*, vol. 102, pp. 417–432, Mar. 2017, doi: 10.1016/j.renene.2016.10.062.

[134] A. Arsalis, "Thermoeconomic modeling and parametric study of hybrid SOFC-gas turbine-steam turbine power plants ranging from 1.5 to 10 MWe," *J Power Sources*, vol. 181, no. 2, pp. 313–326, Jul. 2008, doi: 10.1016/j.jpowsour.2007.11.104.

[135] A. Bejan, G. (George) Tsatsaronis, and M. J. Moran, *Thermal design and optimization*. Wiley, 1996.

[136] A. Atienza-Márquez, D. S. Ayou, J. C. Bruno, and A. Coronas, "Energy polygeneration systems based on LNG-regasification: Comprehensive overview and techno-economic feasibility," *Thermal Science and Engineering Progress*, vol. 20, Dec. 2020, doi: 10.1016/j.tsep.2020.100677.

[137] M. Khaljani, R. Khoshbakhti Saray, and K. Bahlouli, “Comprehensive analysis of energy, exergy and exergo-economic of cogeneration of heat and power in a combined gas turbine and organic Rankine cycle,” *Energy Convers Manag*, vol. 97, pp. 154–165, 2015, doi: https://doi.org/10.1016/j.enconman.2015.02.067.

[138] Z. Wu *et al.*, “Thermo-economic modeling and analysis of an NG-fueled SOFC-WGS-TSA-PEMFC hybrid energy conversion system for stationary electricity power generation,” *Energy*, vol. 192, p. 116613, 2020, doi: https://doi.org/10.1016/j.energy.2019.116613.

[139] Y. S. Sanusi and E. M. A. Mokheimer, “Thermo-economic optimization of hydrogen production in a membrane-SMR integrated to ITM-oxy-combustion plant using genetic algorithm,” *Appl Energy*, vol. 235, pp. 164–176, 2019, doi: https://doi.org/10.1016/j.apenergy.2018.10.082.

[140] M. Meratizaman, S. Monadizadeh, A. Ebrahimi, H. Akbarpour, and M. Amidpour, “Scenario analysis of gasification process application in electrical energy-freshwater generation from heavy fuel oil, thermodynamic, economic and environmental assessment,” *Int J Hydrogen Energy*, vol. 40, no. 6, pp. 2578–2600, 2015, doi: https://doi.org/10.1016/j.ijhydene.2014.12.072.

[141] M. Martínez, A. Neut, and D. Ramírez, “Equilibrium of the Euro-Dollar Exchange Rate: A Long-Term Perspective Executive summary”.

[142] D. Katla-Milewska, S. M. Nazir, and A. Skorek-Osikowska, “Synthetic natural gas (SNG) production with higher carbon recovery from biomass: Techno-economic assessment,” *Energy Convers Manag*, vol. 300, p. 117895, 2024, doi: https://doi.org/10.1016/j.enconman.2023.117895.

[143] N. Yang, F. Kang, Z. Liu, X. Ge, and Y. Zhou, “An integrated CCU-plant scheme and assessment for conversion of captured CO2into methanol,” *International Journal of Low-Carbon Technologies*, vol. 17, pp. 550–562, 2022, doi: 10.1093/ijlct/ctac038.

[144] A. Skorek-Osikowska, Ł. Bartela, J. Kotowicz, A. Sobolewski, T. Iluk, and L. Remiorz, “The influence of the size of the CHP (combined heat and power) system integrated with a biomass fueled gas generator and piston engine on the thermodynamic and economic effectiveness of electricity and heat generation,” *Energy*, vol. 67, pp. 328–340, 2014, doi: https://doi.org/10.1016/j.energy.2014.01.015.

[145] N. Yusuf, R. Govindan, and T. Al-Ansari, “Techno-economic analysis of flexible AP-X LNG production process under risks and uncertainties,” 2022, pp. 367–372. doi: 10.1016/b978-0-323-95879-0.50062-x.

[146] M. Ostadi, G. Zang, L. Bromberg, D. R. Cohn, and E. Gençer, “Enhancing Biomass-to-Liquid conversion through synergistic integration of natural gas pyrolysis: process options and environmental implications,” *Energy Convers Manag*, vol. 302, Feb. 2024, doi: 10.1016/j.enconman.2024.118142.

[147] M. Wierzbowski, I. Filipiak, and W. Lyzwa, “Polish energy policy 2050 – An instrument to develop a diversified and sustainable electricity generation mix in coal-based energy system,” *Renewable and Sustainable Energy Reviews*, vol. 74, pp. 51–70, Jul. 2017, doi: 10.1016/J.RSER.2017.02.046.

[148] B. Sliz-Szkliniarz, J. Eberbach, B. Hoffmann, and M. Fortin, “Assessing the cost of onshore wind development scenarios: Modelling of spatial and temporal distribution of wind power for the

case of Poland," *Renewable and Sustainable Energy Reviews*, vol. 109, pp. 514–531, Jul. 2019, doi: 10.1016/J.RSER.2019.04.039.

[149] S. A. Aromada, N. H. Eldrup, F. Normann, and L. E. Øi, "Techno-Economic Assessment of Different Heat Exchangers for CO2 Capture," *Energies (Basel)*, vol. 13, no. 23, 2020, doi: 10.3390/en13236315.

[150] T. Taner, S. A. H. Naqvi, and M. Ozkaymak, "Techno-economic Analysis of a More Efficient Hydrogen Generation System Prototype: A Case Study of PEM Electrolyzer with Cr-C Coated SS304 Bipolar Plates," *Fuel Cells*, vol. 19, no. 1, pp. 19–26, 2019, doi: https://doi.org/10.1002/fuce.201700225.

[151] H. Rostamzadeh, H. Ghiasirad, M. Amidpour, and Y. Amidpour, "Performance enhancement of a conventional multi-effect desalination (MED) system by heat pump cycles," *Desalination*, vol. 477, p. 114261, 2020, doi: https://doi.org/10.1016/j.desal.2019.114261.

[152] Z. Zhang, B. Delcroix, O. Rezazgui, and P. Mangin, "Simulation and techno-economic assessment of bio-methanol production from pine biomass, biochar and pyrolysis oil," *Sustainable Energy Technologies and Assessments*, vol. 44, Apr. 2021, doi: 10.1016/j.seta.2021.101002.

[153] G. Pasini, A. Baccioli, L. Ferrari, M. Antonelli, S. Frigo, and U. Desideri, "Biomethane grid injection or biomethane liquefaction: A technical-economic analysis," *Biomass Bioenergy*, vol. 127, Aug. 2019, doi: 10.1016/j.biombioe.2019.105264.

[154] M. Panahi, A. Rafiee, S. Skogestad, and M. Hillestad, "A natural gas to liquids process model for optimal operation," *Ind Eng Chem Res*, vol. 51, no. 1, pp. 425–433, Jan. 2012, doi: 10.1021/ie2014058.

[155] S. Mingolla *et al.*, "Effects of emissions caps on the costs and feasibility of low-carbon hydrogen in the European ammonia industry," *Nature Communications 2024 15:1*, vol. 15, no. 1, pp. 1–23, May 2024, doi: 10.1038/s41467-024-48145-z.

[156] "ISO 14040:2006 - Environmental management — Life cycle assessment — Principles and framework." Accessed: Feb. 03, 2025. [Online]. Available: https://www.iso.org/standard/37456.html

[157] N. E.-S. A. at the 21st century and undefined 2019, "Attributional and consequential life cycle assessment," *books.google.comT EkvallSustainability Assessment at the 21st century, 2019•books.google.com*, Accessed: Aug. 23, 2025. [Online]. Available: https://books.google.com/books?hl=en&lr=&id=yJj8DwAAQBAJ&oi=fnd&pg=PA41&dq=Chapter++Attributional+and+Consequential++Life+Cycle+Assessment++Tomas+Ekvall&ots=4vCxJeSIXf&sig=al7d5KvUM9_BeeUvhhFqAIv3azE

[158] A. Zamagni, J. Guinée, R. Heijungs, P. Masoni, and A. Raggi, "Lights and shadows in consequential LCA," *International Journal of Life Cycle Assessment*, vol. 17, no. 7, pp. 904–918, Aug. 2012, doi: 10.1007/S11367-012-0423-X/TABLES/2.

[159] Y. Yang, "A unified framework of life cycle assessment," *International Journal of Life Cycle Assessment*, vol. 24, no. 4, pp. 620–626, Apr. 2019, doi: 10.1007/S11367-019-01595-W/FIGURES/1.

[160] D. Rajagopal and D. Zilberman, “On market-mediated emissions and regulations on life cycle emissions,” *Ecological Economics*, vol. 90, pp. 77–84, Jun. 2013, doi: 10.1016/J.ECOLECON.2013.03.006.

[161] M. A. Thomassen, R. Dalgaard, M. A. Thomassen, I. De Boer, R. Dalgaard, and R. Heijungs, “LCA FOR ENERGY SYSTEMS AND FOOD PRODUCTS • CASE STUDY Attributional and consequential LCA of milk production,” *Int J Life Cycle Assess*, vol. 13, pp. 339–349, 2008, doi: 10.1007/s11367-008-0007-y.

[162] N. Bamber *et al.*, “Comparing sources and analysis of uncertainty in consequential and attributional life cycle assessment: review of current practice and recommendations,” *Int J Life Cycle Assess*, vol. 25, pp. 168–180, 2020, doi: 10.1007/s11367-019-01663-1.

[163] T. Schaubroeck, S. Schaubroeck, R. Heijungs, A. Zamagni, M. Brandão, and E. Benetto, “Attributional & Consequential Life Cycle Assessment: Definitions, Conceptual Characteristics and Modelling Restrictions,” *Sustainability 2021, Vol. 13, Page 7386*, vol. 13, no. 13, p. 7386, Jul. 2021, doi: 10.3390/SU13137386.

[164] J. M. Lessard, G. Habert, A. Tagnit-Hamou, and B. Amor, “Assessing robustness of consequential LCA: Insights from a multiregional economic model tailored to the cement industrial symbiosis,” *J Ind Ecol*, vol. 28, no. 6, pp. 1392–1408, Dec. 2024, doi: 10.1111/JIEC.13546.

[165] B. P. Weidema, M. Pizzol, J. Schmidt, and G. Thoma, “Social responsibility is always consequential — Rebuttal to Brander, Burritt and Christ (2019): Coupling attributional and consequential life cycle assessment: A matter of social responsibility,” *J Clean Prod*, vol. 223, pp. 12–13, Jun. 2019, doi: 10.1016/J.JCLEPRO.2019.03.136.

[166] “ecoinvent v3.11 - ecoinvent.” Accessed: Sep. 05, 2025. [Online]. Available: https://ecoinvent.org/ecoinvent-v3-11/?utm_source=chatgpt.com

[167] O. Jolliet *et al.*, “IMPACT 2002+: A New Life Cycle Impact Assessment Methodology,” *International Journal of Life Cycle Assessment*, vol. 8, no. 6, pp. 324–330, 2003, doi: 10.1007/BF02978505/METRICS.

[168] “European Platform on LCA | EPLCA.” Accessed: Sep. 05, 2025. [Online]. Available: https://eplca.jrc.ec.europa.eu/ilcd.html

[169] K. Chomkhamsri, M.-A. Wolf, and R. Pant, “International Reference Life Cycle Data System (ILCD) Handbook: Review schemes for Life Cycle Assessment,” 2011. [Online]. Available: https://api.semanticscholar.org/CorpusID:162785595

[170] F. Ebrahimian, B. Khoshnevisan, A. Mohammadi, K. Karimi, and M. Birkved, “A biorefinery platform to valorize organic fraction of municipal solid waste to biofuels: An early environmental sustainability guidance based on life cycle assessment,” *Energy Convers Manag*, vol. 283, May 2023, doi: 10.1016/j.enconman.2023.116905.

[171] F. Ebrahimian and A. Mohammadi, “Assessing the environmental footprints and material flow of 2,3-butanediol production in a wood-based biorefinery,” *Bioresour Technol*, vol. 387, Nov. 2023, doi: 10.1016/j.biortech.2023.129642.

[172] B. P. Weidema, N. Frees, and A.-M. Nielsen, “Marginal Production Technologies LCA Methodology ~i ! ~i i i ! i i i ~j ~r , ! i ~ 84 :~i~i! Marginal Production Technologies for Life Cycle Inventories.”

[173] M. A. J. Huijbregts *et al.*, “ReCiPe2016: a harmonised life cycle impact assessment method at midpoint and endpoint level,” *International Journal of Life Cycle Assessment*, vol. 22, no. 2, pp. 138–147, Feb. 2017, doi: 10.1007/S11367-016-1246-Y/TABLES/2.

[174] M. A. J. Huijbregts *et al.*, “ReCiPe2016: a harmonised life cycle impact assessment method at midpoint and endpoint level,” *International Journal of Life Cycle Assessment*, vol. 22, no. 2, pp. 138–147, Feb. 2017, doi: 10.1007/s11367-016-1246-y.

[175] “Poland energy mix 2023 - IEA.” Accessed: Apr. 03, 2025. [Online]. Available: https://www.iea.org/countries/poland/energy-mix

[176] D. Humbird *et al.*, “Process Design and Economics for Biochemical Conversion of Lignocellulosic Biomass to Ethanol: Dilute-Acid Pretreatment and Enzymatic Hydrolysis of Corn Stover,” 2002, Accessed: Sep. 06, 2025. [Online]. Available: http://www.osti.gov/bridge

[177] H. Ghiasirad and A. Skorek-Osikowska, “PARAMETRIC ANALYSIS OF BIOMETHANOL PRODUCTION UNIT USING BIOMASS GASIFIER AND HIGH-TEMPERATURE ELECTROLYZER,” *Proceedings of WHEC 2022 - 23rd World Hydrogen Energy Conference: Bridging Continents by H2*, pp. 252–254, 2022, Accessed: Sep. 16, 2025. [Online]. Available: https://www.scopus.com/pages/publications/85147194871

[178] T. F. Stocker *et al.*, “Climate Change 2013 – The Physical Science Basis: Working Group I Contribution to the Fifth Assessment Report of the Intergovernmental Panel on Climate Change,” *Climate Change 2013 the Physical Science Basis: Working Group I Contribution to the Fifth Assessment Report of the Intergovernmental Panel on Climate Change*, vol. 9781107057999, pp. 1–1535, Jan. 2014, doi: 10.1017/CBO9781107415324.

[179] R. Frischknecht *et al.*, “Swiss Centre for Life Cycle Inventories A joint initiative of the ETH domain and Swiss Federal Offices Implementation of Life Cycle Impact Assessment Methods Data v2.0 (2007),” 2007, Accessed: Sep. 06, 2025. [Online]. Available: www.ecoinvent.org

[180] L. Appels, J. Degrève, B. Van der Bruggen, J. Van Impe, and R. Dewil, “Influence of low temperature thermal pre-treatment on sludge solubilisation, heavy metal release and anaerobic digestion,” *Bioresour Technol*, vol. 101, no. 15, pp. 5743–5748, 2010, doi: https://doi.org/10.1016/j.biortech.2010.02.068.

[181] G. Tsatsaronis and T. Morosuk, “Advanced exergetic analysis of a novel system for generating electricity and vaporizing liquefied natural gas,” *Energy*, vol. 35, no. 2, pp. 820–829, 2010, doi: https://doi.org/10.1016/j.energy.2009.08.019.

[182] J. Joy and K. Chowdhury, “Enhancing generation of green power from the cold of vaporizing LNG at 30 bar by optimising heat exchanger surface area in a multi-staged organic Rankine cycle,” *Sustainable Energy Technologies and Assessments*, vol. 43, p. 100930, 2021, doi: https://doi.org/10.1016/j.seta.2020.100930.

[183] Y. Xiang, L. Cai, Y. Guan, W. Liu, Z. Cheng, and Z. Liu, “Study on the effect of gasification agents on the integrated system of biomass gasification combined cycle and oxy-fuel combustion,” *Energy*, vol. 206, Sep. 2020, doi: 10.1016/j.energy.2020.118131.

[184] M. Soltani *et al.*, “Diabatic Compressed Air Energy Storage (CAES) Systems: State of the Art,” in *Encyclopedia of Energy Storage*, L. F. Cabeza, Ed., Oxford: Elsevier, 2022, pp. 173–187. doi: https://doi.org/10.1016/B978-0-12-819723-3.00066-4.

[185] G. Lucio Tiago Filho, G. Andrés Lozano Vela, L. J. da Silva, M. Tonon Bitti Perazzini, E. Fernandes dos Santos, and D. Fébba, “Analysis and feasibility of a compressed air energy storage system (CAES) enriched with ethanol,” *Energy Convers Manag*, vol. 243, p. 114371, 2021, doi: https://doi.org/10.1016/j.enconman.2021.114371.

[186] “https://ispt.eu/media/2023-SOE-public-report_ISPT.pdf.”

[187] “SimaPro - Sustainability insights for informed changemakers.” Accessed: Sep. 11, 2025. [Online]. Available: https://simapro.com/

[188] C. Arnaiz del Pozo, S. Cloete, and Á. Jiménez Álvaro, “Techno-economic assessment of long-term methanol production from natural gas and renewables,” *Energy Convers Manag*, vol. 266, p. 115785, Aug. 2022, doi: 10.1016/J.ENCONMAN.2022.115785.

[189] A. A. AlZahrani and I. Dincer, “Modeling and performance optimization of a solid oxide electrolysis system for hydrogen production,” *Appl Energy*, vol. 225, pp. 471–485, Sep. 2018, doi: 10.1016/j.apenergy.2018.04.124.

[190] J. Milewski, J. Kupecki, A. Szczęśniak, and N. Uzunow, “Hydrogen production in solid oxide electrolyzers coupled with nuclear reactors,” *Int J Hydrogen Energy*, vol. 46, no. 72, pp. 35765–35776, 2021, doi: https://doi.org/10.1016/j.ijhydene.2020.11.217.

[191] H. Ghiasirad, H. Rostamzadeh, and S. Nasri, “Design and Evaluation of a New Solar Tower-Based Multi-generation System: Part II, Exergy and Exergoeconomic Modeling,” in *Integration of Clean and Sustainable Energy Resources and Storage in Multi-Generation Systems*, Cham: Springer International Publishing, 2020, pp. 103–120. doi: 10.1007/978-3-030-42420-6_6.

[192] L. Wang, J. Düll, F. Maréchal, and J. Van herle, “Trade-off designs and comparative exergy evaluation of solid-oxide electrolyzer based power-to-methane plants,” *Int J Hydrogen Energy*, vol. 44, no. 19, pp. 9529–9543, 2019, doi: https://doi.org/10.1016/j.ijhydene.2018.11.151.

[193] G. Vilardi, C. Bassano, P. Deiana, and N. Verdone, “Exergy and energy analysis of three biogas upgrading processes,” *Energy Convers Manag*, vol. 224, p. 113323, 2020, doi: https://doi.org/10.1016/j.enconman.2020.113323.

[194] H. Ghiasirad, C. Wulf, T. Gholizadeh, and A. Skorek-Osikowska, “Electrical Performance of a Liquid Biofuel Storage System Based on Renewable Energy,” *Proceedings - EUROCON 2025: 21st International Conference on Smart Technologies*, 2025, doi: 10.1109/EUROCON64445.2025.11073285.

[195] C. Loha, H. Chattopadhyay, and P. K. Chatterjee, “Three dimensional kinetic modeling of fluidized bed biomass gasification,” *Chem Eng Sci*, vol. 109, pp. 53–64, 2014, doi: https://doi.org/10.1016/j.ces.2014.01.017.

[196] H. Ishaq and C. Crawford, “CO2-based alternative fuel production to support development of CO2 capture, utilization and storage,” *Fuel*, vol. 331, p. 125684, Jan. 2023, doi: 10.1016/j.fuel.2022.125684.

[197] A. S. Kalan, H. Ghiasirad, R. K. Saray, and S. Mirmasoumi, “Thermo-economic evaluation and multi-objective optimization of a waste heat driven combined cooling and power system

based on a modified Kalina cycle," *Energy Convers Manag*, vol. 247, Nov. 2021, doi: 10.1016/j.enconman.2021.114723.

[198] H. Ghiasirad, T. Gholizadeh, J. Ochmann, M. Jurczyk, L. Bartela, and A. Skorek-Osikowska, "Synergizing compressed air energy storage and liquefied natural gas regasification in a power-to-biofuels plant," *Energy*, vol. 308, Nov. 2024, doi: 10.1016/j.energy.2024.132859.

[199] Y. Cao, H. A. Dhahad, H. Togun, A. E. Anqi, N. Farouk, and B. Farhang, "Proposal and thermo-economic optimization of using LNG cold exergy for compressor inlet cooling in an integrated biomass fueled triple combined power cycle," *Int J Hydrogen Energy*, vol. 46, no. 29, pp. 15351–15366, Apr. 2021, doi: 10.1016/j.ijhydene.2021.02.111.

[200] Z. F. Huang, K. Y. Soh, M. R. Islam, and K. J. Chua, "Digital twin driven life-cycle operation optimization for combined cooling heating and power-cold energy recovery (CCHP-CER) system," *Appl Energy*, vol. 324, Oct. 2022, doi: 10.1016/j.apenergy.2022.119774.

[201] H. Ghiasirad, N. Asgari, R. Khoshbakhti Saray, and S. Mirmasoumi, "Thermoeconomic assessment of a geothermal based combined cooling, heating, and power system, integrated with a humidification-dehumidification desalination unit and an absorption heat transformer," *Energy Convers Manag*, vol. 235, p. 113969, 2021, doi: https://doi.org/10.1016/j.enconman.2021.113969.

[202] Ł. Bartela, D. Katla, and A. Skorek-Osikowska, "Evaluation of conceptual electrolysis-based energy storage systems using gas expanders," *Int J Hydrogen Energy*, vol. 46, no. 38, pp. 20171–20182, 2021, doi: https://doi.org/10.1016/j.ijhydene.2020.01.233.

[203] H. Ghiasirad and A. Skorek-Osikowska, "Biomethanol production via electrolysis, oxy-fuel combustion, water-gas shift reaction, and LNG cold energy recovery," *Int J Hydrogen Energy*, Oct. 2023, doi: 10.1016/j.ijhydene.2023.10.089.

[204] A. A. D. Zare, M. Yari, F. Mohammadkhani, H. Nami, and U. Desideri, "Thermodynamic and exergoeconomic analysis of a multi-generation gas-to-X system based on fuel-rich combustion to produce power, hydrogen, steam and heat," *Sustain Cities Soc*, vol. 86, Nov. 2022, doi: 10.1016/j.scs.2022.104139.

[205] J. Catalano, F. Guazzone, I. P. Mardilovich, N. K. Kazantzis, and Y. H. Ma, "Hydrogen Production in a Large Scale Water–Gas Shift Pd-Based Catalytic Membrane Reactor," *Ind Eng Chem Res*, vol. 52, no. 3, pp. 1042–1055, 2013, doi: 10.1021/ie2025008.

[206] S. P. Sukhatme, "Solar energy : principles of thermal collection and storage," 1997.